UNIVERSITY OF NAPLES FEDERICO II

Department of Chemical, Materials and Industrial Production Engineering

XXX PhD Programme in

Industrial Products and Processes Engineering

Surface Green Technologies for Aeronautic Industry

PhD Tutor

Prof. Francesco Bellucci

PhD Candidate

Ing. Anna Carangelo

PhD Coordinator

Prof. Giuseppe Mensitieri

PhD Programme: November 2014 – October 2017

Unione Europea

PON Ricerca e Innovazione 2014- 2020

Ministero dell'Istruzione, dell'Università e della Ricerca

Dottorato di Ricerca in Ingegneria dei Prodotti e dei Processi Industriali

UNIVERSITY OF NAPLES FEDERICO II

Department of Chemical, Materials and Industrial Production Engineering

XXX PhD Programme in

Industrial Products and Processes Engineering

Surface Green Technologies for Aeronautic Industry

PhD Tutor

Prof. Francesco Bellucci

PhD Candidate

Ing. Anna Carangelo

PhD Coordinator

Prof. Giuseppe Mensitieri

PhD Programme: November 2014 – October 2017

List of Contents

List of figures

List of tables

List of publications

A. Carangelo, M. Curioni, A. Acquesta, T. Monetta and F. Bellucci - *"Application of EIS to in-situ characterization of hydrothermal sealing of anodized aluminum alloys comparison between hexavalent chromium-based sealing, hot water sealing and cerium-based sealing",* Journal of The Electrochemical Society, **163** (10) C619-C626, (2016).

A. Carangelo, M. Curioni, A. Acquesta, T. Monetta and F. Bellucci - *"Cerium-based sealing of anodic films on AA2024T3: Effect of pore morphology on anticorrosion performance",* Journal of The Electrochemical Society, **163** (14) C907-C916, (2016).

A. Bossio, C. Bitondo, A. Carangelo, A. Formisano, T. Monetta, R. Landolfo, F. M. azzolani, F. Bellucci - *"The use of Cold Spray to repair corroded AA6005A-T6 used for bolt-channel joints",* Key Engineering Materials, ISSN: 1662-9809, Vol.710, pp.192-197, DOI:10.4028/www.scientific.net/KEM.710.192, © 2016 Trans Tech Publications, Switzerland , (2016).

T. Monetta, A. Acquesta, A. Carangelo, F. Bellucci – "*Studio dell'effetto del grafene sulla resistenza a corrosione di rivestimenti organici - The effect of graphene loading on the corrosion resistance of organic coatings"*, (GNC) La Metallurgia Italiana, **109** (7-8) 91, (2017).

A. Carangelo, M. Curioni, A. Acquesta, T. Monetta and F. Bellucci – "*Comportamento alla corrosione di AA2024-T3 anodizzata in acido solfo-tartarico e sigillata in soluzioni eco-compatibili - Corrosion behaviour of AA2024-T3 anodized in tartaric sulphuric acid and sealed in environmentally friendly* solutions", (GNC) La Metallurgia Italiana, **109** (7-8) 83, (2017).

T. Monetta, A. Acquesta, A. Carangelo, F. Bellucci - *"The effect of graphene on the protective properties of water based epoxy coatings on Al2024-T3",* Internation Journal of Corrosion, **2017** 1-9, (2017).

T. Monetta, A. Acquesta, A. Carangelo, F. Bellucci - *"TiO_2 nanotubes on Ti dental implant. Part 1: Formation and aging in Hank's solution",* Metals, **7** (5) 167, (2017).

T. Monetta, A. Acquesta, A. Carangelo, F. Bellucci - *"TiO_2 nanotubes on Ti dental implant. Part 2: EIS characterization in Hank's solution",* Metals, **7** (6) 220, (2017).

D. B. Mitton, A. Carangelo, A. Acquesta, T. Monetta, M. Curioni and F. Bellucci - *"Selected Cr(VI) replacement options for aluminium alloys: a literature survey",* Corrosion Reviews, DOI: https://doi.org/10.1515/corrrev-2016-0059.

T. Monetta, A. Acquesta, A. Carangelo, N. Donato and F. Bellucci - *"Durability of AZ31 magnesium biodegradable alloys polydopamine aided: Part 1",* Journal of Magnesium and alloys, DOI: https://doi.org/10.1016/j.jma.2017.09.006.

T. Monetta, A. Acquesta, A. Carangelo, F. Bellucci - "Considering the effect of graphene loading in water based epoxy coatings", Journal of Coatings Technology and Research, under review.

Abstract

Chromic acid anodizing has been used for almost a century to enhance corrosion protection of aerospace alloys. For some applications, hydrothermal sealing in hexavalent chromium-containing solution is required to enhance further the corrosion resistance but, due to environmental concerns, the use of hexavalent chromium must be discontinued. Good progress has been made to replace chromates during anodizing but comparatively less effort has focused on the sealing process. In this work, porous anodic oxides were produced by traditional and modified tartaric sulfuric anodizing (TSA) processes and sealed in hot water, chromate and cerium based solutions. The sealing behaviour of a film with relatively coarse porosity, generated at high voltage (traditional TSA), was compared to the sealing behaviour of a film with finer porosity and generated at reduced potential (modified TSA). After sodium chromate sealing, the two anodizing cycles produced film with similar anticorrosion performance.

Conversely, after hot water or cerium sealing, the finer oxides generated at low voltage (modified TSA) provided much better corrosion resistance. EIS performed in-situ during sealing revealed that chromate sealing is very aggressive to the porous skeleton compared to the other sealing treatments. Therefore, the original morphology has little effect on the final performance, since both fine and coarse oxides are substantially attacked. In contrast, the oxide morphology has a substantial effect when sealing is performed in hot water or cerium-based solution. Overall, it is possible to obtain films with anticorrosion performance equivalent or improved compared to that obtained by traditional TSA anodizing cycle sealed with chromate by combining the low voltage anodizing cycle with the cerium-based sealing.

This thesis focuses also on the trivalent chromium pre-treatment (TCP) and its commercially available variants. The rationale for the focus of this paper is that in the near term, the aeronautics industry needs to move away from Cr(VI) towards a more benign commercially available chemical

treatment that can help protect the aluminium alloys used by that industry. TCPs are currently available commercially and have undergone numerous tests by multiple organizations to establish their effectiveness in reducing corrosion of both bare and painted aluminium alloys.

Chapter 1 - Aluminium Alloys

1.1 Introduction

Aluminium has a relatively short history. Today it is extensive used for its high corrosion resistance and its extreme versatility that make it suitable for a wide range of products from the essential construction material for generations of aircraft and space vehicles. Aerospace applications need strength, toughness, corrosion resistance and light weight; so aerospace industry has provided the greatest stimulus for alloy development and corrosion research, which continues even today.

Aluminium and its alloys offer a diverse range of desirable properties that can be matched precisely to the demands of each application by the appropriate choice of composition, temper and fabrication mode. Aluminium can be rolled, forged, slit and sheared and shaped by extrusion through dies of a multiplicity of shape or can be cast directly into shaped products. Aluminium and its alloys are readily recyclable, with recycled scrap providing an increasingly important and growing contribution of 23 Mt per year to the more than 60 Mt total annual metal supply [1, 2].

1.2 Aluminium and its alloys

In nature, aluminium exists as the mineral bauxite, rich in alumina. Because of its high reactivity with oxygen, aluminium requires a large amount of energy to be extracted from its ore. In 1885 aluminium was isolated as a pure element by Hans Christian Oerstedand. Its commercial production started in 1886 [3]. Nowadays bauxite production has reached 200 million tonnes worldwide; where Australia and China are the largest producers. Four tons of bauxite is used to produce two tons of alumina, which then produces one ton of aluminium [4].

Aluminium is silver-white with an atomic number of 13, an atomic weight of 27 and a melting point 683°C. It is a soft, ductile, non-toxic and paramagnetic material, with a high electric and thermal conductivity and has an excellent resistance to corrosion [3, 5, 6]. Aluminium reacts

with oxygen to produce coherent thin oxide aluminium (Al_2O_3) layer of 1-5 nm on its surface that protects the metal from further corrosion.

It can be easily extruded to form bars and tubes and rolled to foils, sheets and plates and is suitable for low cost recycling processing [3, 5]. These properties make it irreplaceable for food and pharmaceutical packaging. Additionally, it can be cast, mainly by sand and/or die casting, and machined. It is widely used in both mechanical and electrical conducting applications in modern industry.

1.3 Description of alloys and tempers

Traditionally, the global prescription of aluminium alloys for use in engineering was difficult owing to the alloy designations differing from country to country [3]. For this reason, the introduction of an International Alloy Designation System (IADS) introduced in the 1970s was a welcome rationalization and advance. The IADS, and its European Standard equivalent (EN573), give each wrought alloy a four-digit number of which the first digit is assigned on the basis of the major alloying element(s), as is summarized in Table 1, along with the associated temper description [2, 3].

Table 1 - Aluminium alloy and temper designation systems [3].

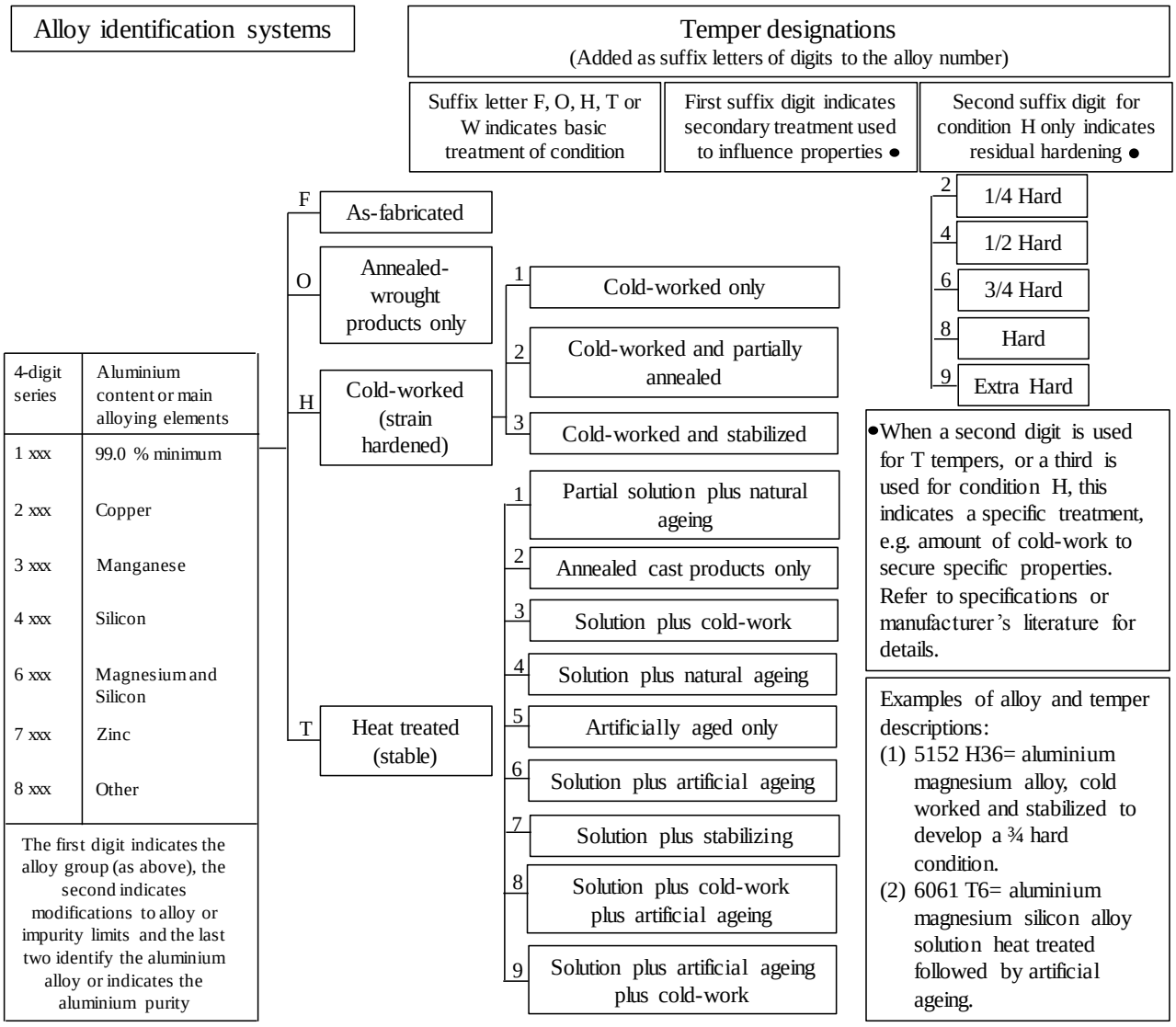

Since additions of alloying elements have great effect on the performance of aluminium alloys, an international designation system was required. The American aluminium association developed a designation system for wrought and casting alloys [7]. A four-digit numerical system was adopted; XXXX for wrought and XXX**.**X for cast aluminium alloys, respectively, where the latter incorporate three digits followed by a decimal. The first digit indicates the aluminium alloy series, representing its main alloying element. For example, 2XXX is for the aluminium-copper alloy series where the main alloying element is copper. In the 3XXX series; manganese is the main

alloying element. The second digit indicates the modification or level of impurities, if the second digit is zero it means an original alloy. The last two digits identify different aluminium alloys in a group of aluminium alloys [5-9]. Table 2 summarises the aluminium alloy series, according to their microstructure precipitates, reactivity towards the aluminium matrix as well as the applications of these series.

Table 2 - Designation, precipitates and applications of wrought and cast aluminium alloys [9].

Wrought Alloys	**Cast alloys**	**Description**	**Typical precipitates and their reactivity**	**Applications**
1XXX	1XXX	Aluminium of 99% minimum purity.	Al_3Fe [Cathodic], Al_3Mn_2 [Cathodic], α-(Fe-Mn)Si [Cathodic]	Electrical conductors, chemical process equipment foils, decorative finishes, food & pharmaceutical, packaging
2XXX	2XXX	Aluminium-copper alloys	Al_2Cu [Cathodic], Al_2CuMg [Anodic], Al(Cu-Fe-Mn) [Cathodic], Mg_2Si	Pistons, rivets, fuselage for aircraft constructions, fuel thanks
3XXX	3XXX	Aluminium-manganese alloys. Silicon and copper and/or magnesium alloys.	Al_3Mn[Cathodic], Al_6Mn[inert], Al_3(Fe-Mn)[Cathodic], Al_6(Fe-Mn) [Cathodic].	Foil, roofing sheets, manufacturing beverage cans
4XXX	4XXX	Aluminium-silicon alloys	Si [Cathodic], α-AlFeSi [Cathodic], α-Al(Fe-Mn)Si [Cathodic]	
5XXX	5XXX	Aluminium magnesium alloys	β-Al_8Mg_5 [Anodic], Al_6(Fe-Mn) [Cathodic]	Transportation structural plates, large tanks for petrol, milk, grain, pressure vessel, architectural components.
6XXX	Unused	Aluminium magnesium-silicon alloys	β-Mg_2Si[Anodic], $Al_5Cu_2Mg_8Si_8$ [Cathodic]	
7XXX	7XXX	Aluminium-zinc-magnesium alloys. Aluminium and zinc alloys.	η-$MgZn_2$ [Anodic], Al_7Cu_2Fe [Cathodic]	
8XXX	8XXX	Miscellaneous alloys, e.g. Aluminium-lithium alloys. Aluminium-tin alloys.		Nuclear energy installation, Bottle caps and soft bearing

The mechanical properties of aluminium alloys can be modified by different tempers, via selecting the temperature and time of heat treatment duration, to change the size, volume fraction and type of precipitated particles that greatly affect the mechanical properties of the treated alloy [10, 11]. These techniques and others are designated with different tempers as shown in Table 3 [12].

Table 3 - Temper designations for techniques applied for alloy performance enhancement [12].

Temper	**Enhancement techniques**
F	As-fabricated
O	Annealed
H	Strain-or work-hardened
W	Solution heat treated
T	Treated

A second treatment is represented by the first suffix digit, for example, cold worked. A second suffix digit indicates second cold worked and annealed [3] as in Table 4.

Table 4 - Mechanical properties of AA 2024 at different tempers [3, 13].

Temper	**Temper details**	**Tensile Strength (MPa)**	**Yield strength (MPa)**	**Hardness (HB)**
O	Annealed.	185	75	47
T3	Solution heat treated, cold worked and natural aged.	485	345	120
T351	Solution heat treated at 495°C, quenched, stretched 1.5-3% and natural aged for several months.	470	325	120
T4	Solution heat treated and naturally aged.	470	325	120
T6	Solution heat treated and artificial aged at 190°C for 12hrs.	475	395	-
T8	Solution heat treated, cold worked and artificially aged at 190°C for 12hrs.	480	450	-

More common heat treatment tempers are added as suffix letters and digits to the alloy number. For example, temper T351 means that the alloy is solution heat treated, quenched, stretched 1.5-3% and naturally aged for several months [3]. In general T3 and T4 are used to indicate naturally aged tempers with combination of high strength and good damage tolerance as in AA2024-T3 alloy. AA2024-T351 alloy is one of 2xxx heat treatable aluminium alloys and is the focus of this study.

1.4 Pure aluminium

Corrosion resistance of unalloyed aluminium increases with increasing metal purity. The use of the 99.8% and 99.9% grades is usually confined to those applications in which very high corrosion resistance or ductility is required. The chemical industry can advantageously use these purities for handling some products, but because of their low mechanical strength, they are sometimes used as a cladding material for a stronger substrate. Decreasing the purity results in modestly increased strength for the 99% and 99.5% grades, which still retain a high resistance to corrosion.

The 99% pure metal may be considered the more useful general-purpose metal for lightly stressed applications such as cooking utensils. These alloys are known as the 1xxx series alloys, and the last two of the four digits indicate the minimum aluminium percentage. For example, 1050 is aluminium with a minimum purity of 99.5%. Alloys for electrical use are of special composition (i.e., AA1350 conductor alloys).

1.5 Aluminium-manganese alloys

Manganese has a relatively low solubility in aluminium. The maximum solubility of manganese in α solution is 1.82 wt.% at the eutectic temperature of 657.8°C [14]. A minor addition of manganese to Al-Cu series alloys can modify the precipitation process, forming fine precipitates that restrict grain boundary movements resulting in greater age hardening and an increased cathodic polarization, providing higher corrosion resistance [15]. Additions of manganese of up to 1% form the basis for an important series of non-heat-treatable (3xxx series) wrought alloys, which have good corrosion resistance, moderate strength and high formability. These alloys are applied in construction; beverage cans industries, pressure vessels and gasoline and oil tanks [8, 14, 16].

1.6 Aluminium-magnesium alloys

Magnesium has a relatively high solubility in aluminium. Magnesium intensifies precipitation, which considerably improves the alloy strength. The improvement in performance is highly dependent on the amount of added magnesium [14]. However, additions of magnesium as an alloying element are known to reduce solid solubility of copper in Al-Cu-Mg alloys [17, 18].

Aluminium-magnesium alloys are widely used in construction, chemical storage tanks as well as in automotive and marine industries [8], because of their weld ability and relatively high corrosion resistance.

1.7 Aluminium-silicon alloys

Silicon additions alone can lower the melting point of aluminium while simultaneously increasing fluidity, which is very important and is largely the basis of aluminium casting alloys and the associated shape-casting industry [19]. Wrought 4xxx series aluminium–silicon alloys are used extensively as cladding materials for brazing alloys. Where free machining characteristics are required, this may be achieved by additions of cadmium, antimony, tin or lead.

1.8 Aluminium-copper alloys

Copper is one of the most common alloying additions to aluminium since it has both good solubility and a significant strengthening effect by its promotion of age-hardening response. Because of the low solid solubility of copper in aluminium solid solution, copper is added with less than 5 wt.%. The addition of copper along with magnesium in 2xxx series alloys has a great effect on the strength and toughness of the alloy, but conversely decreases the alloy weld ability and corrosion resistance [3, 8, 19]. Hence, aluminium-copper alloys are widely used in the aerospace industry, for example as pistons, rivets and fuselage skin in aircraft construction.

1.9 Aluminium-zinc alloys

Zinc is added to certain types of casting alloys, and wrought binary aluminium-zinc alloys are used as clad layers to sacrificially protect aerospace and armour alloys. However, binary alloys show a limited age hardening response, which is significantly increased by the addition of magnesium and copper. The high-strength 7xxx series alloys derive much of their strength from the precipitation of the Z-phase (MgZn2) and its precursor forms. The heat treatment of the 7xxx series alloys is complex, involving a range of heat treatments that have been developed to balance strength and stress corrosion cracking performance [20].

1.10 Other alloys classified as 8xxx alloys

Certain alloys high in lithium are classified as 8xxx alloys. This designation also includes alloys containing high levels of iron and manganese near the ternary eutectic content, such as 8006, that have useful combinations of strength and ductility at room temperature and retain their strength at elevated temperatures. These properties are due to the fine grain size stabilized by the finely dispersed iron-rich second phase. These alloys are used in nuclear power generation for applications demanding resistance to aqueous corrosion at elevated temperatures and pressures. Other alloys included in the 8xxx series are bearing alloys commonly used in cars and trucks which are based on the Al–Sn system (e.g., 8280 and 8081) [21].

Chapter 2 - Aluminium alloy 2024

2.1 Introduction

AA2024 alloy belongs to the aluminium-copper alloy 2xxx series characterized by high strength, but suffers from low corrosion resistance. In general, this series is used where strength and toughness are required. Therefore, AA2024 alloy is normally used in aircraft structure, rivets, truck wheels, and screw machine products.

2.2 Chemical compositions

It is well-known that the desired mechanical properties of aluminium alloys especially high strength are developed, as a result of a heterogeneous microstructure which is produced by careful addition of alloying elements and heat treatment [12]. The additives in AA2024 alloy are within the range limit of their solubility in the aluminium solid solution. The chemical compositions of AA2024 alloy in weight percentage as a maximum and a minimum are presented in Table 5 [13].

Table 5 - Composition limits of AA2024 in wt.% [13].

Element	Cu	Mg	Fe	Mn	Si	Zn	Cr	Ti	Others	Al
Min.	3.8	1.2	0.0	0.30	0.0	0.0	0.0	0.0	0.0	Bal.
Max.	4.9	1.8	0.9	0.5	0.5	0.25	0.10	0.15	0.15	Bal.

Copper is the major alloying element and plays a major role in strengthening of aluminium. It is added in a percentage within the solid solubility. The maximum solid solubility of copper in aluminium is 5.67 wt.% at 548°C and decreases to less than 0.25 wt.% at room temperature [11].

Magnesium accelerates the hardening process by enhancing the strength through precipitation of particles during aging. The presence of manganese increases the resistance of aluminium against pitting corrosion [22].

2.3 Microstructure development in Al-Cu alloys

Chemical composition and presence of Cu, Mg and other elements alongside impurities such as Si and Fe produce insoluble compounds distributed uniformly in the aluminium matrix. These intermetallics are identified as Al_2Cu, Al_2CuMg, Al_2Cu_2Fe, Al_7Cu_2Fe, $Al_{12}Si(FeMn)_3$, $Al_{20}Cu_2(FeMn)_3$, $Al_{20}Cu_3Mn_3$ in AA2024-T3 with different electrochemical behaviour of anodic and cathodic cells [22-24]. Intermetallic particles with their comparatively large size, up to 50 μm, are randomly distributed in the AA2024 alloy microstructure with spherical and irregular shapes, and are visible with low magnification optical microscopy. In AA2024 alloy Cu and Mg are the highest wt.% alloying elements compared to other elements where, they provide precipitate enhancement. Precipitates are formed during natural ageing by nucleation and growth from supersaturated solid solution. They can be in different shapes such as laths, needles and plates with small sizes ranging from a few angstroms to 0.1 μm [3, 25]. Cu in aluminium does not simply precipitate, but rather it forms metastable precipitates phase, before finally forming the equilibrium phase, such as Al_2Cu called θ-phase and Al_2CuMg called S-phase. The S-phase (Al_2CuMg) is one of the key strengthening precipitates in AA2024 alloy.

However, this phase can cause a significant reduction in the corrosion resistance [15]. A preferential growth of precipitates at grain boundaries leads to copper-depleted zones, as a result of Cu consumed by the formation of these precipitates, as suggested by Zhang et al. [26] in their studies on AA2024 alloy, accumulation of S-phases along the grain boundaries in a chain formation lead to intergranular corrosion.

Chapter 3 - Fundamentals of corrosion

3.1 Introduction

Corrosion is an electrochemical reaction of a metal with its environment [27]. So that a phenomenon of corrosion happens are necessary i) an anode (an active metal), where electrons are produced or lost; ii) a cathode (a more noble and less active metal), where electrons are consumed or gained; iii) a conductor for the transport of electrons; iv) an ionic conductor which is so called electrolyte for transport of ions in a solution.

If one of the four components is missing, corrosion cannot occur [27]. There are two types of reaction occurring on the surface of a corroding metal, i.e. oxidation and reduction reactions. Oxidation reactions release electrons at the anode to be consumed by reduction reactions at the cathode. Corrosion occurs at a rate determined by the equilibrium between these opposing electrochemical reactions. A potential difference between the anodic and cathodic reactions on the metal surface represents the driving force for the corrosion reaction.

3.2 Electrochemical reactions

Electrochemical reactions result in an electrical current which depends on the difference in potential between the metal and the solution. The metal is oxidized forming M^{n+} cations of the metal which are freed into the solution [8]:

$M \rightarrow M^{n+} + ne^{-}$ *(Loss of electrons, resulting in anodic current(-ve current))* (1)

A flux of electrons within the metal is called anodic current flow Ia, by equal consumption of these electrons from the ions in the solution and transformed to another chemical species. Ions

are reduced in the solution resulting in a cathodic current flow Ic, flowing from the solution to the metal.

$M^{n+} + ne^- \rightarrow M$ (*Reduction of ions, resulting in cathodic reduction current Ic(+ve current))* (2)

When there is no external source for electric current, the circuit formed by the metal and the solution is an open electric circuit. This means the anodic current and the cathodic current are flowing in opposite directions at equal rates. At this point, the intersection between two polarization curves, defines the corrosion intensity I_{corr} and the corrosion potential E_{corr} which is also called solution potential [28].

The study of corrosion phenomena is done through these polarisation curves which are determined experimentally, either by varying I and measuring E, or by varying E and measuring I. Kinetics of anodic and cathodic electrochemical reactions are represented by the relationship between the potential E and the corresponding electrical intensity I [8, 27]. The driving force for a corrosion reaction is the potential difference between anodic and cathodic reactions on the metal surface. Under this driving force a current flows through the corrosion cell [16, 29, 30]. The standard electrode potential for a reaction is related to the change in free energy by the equation.

$\Delta G^0 = -RTlnk$ (3)

Where ΔG^0 is the standard Gibbs free energy change of the reaction, *R* is the universal gas constant (R= 8.3144595 J $mol^{-1}K^{-1}$), *T* the absolute temperature and k is the equilibrium constant.

$Me \rightarrow Me^{n+} + ne^- \; equals \; Me^{n+} + ne^- \rightarrow Me$ (4)

The potential of this electrode is then given by the Nernst equation:

$$E = E^0 + \frac{RT}{nF} log M^{n+} \quad (5)$$

Where n is the number of electrons involved (valence electrons) and *F* is Faraday 's constant (*F* = 96.485,3365 C mol^{-1}), E^0 is the standard potential for the metal and [Me^{n+}] is the concentration of the metal ions in the solution.

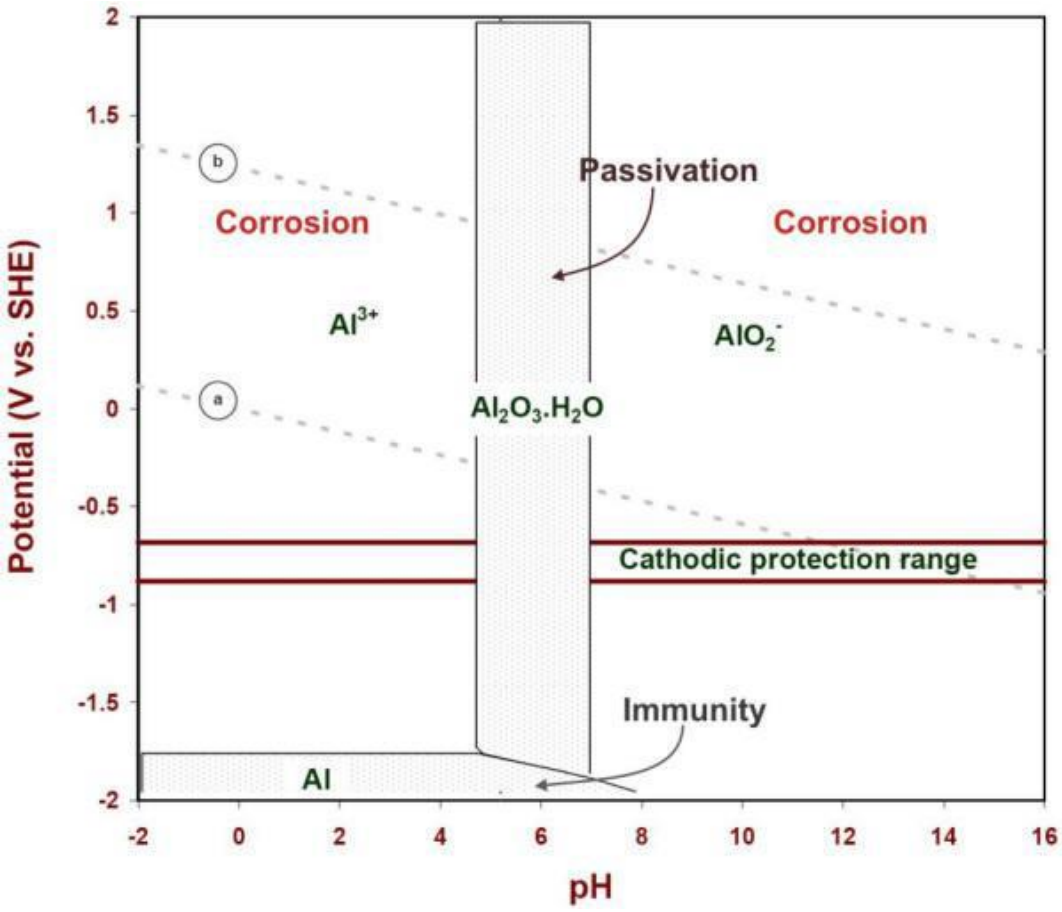

Figure 1 - Pourbaix diagrams for the Al-H_2O system at 25°C [16].

The Nernst equation is very important in electrochemistry as it relates the cell potential *E* to the standard potential E^0 and concentration of the electro-active ion [27, 30]. It is used for construction of Pourbaix diagrams shown in Figure 1, which shows the thermodynamically most stable species at different combinations of electrode potential, pH and ion activity [27, 31].

The Pourbaix diagram for the Al-H_2O system, Figure 1, shows different regions for the behaviour of aluminium in water. In the corrosive region, corrosion occurs by general dissolution of the metal. In the immune region, the metal is immune because the potential of the metal is so far depressed that the reaction is not thermodynamically possible. In the passive region, the potential of the metal is elevated and the metal becomes covered with a protective oxide film, isolating the metal from its environment. The metal is possibly resistant to corrosion in areas where the film is stable, because this thin layer, usually based on oxide, leads to a decrease in the rate of the anodic reaction.

3.3 Electrochemical polarisation

The current density due to the anodic or cathodic reaction at E_{corr} is called the corrosion current density, I_{corr}, and is a measure of the corrosion rate. Hence polarization can be defined as potential change from the equilibrium potential to the corrosion potential [32]. When the metal is not in equilibrium with the solution $|I_a| > |I_c|$ the metal is corroding, where $|I_a| < |I_c|$ the metal is plated from solution. This means that Nernst equation is not obeyed so the actual potential is different from the equilibrium potential which can be obtained by subtracting $E - E^0 = \eta$ which is known as the polarization potential or overvoltage.

A polarization curve of metal that shows active-passive behaviour is shown in Figure 2, which represents the potential versus current density. The polarization curve shows three specific behaviours: active, passive and transpassive. To be noted is the fact that the anodic polarization (dissolution) curve in Figure 2 is only possible for those metals capable of passivation, i.e. able to

form an oxide layer which protects the metal from further corrosion. Examples of metals and alloys which passivate include aluminium, titanium and stainless steels.

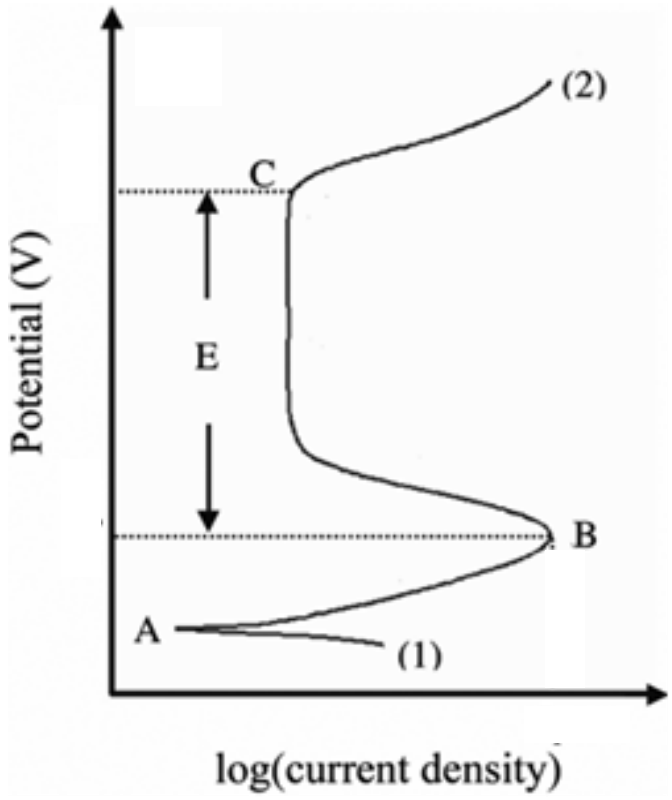

Figure 2 - Schematic diagram of polarization behaviour of metal [33].

As can be seen in the figure, the scan starts from point 1 and progresses in the positive (potential) direction until termination at point 2. There are a number of notable features on the curve. The open circuit is located at point A. At this potential the sum of the anodic and cathodic reaction rates on the electrode surface is zero. As a result, the measured current will be close to zero.

At point A, the potential is called the corrosion potential E_{corr} or open circuit potential and the current density I_{corr} can be evaluated. For potentials higher than this point, the corrosion current density increases as potential value increase and reaches a maximum at the passivation potential at

point B (E_{pp}). Further increase in potential over E_{pp}, a passive region (region E), is formed, because of aluminium forming an oxide film Al_2O_3 on the surface, reducing the corrosion rate, where the formed oxide film is characterised by poor ionic/electronic conductivity. A sudden rapid increase in current as indicated at point F is the pitting potential E_p and defined as breakdown of the passive film where pits grow and propagate with the breakdown of the oxide layer above E_p.

3.4 Corrosion of aluminium alloys

Aluminium is a very reactive metal with high affinity for oxygen. This is indicated from its position on the electromotive force series. The metal is nevertheless highly resistant to most atmospheres and to a great variety of chemical agents. This resistance is due to the inert and protective character of the aluminium oxide film which forms on the metal surface and reforms rapidly if damaged. The protective oxide film on aluminium attains a thickness of about 1 nm on freshly exposed metal in seconds. The protective oxide film inhibits corrosion because it is both resistant to dissolution and a good insulator that prevents electrons produced by oxidation of the metal from reaching the oxide/solution interface, where either the cathodic reduction of oxygen or water can take place.

Corrosion of aluminium is an electrochemical process that involves the dissolution of metal atoms; so it can take place only once the protective oxide film has been dissolved or damaged. Aluminium is amphoteric in nature, meaning its oxide film is stable in neutral conditions but soluble in acidic and alkaline environments. The thermodynamic stability of aluminium's oxide film is expressed by the potential versus pH (Pourbaix) diagram shown in Figure 3 [34].

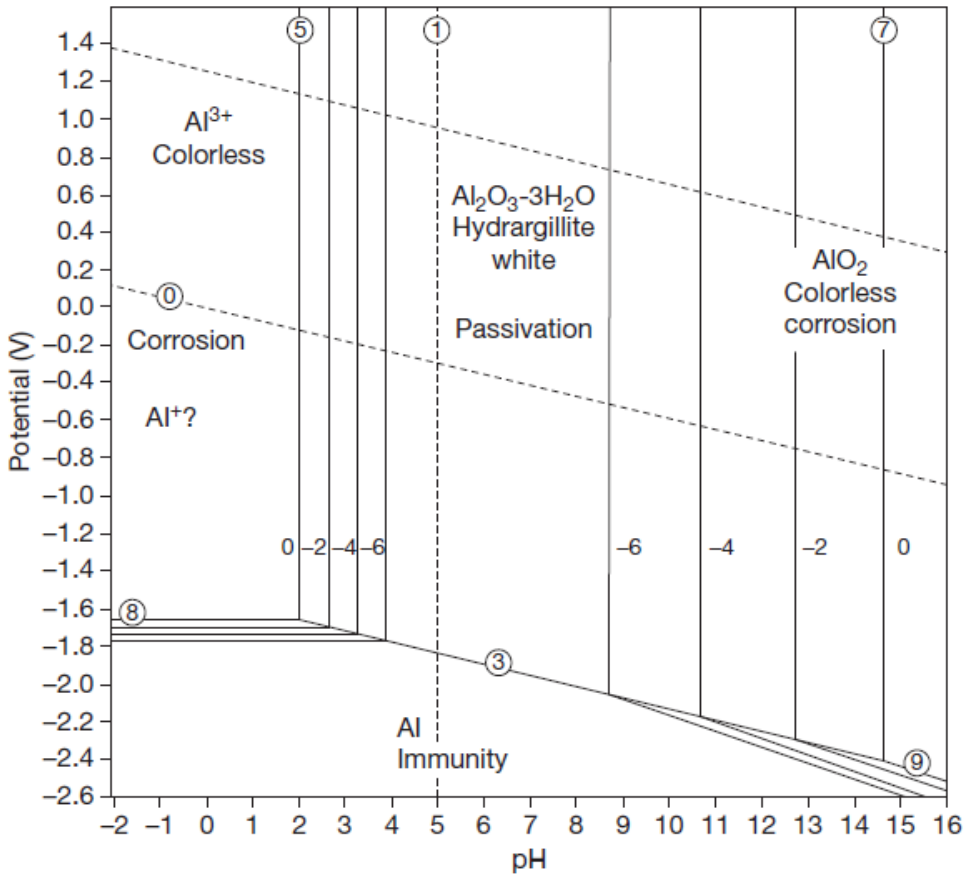

Figure 3 - Pourbaix diagram for Aluminium.

This diagram indicates the theoretical circumstances in which aluminium should show corrosion (forming Al^{3+} at low pH values and AlO^{2-} at high pH values), passivity due to hydrargillite, that is, Al_2O_3 $3H_2O$ (at near-neutral pH values) and immunity (at high negative potentials).

The nature of the oxide actually varies according to temperature, and above about 75°C boehmite (Al_2O_3 H_2O) is the stable form. It should be noted that the potential versus pH diagram does not indicate one of the most important properties of aluminium, that is, its ability to become passive in strongly acidic solutions of high redox potential such as concentrated nitric acid. The corrosion behaviour of aluminium alloys is dependent on the existence of intermetallic particles on the surface of the alloy [35]. These intermetallic particles have different electrode potentials from

the α-Al matrix, creating microgalvanic cells (anodic sites). On the other hand, these intermetallics result in a deformed and thinner oxide film layer, allowing the alloy to be more prone to corrosion [36, 37].

For aluminium-copper alloys, e.g. AA2024-T351 alloy, due to the large difference of electrode potentials between the copper-containing particles and the aluminium matrix, the resultant galvanic cells initiate corrosion in the presence of aqueous solution [21]. In addition, the thinner Al_2O_3 film grown on top of those intermetallic particles leads to an increase in the rate of dissolving film thus accelerating corrosion. The dissolution of aluminium in aqueous solution is as follows [38].

The dissolution of aluminium in water:

$$Al \rightarrow Al^{+3} + 3e^{-} \quad (6)$$

It undergoes a possible hydrolysis reaction as follows:

$$Al^{+3} + H_2O \rightarrow Al(OH)^{+2} + H^{+} \quad (7)$$

$$Al + 2H_2O \rightarrow AlO_2^{-} + 4H^{+} + 3e^{-} \quad (8)$$

$$Al + 2H_2O \rightarrow Al(OH)^{2+} + H^{+} + 3e^{-} \quad (9)$$

$$Al + 3H_2O \rightarrow Al(OH)^{3+} + 3H^{+} + 3e^{-} \quad (10)$$

$$2Al + 4H_2O \rightarrow Al_2O_3 \cdot H_2O + 6H^{+} + 6e^{-} \quad (11)$$

Dissolution of aluminium in chloride

$$Al^{+3} + Cl^{-} \rightarrow AlCl^{+2} \quad (12)$$

A faster reaction is:

$$AlOH^{+2} + Cl^{-} \rightarrow Al(OH)Cl^{+} \quad (13)$$

The dissolution of aluminium in sulphate aqueous solutions is as follows [38]:

$$2Al^{+3} + 3SO_4^{2-} \rightarrow Al_2(SO_4)_3 \quad (14)$$

$$AlOH^{+2} + SO_4^{2-} \rightarrow Al(OH)SO_4 \quad (15)$$

The above reactions illustrate the reactions leading to the corrosion of aluminium.

3.4.1 General dissolution

As a general rule, general dissolution occurs spontaneously in strongly acidic or strongly alkaline solutions (as predicted by the Pourbaix diagram), but there are specific exceptions. Thus, in concentrated nitric acid, the metal is passive and the kinetics of the process is controlled by ionic transport through the oxide film, while inhibitors such as silicates permit the use of some alkaline solutions (up to pH 11.5) to be used with aluminium.

Even where corrosion may occur to a 'limited' extent, aluminium is often preferred to other metals because its corrosion products are colourless.

3.4.2 Pitting corrosion

This is the most commonly encountered form of aluminium corrosion. In certain near-neutral aqueous solutions, a pit once initiated will continue to propagate as the solution within the pit becomes acidified and the alumina is no longer able to form a protective film to prevent pit growth [39]. Pitting corrosion is generally associated with localised breakdown of the protective film on the surface of a metal when exposed to environment containing aggressive Cl^- ions [4]. Pits may form at scratches, mechanical defects or stochastic local discontinuities in the oxide film. Pitting occurs only in the near neutral pH range since the oxide is unstable in a bulk sense under acidic or alkaline conditions. Chlorides facilitate the breakdown of the film by forming $AlCl^3$, which is also usually present in the solution in the pits. When aluminium ions migrate away from the pits, alumina precipitates as a membrane, further isolating and intensifying local acidity, and sustained pitting of the metal results.

Pitting corrosion in aluminium alloys follows three stages:

1. Pits initiation: the presence of intermetallic particles on the surface work as preferential site for pits to initiate, because of difference in potentials with the substrate.

2. Metastable pits: pits initiate and then grow up to a point below the critical pitting potential and then re-passivate for a short time (at low current pits re-passivate). At the end of this stage the protective thin film breaks down.

3. Pits stabilization: Pits propagate again and reach stability in growth. This occurs when the potential reaches a certain level called critical pitting potential (i.e. 10^{-2} A/cm^2 is required for stable growth of pits to be maintained in the aggressive solution) [15, 31, 39].

There are several factors playing important roles in the process of pitting corrosion in aluminium and aluminium alloys. Two electrochemical reactions, i.e. anodic and cathodic reactions, occur in a pit as illustrated in Figure 4.

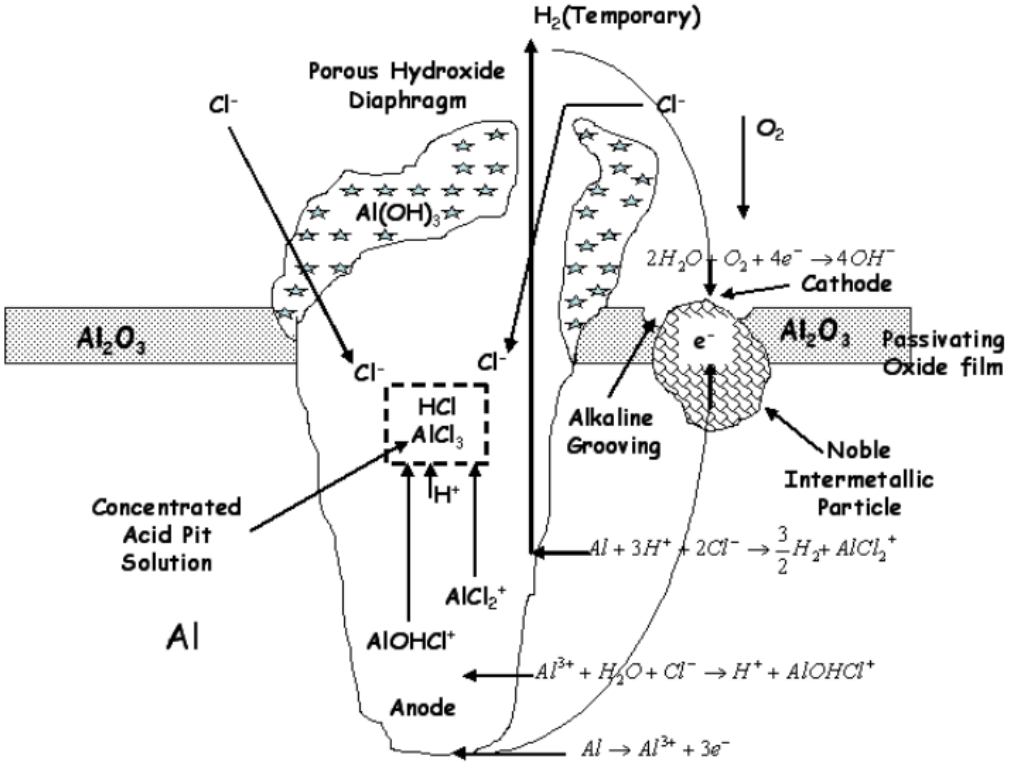

Figure 4 - Schematic diagram for pit propagation mechanism of aluminium alloy in chloride solution adapted from reference [21].

Anodic reaction proceeds with dissolution of aluminium at the base of the pit:

$$Al \rightarrow Al^{+3} + 3e^{-} \quad (16)$$

In order to initiate pitting, aggressive anions are necessary. Chloride anions can migrate from the bulk electrolyte to pits in order to satisfy charge neutrality. This leads to the decrease in pH by hydrolysis as follow:

$$Al^{+3} + 3H_2O \rightarrow Al(OH)^{3+} + 3H^+ \quad (17)$$

$$Al^{+3} + H_2O + Cl^- \rightarrow H^+ + AlOHCl^+ \quad (18)$$

$$2H^+ + 2e^- \rightarrow H_2 \quad (19)$$

$$2Al + 6H^+ + 4Cl^- \rightarrow 3H_2 + 2AlCl_2^+ \quad (20)$$

In neutral/alkaline environment:

$$2H_2O + 2e^- \rightarrow H_2 + 2OH^- \text{ (Hydrogen evolution)} \quad (21)$$

$$O_2 + 2H_2O + 4e^- \rightarrow 4OH^- \text{ (Oxygen reduction)} \quad (22)$$

While the shape of the pits can vary rather significantly depending on the alloy type and environment, pit cavities are nominally hemispherical. This distinguishes pits from other forms of corrosion such as intergranular or exfoliation corrosion. Pitting is strongly influenced by the alloy type and microstructure, electrolyte concentration and temperature.

3.4.2.1 Influence of alloy composition

Alloying composition determines the formation of second-phase particles such as Al_2CuMg and Al_2Cu that appear on the aluminium alloy surface. Alloying noble elements like Mo, Cr, W, Nb or Cu increase the pitting potential, where alloying active elements like Ga, Hg, Mg or Zn decrease the pitting potential. Alloys containing high alloying levels of Cu are basically more prone to pitting corrosion than those with lower levels or no Cu [40].

3.4.2.2 Effect of electrolyte concentration

Pit nucleation rate increases with an increase in Cl^- ion concentration and applied anodic potential, during polarisation testing [41]. However, Berzins et al. [42] suggested that, there is no threshold for the chloride concentration below which pitting will not occur. In fresh water, the chloride ions directly affect the corrosion potential of aluminium. The higher the chloride ion concentration, the more negative the corrosion potential is, resulting in a faster corrosion of a metal [43]. The outcome is that chloride ions accelerate the corrosion process. Whether due to oxide film breakdown or supporting the anodic reaction an explanation is still unclear [43].

3.4.2.3 Effect of variation in pH

Duan Weng and Shizhong Huo studied the effect of pH on pit development [44]. They found that the pit's growth in aluminium in seawater (3-4 % NaCl) was autocatalytic in the early stage. This can be related to pH decrease and chloride concentration increase within the pit as a result of the formation of hydrogen ions by hydrolysis of aluminium ions. Furthermore, the violent hydrogen release from pit causes the fluctuation of anodic current. Mc Cafferty et al. [45] calculated the pH within the internal pit to be around of 2.28. However, over a range of pH values of 4 to approximately 8.5, the pitting potential was found to be independent of pH [45, 46]. Tabrizi et al.

[47] studied the effect of pH values from 8 to 13 for alkaline solutions on corrosion rate of aluminium in long term corrosion, and showed that the corrosion rate increased rather slowly with an increase in pH value from 8 to 10; however, when pH value is above 10, much larger increase in corrosion rates were obvious. Their interpretation was that below pH value of 10, the specimens developed pit-like morphology under the thin film. At pH value of 11, cavities developed in the crystalline film can allow greater solution access result in an increase in corrosion rate. At pH value of 12, cavities developed into pits followed by rapid disintegration and dissolution of the exposed substrate [47].

3.4.2.4 Effect of temperature

Temperature can greatly affect passive film stability, for instance, the oxide film on aluminium surface can be unstable at temperature above 230°C [6, 8, 48]. Further, in chloride solutions pitting potential E_{pit} of aluminium decreases very slowly with an increase in temperature from 1 to 30°C and decreases faster with the increase of temperature up to 70°C. It was found that, at lower temperatures, the film is a single layer of bayerite, while at higher temperatures it consists of an inner layer of pseudo-boehmite and an outer layer of bayerite [49].

3.4.3 Galvanic corrosion

Aluminium is anodic to many other metals, and when it is joined to them in a suitable electrolyte which may even be a damp, porous solid, the resultant potential difference (see Table 6) causes a current to flow and result in considerable corrosion. Corrosion is most severe when the resistance of the electrolyte is low, for example, seawater. In some cases, surface moisture on structures exposed to an aggressive atmosphere can give rise to galvanic corrosion.

Table 6 – Comparison of measured corrosion potentials according to ASTM G-69.

Alloy/material	**Corrosion potential (V_{SCE})**
Al (99.999)	-0.75
Cr (99.9)	+0.23
Cu (99.999)	+0.00
Fe	-0.55
Mg	-1.64
Zn	-0.99
1100	-0.74
2014-T6	-0.69
2024-T3	-0.60
3003	-0.74
5052	-0.76
5154	-0.77
6061-T4	-0.71
6061-T6	-0.74
6063	-0.74
7039-T6	-0.84
7055-T77	-0.75
7075-T6	-0.74
7075-T7	-0.75
7079-T6	-0.78
8090-T7	-0.75

The corrosion potentials for aluminium alloys with some other standard corrosion potentials based on measurements made according to ASTM G69 are shown in Table 6. In practice, copper, brasses and bronzes in marine conditions cause the most trouble. The danger from copper and its alloys is enhanced by the slight solubility of copper in many solutions and its subsequent redisposition on the aluminium to set up active local cells. This can occur even when the copper and aluminium are not originally in contact: for example, when water running over cuprous surfaces subsequently comes into contact with aluminium. Similarly, water washings from lead can cause pitting of aluminium.

The controlling factor with lead and cuprous washings is the solvency of the water, so soft water is the most damaging in this respect. The successful utilization of these metals in close proximity to aluminium, for example, in plumbing and roofing, therefore requires careful design to avoid the transfer of a harmful solute to the aluminium. Contact with steel, though less harmful, may accelerate attack on aluminium, but in some natural water and other special cases, aluminium can be protected at the expense of ferrous materials. Stainless steels may increase attack on aluminium, notably in seawater or marine atmosphere, but the high electrical resistance of the two surface oxide films minimizes bimetallic effects in less aggressive environments. Titanium appears to behave in a similar manner to steel. Aluminium–zinc alloys are used as sacrificial anodes for steel structures, usually with trace additions of tin, indium or mercury to enhance dissolution characteristics and to render the operating potential more electronegative. Aluminium-55% zinc alloys applied as hot dip coatings are also used extensively as a protective coating for steel for roofing and automotive applications.

Additions of elements such as zinc, tin, indium and mercury activate aluminium electrochemically and are 4 of the 10 elements that can enhance aluminium dissolution in aqueous electrolytes when contained as solute in the aluminium solid solution. The full list of these activators is antimony, zinc, lead, cadmium, thallium, bismuth, tin, indium, gallium and mercury in

the order of increasingly negative potential. When these activators are mixed, the potential is controlled by the dominant activator which is the one with the highest melting point. Aluminium alloys are similarly activated by additions of the activator elements to the electrolyte. These additions may be used to turn aluminium into an anode plate for dry cells or metal-air batteries. The best addition for this purpose has been found to be tin together with an addition of magnesium. The magnesium addition is required to prevent a higher level of activation, and hydrogen production associated with the use of activators that can form hydrides [50].

Aluminium in contact with galvanized steel may accelerate attack on the zinc coating and this is particularly noticeable when there is an unfavourable area ratio, as with galvanized fittings on aluminium sheets. In alkaline solutions, however, aluminium may be preferentially attacked. The copper-bearing aluminium alloys are nobler than most other aluminium alloys and this can accelerate galvanic attack on these, notably in seawater. Mercury and all the precious metals are harmful to aluminium. Bimetallic corrosion of aluminium is a frequent cause of service-related corrosion failures, as the rate of attack can be rapid and corrosion can be severe and unexpected. In automotive applications, galvanic corrosion of aluminium is found in accelerated vehicle and component tests, particularly where aluminium is in direct electrical and electrolytic contact with a nobler metal. The solution is generally simple and involves providing sufficient protection using combinations of paints and barrier tapes to ensure that either electrical or electrolytic continuity is broken.

3.4.4 Crevice corrosion

If a crevice is formed between two aluminium surfaces, or between the surfaces of aluminium and a non-metallic material (i.e., a polymer) localized corrosion may occur within the crevice in the presence of electrolyte. Crevice corrosion is due to the formation of a local cell, since at the mouth of the crevice (whether it is submerged or not) the concentration of oxygen is higher

than that within the crevice. The difference in oxygen concentration leads to a difference in local corrosion potentials leading to corrosion in the 'less noble' area, which is the oxygen depleted zone.

Concomitantly, the oxygen rich zone (i.e., the mouth) assumes the role of the cathode. This mode of attack is often termed 'differential aeration cell corrosion' or 'concentration cell corrosion,' which are terms that may be applied more generally to describe corrosion phenomena other than crevice corrosion. Crevice corrosion can be a very problematic form of corrosion in an engineering sense, as the sites for crevice corrosion are often difficult to avoid in 'real' constructions which include welded lap joints, rivetings, valve seats, or even deposits that arise in service [51]. Crevice geometry is the governing factor that determines the susceptibility, or conversely the resistance, to crevice corrosion. As a result, crevices are defined by their degree of tightness and their depth (distance from the mouth). The general rules for the severity of crevice corrosion are presently under active research for several metal alloy systems, including aluminium [51-53]. Typically, in aluminium, tighter crevices lead to more rapid initiation of attack (owing to less electrolyte and a steeper oxygen concentration profile being achieved more rapidly). In addition, increasing crevice depth may also increase the likelihood of crevice initiation. Elimination of crevices should be done at the design stage where possible, and when unavoidable, they should be kept as open and shallow as possible or possibly even sealed with some type of appropriate non-crevice-forming sealant.

3.4.5 Intergranular corrosion

Intergranular corrosion can be summarized as a process whereby the grain boundary region of the alloy is anodic to the bulk or adjacent alloy microstructure. Corrosion is often microgalvanic (or even nanogalvanic), with activity developing as a result of some heterogeneity in the grain boundary structure. In aluminium–copper alloys, precipitation of Al_2Cu particles at the grain boundaries leaves the adjacent solid solution anodic and more prone to corrosion [54]. With aluminium-magnesium alloys, the opposite situation occurs, since the precipitated Mg_2Al_3 phase is

less noble than the solid solution. However, serious intergranular attack in these two alloys may be avoided, provided correct manufacturing and heat treatment conditions are observed. Intergranular corrosion differs from pitting corrosion.

While intergranular corrosion may initiate from a pit, propagation of intergranular corrosion proceeds more rapidly than pitting corrosion, and while both may have a deleterious effect on corrosion fatigue, intergranular corrosion is more detrimental as the sharper corrosion front compared to a more rounded pit front is a higher stress concentrator that reduces the number of cycles to failure.

3.4.6 Exfoliation corrosion

Exfoliation corrosion [55] of aluminium alloys is also frequently due to intergranular corrosion. Exfoliation corrosion is a form of intergranular corrosion associated with high strength aluminium alloys. Alloys that have been extruded or otherwise worked intensively, with a microstructure of elongated grains, are mostly prone to this damage [55]. In exfoliation corrosion, a separation or detachment of non-corroded layer or layers from the bulk alloy occurs due to the action of the volume of the corrosion products at the interface of the separation [56]. It was suggested that the initiation of exfoliation corrosion is related to the breaking down the passive film [52].

Exfoliation corrosion is observed on aircraft components, for example, around riveted or bolted components or wing brackets. Testing for exfoliation corrosion is carried out by a number of ASTM tests. AA2xxx, AA5xxx, and AA7xxx alloys with elongated microstructure have high susceptibility to exfoliation corrosion while aluminium alloy series AA1xxx, AA3xxx and AA6xxx have excellent resistance to exfoliation corrosion [52, 56, 57].

3.4.7 Stress-corrosion cracking

Stress-corrosion cracking is a time-dependent, predominantly intergranular fracture mode in aluminium alloys that requires the simultaneous presence of a susceptible alloy, a sustained tensile stress and a corrosive environment. The minimum tensile stress required to cause stress-corrosion cracking in susceptible alloys is usually small and significantly less than the macroscopic yield stress [58, 59]. The effect of an electrolyte is to cause the metal to fail prematurely at lower stresses due to stress-corrosion cracking, as indicated in Figure 5.

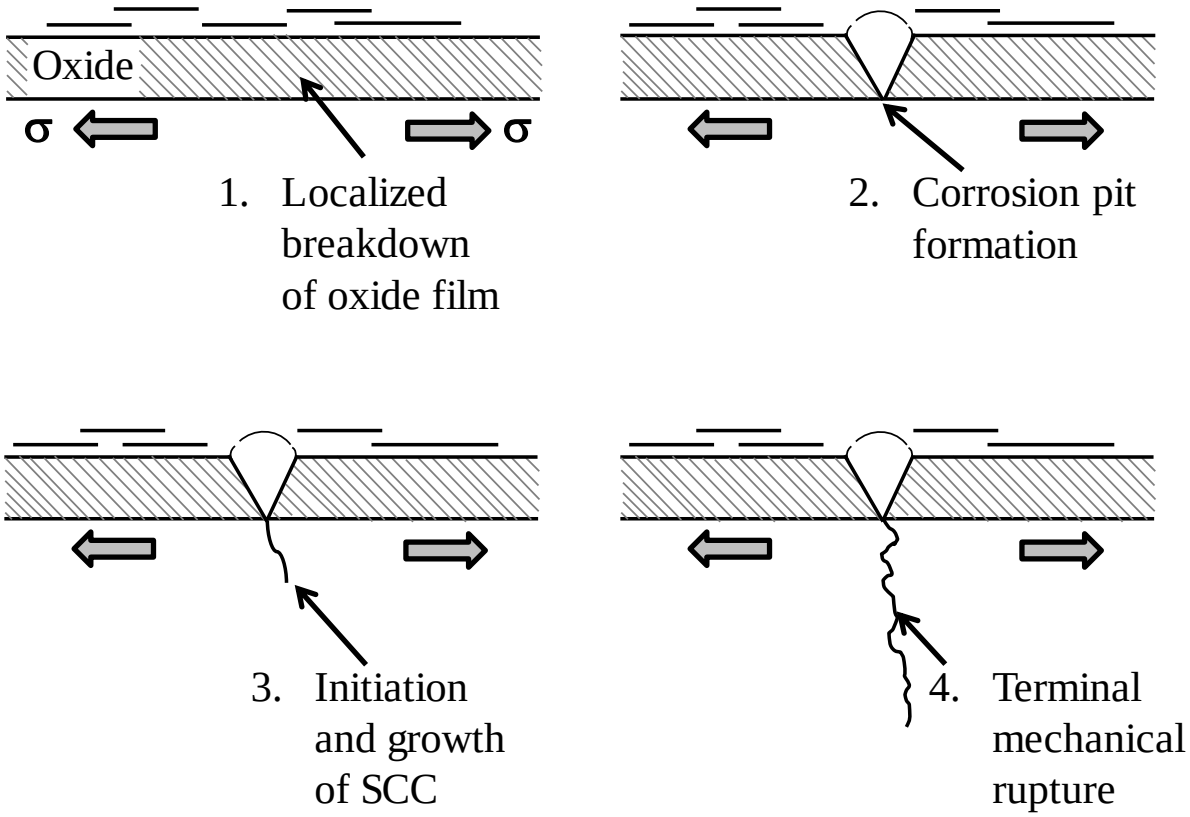

Figure 5 - Schematic diagrams of four stages in the initiation of stress-corrosion cracks with takes place in an intergranular corrosion cracking form. σ denotes the direction of applied stress and the fourth stage is the propagation stage [60].

Both film rupture and anodic dissolution take place in the process of stress-corrosion cracking in AA2xxx aluminium alloys [61]. However, anodic dissolution and hydrogen-induced

cracking occur in the mechanism of stress-corrosion cracking in AA7xxx aluminium alloy [57].

Compression stress tends to decrease susceptibilities to stress-corrosion cracking, because it acts as a crack closer, conversely tensile stress accelerates the crack opening [60, 62]. stress-corrosion cracking can be minimised by relieving of residual stress, avoiding applied stress as well as by reducing the precipitation of second phase particles at the grain boundaries [56].

3.5 Corrosion behaviour of copper-containing aluminium alloys

3.5.1 Introduction

There is significant interest in the corrosion behaviour of copper-containing aluminium alloys [63]. Copper, whether it is present at matrix regions or as a constituent of secondary phases, is generally considered to affect the corrosion resistance. Generally, the microstructure of the aluminium alloys has a large influence on their corrosion behaviour. The dominant feature of alloy microstructures is the distribution of second phase particles that contains high concentrations of alloying and impurity elements [64]. These particles often exhibit distinctly different electrochemical characteristics compared to the surrounding matrix microstructure. In particular, the presence of intermetallic compounds of copper, which act as cathodic sites, play an important role in the corrosion behaviour of aluminium alloys [65].

3.5.2 Effect of intermetallic particles

Localized corrosions in AA2024-T3 alloy often occurs in the vicinity of copper containing second phase particles [40]. It can strongly depend on anodic/cathodic activities of Cu-rich intermetallic particles such as S-phase (Al_2CuMg), θ-phase (Al_2Cu), and particles of varying composition containing Al, Cu, Mn, and Fe with copper as the main alloying element. The importance of intermetallic particles as initiation sites for corrosion have been discussed from many

authors [65-68]. The susceptibility of aluminium alloys to localised corrosion strongly depends on the distribution and electrochemical properties of intermetallic compounds and second phase particles [69, 70]. Several studies have shown that the susceptibility of commercial Al-Cu alloys to corrosion is principally due to copper-rich, magnesium-rich and iron-rich intermetallics [17, 18, 66, 71].

3.5.2.1 Al_2Cu (θ-phase)

Al_2Cu (θ-phase) contains about 70 Al and 27 Cu (at.%) [72]. The presence of Cu in the -phase supports cathodic transfer reaction [73]. It has a cathodic behaviour with respect to the Al matrix [74, 75]. The open circuit potentials of the Cu and Al_2Cu are ≥ 0.75 V more positive than that of Al in inert solutions ranging from pH 2 to 12 [73, 76, 77]. In aerated/deaerated solutions containing 0.2 to 1.0 M chloride ions, the OCP of θ-phase ranges from -590 to -700 mV [74]. The higher potential of θ-phase with respect to the aluminium matrix plays an important role in determining the susceptibility of Al-Cu alloys to localized corrosion. Scully et al. [78] suggested that the presence of Al_2Cu phase can make the potential of the Al matrix sufficient to promote pit initiation. It was also reported that the precipitation of θ-phase at the grain boundaries make Al-Cu alloys susceptible to intergranular corrosion [75, 79].

3.5.2.2 Al_2CuMg (S-phase)

A further, important copper-rich intermetallic particle is the S-phase (Al_2CuMg). These particles are the ones most often observed in AA2024-T3 alloys. Chemical composition of S-phase Al_2CuMg is 56.3±3.8Al, 20.4±1.5 Cu and 21.9±2.4 Mg in at.% [80]. S-phase (Al_2CuMg) is anodic with respect to the aluminium matrix [15, 81, 82], causing severe pitting corrosion of the alloy when exposed to a chloride-containing environment [23, 82-86]. The mechanism for pitting

associated with S-phase intermetallic particles in AA2024-T3 has been discussed by Buchheit et al. [23]. They found that corrosion of AA2024-T3 starts from the dealloying of anodic S-phase particles as a result of galvanic corrosion driven by the galvanic couple of anodic S-phase and the cathodic aluminium matrix. The schematic illustration of corrosion mechanism is illustrated in Figure 6.

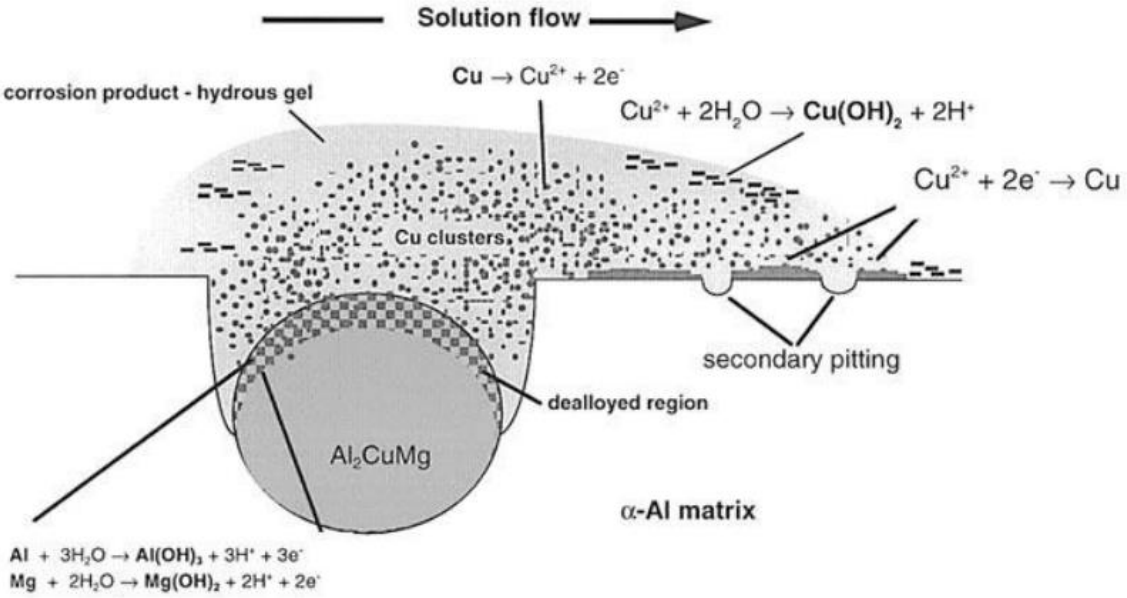

Figure 6 - Schematic illustration of corrosion mechanism of Al_2CuMg phase in Al alloys [83].

The S-phase dissolution leaves Cu-rich particle remnants or as a residue, which were cathodic to the aluminium matrix and consequently caused the peripheral formation of pits around the particle. The presence of S-phase is a major contributor to the poor corrosion resistance of AA2024 alloy. Moreover, S-phase in Al-Cu alloys is responsible for the initiation of intergranular corrosion which could also lead to stress corrosion cracking (SCC) [81].

Chapter 4 - Corrosion preventions

4.1 Inhibitors

Corrosion of aluminium and aluminium alloys can be controlled by use of inhibitors added to aggressive aqueous environments. For the purpose of this discussion, an inhibitor is a chemical substance, soluble in water, that slows the corrosion cell process on aluminium. The range of inhibitors that slow corrosion of aluminium is large, and there are a number of useful ways to deliver chemical inhibitors when corrosion is a risk.

Soluble corrosion inhibitors act by slowing either the anodic reaction or the cathodic reaction or both. This gives rise to a useful scheme for classifying chemical inhibitors. Those that slow the anodic reaction are referred to as ‘anodic’ inhibitors, those that slow the cathodic reaction are ‘cathodic’ inhibitors, and those that slow both reactions are ‘mixed’ inhibitors.

For aluminium alloys, anodic inhibitors typically act to increase the pitting potential in electrochemical testing, or slow or suppress the onset of pitting in exposure testing. Even with good anodic inhibitors, pitting may occasionally occur if pre-existing defects on the alloy surface are weak enough. Additionally, anodic inhibitors may have no effect on slowing the growth of existing pits. Cathodic inhibitors are usually substances that slow the rate of the oxygen reduction reaction on aluminium alloy surfaces. By slowing down oxygen reduction, the companion aluminium oxidation reaction must also slow down. This results in an overall decrease in the corrosion cell kinetics, as well as a decrease in the free corrosion potential. For the best inhibitors, the decrease in the corrosion potential is usually to a value well below the alloy’s pitting or repassivation potential.

Cathodic inhibitors have the advantage of being able to improve corrosion resistance at very low concentrations. For example, chromate added at micromolar concentrations to an aerated dilute chloride solution is enough to significantly reduce the rate of oxygen reduction leading to significant corrosion protection. Soluble corrosion inhibitors are usually ions in solution. Important

inorganic anions that inhibit aluminium corrosion include chromate, phosphate, permanganate, nitrate, vanadate, molybdate, tungstate and silicate. Cations of strontium, cerium and the lanthanides as well as zinc are inorganic cationic inhibitors. Organic substances that are inhibitors of aluminium corrosion include phosphonates, sulfonates, benzoates, thiols, azoles, amines, fatty acids and natural compounds such as tannins. Among these, special attention must be given to chromates.

Chromate is an exceptionally powerful inhibitor of oxygen reduction and an excellent inhibitor of aluminium corrosion. Chromates are used across all industries as aluminium corrosion inhibitors. However, their use is becoming increasingly restricted over concerns for work-place safety and environmental pollution because chromates are human carcinogens. Inhibitors can be incorporated into coating systems in a variety of ways. Sparingly soluble inorganic compounds and ion exchange materials are used as corrosion inhibiting pigments in coating formulations. Inhibitor ions can be attached to reactive sites on coating resin polymers or directly applied to aluminium surfaces using an evaporable solvent.

4.2 Conversion coatings

Aluminium alloys are often treated by conversion coating to convert the metal substrate to a corrosion resistant surface that more easily accepts and bonds to subsequently applied coatings [87, 88]. This method of protecting aluminium and its alloys from corrosion by conversion coatings has been in use since 1915 [89]. The conversion coating process involves contacting the surface to be coated with an aqueous solution containing surface activators and coating-forming ingredients.

Conversion coatings can be applied to aluminium alloys by conventional techniques (rinse, immersion or spray) or by non-rinse processes. An important criterion for non-rinse formulations is that they do not leave water soluble salts in the pre-treatment film following reaction with the metal surface [90]. As a result, some formulations developed for rinse application are not suitable as non-

rinse. Non-rinse processes give films of a generally uniform composition throughout the full film thickness apart from some concentration of the polymeric species in the surface regions of the film [90]. The thickness of the conversion film formed using the non-rinse processes can be controlled by the formulation concentration or by the thickness of solution applied to the surface. Conversion coatings are not as protective as anodized coatings, and in most cases, conversion coated surfaces are subsequently primed or painted. Conversion coatings are used for stand-alone corrosion protection when mild to moderate, occasionally condensing, atmospheric exposure conditions are expected, or for temporary corrosion protection.

4.2.1 Chromate-based conversion coatings

Chromate conversion coatings are noted for their ability to self-heal. Self-healing refers to the ability of the coating to resist corrosion from scribes or defects in the coating. This phenomenon is attributed to the release of labile hexavalent chromium in the coating into an aggressive solution contacting the surface. The performance of the chromate conversion coatings has been attributed to several factors [91, 92]. In particular, chromate conversion coatings contain residual hexavalent chromium which provides a barrier that separates aggressive environments from the aluminium substrates [93]. Hexavalent chromium compounds adsorb on aluminium oxides so as to minimise the otherwise positive surface charge, which makes the films less susceptible to adsorption of chloride. Moreover, it provides barrier protection of aluminium matrix due to its hydrophobic character. Chromate conversion coating on aluminium alloys is generated by the reaction of the alloy with an acidic solution containing dichromate. The formation of chromate conversion coating on aluminium alloys requires the presence of fluoride at a pH of 1.2-1.9, to thin the oxide on the surface, thus allowing the charge transfer reactions to proceed [87, 91]. The chromate-fluoride baths contain about 3 to 4 g/l of chromic acid, 3 to 5 g/l of sodium dichromate, and about 1 g/l sodium fluoride.

The morphology and composition of the chromate conversion film can be influenced by the formulation of the bath, although structurally the films are composed of amorphous, hydrated Cr_2O_3 nH_2O with an underlying, thin Al_2O_3 layer which has been penetrated by fluoride species. The temperature, pH and concentration of fluoride affect the growth rate of chromate conversion coatings. In particular, at low temperature thick coatings are obtained: the coatings produced above pH 2.5 are thin and less protective and finally too high fluoride concentration results in powdery and thin coatings which give poor corrosion resistance. The growth of chemical conversion coatings on high strength copper-containing aluminium alloys such as AA2024 and AA7075 is complicated by their heterogeneous microstructure, which includes a matrix phase and a variety of intermetallic particles of varying sizes and electrochemical behaviour. Meng et al. [94] suggested that the chromate conversion coating formation on intermetallic particles is dependent on several factors, such as electrochemical reactivity of the intermetallics, local pH, and the reaction between the intermetallic particles and the bath composition. Waldrop and Kendig [95] studied the nucleation and growth of chromate conversion coatings on AA2024-T3 aluminium alloys.

The chromate conversion coating deposited on the aluminium matrix phase was found to nucleate and grow very fast in the form of nodules. Nucleation and growth of the conversion coating was observed to be faster on Al-Fe-Cu-Mn particles than on Al-Cu-Mg. This is due to the fact that Al-Fe-Cu-Mn intermetallic particles are more cathodically active than the matrix while the Al-Cu-Mg intermetallics are less cathodically active than the matrix thus supporting slow growth of coating [95, 96]. Chromate conversion coating formation and growth of on intermetallic particles strongly depend on the size, shape and composition intermetallic particles [95, 96]. This result is consistent with the observation by Hagans and Haas [97] observing that the matrix of the AA2024-T3 aluminium alloys rapidly oxidise followed by slower oxidation copper-rich and iron-rich intermetallics under chromating bath conditions.

The corrosion protection provided by chromium-based conversion coatings on aluminium alloys can be influenced by many factors such as alloy composition, microstructure and enrichments of the alloying elements within the alloy. The microstructure and morphology of the surface of aluminium alloys is are factors that affect the nucleation, growth and protective properties of chromate conversion coatings. Liu et al. [98] studied the growth kinetics of chromate conversion coatings on high purity aluminium. They found that the addition of copper and gold to aluminium reduces the kinetics of growth of the coating. In the case of gold, increased addition further slows coating development. The results showed enrichments of copper and of gold developing in the alloy beneath the coating. Moreover Liu et al. [98] studied that chromate conversion coatings on Al-Cu and Al-Au alloys contain increased numbers of cathodic sites following achievement of the relevant maximum enrichments of the alloys.

Several possibilities may then arise: the particles may physically weaken the bonding of the coating to the substrate; enhanced reduction of chromate may generate new coating material at a relatively high rate within the existing coating, with stresses leading to detachment; hydrogen gas may be evolved with pressures mechanically disrupting the pre-existing and newly forming coating near the alloy/coating interface [98]. Increased evolution of hydrogen may also slow down coating growth if the rate of reaction is under anodic control.

Waldrop and Kendig [95] studied the difference in coating nucleation behaviour on the alloy matrix and on two distinct intermetallic phases. After a short immersion in a chromate bath, the film nucleation was reported to be faster on the Al-Cu-Fe-Mn particles than on the aluminium matrix, whereas that on the Al-Cu-Mg particles was considerably slower [95].

Alodine 1200s is a hexavalent chromium-based pre-treatment from Henkel Corporation. The final solution is mixed from a powder and can be applied by immersion, spray, or wipe. Depending on the substrate alloy, the colour ranges from light tan to gold. It has been used as the control standard

by many researchers during testing of Cr(VI) alternatives [99]. The primary components are chromic acid, complex fluorides, and ferric compounds [100].

4.2.2 Trivalent chromium conversion coatings

Conversion coatings can be developed on aluminium using baths containing trivalent chromium [101, 102]. With the demand for a safer alternative, there is no question that there is a need to define and test a process that can readily be industrialized and can replace hexavalent chromium conversion coatings. The process needs to be able to provide a similar level of corrosion protection to that currently provided by Cr(VI)-containing treatments. However, it also needs to be devoid of the environmental complications associated with Cr(VI). It must comply with the European directives including REACH (Registration, Evaluation, Authorisation of Chemicals) [103], RoHS (Removal of Hazardous Substances) [104], WEEE (Waste Electrical and Electronic Equipment) [105], and ELV (End of Life Vehicles) [106], as well as the new regulations from OSHA (Occupational Safety and Health Administration) in the USA [107]. Not only must the Cr(VI) alternative be able to protect the aluminium substrate, but it also needs to be adaptable to an industrial process. In practice, it is desirable to develop a "drop-in process" that can easily replace the current procedure using hexavalent chromium.

4.2.2.1 Formation of trivalent coatings

Trivalent Chromium Process (TCP) coatings formed during immersion develop through multiple chemical steps. The formation appears to be associated with a pH increase at the interface. The initial step is believed to be the dissolution of the air formed (native) oxide layer [108]. It is supposed that the oxygen reduction reaction (ORR) and possibly the hydrogen evolution reaction (HER) result in an increase in pH at cathodic sites. Aluminium is amphoteric and is therefore

susceptible to corrosion at both low and high pH values. The air-formed aluminium oxide is dissolved as a result of an increase in pH near the cathodic sites. It is generally assumed likely that dissolution of the air-formed oxide film to expose the bare aluminium is an essential first step in the formation of the TCP coating. It is also likely that the as-formed coating consists primarily of Cr(III) species such as Cr(OH)3, Cr2O3 and CrOOH.

Research [108] also suggests that the Cr(III) forms on most areas of the aluminium alloy but not over all the Cu-rich intermetallics. Others [109] have suggested that the high potential difference at Al-Cu in 2024-T3 could inhibit the deposition of the film at these cathodic sites. Guo [110] indicates that the Cr(VI) coating on the surface of 2024-T3 has a non-uniform thickness and that it is known to be thinner above intermetallics. He suggests that further work should be done to see if this is the case for TCP - especially above the Cu-rich intermetallics. Although no Cr(VI) species were detected by the authors [108] immediately after coating formation (or in the TCP solution), Cr(VI) was sometimes observed after as little as one hour of air drying and in all coatings after immersion in air saturated NaCl or Na2SO4. Interestingly, they observed that the Cr(III) and Cr(VI) oxide peaks are not distributed uniformly over the entire TCP-coated surface but rather appear to be localized in and around pits.

Liangliang, et al. [111] were able to show definitively that there is a significant pH increase during the formation of two different pretreatment conversion coatings - one a Cr(III) coating (Alodine 5900) and the other a Non-Cr system (Alodine 5200). They used a tungsten microelectrode to measure the interfacial pH change. They report that the pH increased from 3.9 to 4.8 in the case of the Cr(III) TCP and from 2.5 to 6.9 for the non-Cr treatment.

4.2.2.2 Structure of trivalent coatings

Early work by Nickerson [109] indicated that the NAVAIR TCP is essentially a zirconium and oxygen film with an embedded hydrated trivalent chromium oxide inhibitor species. NAVAIR

(Naval Air Systems Command) patented trivalent (Cr^{+3}) chromium conversion coating chemistry for aluminium in 2002 [112]. Zirconium oxide coating alone has very little corrosion protection; however, by adding small amounts of trivalent chromium oxides and hydroxides, a non-toxic, non-carcinogenic conversion coating (CC) is formed. A coating model based on zirconium oxide and Cr(III) species was proposed for the trivalent chromium coating. These authors proposed a three layer structure. The following three figures present simplified versions of the various proposed coatings. This has been done in order to make comparison of the different concepts possible. A simplified version of the TCP structure proposed by Nickerson [109] is presented in Figure 7. It shows an aluminium/coating interface having Al / O / F. The central layer is composed of zirconium and chromium oxides and the external layer is made up of Zr / Cr / O / F.

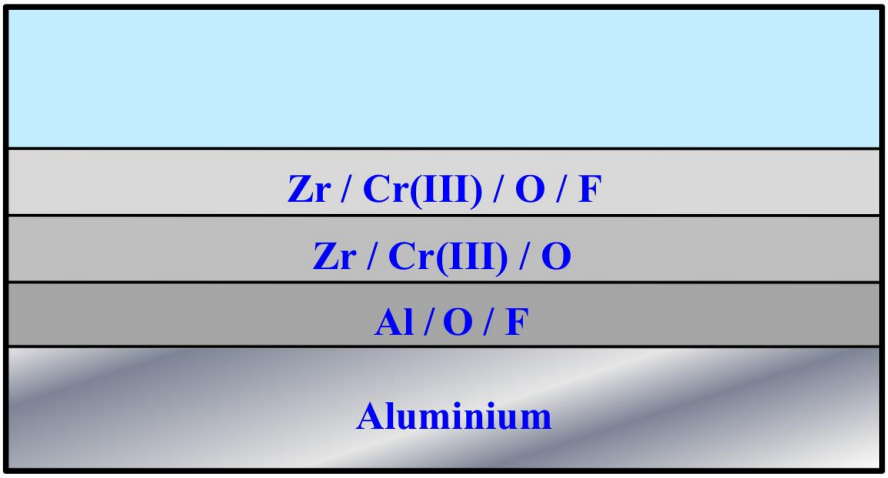

Figure 7 - Simplified version of Nickerson's structure [99].

Guo [110] indicated that the TCP (Alodine 5900) coating has a bi-layered structure primarily composed of Zr oxide with a small amount of Cr(III). This is shown schematically in Figure 8. She observed that there was an aluminium oxide and/or oxyfluoride at the interface between the AA2024-T3 substrate and the TCP coating. Guo and Frankel [113] report that the thickness of the layer depend on conversion time, with the film being 40-70 nm after 10 minutes.

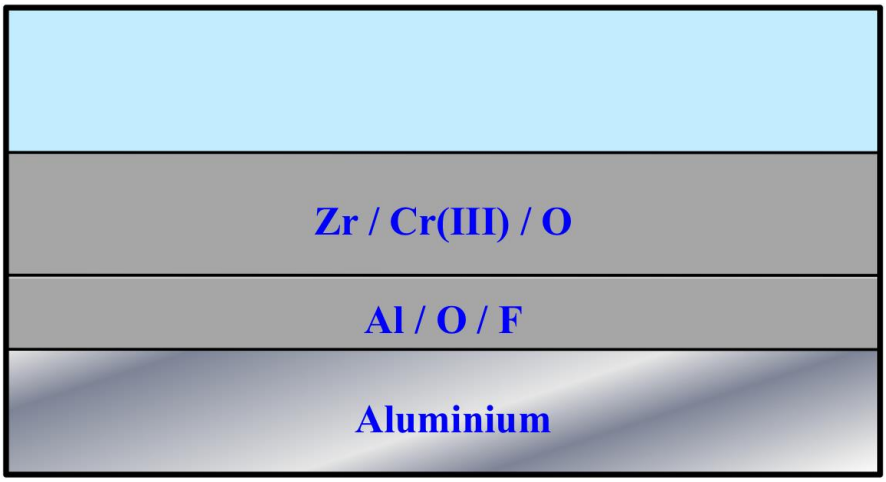

Figure 8 – Guo's concept of a two layer TCP structure [99].

The work by Qi, et al. [114] with SurTec 650 also indicates that the coating formed on high-purity aluminium consists of two layers (schematically shown in Figure 9). An inner aluminium rich layer having a thickness of a few nanometers, and an outer layer having a thickness that increases significantly with time of immersion in the coating bath. They propose that the protective characteristics of the coating are primarily from the inner layer. The absence of diffraction patterns also suggests that the coating is amorphous.

Coating thickness was determined from multiple measurements along the length of ultramicrotomed cross sections and found to be about 93 nm after a 600 s immersion. This is in reasonable agreement with the work by Guo [110]. According to Qi, the trivalent chromium conversion coating formed on the high purity aluminium consists of two main layers. The outer layer, which constitutes most of the coating thickness, consists of AlF_3, Al_2O_3, AlO_xF, $Cr(OH)_3$, CrF_3, $Cr_2(SO_4)_3$, ZrO_2 and ZrF_4 species. The inner layer is aluminium-rich, with the presence of oxide and fluoride species. They believe that the inner coating layer provides the main corrosion protection.

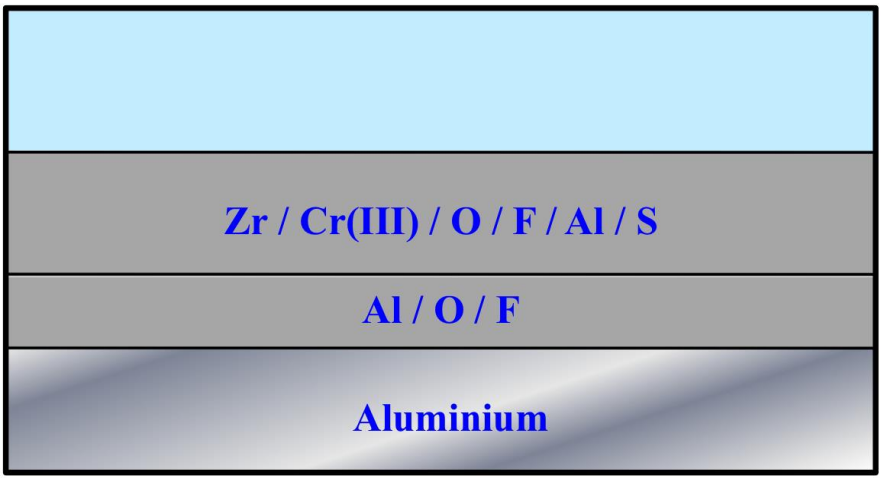

Figure 9 – Structure of TCP coating based on Qi's results [99].

While the three structure concepts are not identical there is a substantial amount of agreement. All see an aluminium-fluoride-oxygen inner layer. The outer layer (or outer two layers in the case of Nickerson) consist of zirconium / chromium (III) / oxygen. Both Nickerson and Qi report the presence of fluoride in the outer layer, but Guo does not. Qi observes the presence of sulphur throughout the depth of the coating, but neither Nickerson nor Gao report this. Qi attributes the sulphur to sulphur in the coating bath. Dardonaa and Jaworowski [115] employed *in situ* spectroscopic ellipsometry to monitor the development of a TCP film in real time. The film was developed on pure (99.998%) aluminium using 15% SurTec 650. The authors were able to confirm that the chemical thinning of the native oxide is a requirement for the initiation of TCP film formation on aluminium. The initial reduction in the thickness of the native oxide would increase the probability of electron tunneling as well as the electric field across the oxide enabling the migration of Al ions. In addition they were able to identify three distinct periods during film-development: (i) an initial induction period of approximately 100 s. During this period there is no significant growth of the film and the authors assume the chemical thinning of the native oxide occurs during this time; (ii) a linear growth period during which the TCP film develops at a constant

rate of 0.4 nm s^{-1} to a thickness of about 50 nm; and finally (iii) a logarithmic growth period to an ultimate film thickness of 125 nm after 880 s.

4.2.2.3 Electrochemical behaviour of TCP-coated aluminium alloys 2024-T3

Li et al. [108] studied the formation of the TCP coating on AA2024-T3. They present open circuit potential (OCP) data during the formation of the coating. They note that within the initial 50-75 seconds the OCP displays a negative shift of more than 400 mV and equate this to the dissolution of the air-formed aluminium oxide. After going through a minimum, the OCP recovers slightly to achieve a reasonably steady state. They repeated the test with a thicker oxide and note that the cathodic shift in OCP is slower, but the final OCP values for the thick surface oxide and the thinner surface oxide are within 50 mV of each other. They conclude that once the oxide is dissolved the TCP formation likely proceeds in an identical manner considering the similarity in the OCP values. In addition, the research revealed little difference in OCP values between the TCP-coated and TCP-uncoated samples.

Qi, et al. [114] report similar behaviour of the OCP in naturally aerated SurTec 650. Initially there is a rapid decrease in the OCP followed by a gradual rise to a relatively stable value. He also proposes that the initial fall in potential is due to thinning of the native oxide film. In Qi's case, the initial rapid decrease in potential is reported to be 350 mV. This is comparable to that reported by Li, et al. (400 mV), despite the fact that Li's research is on AA2024-T3 and Qi's data is for a high-purity electropolished aluminium - in addition, the research was carried out with two different TCP solutions - Qi uses SurTec 650 and Li used Alodine 5900.

Potentiodynamic curves [108] for TCP-coated and TCP-uncoated samples carried out in 0.5 M Na_2SO_4 revealed that both the anodic and cathodic currents were substantially attenuated for the TCP-coated sample. The R_p value is inversely proportional to the corrosion rate, so as the R_p increases the corrosion rate decreases. The R_p values found for TCP-coated samples were

approximately 10 times that of the non-TCP coated sample - indicating that the TCP is providing some protection to the alloy.

Potentiodynamic polarization curves for AA2024-T3 in aerated dilute Harrison's solution (0.35 wt.% $(NH4)_2$ SO_4 and 0.05 wt.% NaCl in distilled water) reported by Guo et al. [113] indicated that the breakdown potential (E_b) for the surface treated with TCP was 200 mV higher than the non-coated sample; however, similar behaviour was observed for a non-TCP-coated sample that had undergone desmutting (acid treatment). They suggest that this indicates desmutting is a critical step for improving corrosion performance. This observation would seem to agree with findings that indicate the corrosion protection provided by TCP is sensitive to the pretreatment process. The cathodic polarization curves indicate that the oxygen reduction reaction on the 2024-T3 substrate is suppressed by the presence of the TCP coating. This is in agreement with early work that was carried out by Nickerson and Lipnickas [109] who observed that the trivalent chromium coating inhibits the initiation of corrosion through suppression of the oxygen reduction reaction. In addition, the authors also comment that their electrochemical studies indicate that the trivalent chromium coating exhibits significantly lower protection with respect to the hexavalent chromium coating.

4.2.3 Other non-chromate conversion coatings

The hexavalent chromium present in several coating systems is known to be carcinogenic and environmentally hazardous [116-118]. This is the reason why the development, testing and usage of chromate-free conversion coating systems are increasing.

4.2.3.1 Zirconium-based conversion coating

Zirconium-based conversion coating on aluminium alloys is generated by the reaction of the alloy substrate with a zirconium-based bath. Film formation occurs by interaction of the fluorozirconate with hydroxides at the surface of the metal substrate. Zirconium-based conversion coating is assumed to form by the precipitation of zirconium oxide due to an increase in pH (hydrogen evolution at cathodic sites leads to a local increase in pH) of the bath solution at the metal oxide/liquid interface. The solubility of the coating compound decreases when the pH increases, resulting in precipitation of coating material.

Zirconium, aluminium, oxygen and fluorine are the main constituents of the conversion film, with zirconium accounting for about 36% of the total weight [90]. It has been considered that zirconium species are bonded to the hydrated aluminium film covering the aluminium surface [90]. From in-depth elemental profiles through the resultant film, the film has been considered to be multi-layered, with Al_2O_3 adjacent to the aluminium surface, a Zr / O / F containing outer layer and ZrO_2 sandwiched between the previous layers. The literature reveals that zirconium is always present in its dioxide form ZrO2, and some hydroxy-oxide or hydroxyfluoride may also be present depending on the composition of the conversion bath [119].

4.2.3.2 Titanium-based conversion coating

The performance of several titanium-based conversion coatings has been studied by Fedrizzi et al. [120]. They reported that fluorotitanate or fluorozirconate coatings can give similar performance to conventional chromate-based treatments, when used as pre-treatment for an organic coating. Smit et al. [121] studied the performance and characteristics of a no-rinse titanium-based conversion coating on AA3003 aluminium alloy. They concluded that the application of a H_2TiF_6 based conversion coating to AA3003 aluminium alloy improves the anodic inhibition of the alloy and reduces the corrosion current density [121].

4.2.3.3 Cobalt-based conversion coating

Cobalt-based conversion coatings have been developed primarily for the aircraft industry as possible replacements for chromate-based formulations [90]. This coating process is currently finding application in the marine and automotive industries. The conversion coating contains a trivalent or tetravalent cobalt/valence stabiliser complex. The coating formulations are prepared by dissolution of Co(III) salts and a metal acetate to form a solution of cobalt (III) hexacarboxylate complex [90]. Bath formulations based on cobalt acetate give the best overall performance, but the best paint performance is obtained using cobalt nitrate [90]. Conversion coating can be applied on aluminium surfaces by immersion, hand or spray processes.

4.2.3.4 Cerium-based conversion coating

Some of the most promising chromate replacement conversion coatings are derived from these rare-earth elements, particularly cerium (Ce), which is relatively abundant in nature and offers the best degree of inhibition due to the formation of a compact film of cerium oxide and hydroxides. Corrosion protective film can be simply formed by immersion of an aluminium alloy in a solution

containing 100-1000 ppm cerium chloride [90]. Many studies have been undertaken on the mechanism of inhibition of cerium conversion coatings deposited on copper-containing aluminium alloys in aqueous solutions containing cerium salts. Aldykiewicz, et al. [122] suggested that the inhibition of the aluminium alloys is achieved by deposition of a cerium-rich film on the copper-containing intermetallics which blocks the cathodic reduction of oxygen at these sites. Inhibition of corrosion by cerium is also believed to involve decreasing the rate of cathodic oxygen (O_2) reduction by precipitation of Ce(III) hydroxide ($Ce[OH]_3$) at regions of high pH [90, 123]. This mechanism requires the activation across the metal surface of many electrochemical cells associated with microscopic features such as grain boundaries, precipitates, constituent phases and inclusion, or submicroscopic features such as flaws in existing naturally occurring oxide films [124]. The cathodic processes generate alkaline conditions close to the metal surface. These conditions lead to localized precipitation of an hydrated cerium oxide and the formation of the film.

4.3 Anodizing and sealing processes

4.3.1 Introduction

Aluminium and aluminium alloys can be anodized to enhance corrosion protection and improve adhesion of subsequently applied coatings, and improve a range of other surface properties. Anodized coatings are formed electrochemically in an aqueous solution that results in an aluminium oxide surface film. Anodized coatings on aluminium alloys are on the order of 2–50 μm in thickness. Anodizing is most commonly carried out in chromic acid solutions and sulfuric acid solutions. To improve corrosion protection, anodized coatings can be sealed in a second step in the process.

4.3.2 Pre-treatment of aluminium surface prior to anodizing

Pre-treatment of aluminium prior to anodizing is of considerable importance because the method used inevitably determines the final texture of the finish, since with the most popularly used sulphuric acid anodizing process the anodic coating formed is essentially transparent and follows the contours of the pre-treated surface almost exactly.

4.3.2.1 Cleaning and degreasing

In order to remove oil, grease and soil on the aluminium surface, is need a clean with a rag, moistened with an organic solvent. This method leaves the metal surface in a suitable conditions for the subsequent treatment.

Another method of degreasing is to use an emulsion. Emulsion cleaning consists of immersing components in a bath containing organic solvents and wetting agents added to a paraffin base. The aluminium is soaked in the mixture for 5-10 minutes, allowing grease or oil to be loosened or removed, followed by two running water rinses to emulsify and remove any residual surface contaminants.

4.3.2.2 Alkaline etching

An effective etch or pre-treatment prior to anodizing is such as to produce a surface which, when anodized, appears smooth, of the right degree of mattness or brightness and without any visible blemishes of any description. The most frequently used method for etching aluminium is in aqueous solutions of sodium hydroxide, with or without additives.

4.3.2.3 Desmutting treatment

After a sodium hydroxide-based etch, a black smut is left on the aluminium surface. This tends to be greater the lower the purity of the aluminium and the more highly alloyed it is, and it is particularly heavy on copper-based alloys. It consists of particles of oxide, intermetallics, silicon, etc., which are insoluble in the alkaline solution, and in general are quite loosely held on the surface. Smut is usually removed by a dip in an acid solution, most commonly 25-50% V/V nitric acid, used at room temperature. This removes normal smut layers, including those on high copper containing alloys quite quickly.

4.3.3 Anodizing processes

4.3.1 Introduction

When aluminium is anodically polarized in an electrolyte, the negatively charged anion in solution migrates to the anode where it is discharged with the loss of one or more electrons. In an aqueous solution the anion consists in part of oxygen which unites chemically with the aluminium. The result of the anodic oxidation depends on a number of factors, particularly the nature, concentration and temperature of the electrolyte and the electrolytic operating conditions such as current and voltage. There are some processes that can occur at the anode:

1) The reaction products may be essentially insoluble in the electrolyte, and form a strongly adherent barrier-type film on the aluminium. Film growth continues until its resistance prevents current from reaching the anode. The films are extremely thin and dielectrically compact.

2) The reaction products may be sparingly soluble in the electrolyte. An adherent film forms as above, but is accompanied by localized field-assisted dissolution which produces a regular array of essentially parallel-sides pores in the film. There pores allow continuing current flow and thus film growth. Electrolytes used are generally acid and include sulphuric, phosphoric, chromic and oxalic acids. The films formed are used to pre-treat aluminium surfaces to facilitate good adhesion of paints, lacquers or adhesives, and as they may be very hard and many microns thick, they find extensive application for protective and decorative purposes.

3) The reaction products may be moderately soluble. Under these conditions, electropolishing may be possible if a suitable electrolyte is used.

4) If the anode reaction products are fully soluble in the electrolyte, then the meal is dissolved until the solution is saturated. This reaction takes place in some strong inorganic acids and bases.

Anodizing is a passivation process to increase the thickness of the natural oxide layer formed on the metal to increase the corrosion and wear resistance. Figure 10 shows a simplified apparatus for anodizing treatment.

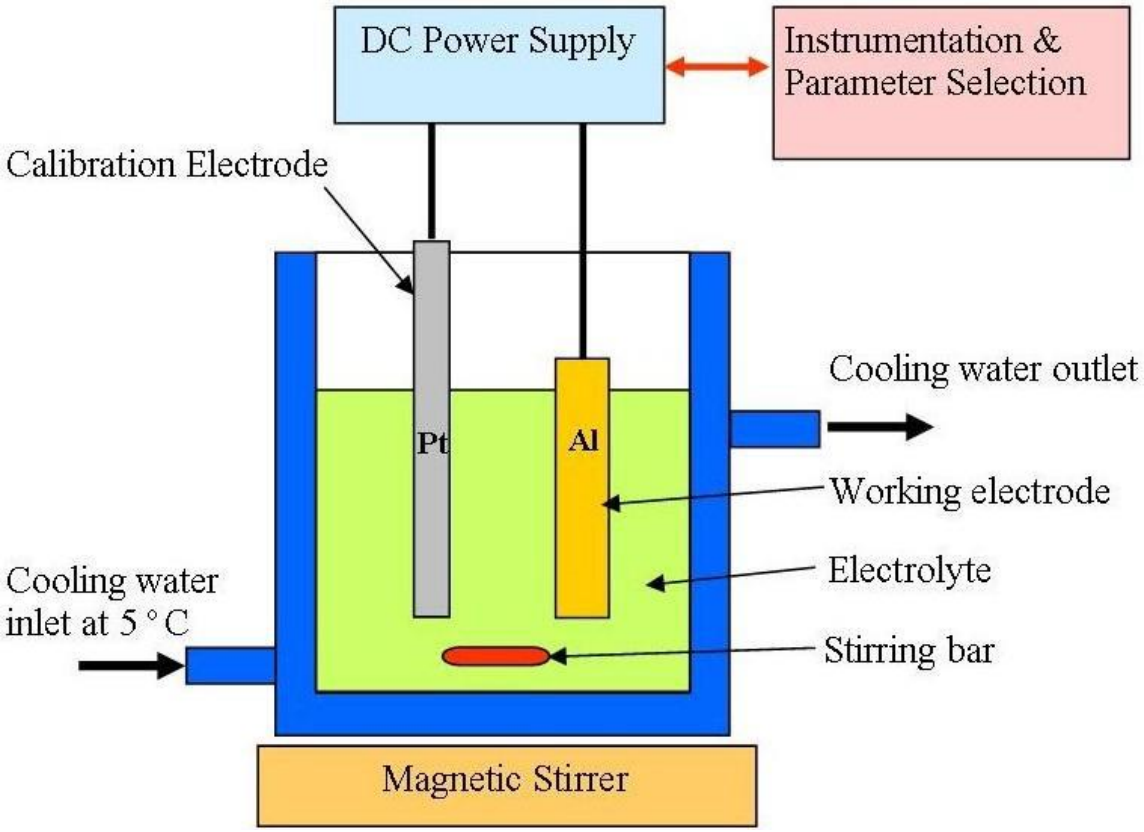

Figure 10 – Schematic diagram of aluminium anodizing in electrolyte.

The electrochemical cell consists of a two-electrode system, e.g., the platinum (Pt) sheet acting as the counter electrode (the cathode), and Al sheet acting as the working electrode (the anode). Both electrodes are immersed in the electrolyte, mostly acids, such as boric acid [125], sulfuric acid [126, 127], oxalic acid [125, 127, 128], and phosphoric acid [129, 130].

Chromic acid anodizing (CAA) is widely used in the aeronautic industry to improve corrosion resistance of aluminium alloys [131]. Since the beginning of the 1990s, however, the high toxicity associated with Cr (VI) has imposed restrictions on their use in industrial applications. As a consequence, numerous attempts have been made to find less toxic alternatives [117, 118]. Anodizing with dilute sulfuric acid (DSA) has been used to obtain thin anodic films (1–5 μm) that provide some protection without excessive deterioration of the fatigue life for specific aerospace alloys. Although the fatigue performance of DSA is acceptable, the corrosion resistance is lower

than that of parts anodized in chromic acid (CAA). More recently, a new anodizing procedure, involving the addition of tartaric acid in dilute sulfuric acid electrolyte and called tartaric-sulfuric acid anodizing (TSA), was introduced [132, 133]. The addition of tartaric acid to sulfuric acid baths improves significantly the anticorrosive properties of the anodic layers compared to those obtained by sulfuric acid anodizing [134].

Recent work [134], however, indicates that the mechanism of porous film growth is not significantly affected by tartaric acid additions and that tartaric acid is not incorporated in significant amounts into the oxide material. Thus the corrosion resistance provided by TSA is likely to be associated with residuals of tartaric acid adsorbed on the porous skeleton. Tartaric acid concentration in the order of ppm, has been proved to be effective in reducing both the oxide dissolution rate in acidic environments and the anodic reaction rate. The effect of tartaric acid on the anodic film morphology and corrosion resistance of anodized AA2024-T3 was studied by Boisier et al. [135]. Observing the anodized surface by SEM, they suggested that the addition of tartaric acid to the anodizing electrolyte generates anodic films with a reduced porosity. However, this observation might be also due to the reduced chemical dissolution of the external pore regions during anodizing rather than to a difference in the growth mechanism. The latter statement is supported by other works indicating that the presence of tartaric acid in the anodizing electrolyte reduces the growth rate under potentiostatic conditions, but it does not change the anodic film composition, morphology or fundamental growth mechanism [134, 136].

4.3.3.2 Types of anodic aluminium oxide

Anodic oxide films can be classified into two types, based on the reactivity of electrolyte with the oxide layer. One is a non-porous barrier film which is dense and has a good wear resistance and behaves as an electrical insulator (Figure 11) [130, 137]. Another is a porous oxide structure (Figure 11) with a high aspect ratio [137]. Barrier oxide film can form on aluminium in several

different neutral or basic solutions, such as boric acid or alkali borates, which possess little or no ability to dissolve the oxide layers. It is generally accepted that the thickness of barrier-type alumina is mainly determined by the applied voltage [138], although the difference of electrolytes and anodizing temperature also play a role [139, 140]. The maximum attainable thickness in the barrier-type alumina film was reported to be less than 1 μm, corresponding to breakdown voltages in the range of 500 - 700 V. Dielectric breakdown of the films occurs above the limiting voltage [138]. Oxide films of this type possess unique electrical properties and have been used extensively in electrolytic capacitors and rectifiers [141].

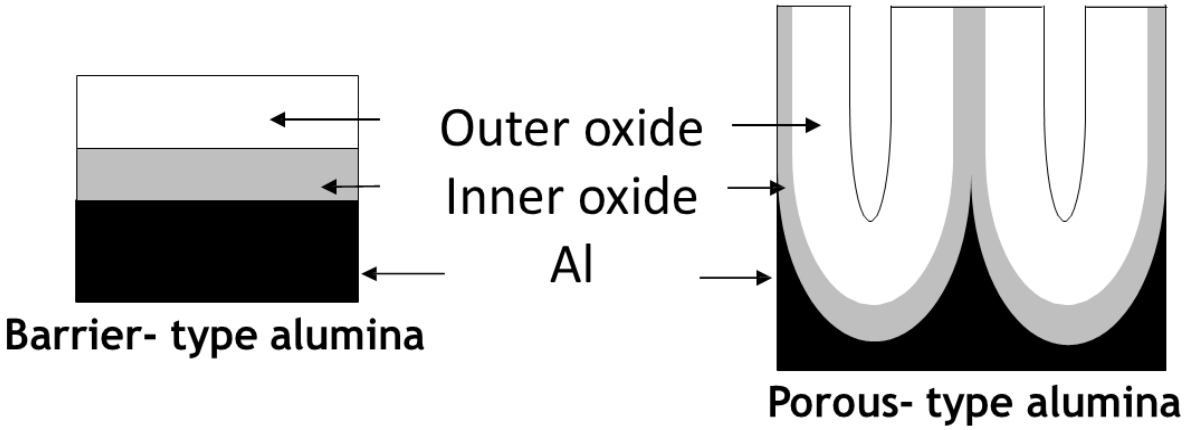

Figure 11 – Schematic diagram of AAO structure: Barrier-type and Porous-type alumina.

However, the anodizing of aluminium in certain strong acid electrolytes, which could dissolve the oxide layers, leads to the formation of an anodic aluminium oxide film on the surface.

This film is comprised of a relatively thick porous outer layer with regularly spaced pores extending from the outer surface toward the aluminium substrate, and a relatively thin nonporous barrier layer adjacent to the aluminium metal/oxide interface (Figure 11). As anodizing time increases, the aluminium metal is converted to aluminium oxide at the aluminium metal/oxide interface, and the pores extend further into the film. This porous aluminium oxide typically exhibits

a uniform array of hexagonal cells, each cell containing a cylindrical pore [137, 142-145]. With films formed in electrolytes that react appreciably with the oxide, a relatively high, steady current flow and continued film growth has been observed. The amount of oxide formed is generally a function of current and time. In this case, the film is formed with a porous structure due to the reaction between the oxide layer and the electrolyte [146].

Both the barrier and porous layer consist of a native oxide layer formed with aluminium an outer oxide layer grown on top of the native oxide layer by the anodizing process.

4.3.3.3 Porous film growth and morphology

Porous anodic films formed on aluminium in electrolytes such as sulphuric acid are characterized by a very uniform morphology. Pores are approximately cylindrical, situated in generally close-packed hexagonal cells and separated from the aluminium by a thin layer of oxide (Figure 12).

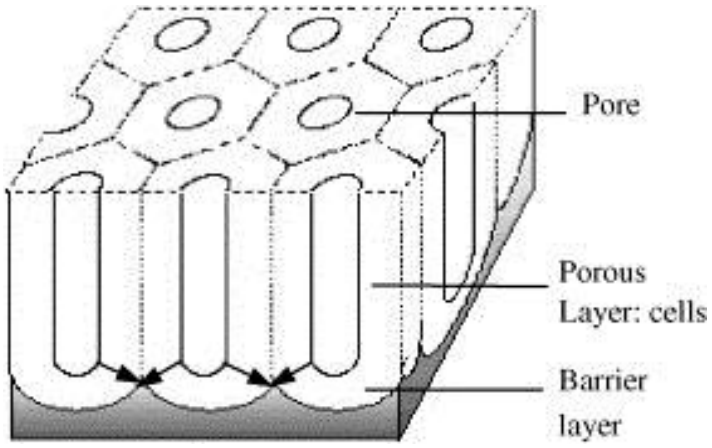

Figure 12 – Model structure of anodic porous alumina.

The course of porous film development is revealed by monitoring the change of voltage when anodizing at constant current, or current when anodizing at constant voltage (Figure 13) [147].

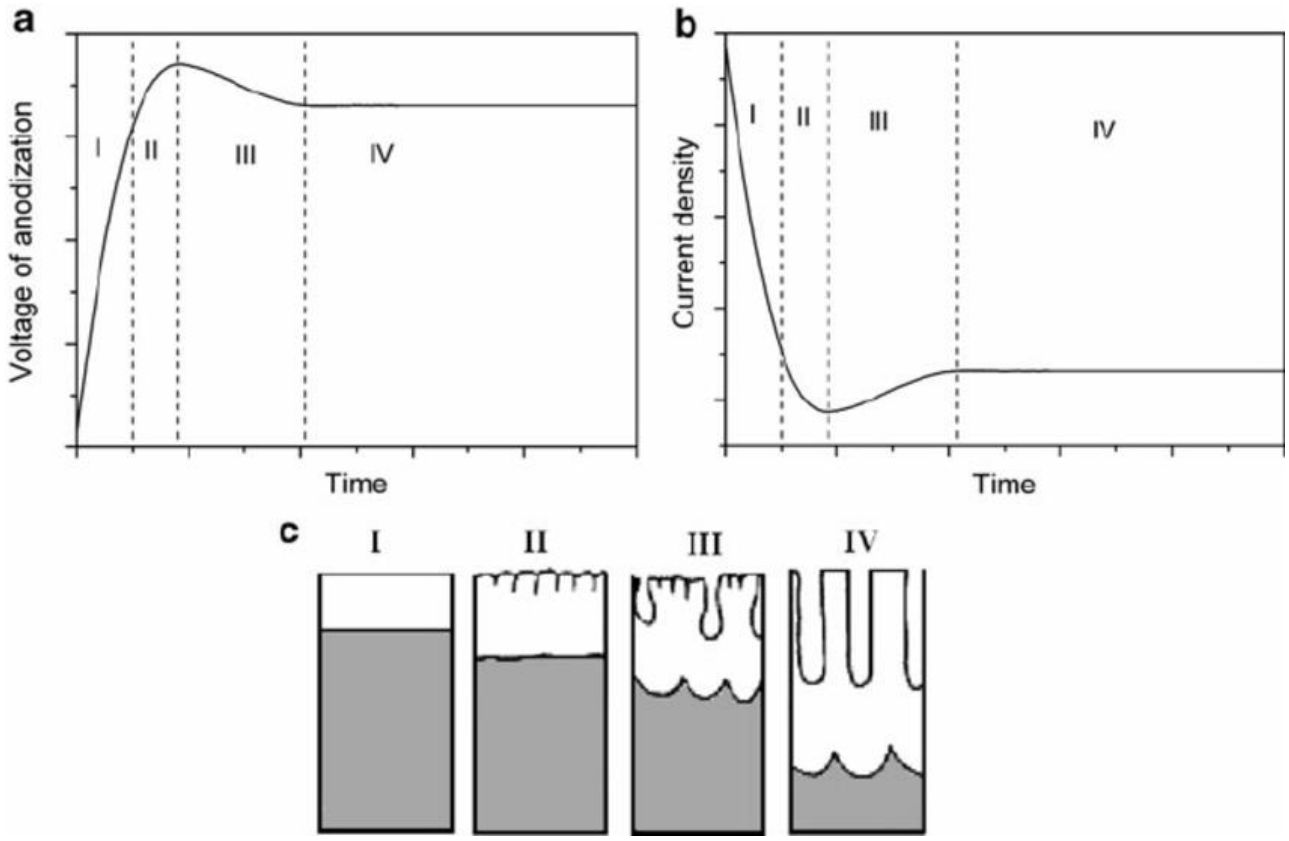

Figure 13 – Schematic diagrams showing the development of a porous anodic film on aluminium in (a) constant current and (b) constant voltage conditions.

The compact barrier layer thickens during stage I (Figure 13). Incipient pores develop in the barrier film during stage II (Figure 13), while the classical film morphology starts to arise during stage III (Figure 13). steady-state propagation of the pores continues through stage IV (Figure 13). Consequently, when anodizing at a constant current density, the film thickness is proportional to the anodizing time. This relationship falls down for thicker films and those produced under particularly aggressive solution conditions, where the effects of chemical dissolution became significant.

The anodic reaction that leads to film growth takes place at the metal/oxide interface, and therefore the film is effectively growing from within rather than building up on its outer surface, as is the case with plating or painting processes. This means that the outer part of the film is in contact with the electrolyte for full anodizing time and may become considerable dissolved chemically by the end of the anodizing process. Underlying regions of the film are progressively attacked to lesser extents. Thus, the pores are tapered being wider at their mouths than near the aluminium substrate.

It then follows that the maximum film thickness achievable depends on the ability of the electrolyte to chemically dissolve the film. When anodizing has been continued for sufficient time that the pore walls at the outer surface are vanishingly thin, then although anodizing may continue to produce film material at the metal/oxide interface, no further net film thickening takes place. Understanding the factors that control this balance between the rate of film formation and the rate of film dissolution forms a vital part of practical anodizing technology.

4.3.4 Sealing process

4.3.4.1 Introduction

The most effective way to improve the corrosion resistance of aluminium anodic oxide is to seal the pore structure and form a thick protective barrier between the Al surface and the environment, which is called sealing. Excellent corrosion resistance can be achieved using the thick porous structure in conjunction with a suitable surface treatment and protective protocol. In this process, the anodized aluminium is immersed in a solution of boiling water or other solutions such as nickel acetate in order to seal the pores. The sealing produces a hydrated oxide layer with improved protective properties. Figure 14 illustrates how the initially porous anodic film evolves during the sealing process.

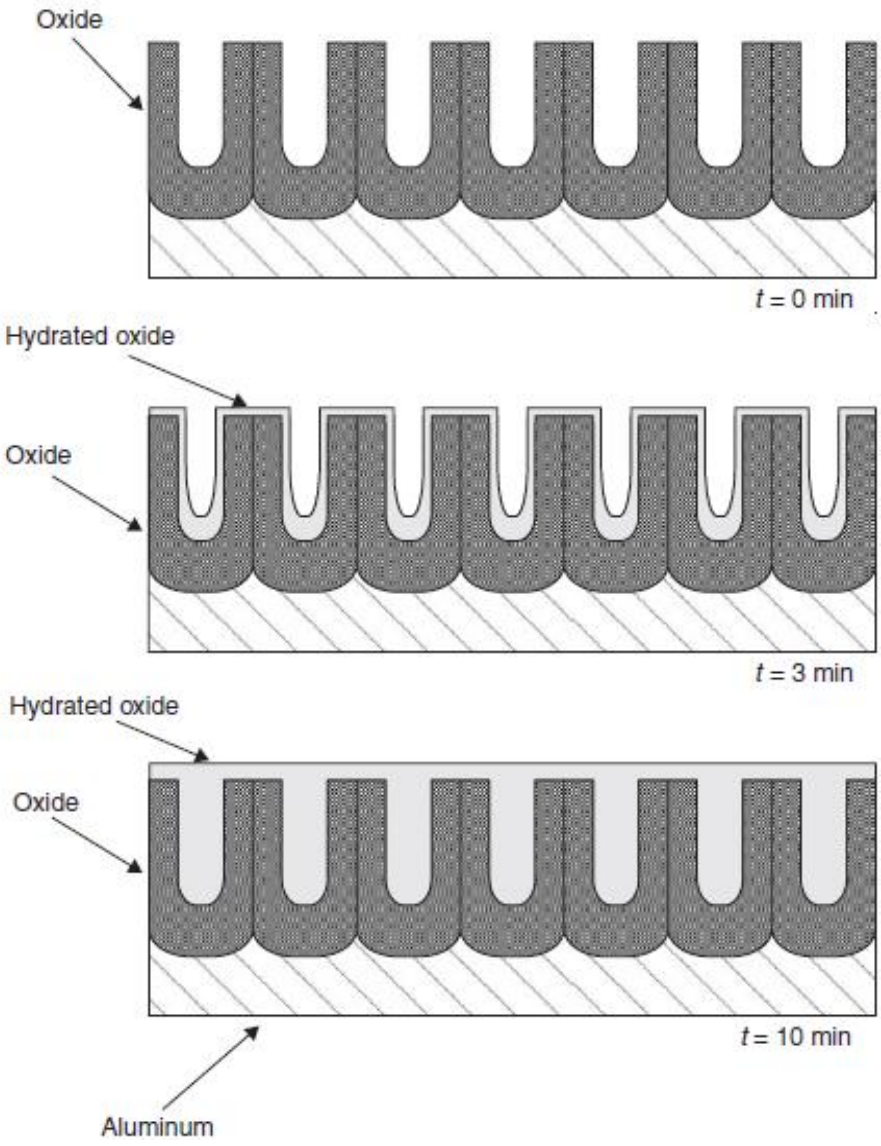

Figure 14 – Schematic description of the evolution of a porous anodic film on aluminium as a function of the sealing rime at 85°C.

Hydrothermal sealing is a treatment that involves the prolonged immersion of the anodized parts in a suitable electrolyte, generally maintained at elevated temperatures (90-100°C). Such procedure results in the partial hydration of the aluminium oxide that constitutes the porous oxide film [148]. Specifically, during the early stages of hydrothermal sealing, the sealing solution fills the pores, and a layer of hydrated products forms at the pore mouths. This layer separates the solution within the pore from the external solution. Inside the pores, the pore walls partially

dissolve, and the internal solution becomes saturated with alumina hydrates. When the temperature is reduced, hydrated alumina precipitates filling the pore and, over time, it crystallizes [149]. The type of electrolyte where sealing is performed has an important impact on the sealing behaviour, on the composition and on the protective performance of the resulting layer. For example, simple hot water sealing increases the durability of the anodic film purely due to an improvement of the barrier effect associated with the pore closure. On the other hand, when sealing is performed in hot hexavalent chromium containing solutions (generally sodium chromate), the re-precipitated products contain significant amounts of hexavalent chromium, and therefore can act as a corrosion inhibitor reservoir [148, 150].

Due to the higher energy costs inherent in hydrothermal sealing, chemical manufacturers have developed mid-temperature seals (70 to 90°C). These seals, which contain metal salts such as nickel, magnesium, lithium, and others, have become very popular due to the lower energy costs and their ease of operation [52].

4.3.4.2 Hot water sealing

The method used to seal the anodic films of the considered samples is the hot water, in which the treated aluminium alloy is immersed in deionized water nearest to the boiling point. This method may partially convert the alumina of anodic coating to aluminium mono-hydroxide. The mechanism of sealing occurred in boiling water is considered as the hydration of the anodic film. The aluminium oxide reacts with water to form aluminium hydroxide, which fills pores in the coating and seals the surface [151]

L. Hao et al. [148] illustrated the hot water sealing. Boiling deionized (DI) water treatment is a traditional sealing process [152, 153] that is environmentally benign, as there are no toxic chemicals involved in hot water sealing. The sealing quality relies on the pH value, purity, and temperature of hot water, sealing time, and current density used in anodizing. If the sealing process

is well controlled, hot water sealing is capable of substantially improving the corrosion resistance of anodized aluminum. Hot water sealing is the best sealing process for enhancing the dielectric strength of anodic coatings on aluminum. Water temperature must be above 95°C in hot water sealing. The optimal pH range is from 5.5 to 6.5. Silicate and phosphate are inhibitors in hot water sealing. Other harmful ions include cupric, ferrous, fluoride, sulfate, and chloride. Sealing time is a function of coating thickness, usually 2 min/micron recommended in common practice. According to an investigation, the weight loss of anodized samples with hot water sealing in acid dissolution tests (ADT) decreases with the increase in anodizing current density.

The anodic coatings on most alloys, except 2024, produced at 1.94 A/dm^2 and 2.58 A/dm^2 followed by hot water sealing, can easily pass the ADT test while the sealed anodic coatings on both 2024 and 7075 resulting from low current density failed in accordance with ISO 7599-1983(E) specification. This result suggests that the anodic coatings produced at 2.58 A/dm2 have superior corrosion resistance to those produced at 1.08 A/dm^2 if hot DI water is used as a post sealing treatment. It is understandable that the sealing quality of the coatings produced at high current density are better than that at low current density, because the pore size at high current density is smaller than that at low current density [1] and the smaller the pore size, the easier the closure of the pore.

Although hot water sealing is able to significantly improve the corrosion resistance of anodic coatings, smut is often produced on the surface leading to an unacceptable appearance. Rapid pH variation and contamination (e.g., phosphate, silicate, and chloride) of boiling water are hard to control in mass production, leading to a short bath life. Hot water requires a relatively long sealing time (2 min/μm). High energy consumption is an apparent disadvantage of hot water sealing. Also, consistency is a great challenge when hot water sealing is used. Buffers, such as 1 g/L ammonium acetate [154] and other proprietary additives [155], may be added to DI water to improve the sealing quality in practice.

4.3.4.3 Sodium chromate-based sealing

Sealing in chromate or dichromate solutions was first patented by Dunham in Britain [156] and by Edwards in the USA [157] for sealing anodic coatings. Coatings possess exceptionally good resistance to corrosion because of the corrosion-inhibiting properties of chromate [90].

Tomashov and Tyukina [158] have shown that chromate sealing consists of absorption of chromate, followed by the formation of either aluminium oxidichromate or aluminium oxychrornate, followed in turn by hydration of the coating due to reaction with water. When the pH of the bath is increased from 3.7 of a straight potassium dichromate solution, the rate of hydration of the film increases. In other words, due to an increase in the rate of hydration, the rate of sealing increases as the pH is increased, a limit being set by rapid dissolution of the film at pH's in excess of 10. The above investigations have shown that the extent of leaching of chromate from sealed films by sodium chloride solution or by water is less when the pH of the sealing bath is increased.

Extremely effective and rapid sealing is claimed by the use of baths of pH between 6 and 7, due to high absorption of chromate and rapid hydration, with but little leaching of chromate from the coatings on exposure. In addition, the stability of the amphoteric Al203 is stated to be greatest between pH 6 and 7.

From the results of these authors two solutions were recommended:

(i) For highest corrosion resistance, a solution containing 100 g/l potassium dichromate and 13 g/1 sodium hydroxide is suggested.

(ii) For reduced chromate consumption, a solution containing 15 g/l potassium dichromate and 3 g/1 sodium hydroxide is suggested.

The suitability of the method has been confirmed in protection coatings on Al-Mn, Al-Mg, Al-Si and Al-Cu-Mg-Mn alloys as well as on clad alloys. The results have been confirmed by corrosion

resistance tests carried out by Whitby [159]. The state of the water attached to the film and the structure and the properties of the film itself depend sharply on temperature. The protective properties of the film were increased to the greatest extent by treatment in water at 90-95°C for 30-60 minutes. The improvement in protective properties was caused by the partial closing of pores in the film. The corrosion protection properties of chromate are well known, but chromate sealing apparently also has less effect on the mechanical properties of anodized aluminium than water sealing. Chromate sealing is therefore generally recommended for aluminium in military or aeronautical use.

4.3.4.3 Cerium(III) nitrate-based sealing

Hinton and Arnott investigated the effectiveness of rare earth metal salts as corrosion inhibitors for aluminium alloys [124, 160, 161]. Mansfeld and co-workers evaluated the effects of chemical passivation by immersion in a cerium chloride solution on corrosion resistance of aluminium alloys [162, 163].

Wilson and Hinton [164] involving the addition of hydrogen peroxide (H_2O_2) to cerium chloride bath to form a cerium oxide/hydroxide film on Al-Cu alloys in a very short time (approximately 10 min). The acceleration effect of H_2O_2 may simply be related to the rapid increase in pH caused by its reduction that favours the precipitation of cerium oxide/hydroxide [165]. Hydrogen peroxide also enhances the oxidation of Ce (III) to Ce (IV) ions in solution and this results in an hydroxide film containing cerium mainly in the 4-valent state, as observed by XPS studies [165, 166].

The formation of a cerium-rich layer on the anodic film involves several chemical reactions. Cerium can be precipitated due to an increase of the pH value on the interface between the anodic

oxide film and the post-treatment solution. The first step is the dissolution of the anodic alumina film in the cerium-based solution (pH 3.75):

$$Al_2O_3 + 6H^+ \rightarrow 2Al^{3+} + 3H_2O \quad (23)$$

The second step is the precipitation of cerium on the surface of the anodic film and within the pores due to the local rise in pH. Hydrogen peroxide present in the solution plays an important role in transforming Ce^{3+} to Ce^{4+} at pH > 2. Oxidation of Ce^{3+} to Ce^{4+} by H_2O_2 occurs also when the pH increases. This process changes the colour of the solution from colourless to yellow, according to [167, 168]. Increase of the pH value contributes to precipitation of cerium oxide/hydroxide through 2 pathways. The first pathway is through Ce (III), present in the initial Ce (III) nitrate solution (Equations 24, 25), and the second pathway is through Ce (IV) species (Equations 26-29) [168]. The latter is possible only in the presence of H_2O_2. Concerning the Ce (III) pathway, the precipitation of cerium products is described by the following reactions:

$$Ce^{3+} + 3OH^- \rightarrow Ce(OH)_3 \quad (24)$$

$$2Ce(OH)_3 \rightarrow Ce_2O_3 + 3H_2O \quad (25)$$

Concerning the Ce(IV) pathway, initial oxidation of Ce(III) takes place in the hydrogen peroxide-containing solution (at pH above 2).

$$2Ce^{3+} + 2OH^- + H_2O_2 \rightarrow 2Ce(OH)_2^{2+} \quad (26)$$

Subsequently, for pH values between 2 and 5:

$$Ce(OH)_2^{2+} + 2OH^- \rightarrow Ce(OH)_4 \rightarrow CeO_2 + 2H_2O \quad (27)$$

Also, other reactions in H_2O_2-assisted solutions are possible, where Ce^{3+} ions can be directly oxidized to Ce(IV) species without intermediate $Ce(OH)_2^{+2}$ by the following reactions:

$$2Ce^{3+} + 6OH^- + H_2O_2 \rightarrow 2Ce(OH)_4 \quad (28)$$

$$2Ce^{3+} + 6OH^- + H_2O_2 \rightarrow 2CeO_2 + 4H_2O \quad (29)$$

These reactions show that the oxidation of Ce^{3+} to $Ce(OH)_4$ occurs through intermediate species, such as $Ce(OH)^{3+}$ at pH < 2 and $Ce(OH)_2^{+2}$ at pH > 2, according to the E-pH diagrams of the

Ce - H_2O - H_2O_2 system.. Thus, Ce(IV) can exist in several species, such as $Ce(OH)^{3+}$, $Ce(OH)_2^{+2}$ and $Ce(OH)_4$.

The concentration of Ce^{3+} is higher for samples anodized in TSA followed by cerium-based post-treatment. It is likely that the addition of tartaric acid to the anodizing electrolyte decreases the chemical dissolution rate of the alumina oxide film in the acidic environment [169]. Thus, the local pH near the interface between the alumina and post-treatment solution remains lower compared to the pH in proximity of the oxides generated in the absence of tartaric acid. This could result in increased Ce^{3+}[170].

Chapter 5- Experimental tests

5.1 Experimental set up

In order to perform an experiment to evaluate the corrosion resistance of materials, a number of components must be assembled and appropriately prepared. First, an electrochemical cell which contains both the metal to be investigated, the environment in which the measurement is to be performed, as well as all of the implements required to conduct the measurement, must be acquired.

Prior to performing the experiment, the specimen surface must be prepared such that the initial condition, or starting point, of the measurement is well defined and does not vary from test to test. Finally, equipment capable of performing the measurement and acquiring data is required.

5.1.1 Electrochemical cell

The typical electrochemical cell is consist of cell body, the electrodes and the implements used to monitor and control the environment.

5.1.1.1 Cell body

The body of the cell is required to contain the test environment, which may or may not be aggressive. The material chosen to construct the cell from should take into consideration the requirements of the experimentation which will be conducted within, such as the operating temperature range, pH, need for aeration/deaeration, etc. Typical materials include glass, acrylic and polytetrafluoroethylene.

5.1.2 Electrodes

There are typically three electrodes - the working electrode, the counter electrode, and the reference electrode. The working electrode is the sample being interrogated, and will vary. The reference electrode provides a stable "reference" against which the applied potential may be accurately measured, as will be illustrated below. The counter electrode is used to provide the applied current, and as such should be composed of a highly corrosion resistant material, such as platinum.

5.1.2.1 Reference electrode

A range of reference electrodes is available (Table 7- [171]).

Table 7 - Common reference electrodes [171].

Common Name	Electrode	Reaction	E (V vs SCE)
Standard Hydrogen (SHE)	H_2(1atm)|H^+(a=1)	$2H^++2e^-=H_2$	0
Saturated Calomel	Hg|Hg_2Cl_2, KCl (sat)	$Hg_2Cl_2+2e^-=2Hg+2Cl^-$	+0.244
Silver/Silver Chloride (0.1M)	Ag|AgCl, KCl (0.1M)	$AgCl+e^-=Ag+Cl^-$	+0.288
Silver/Silver Chloride/seawater	Ag|AgCl, seawater	$AgCl+e^-=Ag+Cl^-$	+0.250
Copper/Copper sulphate	Cu|sat.$CuSO_4$	$Cu^{2+}+2e^-=Cu$	+0.318

The standard reference electrode which is often referred to is the standard hydrogen electrode (SHE) or normal hydrogen electrode (NHE). All other reference electrodes can be expressed in terms of some constant deviation from the SHE. The SHE is based upon the reaction:

$$2H^+ + 2e^- \rightarrow H_2(g) \quad (30)$$

It should be noted that this potential is independent of temperature (not true for many other electrodes) and a function only of the reference electrolyte pH. Some of the more commonly

utilized reference electrodes include the saturated calomel electrode (SCE), the silver-silver chloride reference electrode, and the copper-copper sulphate reference electrode (least accurate, but most durable of the three). The saturated calomel electrode consists of pure mercury covering a platinum wire which passes through a sealed glass tube. The mercury is covered with mercurous chloride and immersed in saturated potassium chloride.

$$Hg_2Cl_2 + 2e^- \rightarrow 2Hg + 2Cl^- \quad (31)$$

The silver-silver chloride reference electrode consists of a silver or silver plated wire, the surface of which has been chloritized (transformed to silver chloride), typically in dilute hydrochloric acid.

$$AgCl + e^- \rightarrow Ag + Cl^- \quad (32)$$

Finally, the copper - copper sulphate reference electrode consists of a piece of reasonably pure copper immersed in saturated copper sulphate.

$$Cu^{2+} + 2e^- \rightarrow Cu \quad (33)$$

Note that the appropriate reference electrode for a particular application will depend on the solution. Thus, a saturated calomel electrode must have saturated KCl as the solution in contact with the Hg/Hg_2Cl_2 paste. This means that the SCE tends to leach chloride (and potassium of course, although this is usually less significant for corrosion) into the solution in contact with it.

This leaching will contaminate the solution in contact with the reference electrode. Whether or not this leads to a serious problem depends on the test solution and the configuration of the reference electrode. In general, it is beneficial to use reference electrodes based on anions that are

already present in the test solution. Thus, SCE is fine for seawater and other solutions containing high concentrations of chloride, but would be undesirable in chloride-free solutions.

5.1.2.2 Counter electrode

In some cases, typically when working with microelectrodes, or when the current is very small for some other reason, it is possible to use the reference electrode as the counter electrode.

The use of a specific counter electrode can also be avoided by using two working electrodes, and this may be useful in the measurement of polarization resistance or electrochemical impedance (seen already). In all other cases where current is applied to the working electrode, a counter electrode is required as the second connection to the test solution. In most cases, the counter electrode should not affect the measurement, and it should therefore have the following properties:

- It should have a relatively low polarization resistance so that the potential drop between the counter electrode and the solution does not limit the polarization that can be applied.

- It should not contaminate the solution. In practice, there will always be some electrochemical reaction at the counter electrode, and what we really need is for the products of that reaction to be harmless or easily removed. Inert electrodes, such as platinum or graphite are often used, in which case the reaction products are usually gases (oxygen or chlorine when anodic or hydrogen when cathodic) that can be removed by bubbling air or nitrogen past the counter electrode (although there may also be a pH change at the counter electrode). In closed systems (e.g., in autoclave studies), it is more difficult to dispose of gaseous reaction products, and it may be better to use a reactive electrode and trap the reaction products close to the counter electrode (e.g., by using an ion-exchange membrane between the counter electrode and the working electrode). It is also wise to check that

supposedly inert electrodes are actually inert – some platinum dissolution can occur at high enough anodic current densities and graphite electrodes tend to release traces of impurities into the solution as the graphite is oxidized to CO_2. Note that many metals, including carbon steels and stainless steels, are essentially inert when cathodically polarized, and they can therefore be used as counter electrodes when only anodic polarization of the working electrode is required (e.g., when studying pitting breakdown potentials of stainless steel).

- It is often stated that the area of the counter electrode should be large compared with the working electrode, but this may be less important than ensuring that the overall cell configuration provides the required current density distribution. Thus, a counter electrode of the same size as the working electrode, mounted parallel to it, may optimize the current distribution without significant adverse effects from the size of the counter electrode.

5.2 Potentiodynamic polarization measurements

Polarization studies can provide valuable information regarding the corrosion mechanism, corrosion rate and susceptibility to corrosion of metallic specimens in designated environments. One of the most common electrochemical methods in corrosion research and testing is the determination of the polarization curve – the relationship between the current and the potential, usually over a relatively wide range (of the order of a volt). Polarization curves can be measured either by controlling the current and measuring the potential or by controlling the potential and measuring the current. The characteristics of passive/active conditions for metals can be readily defined using this technique. Details for laboratory application can be found in ASTM Standard G5.

The potential changes with a certain scan rate while the potentiodynamic is being performed. The speed of the scan rate will largely influence the type of information obtained. In general, higher scan rates do not allow sufficient time for the system to stabilize at each potential.

As a result, parameters such as the location and size of the active nose, the passivation potential, and the pitting potential are often shifted to more positive values. The ASTM standard scan rate is 0.1667 mV/s.

5.2.1 Anodic and cathodic curves

A schematic anodic polarization curve is illustrated in Figure 2 and more details regarding the curve are discussed above in Section 3.3. A schematic cathodic polarization scan is present in Figure 15.

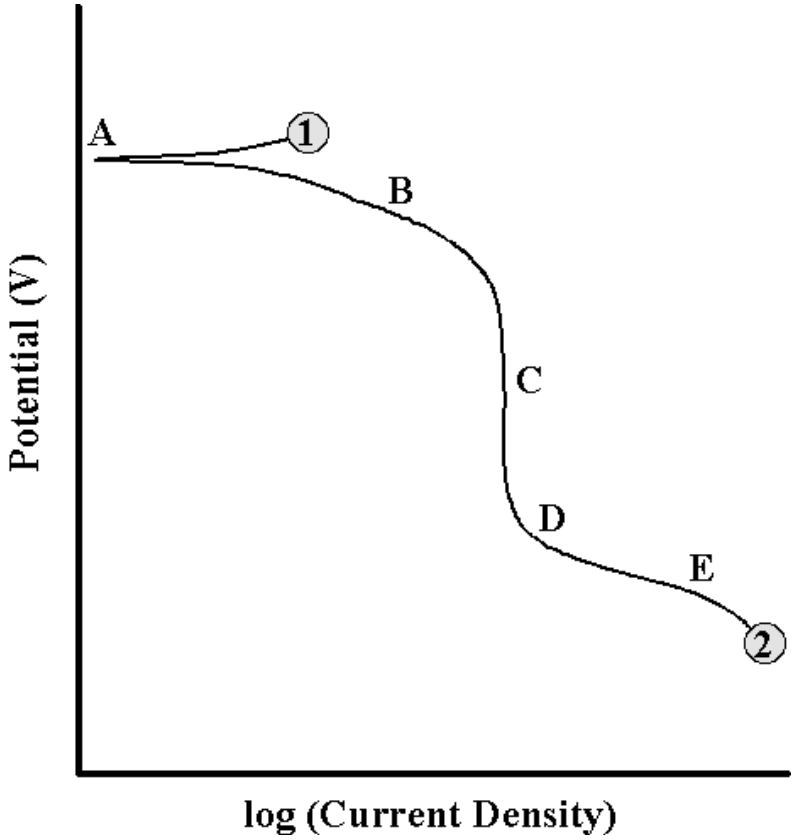

Figure 15 – Schematic cathodic polarization curve.

In a cathodic potentiodynamic scan, the potential is varied from point 1 in the negative direction to point 2. The open circuit potential is located at point A. As with the anodic scan, the

open circuit potential represents the potential at which the sum of the anodic and cathodic reactions occurring on the electrode surface is zero. Depending on the pH and dissolved oxygen concentration in the solution, region B may represent the oxygen reduction reaction. Since this reaction is limited by how fast oxygen may diffuse in solution there will be an upper limit on the rate of this reaction, known as the limiting current density. Further decreases in the applied potential result in no change in the reaction rate, and hence the measure current (region C). Eventually, the applied potential becomes sufficiently negative for another cathodic reaction to become operative, such as illustrated at point D. As the potential, and hence driving force, becomes increasingly large, this reaction may become dominant, as illustrated in region E. This additional reaction is typically the reduction of other species in the environment (such as the hydrogen evolution reaction, also known as the water reduction reaction).

5.3 Electrochemical Impedance Spectroscopy (EIS)

The Electrochemical Impedance Spectroscopy (EIS), also known as AC impedance method, is a widespread experimental technique usually applied in electrochemical system analysis, and mainly used to characterize both the electrode and the interface processes [172]. Electrochemical impedance is usually measured by applying an AC potential to an electrochemical cell and then measuring the current through the cell. Assume that we apply a sinusoidal potential excitation. The response to this potential is an AC current signal. This current signal can be analysed as a sum of sinusoidal functions (a Fourier series). Electrochemical impedance is normally measured using a small excitation signal. This is done so that the cell's response is pseudo-linear. In a linear (or pseudo-linear) system, the current response to a sinusoidal potential will be a sinusoid at the same frequency but shifted in phase (see Figure 16).

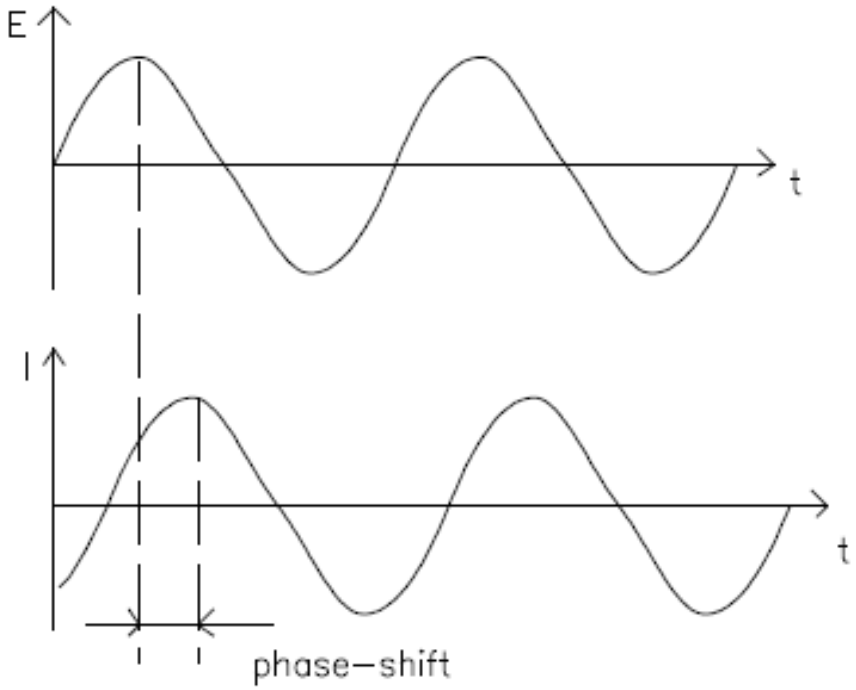

Figure 16 – Sinusoidal current response in a linear system.

The excitation signal, expressed as a function of time, has the form

$$E_t = E_0 \sin(\omega t) \quad (34)$$

where E_t is the potential at time t, E_0 is the amplitude of the signal, and ω is the radial frequency. The relationship between radial frequency ω (expressed in radians/second) and frequency f (expressed in hertz) is:

$$\omega = 2\pi f \quad (35)$$

In a linear system, the response signal, It, is shifted in phase (φ) and has a different amplitude, I_0.

$$I_t = I_0 \sin(\omega t + \varphi) \quad (36)$$

An expression analogous to Ohm's Law allows us to calculate the impedance of the system as:

$$Z = \frac{E_t}{I_t} = \frac{E_0 \sin(\omega t)}{I_0 \sin(\omega t + \varphi)} = Z_0 \frac{\sin(\omega t)}{\sin(\omega t + \varphi)} \quad (37)$$

The impedance is therefore expressed in terms of a magnitude, Z_0, and a phase shift, φ. If we plot the applied sinusoidal signal E(t) on the X-axis of a graph and the sinusoidal response signal I(t) on the Y-axis, the result is an oval (see Figure 17).

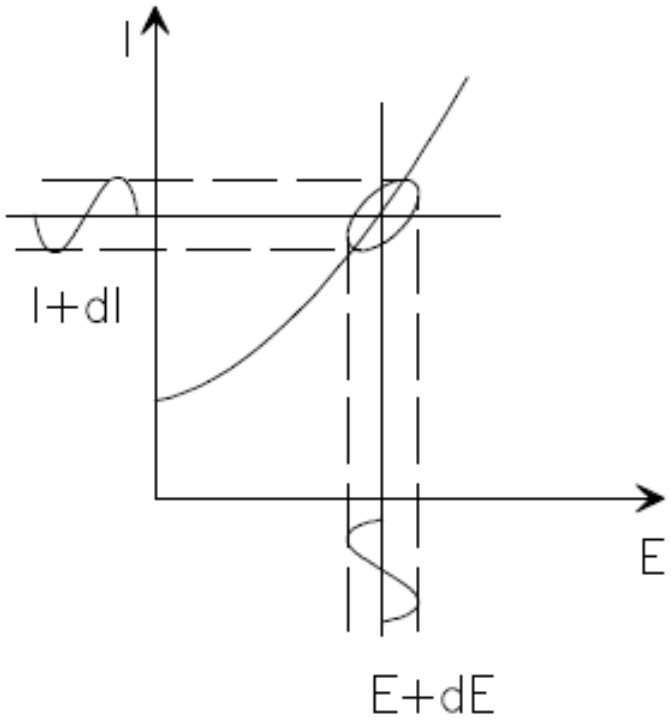

Figure 17 – Origin of Lissajous figure.

This oval is known as a "Lissajous Figure". Analysis of Lissajous Figures on oscilloscope screens was the accepted with Eulers relationship,

$$exp(j\varphi) = \cos\varphi + \mathrm{j}\sin\varphi \quad (38)$$

It is possible to express the impedance as a complex function. The potential is described as,

$$E_t = E_0 exp(j\omega t) \quad (39)$$

and the current response as,

$$I_t = I_0 exp(j\omega t - \varphi) \quad (40)$$

The impedance is then represented as a complex number,

$$Z(\omega) = \frac{E}{I} = Z_0 \exp(j\varphi) = Z_0 (\cos\varphi + \mathrm{j}\sin\varphi) \quad (41)$$

The application of a perturbation to a system in equilibrium conditions causes a response, which is entirely determined by the injected signal. If the system is at equilibrium, it should be able to return to its original state when the perturbation is removed. Moreover, if the system has a linear behaviour, the response to a sum of single perturbations is equal to the sum of each response; this is the principle of the EIS.

The EIS measurement produces a set of amplitude and phase values for a range of frequencies, and there are two main ways of presenting these:

- The Bode plot presents log(amplitude) and phase against log(frequency). Figure 18 presents a Bode plot.

- The Nyquist plot normally plots the imaginary part of the impedance against the real part (Figure 19). The Nyquist plot invariably inverts the imaginary axis (i.e., it plots the imaginary component of impedance with increasingly negative values on the y-axis), so that capacitive circuit elements plot above the x-axis. One weakness of the Nyquist plot compared with the Bode plot is that it does not implicitly include the frequency of each measurement point, so at least some points should have their frequency indicated.

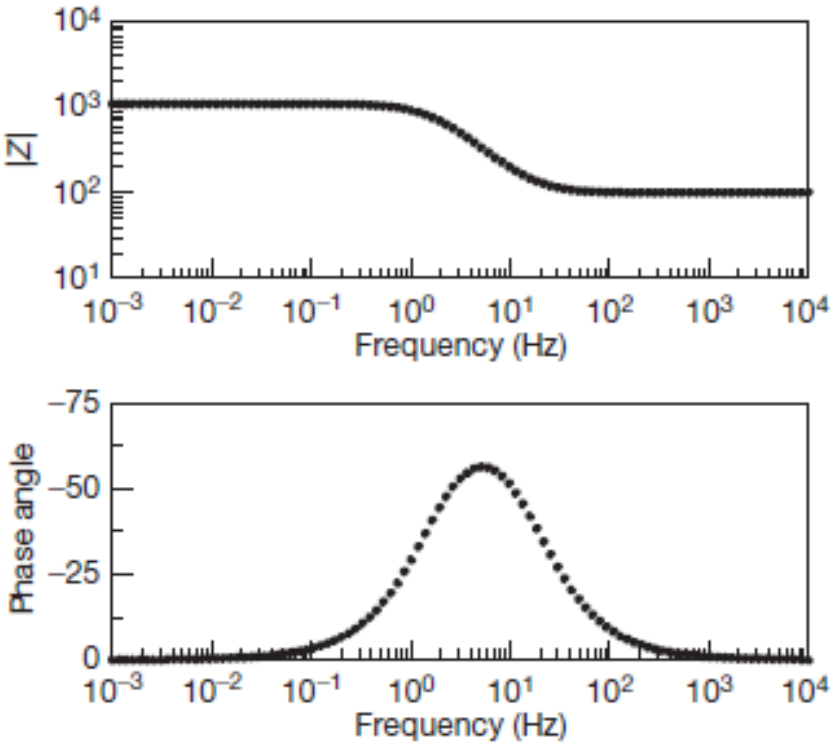

Figure 18 – Example Bode plot.

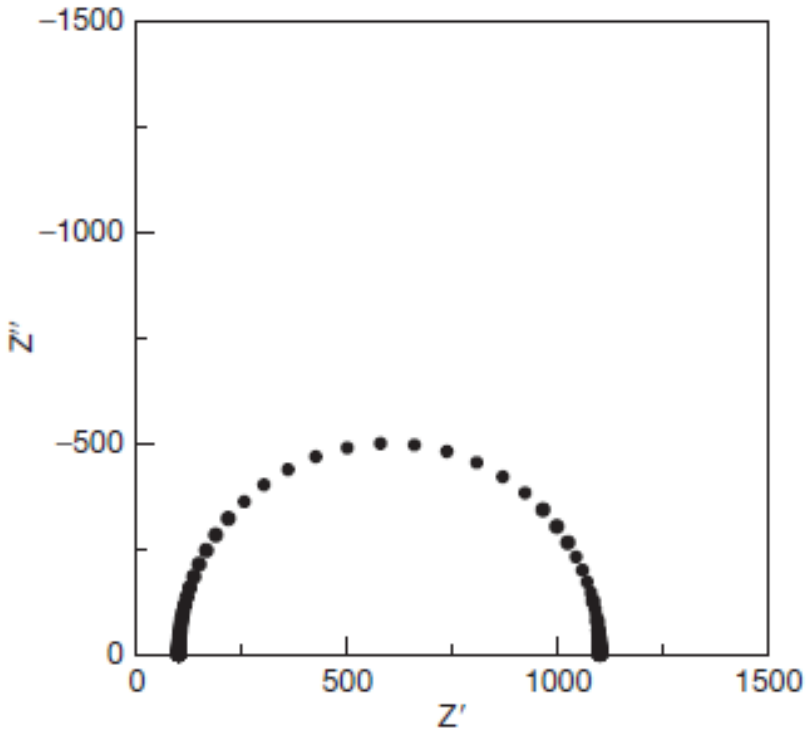

Figure 19 – Example Nyquist plot.

5.3.1 Interpretation of EIS measurements

The interpretation of the EIS data can be supported through mathematical models. Particularly, equivalent circuit models (ECM) are suitable tools for electrode/electrolyte interface characterization [173]. Adopting an equivalent circuit, different electrical components are used to characterize the different physical processes. For example, the impedance plot in Figure 18 can be fitted using the circuit in Figure 20.

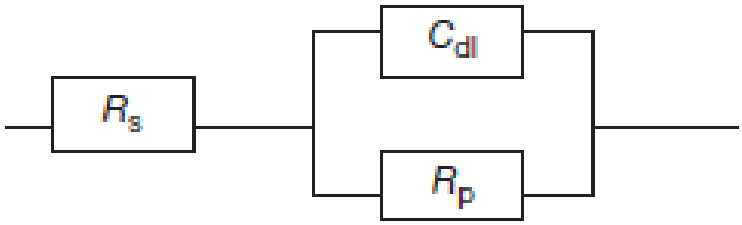

Figure 20 – The Randles equivalent circuit for a corrosion interface.

This circuit is known as the Randles equivalent circuit and has three components: R_s is the resistance of the solution, R_p is the polarization resistance of the metal–solution interface, and C_{dl} is the double-layer capacitance of the metal–solution interface). On the Bode plot, a resistor produces a horizontal line on the amplitude plot with amplitude equal to the resistance and a constant phase of zero on the phase plot. A capacitor produces an amplitude that falls with a slope of -1 as the frequency increases (the amplitude of the impedance is $1/(2\pi fC)$, where f is the frequency and C the capacitance), and a constant phase of -90°; as we are normally dealing with resistors and capacitors, it is common to invert the phase axis (i.e., plot–phase) so that capacitive circuit elements give data above zero.

Any resistor network will appear from the outside as a pure resistor (i.e., the measured impedance will have constant amplitude and zero phase). Consequently, in order to obtain a valid interpretation, it is important to use prior knowledge of the expected behaviour in order to model the real physical system. the components of the system under investigation to be modelled by electrical equivalent circuit elements that have similar characteristics to the actual processes concerned. Thus, a paint film can be modelled as a resistor (corresponding to ionic current passing through the film) in parallel with a capacitor (corresponding to the capacitance of the paint film acting as a parallel plate capacitor); underneath the paint film the metal–solution interface gives rise to a resistor (corresponding to the charge transfer resistance) in parallel with a capacitance (the

double layer capacitance). The response of the resultant electrical circuit is then modelled using conventional methods from electrical engineering, and the parameter values adjusted to optimize the fit between the model and real data. Note that the equivalent circuit is derived first, based on the physical processes occurring; it may then be necessary to modify the equivalent circuit to fit features of the measured data. It is important that the added elements are linked to a physical process; some less-experienced workers try different equivalent circuits to find the one that best fits the measured data and then try to work out what the elements correspond to; while this may provide a good fit to the data, the circuit may have the wrong configuration so that the values of circuit elements give no information about the real processes occurring.

5.3.1.1 Resistor

The current $\Delta i(t)$ and voltage $\Delta v(t)$ relation for a resistor is

$$\Delta v(t) = R\Delta i(t) \quad (42)$$

where R is the resistance. Laplace transform of (Equation 42) for the sinusoidal input gives

$$\Delta V(j\omega) = R\Delta I(j\omega) \quad (43)$$

The impedance for the resistor is thus

$$Z(j\omega) = \frac{\Delta V\,(j\omega)}{\Delta I(j\omega)} = R \quad (44)$$

The impedance of a resistor is independent of frequency and has no imaginary component. With only a real impedance component, the current through a resistor stays in phase with the voltage across the resistor.

5.3.1.2 Inductor

The current $\Delta i(t)$ and voltage $\Delta v(t)$ relation for an inductor is

$$\Delta v(t) = L \frac{d\Delta i(t)}{dt} \quad (45)$$

Laplace transform of (Equation 45) for the sinusoidal input gives

$$\Delta V(j\omega) = j\omega L \Delta I(j\omega) \quad (46)$$

where L is the inductance. The impedance for the inductor is thus

$$Z(j\omega) = \frac{\Delta V(j\omega)}{\Delta I(j\omega)} = j\omega L \quad (47)$$

The impedance of an inductor increases as frequency increases. Inductors have only an imaginary impedance component. As a result, the current through an inductor is phase-shifted -90 degrees with respect to the voltage.

5.3.1.3 Capacitor

The current $\Delta i(t)$ and voltage $\Delta v(t)$ relation for a capacitor is

$$\Delta i(t) = C\frac{d\Delta v(t)}{dt} \quad (48)$$

where C is the capacitance. Laplace transform of (Equation 48) for the sinusoidal input gives

$$\Delta I(j\omega) = j\omega C\Delta V(j\omega) \quad (49)$$

The impedance for the capacitor is thus

$$Z(j\omega) = \frac{\Delta V(j\omega)}{\Delta I(j\omega)} = \frac{1}{j\omega C} \quad (50)$$

The impedance versus frequency behaviour of a capacitor is opposite to that of an inductor. A capacitor's impedance decreases as the frequency is raised. Capacitors also have only an imaginary impedance component. The current through an capacitor is phase shifted 90 degrees with respect to the voltage.

5.3.1.3.1 Constant Phase Element (CPE)

The Constant Phase Element [174] (CPE) is a non-intuitive circuit element that was invented while looking at the response of real-world systems. Mathematically, it is defined as

$$Z(j\omega) = \frac{1}{j\omega^{\alpha}C_{\alpha}} \quad (51)$$

with two parameters α and C_α. It reduces to pure resistor, capacitor and inductor when α = 0, α = 1 and α = -1 respectively. However, in the real application of this element, α is defined between 0 and 1 and this element can be thought of as a fractional generalization of a conventional capacitor.

5.3.1.4 Generalized Finite-Length Warburg Element

Mathematically, the Generalized Finite-Length Warburg Element (GFLW) is the solution to the one-dimensional anomalous diffusion equation subject to the absorbing boundary [175]

$$Z(j\omega) = R_{GFLW}\frac{\tan(j\omega C_{GFLW})^{\alpha GFLW}}{(j\omega C_{GFLW})^{\alpha GFLW}} \quad (52)$$

with three parameters R_{GFLW}, C_{GFLW} and α_{GFLW}. When $(j\omega\ C_{GFLW})^{\alpha GFLW}$ »1, it reduces to a CPE as in (Equation 51).

When α_{GFLW} = 0:5, it reduces to a Finite-Length Warburg (FLW) element [176]

$$Z(j\omega) = R_{FLW}\frac{tan\sqrt{j\omega C_{FLW}}}{\sqrt{j\omega C_{FLW}}} \quad (53)$$

with two parameters R_{FLW} and C_{FLW}. Again, in the real application of this element, α_{GFLW} is defined between 0 and 0.5. GFLW element gives a half-tear-drop arc called Warburg arc in the Nyquist plot as shown in Figure 21. For the FLW element, the slope at the high-frequency part is 45° as in Figure 21. For the GFLW element, the arc is more depressed and the slope at the high-frequency part is less than 45° as in Figure 21.

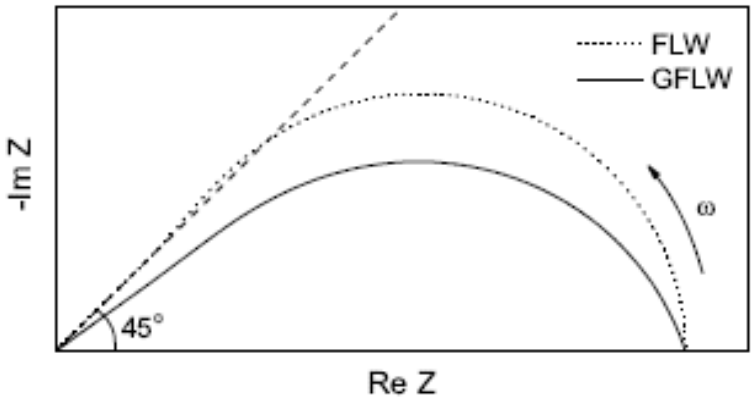

Figure 21 – Schematic Nyquist plots of a Finite-Length Warburg (FLW) element and a Generalized Finite-Length Warburg (GFLW) element.

5.3.1.5 Serial and Parallel combination of circuit element

EIS models usually consist of a number of elements in a network. Both serial (Figure 22) and parallel (Figure 23) combinations of elements occur.

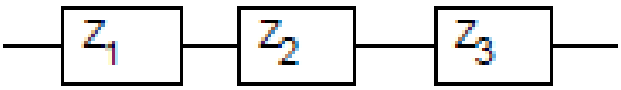

Figure 22 – Impedance in series.

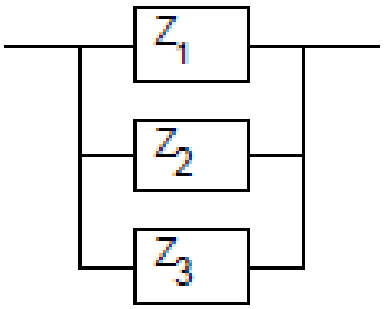

Figure 23 – Impedance in parallel.

Fortunately, there are simple formulas that describe the impedance of circuit elements in both parallel and series combination. For linear impedance elements in series you calculate the equivalent impedance from:

$$\mathrm{Z}_{eq} = Z_1 + Z_2 + Z_3 \quad (54)$$

For linear impedance elements in parallel you calculate the equivalent impedance from:

$$\frac{1}{\mathrm{Z}_{eq}} = \frac{1}{Z_1} + \frac{1}{Z_2} + \frac{1}{Z_3} \quad (55)$$

We will calculate two examples to illustrate a point about combining circuit elements. Suppose we have a 1Ω and a 4Ω resistor in series. The impedance of a resistor is the same as its resistance (see Table 8).

Table 8 - Common electrical elements.

Component	**Current vs. Voltage**	**Impedance**
Resistor	E=IR	Z=R
Inductor	E=L di/dt	Z=jωL
Capacitor	I=C dE/dt	Z=1/ jωC

We thus calculate the total impedance as:

$$\mathrm{Z}_{eq} = Z_1 + Z_2 = R_1 + R_2 = 1\Omega + 4\Omega = 5\Omega \quad (56)$$

Resistance and impedance both go up when resistors are combined in series. Now suppose that we connect two 2 μF capacitors in series. The total capacitance of the combined capacitors is 1 μF.

$$Z_{eq} = Z_1 + Z_2 = \frac{1}{j\omega C_1} + \frac{1}{j\omega C_2} = \frac{1}{j\omega(2e^{-6})+1} + \frac{1}{j\omega(2e^{-6})} = \frac{1}{j\omega(1e^{-6})j} \quad (57)$$

Impedance goes up, but capacitance goes down when capacitors are connected in series. This is a consequence of the inverse relationship between capacitance and impedance.

5.3.2 Physical electrochemistry and equivalent circuit elements

5.3.2.1 Electrolyte resistance

Solution resistance is often a significant factor in the impedance of an electrochemical cell. A modern 3 electrode potentiostat compensates for the solution resistance between the counter and reference electrodes. However, any solution resistance between the reference electrode and the working electrode must be considered when you model your cell. The resistance of an ionic solution depends on the ionic concentration, type of ions, temperature, and the geometry of the area in which current is carried. In a bounded area with area, A, and length, l, carrying a uniform current, the resistance is defined as,

$$R = \rho \frac{l}{A} \quad (58)$$

ρ is the solution resistivity. The reciprocal of ρ(κ) is more commonly used. κ is called the conductivity of the solution and its relationship with solution resistance is:

$$R = \frac{1}{\kappa}\frac{l}{A} \rightarrow \kappa = \frac{l}{RA} \quad (59)$$

Standard chemical handbooks will often list κ values for specific solutions. For other solutions, you can calculate κ from specific ion conductance. The unit of κ is the Siemens per meter (S/m). The Siemens is the reciprocal of the ohm, so 1S=1/Ohm. Unfortunately, most electrochemical cells do not have uniform current distribution through a definite electrolyte area.

The major problem in calculating solution resistance therefore concerns determination of the current flow path and the geometry of the electrolyte that carries the current. A comprehensive discussion of the approaches used to calculate practical resistances from ionic conductance is well beyond the scope of this manual. Fortunately, you usually don't calculate solution resistance from ionic conductance. Instead, you calculate it when you fit experimental EIS data to a model.

5.3.2.2 Double layer capacitance

An electrical double layer exists on the interface between an electrode and its surrounding electrolyte. This double layer is formed as ions from the solution "stick on" the electrode surface.

The charged electrode is separated from the charged ions. The separation is very small, often on the order of angstroms. Charges separated by an insulator form a capacitor. On a bare metal immersed in an electrolyte, you can estimate that there will be 20 to 60 μF of capacitance for every 1 cm^2 of electrode area. The value of the double layer capacitance depends on many variables. Electrode potential, temperature, ionic concentrations, types of ions, oxide layers, electrode roughness, impurity adsorption, etc. are all factors.

5.3.2.3 Polarization resistance

Whenever the potential of an electrode is forced away from its value at open-circuit, that is referred to as “polarizing” the electrode. When an electrode is polarized, it can cause current to flow through electrochemical reactions that occur at the electrode surface. The amount of current is

controlled by the kinetics of the reactions and the diffusion of reactants both towards and away from the electrode. In cells where an electrode undergoes uniform corrosion at open circuit, the open circuit potential is controlled by the equilibrium between two different electrochemical reactions.

One of the reactions generates cathodic current and the other anodic current. The open circuit potential ends up at the potential where the cathodic and anodic currents are equal. It is referred to as a mixed potential. The value of the current for either of the reactions is known as the corrosion current. Mixed potential control also occurs in cells where the electrode is not corroding. While this section discusses corrosion reactions, modification of the terminology makes it applicable in non-corrosion cases as well. When there are two simple, kinetically controlled reactions occurring, the potential of the cell is related to the current by the following equation.

$$I = I_{corr}(e^{\frac{2.303(E-E_{OC})}{\beta a}} - e^{\frac{-2.303(E-E_{OC})}{\beta c}} \quad (60)$$

where,

I = the measured cell current in amps,

I_{corr} = the corrosion current in amps,

E_{oc} = the open circuit potential in volts,

β_a = the anodic Beta coefficient in volts/decade,

β_c = the cathodic Beta coefficient in volts/decade.

If we apply a small signal approximation to Equation 60, we get the following:

$$I_{corr} = \frac{\beta_a \beta_c}{2.303(\beta_a \beta_c)}(\frac{1}{R_p}) \quad (61)$$

which introduces a new parameter, R_p, the polarization resistance. As you might guess from its name, the polarization resistance behaves like a resistor. If the β slopes are known, the Tafel constants, you can calculate the I_{corr} from R_p using Equation 60. I_{corr} in turn can be used to calculate a corrosion rate.

5.3.2.4 Charge transfer resistance

A similar resistance is formed by a single kinetically controlled electrochemical reaction. In this case we do not have a mixed potential, but rather a single reaction at equilibrium. Consider a metal substrate in contact with an electrolyte. The metal can electrolytically dissolve into the electrolyte, according to,

$$Me \leftrightarrow Me^{n+} + ne^{-} \quad (62)$$

or more generally

$$Red \leftrightarrow Ox + ne^{-} \quad (63)$$

In the forward reaction in the first equation, electrons enter the metal and metal ions diffuse into the electrolyte. Charge is being transferred. This charge transfer reaction has a certain speed. The speed depends on the kind of reaction, the temperature, the concentration of the reaction products and the potential. The general relation between the potential and the current (which is directly related with the amount of electrons and so the charge transfer via Faradays law) is:

$$i = i_0\left(\frac{C_o}{C^{*o}}\exp\left(\frac{\alpha nF\eta}{RT}\right) - \left(\frac{C_R}{C^{*R}}\exp\left(\frac{-(1-\alpha)nF\eta}{RT}\right)\right)\right) \quad (64)$$

with,

i_0 = exchange current density

C_O = concentration of oxidant at the electrode surface

C^{O*} = concentration of oxidant in the bulk

C^R = concentration of reductant at the electrode surface

η= overpotential ($E_{app} – E_{oc}$)

F = Faradays constant

T = temperature

R = gas constant

α= reaction order

n = number of electrons involved

When the concentration in the bulk is the same as at the electrode surface, $C_O=C^{O*}$ and $C_R=C^{R*}$. This simplifies Equation 64 into:

$$i = i_0(\exp\left(\alpha\frac{nF}{RT}\eta\right) - \left(\exp(-(1-\alpha)\frac{nF}{RT}\eta\right) \quad (65)$$

This equation is called the Butler-Volmer equation. It is applicable when the polarization depends only on the charge-transfer kinetics. Stirring the solution to minimize the diffusion layer thickness can help minimize concentration polarization. When the overpotential, η, is very small and the electrochemical system is at equilibrium, the expression for the charge transfer resistance changes to:

$$R_{ct} = \frac{RT}{nFi_0} \quad (66)$$

From this equation the exchange current density can be calculated when R_{ct} is known.

5.3.2.5 Diffusion

Diffusion also can create an impedance called a Warburg impedance. The impedance depends on the frequency of the potential perturbation. At high frequencies, the Warburg impedance is small since diffusing reactants don't have to move very far. At low frequencies, the reactants have to diffuse farther, increasing the Warburg-impedance. The equation for the "infinite" Warburg impedance is:

$$Z_W = \sigma(\omega)^{-\frac{1}{2}}(1-j) \quad (67)$$

On a Nyquist Plot the Warburg impedance appears as a diagonal line with an slope of 45°. On a Bode Plot, the Warburg impedance exhibits a phase shift of 45°. In Equation 67, σ is the Warburg coefficient defined as:

$$\sigma = \frac{RT}{n^2F^2A\sqrt{2}}\left(\frac{1}{C^{*o}\sqrt{D_o}} + \frac{1}{C^{*R}\sqrt{D_R}}\right) \quad (68)$$

in which,

ω= radial frequency

D_O = diffusion coefficient of the oxidant

D_R = diffusion coefficient of the reductant

A = surface area of the electrode

n = number of electrons involved

This form of the Warburg impedance is only valid if the diffusion layer has an infinite thickness. Quite often, however, this is not the case. If the diffusion layer is bounded, the impedance at lower frequencies no longer obeys the equation above. Instead, we get the form:

$$Z_o = \sigma\omega^{-\frac{1}{2}}(1-j)\tan(\delta(\frac{j\omega}{D})^{\frac{1}{2}}) \quad (69)$$

with,

δ= Nernst diffusion layer thickness

D = some average value of the diffusion coefficients of the diffusing species

This more general equation is called the "finite" Warburg.

5.3.2.6 Coating capacitance

A capacitor is formed when two conducting plates are separated by a non-conducting media, called the dielectric. The value of the capacitance depends on the size of the plates, the distance between the plates and the properties of the dielectric. The relationship is,

$$C = \frac{\varepsilon_0 \varepsilon_r A}{d} \quad (70)$$

with,

ε_0 = permittivity of free space ("electric constant")

ε_r = dielectric constant (relative electrical permittivity)

A = surface of one plate

d = distances between two plates

Whereas the permittivity of free space is a physical constant, the dielectric constant depends on the material. Table 9 gives you some useful ε_r values.

Table 9 – Typical dielectric constants.

Material	ε_r
Vacuum	1
Water	80.1 (20°C)
Organic coating	4-8

Notice the large difference between the dielectric constant of water and that of an organic coating. The capacitance of a coated substrate changes as it absorbs water. EIS can be used to measure that change.

5.3.3 Common equivalent circuit models

Walter, in a review of impedance plot methods used for corrosion performance analysis of painted metals [177], presented a small library of Bode and Nyquist plot shapes.

5.3.3.1 Simple RC equivalent circuit models

In simple systems, combinations of resistors and capacitors each give a characteristic plot shape in both Nyquist and Bode plots, so that analysis of the plot shape will not only allow calculation of individual component values, but may also indicate how they are combined together. For example, the series resistor/capacitor combination shown in Figure 24 gives a different plot shape to the parallel resistor/capacitor combination shown in Figure 25.

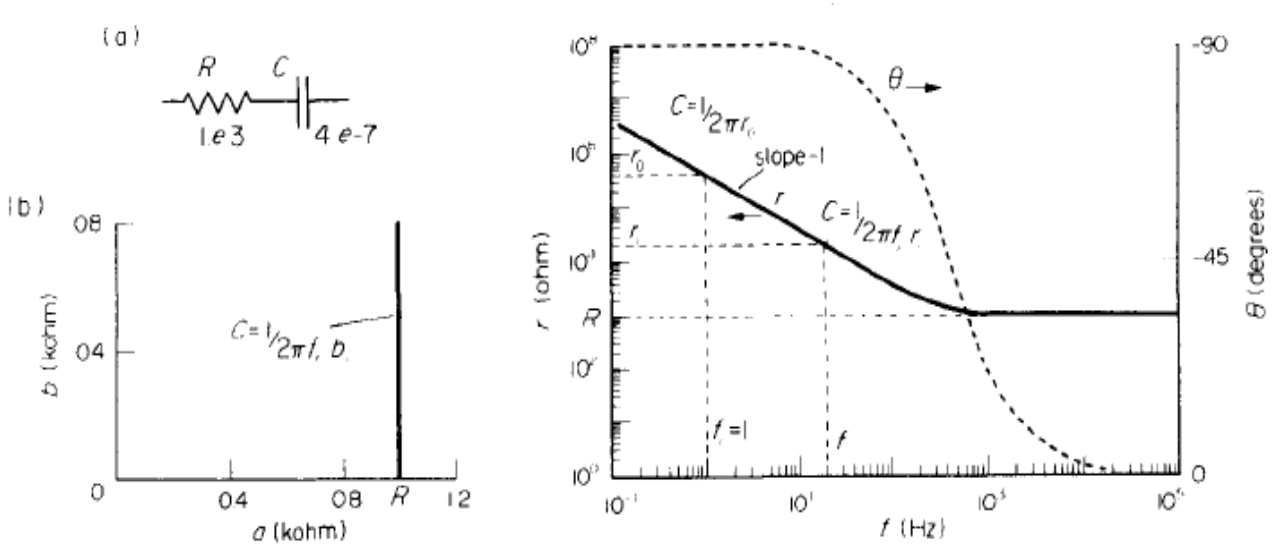

Figure 24 - A series resistor, R, and capacitor, C (a), and its Nyquist (b) and Bode (c) impedance plots [177].

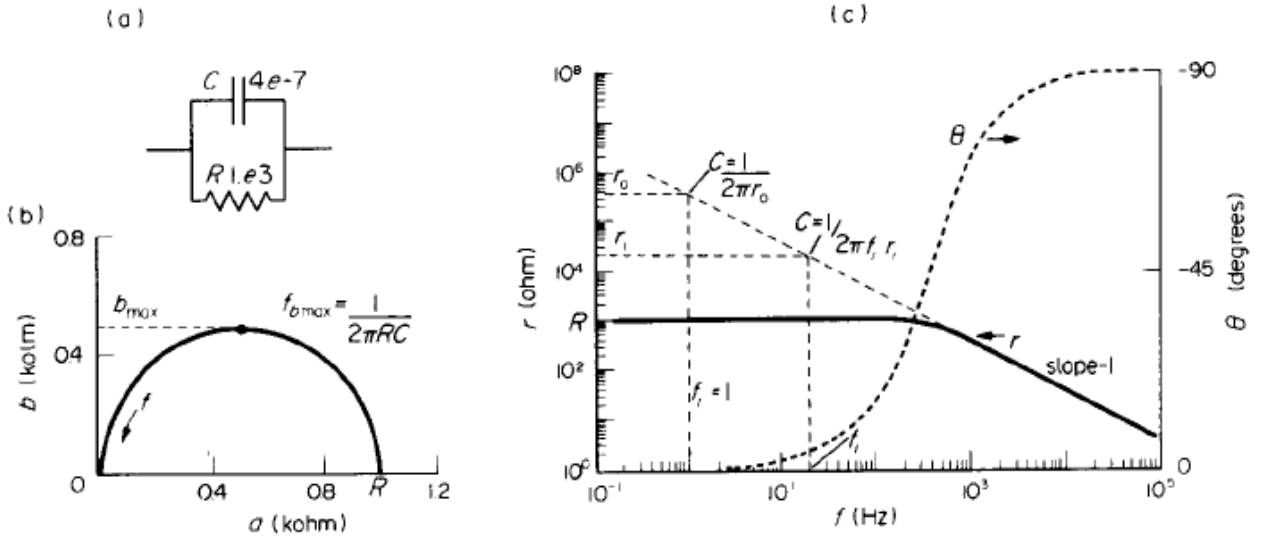

Figure 25 - A parallel resistor, R, and capacitor, C (a), and its Nyquist (b) and Bode (c) impedance plots [177].

However in more complex system the frequency response of a system does not uniquely determine the circuit to be used to model that response, a fact pointed out by MacDonald et al. [178] The resistor, capacitor component values of Figs. 24a and 25a can be determined using the methods shown in Figs 24b,c and 25b, c, respectively.

The value of resistor R, in Figure 24a, is obtained from the Nyquist plot in Figure 24b by reading off the value of *a* at the point where the vertical line intersects the a-axis, i. e. where b=0. From the Bode plot in Figure 24c, the value of R is obtained by extrapolation of the frequency independent horizontal line to the r-axis and reading off the value of r (=R).

The value of capacitor, C, in Figure24a, can be determined from the Nyquist plot in Figure 24b by reading off the value bi at any frequency, f_i, according to Equation 71.

$$C = \frac{1}{2\pi f_i b_i} \quad (71)$$

The value of C can be determined using Equation 72 from the Bode plot in Figure 2c by reading off the value r_i at any frequency, f_i, where the slope of the curve (or an extrapolation of the curve) is -1. At slope =-1,

$$C = \frac{1}{2\pi f_i r_i} \quad (72)$$

5.3.3.2 Unpainted metal equivalent circuits

The impedance of the circuit is shown in Figure 26a.

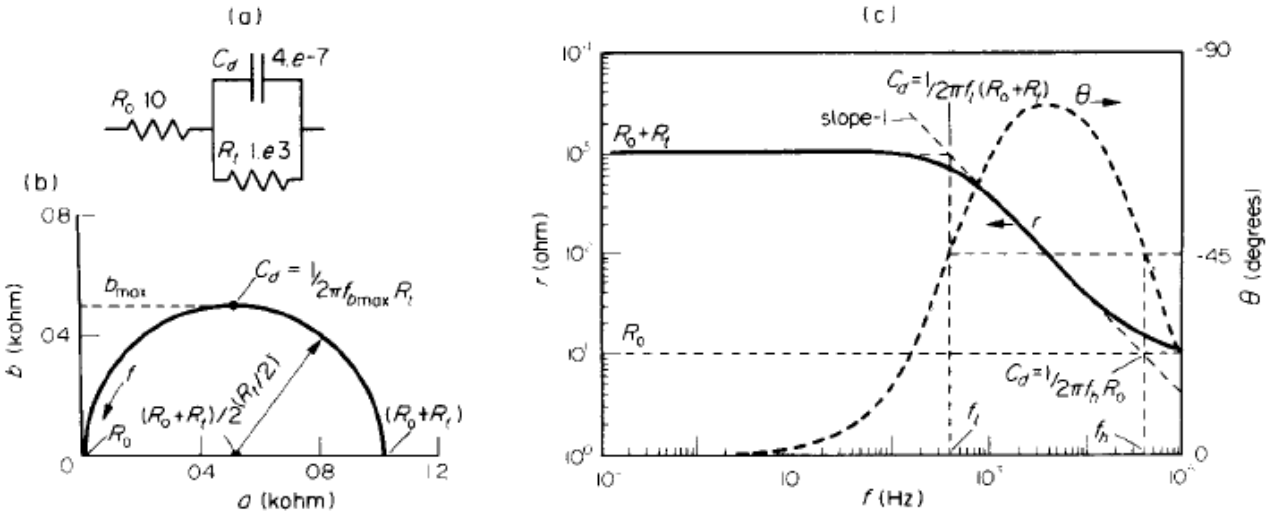

Figure 26 - Equivalent electrical circuit used to represent the unpainted metal/solution interface (a) and its Nyquist (b) and Bode (c) impedance plots [177].

$$Z = R_0 + \frac{R_t(\frac{1}{j\omega C_d})}{R_t(1+j\omega C_d)} = R_0 + \left(\frac{\frac{1}{R_t}}{\frac{1}{R_t^2}+\omega^2 C_d^2}\right) - \frac{j\omega C_d}{\frac{1}{R_t^2}+\omega^2 C_d^2} \quad (73)$$

Which is of the form

$$Z = a - jb \quad (74)$$

where

$$a = R_0 + \left(\frac{\frac{1}{R_t}}{\frac{1}{R_t^2}+\omega^2 C_d^2}\right) \quad (75)$$

$$b = \frac{\omega C_d}{\frac{1}{R_t^2}+\omega^2 C_d^2} \quad (76)$$

The term $\frac{1}{R_t^2} + \omega^2 C_d^2$ can be eliminated from Equations 75 and 76 to give $\omega = \frac{b}{a - R_0(R_t C_d)}$ which can be substituted into Equation 75 and rearranged to give Equation 77:

$$(a - R_0 - \frac{R_t}{2})^2 + b^2 = (\frac{R_t}{2})^2 \quad (77)$$

This is the equation of a circle radius $\frac{R_t}{2}$ and centre at $R_0 + \frac{R_t}{2}$ and explains the shape of the Nyquist complex plane semicircle in Figure 26b which results from parallel combination of R_t and C_d. The shape of the corresponding log r Bode plot (Figure 26c), is two frequency independent horizontal lines at low and high frequencies giving values on the log r axis for R_0 and (R_0+R_t), respectively, and a central portion at intermediate frequencies with a slope approaching -1 caused by the capacitor, C_d. The phase angle, dotted plot in Figure 26c, show θ dropping towards zero at low and high frequencies, corresponding to the resistive behaviour of R_0 and (R_0+R_t), and rinsing towards -90° at intermediate frequencies, corresponding to the capacitive behaviour of C_d.

5.3.3.3 Painted metal equivalent circuits

An equivalent circuit model for the painted metal/solution interface requires inclusion of the paint film parameters to the circuit of Figure 26a.

The resistor, R_{pf}, has been interpreted as the pore resistance due to electrolyte penetration [179, 180] and at damaged areas of the film [179], or as areas where more rapid solution uptake occurs, namely, pre-existing holes or porous areas where inadequate cross-linking of the polymer is present [181]. The capacitor C_{pf}, has been interpreted as the capacitance of the electric capacitor consisting of the metal and electrolyte, with the paint film as dielectric [179]; or simply as the capacitance of the intact film [180], or as the capacitance of the areas where rapid solution uptake does not occur [181]. In many cases, one modification takes into account diffusion processes within

pores in the paint film, which are modelled by the inclusion of a Warburg or pseudo-impedance, Z_ω, placed in series with R_t, where Z_ω is defined according to Equation 78:

$$Z_\omega = \sigma\omega^{-\frac{1}{2}}(1-j) \quad (78)$$

where

σ= Warburg impedance coefficient (Ohm $s^{1/2}$)

Ω= $2\pi f$(rad s^{-1})

Nyquist and Bode plots for the equivalent electrical circuit of Figure 27a are shown in Figures 27b-d.

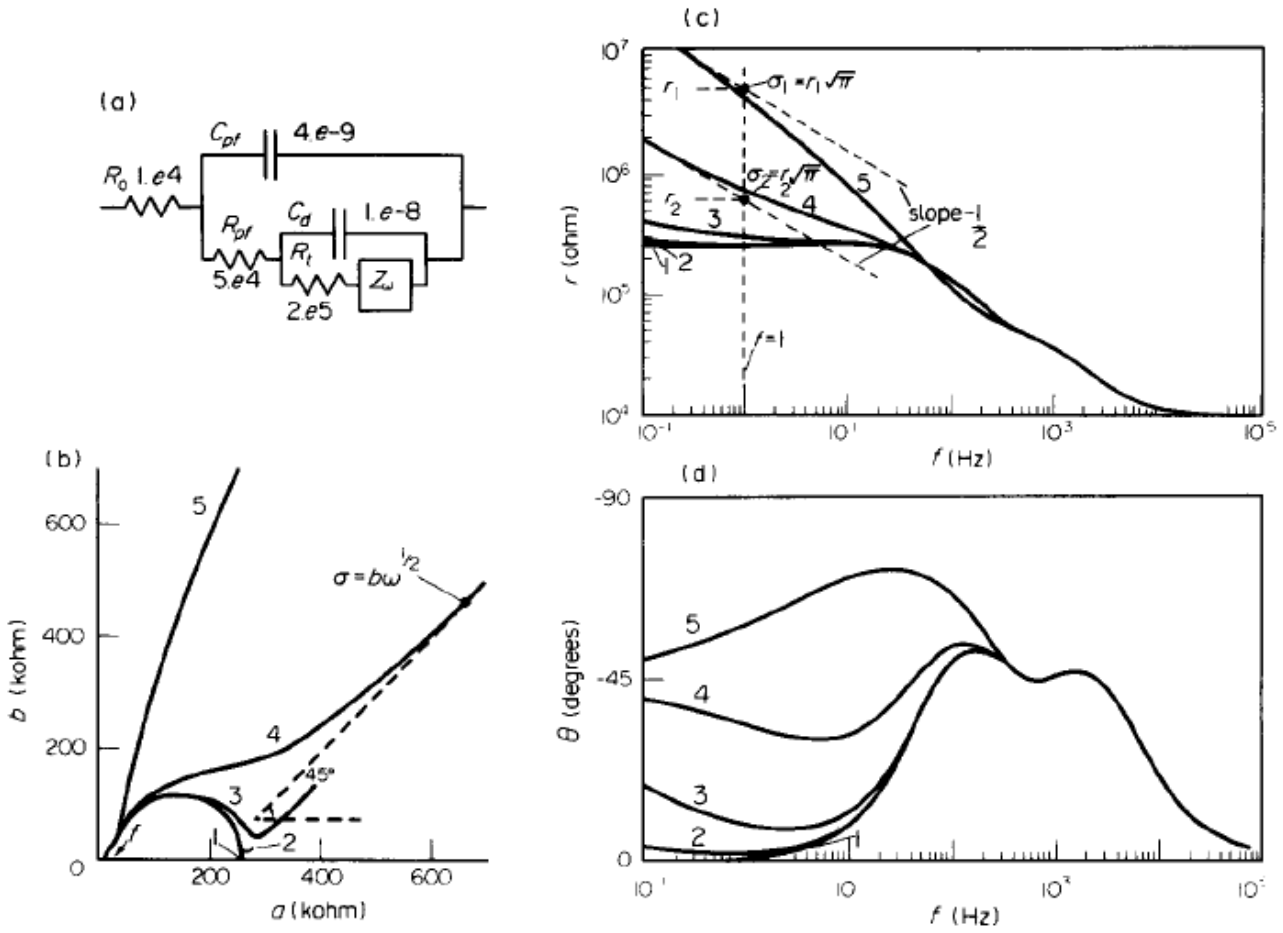

Figure 27 - Painted metal/solution interface equivalent circuit model in the presence of diffusion (a) and its Nyquist (b) and Bode (c,d) impedance plots [177].

When values of σ are about equal to R_t, this diffusion tail begins to overlap the second semicircle (curve 3) and subtends an angle of 45° to the a-axis. As σ increases still further (curve 4), this overlap becomes increasingly more severe, but the diffusion tail eventually becomes inclined at an angle of 45° to the a-axis at low frequencies. Finally, when σ is significantly greater than R_t the diffusion tail completely distorts the semicircular shape (curve 5), being initially greater than 45° to the a-axis. This angle decreases as the frequency is lowered.

When there is no diffusion impedance, σ=0 and the low frequency portion of the log r Bode plot (see curve 1 in Figure 27c) is a line horizontal to the frequency axis indicating a purely resistive value of modulus r equivalent to (R_0+R_t+R_{pf}), whilst the phase angle (curve 1 in Figure 27d)

approaches zero. As the value of σ increases, the log r le at low frequencies is no longer horizontal but curves upwards, becoming steeper and approaching a slope of -1/2 at higher values of σ (curve 4 in Figure 27c). the corresponding low frequency portions of the phase plot (curves 1-4 in Figure 27d) show values of θ decreasing from 0 towards -45° as σ increases. If the values of σ increases still further, becoming significantly greater than R_t as in curve 5 of Figure 27c, the slope of -1/2 is approached at low frequencies around 0.3 kHz, but is a higher slope at higher frequencies up to the break pint at around 30 Hz. The corresponding phase plot (curve 5 in Figure 27c) shows θ approaching -45° at 0.1 Hz from lower θ values.

5.4 Scanning Electron Microscopy (SEM)

The scanning electron microscope (SEM) uses a focused beam of high-energy electrons to investigate surface morphology, chemical composition, etc.

SEM has long been recognised as a tool to give a simulated 'visual' image of a surface, with a magnification which is sufficiently large for both macro- and micro-structures to be studied [182]. The scanning electron microscope (SEM) is a microscope that uses electrons rather than light to form an image. There are many advantages to using the SEM instead of a light microscope. SEM has a large depth of field, which allows a large amount of the sample to be in focus at one time. SEM also produces images of high resolution, which means that closely spaced features can be examined at a high magnification. Preparation of the samples is relatively easy since most SEM only require the sample to be conductive. The combination of higher magnification, larger depth of focus, greater resolution, and ease of sample observation makes the SEM one of the most important tool used in research areas today [183]. Conventional light microscopes use a series of glass lenses to bend light waves and thus create a magnified image. The SEM (Figure 28) creates the magnified images by using electrons instead of light waves.

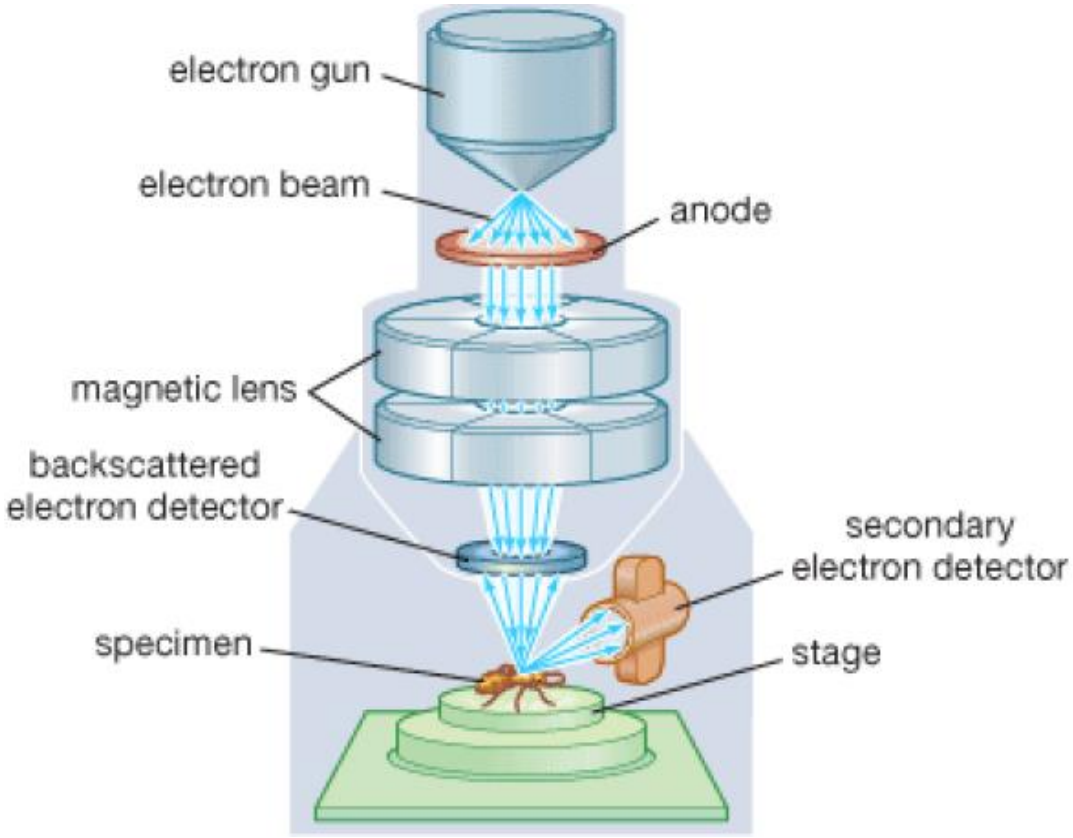

Figure 28 - Schematic view of the operation of SEM.

It shows very detailed 3-dimensional images at much higher magnifications than is possible with an ordinary light microscope. The images created without light waves are rendered black and white. The specimen (which has been carefully prepared to withstand the vacuum inside the microscope) is then placed inside the microscope's vacuum column through an air-tight door. After the air is pumped out of the column, an electron gun, situated at the top, emits a beam of high energy electrons. This beam travels downward through a series of magnetic lenses which are designed to focus the electrons to a very fine spot. Near the bottom, a set of scanning coils hastens the focused beam back and forth across the specimen. As the electron beam hits each spot on the specimen, secondary electrons are knocked loose from the specimen surface. An electron detector counts these electrons and sends the signals to an amplifier. The final image is built up from the

number of electrons emitted from each spot on the specimen. The intensity of the emitted electrons from a specimen of a given homogenous composition depends on the local angle of the surface to the scanning beam moderated by the probability of their reaching the detector [182]. Thus, the image of the surface appears to have been viewed along the axis of the incident beam with a contrast that is expected if the sample is illuminated by a beam of light from the direction of the detector [182].

EDS can be used to determine which chemical elements are present in a sample, and can be used to estimate their relative abundance. The accuracy of this quantitative analysis of sample composition is affected by various factors. Many elements will have overlapping X-ray emission peaks (e.g., Ti K_β and V K_α, Mn K_β and Fe K_α). The accuracy of the measured composition is also affected by the nature of the sample. X-rays are generated by any atom in the sample that is sufficiently excited by the incoming beam. These X-rays are emitted in all directions (isotropically), and so they may not all escape the sample. The likelihood of an X-ray escaping the specimen, and thus being available to detect and measure, depends on the energy of the X-ray and the composition, amount, and density of material it has to pass through to reach the detector. Because of this X-ray absorption effect and similar effects, accurate estimation of the sample composition from the measured X-ray emission spectrum requires the application of quantitative correction procedures, which are sometimes referred to as matrix corrections [184].

Chapter 6 - Experimental work

6.1 Anodizing and sealing processes

6.1.1 Materials and pre-treatments of anodizing

The material used in this study was AA2024-T3 wrought aluminium alloy, with nominal chemical composition given Table 10. Specimens were obtained from 1.6 mm thick sheets by guillotine cutting and degreased in acetone. Degreasing was followed by etching in 10wt. % sodium hydroxide at 60°C for 30 s. After etching, the specimens were desmutted in 30vol. % nitric acid for 15 s at room temperature and dried in a cool air stream. The pretreated specimens were stored in a desiccator until required. Prior to anodizing, the specimens were masked with beeswax, in order to expose an area of 10 cm^2 to the anodizing electrolyte.

Table 10 - Nominal composition of AA2024-T3 alloy in weight %.

Alloy	**Cu**	**Mg**	**Mn**	**Si**	**Fe**	**Zn**	**Ti**	**Al**
2024-T3	4.50	1.44	0.60	0.06	0.13	0.02	0.03	Bal.

6.1.2 Anodizing process

For the traditional TSA, anodizing was undertaken in 0.46 M sulfuric acid with the addition of 80 g/l tartaric acid (TSA). The anodizing electrolyte was gently stirred during the anodizing process. Anodizing was performed at 37°C for 20 min under potentiostatic control following a typical industrial voltage/time cycle, which involved an initial voltage ramp, followed by 20 minutes potentiostatic anodizing at 14 V (SCE). The modified TSA cycle was undertaken in 3.2 M sulphuric acid with the addition of 0.53 M tartaric acid at 25°C. Anodizing was performed under potentiostatic control with a very fast voltage ramp (applied only with the aim of limiting the

initial current overshoot) followed by potentiostatic anodizing at 7 V for 20 minutes. The concentration of sulfuric acid for the modified TSA cycle was selected on the basis of previous results [185-187], such as the steady current attained during anodizing at 7 V (25°C) was similar to that attained during anodizing at 14 V and 37°C (circa 8 mA cm^{-2}). As a result, the charge passed during both anodizing cycles was closely similar (circa 10.2 C cm^{-2} and 9.5 C cm^{-2} for traditional and modified TSA, respectively), and films with similar thickness could be obtained. Thus, the comparison of the behaviour of films with a similar thickness but obtained applying different potential/time regimes enables evaluation of the contributions due to oxide morphology alone.

A three-electrode cell was used, with the specimen as the working electrode, a saturated calomel reference electrode and an aluminium cathode. The anodizing electrolyte was stirred during both the anodizing processes. Following anodizing, the specimens were rinsed repeatedly in deionized water to remove residual acid and dried in a cool air stream.

6.1.3 Sealing process

Following anodizing, three different sealing treatments were applied: the first in hot water, the second in a solution containing sodium chromate and the third in a cerium (III) nitrate-containing solution. During sealing, electrochemical impedance spectra were acquired, as described in detail later. As a control for a condition where no sealing occurs, EIS measurements were also performed on as-anodized specimens immersed in cold water with the addition of 1g/l of sodium sulphate, to enhance the electrolyte conductivity during EIS measurement.

Hot water sealing was performed in a solution of deionized water, with the addition of 1g/l of sodium sulphate to increase the conductivity to enable reliable EIS measurements. The pH was corrected at pH=6 with a few drops of a solution 10g/l sulfuric acid. The treatment required 30 minutes at 96°C.

Chromate sealing was performed in 70g/l Na_2CrO_4 and deionized water. The specimens were immersed in this solution for 30 min at 96°C.

The solution for cerium (III) nitrate sealing was prepared with 0.015 M hydrated $Ce(NO_3)_3$, 0.029 M H_2O_2 and deionized water. The hydrogen peroxide was added to increase the deposition rate since it accelerates the oxidation of Ce^{+3} ions to Ce^{+4}, thereby reducing the time required to form the layer and improving its uniformity. The treatment time was 30 minutes at a temperature of 37°C.

6.1.4 Electrochemical Impedance Spectroscopy (EIS) measurements

6.1.4.1 Monitoring of the sealing treatment

The monitoring of the sealing treatment was carried out by EIS. A two-electrode cell was used for the measurement, with one specimen as the working electrode (connected to the working and sense cable of the potentiostat), and another identical specimen as counter electrode and reference electrode (connected to the counter and reference electrode cables of the potentiostat). This two electrode configuration was selected since it enables to measure the EIS spectra without imposing a constraint on the absolute value of the electrodes potential, as discussed in detail in [188]. Thus, the perturbation of the sealing process due to the measurement of EIS is minimized, even in conditions where a significant transient in potential occurs.

By using this configuration, the measured impedance is the sum of the impedances of the individual electrodes, since they are placed in series. Under the assumption that the two electrodes are identical (i.e. have identical impedance), the impedance of each electrode (including half of the total solution resistance) can be calculated by dividing by two the measured impedance. The result can be then be normalized by dividing for the area of one electrode. Considering that the two electrodes are in series, if the assumption of identical electrodes is violated, for example due to a

localized reaction occurring only on one of the two electrodes, the overall response is dominated by the high impedance electrode. This might be an issue during corrosion measurement, when localization is likely to take place, but it is unlikely to occur during the processes investigated here.

The spectra were acquired continuously, and each acquisition required approximately 6 minutes. Thus, each spectrum represents a 6 minute window in the sealing process, i.e.0-6 min; 6-12 min; 12-18 min; 18-24 min; 24-30 min. It should be noted that the majority of the time required to acquire an EIS spectrum is needed to obtain the last low-frequency points; thus, the high/medium frequency of the spectrum effectively provides information at 0, 6, 12 minutes and so on. In order to be reliable, electrochemical impedance measurements require the measured system to be stationary, i.e. that it does not evolve with time. Clearly, the measurement of EIS spectra during sealing is not conducted under stationary conditions, due to the progressive modification of the electrodes surface. If the surface evolves relatively rapidly, as for the systems studied in this work, the reliability of the complete impedance spectra might be questionable. However, considering one by one the points of an impedance spectrum, it is evident that the time required to acquire a point at high frequency is substantially lower than that required to acquire a point at low frequency. Thus, the vast majority of the measurement time is employed for the last few low-frequency points. As a consequence, the high frequency region of the spectra is intrinsically reliable (since the timescale of evolution of the system is large with respect to the measurement time) whereas the low frequency region is less reliable and might contain artefacts (since the changes on the surface occur on a timescale that is comparable to that of the measurement). In this situation, one can either avoid the acquisition of the spectra, or acquire the spectra even on the non-stationary system and then consider critically the results obtained, i.e. remembering that the high frequency regions are intrinsically more reliable than the low-frequency regions.

The specimens were immersed in the respective sealing solutions and the area exposed was 10 cm^2. EIS was performed in potentiostatic mode, applying a sinusoidal potential perturbation with

amplitude of 10 mV in the frequency range from 100 kHz to 20 mHz. The DC level between the two identical electrodes was set to 0 V, which is equivalent to short circuiting the two electrodes. After sealing, the specimens were rinsed in deionized water and dried in a cool air stream.

6.1.4.2 EIS measurements after sealing treatments

Following sealing, EIS was also carried out in cold 1M Na2SO4 solution at room temperature, to characterize the sealed oxides after all the dissolution and precipitation processes had terminated. In this case, a three-electrode cell was used, with the specimen as the working electrode, a saturated calomel reference electrode and an aluminium cathode. The area exposed for these measurements was 2 cm^2. The impedance spectra were acquired in potentiostatic mode at the open circuit potential by applying voltage sinusoidal perturbation with amplitude of 10 mV over the frequency range from 100 kHz to 5 mHz. Before EIS, the open circuit potential was monitored for 15 minutes. Each electrochemical test was repeated three times in order to evaluate the reproducibility; generally, very minor differences (of the order of 10% of the impedance modulus), if any, between repeated tests were found.

6.1.4.3 EIS measurements during corrosion tests

In order to monitor the corrosion resistance , the specimens were immersed in aggressive solution of 3.5 wt.% sodium chloride for 15 days. EIS spectra were measured at regular intervals with the same three electrodes setup and amplitude. The frequency range inspected varied from 100 kHz to 5 mHz. Between measurements, the specimens were left to corrode freely in the sodium chloride solution.

6.1.5 Scanning Electron Microscopy (SEM)

Scanning Electron Microscopy (SEM) was undertaken by using an EVO 60 microscope and TM 3000 Hitachi operating at an accelerating voltage 20 kV in high vacuum, in order to analyse the surface morphologies of specimens after anodizing and after sealing. The specimens were not metalized prior to observation.

6.2 Trivalent chromium conversion coating

6.2.1 Materials and pre-treatments

The material used in this study was AA 2024-T3 with nominal composition given in Table 10. The specimens supplied by aeronautical industry, Leonardo Company, with dimensions of 75mmx250mmx1mm. The list and operating parameters of the pickling solutions used are in Table 11.

Table 11 – List and operating parameters of the pickling solutions.

Pickling	Composition	Concentration (g/l)	pH	T (°C)	Time
Deoxidizer 6-16	Deoxidizer BAC 5765 Nitric Acid 42B	650	1.1	70	5-15 min
Turco Aluminetch#2	Aluminetch	30-40	12.3	60	30 sec
Turco Smut Go NC	Smut Go NC Nitric Acid 42 B	200-245 50-80	0.68	25	10 min
Turco Deoxalume 2310	Deoxalume Nitric Acid 42 B	140-280 280-420	0.35	25	10 min
Oakite LNC	Nitric Acid 42B	25-43	0.7	25	10 min

Specimens were degreased in acetone. Degreasing was followed by alkaline cleaning (Turco 4215NC-LT) and the specimens were rinsed in in industrial water (B grade). This type of water has

a pH value of 5.0-8.5 and a conductivity of < 400µS/cm. After cleaning, the specimens were deoxidizing in four different solutions. The first was an acid solution containing Cr (VI), Deoxidizer 6-16, and it was considered as benchmark. The specimens were immersed at 70°C for 5-15 min.

The second pre-treatment provided a first alkaline solution containing Turco Aluminetch#2 where the specimens were immersed at 60°C for 30 s, after the specimens were rinsed and following it was immersed in acid Turco Smut Go NC at 25°C for 10 min. The third acid solution containing Turco Deoxalume 2310 and the specimens were immersed at 25°C for 10 min; finally the fourth acid solution is Oakite LNC and the specimens were immersed at 25°C for 10 min. After each pre-treatment the specimens were rinsed in B grade water. The surface chemical pre-treatments were summarized in Figure 29.

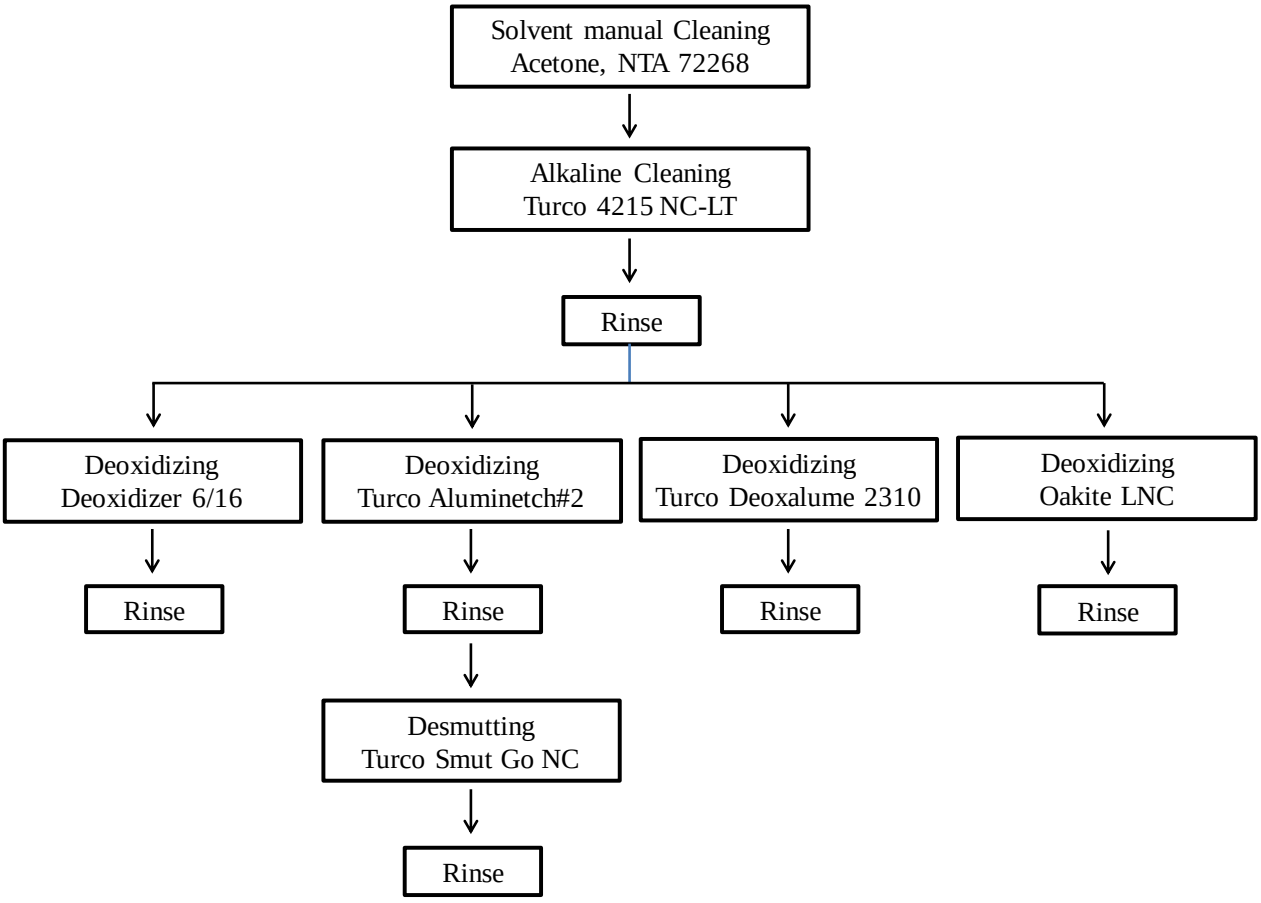

Figure 29 – Process flow.

6.2.2 Industrial cycle of Alodine 1200s

The list and operating parameters of the Alodine 1200s conversion coating used is in Table 12.

The surface treatment of Alodine 1200s on alloy 2024-T3 involves a series of steps schematized in Table 13.

Table 12 - List and operating parameters of hexavalent chromium conversion treatment.

Chemical conversion coating	Commercial name	Operating parameters	Range
Hexavalent Chromium	Alodine 1200s	Concentration	7.5-22.5 g/l
		pH	1.3-1.7
		Temperature	35-38°C
		Time	1-3 min.

Table 13 – Industrial cycle of Alodine 1200s.

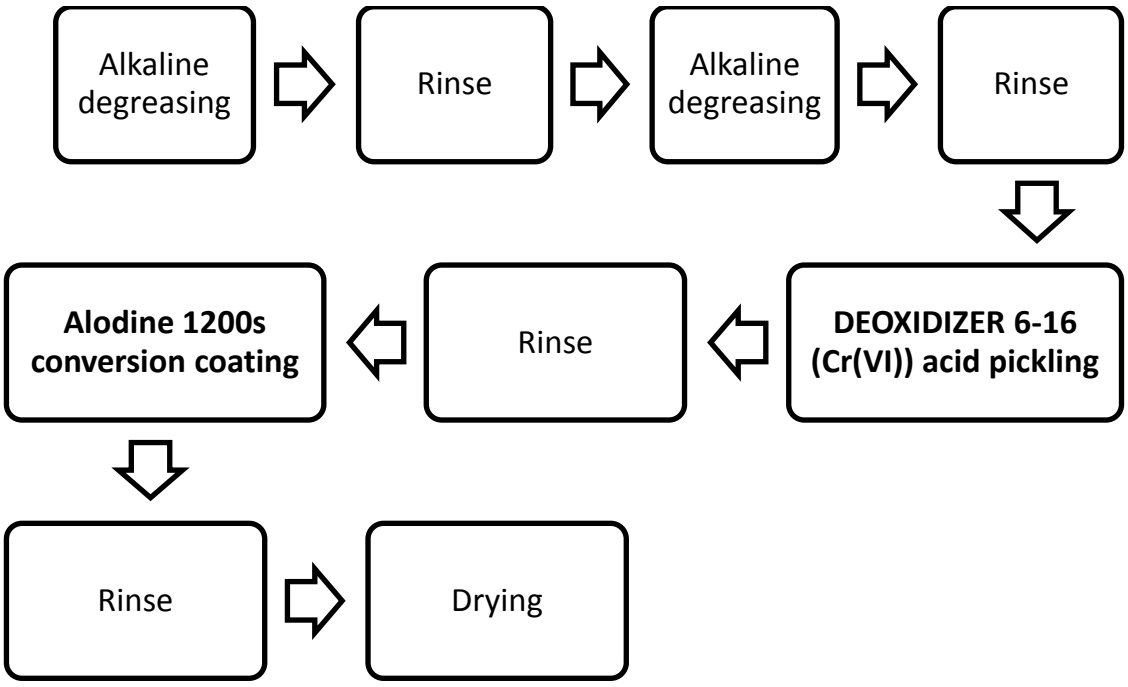

6.2.3 Innovative cycle – Total Green

The list and operating parameters of the Cr(III)conversion coating used is in Table 14. The surface treatment of Cr(III)on alloy 2024-T3 involves a series of steps schematized in Table 15.

Table 14 - List and operating parameters of trivalent chromium conversion treatment.

Chemical conversion coating	Commercial name	Operating parameters	Range
Trivalent Chromium	SurTec 650	Concentration pH Temperature Time	20% 3.70-3.95 30°C 4 min.

Table 15 – Innovative cycle - Total Green.

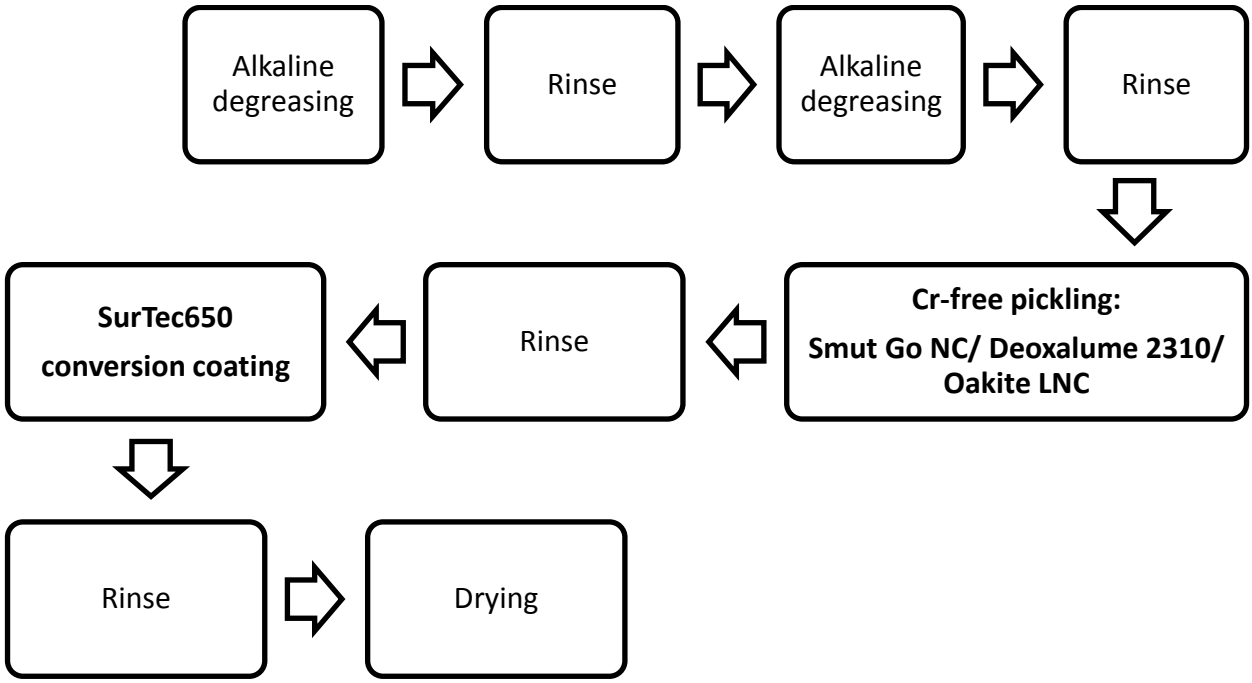

6.2.4 Surface analysis

In order to analyse the surface morphologies of specimens after each pre-treatment, scanning electron microscopy (SEM) images were taken with Hitachi TM 3000 equipped with energy dispersive X-ray spectroscopy (EDS).

6.2.5 Electrochemical measurements

6.2.5.1 Potentiodynamic polarization measurements

The surface of specimens after each pre-treatment and after each conversion coatings in Cr (VI) and Cr-free, respectively, were characterised by potentiodynamic polarizations. Electrochemical measurements were performed in 3.5 wt.% sodium chloride (NaCl) solution at room temperature. A conventional electrochemical three-electrode cell was used with the specimen as the working electrode, a saturated calomel reference electrode (SCE) and a platinum counter electrode.

Before tests open circuit potential (OCP) was evaluated waiting the steady state at least for 15 min. Cathodic curves were carried out starting 10 mV above the OCP value while anodic curves were carried out starting 10 mV below the OCP value; both curves were recorded using a scan rate of 0.16 mV/s. Experiments were repeated at least three times in order to evaluate the reproducibility.

6.2.5.2 Electrochemical Impedance Spectroscopy measurments

Corrosion behaviour was carried out by EIS in aerated 3.5 wt.% NaCl solution for 14 days at room temperature with three electrodes setup cell with amplitude of sinusoidal potential perturbation of 10 mV; the area exposed was 7 cm^2. The frequency range inspected varied from

100 kHz to 20 mHz. Before each measurement, the OCP was acquired for 15 minutes. Between measurements, the specimens were left to corrode freely in the test solution.

Chapter 7 - Results and discussions

7.1 Anodizing and sealing processes

7.1.1 Anodizing results

Anodizing was carried out according to two different electrical regimes, as depicted in **Figure 30.**

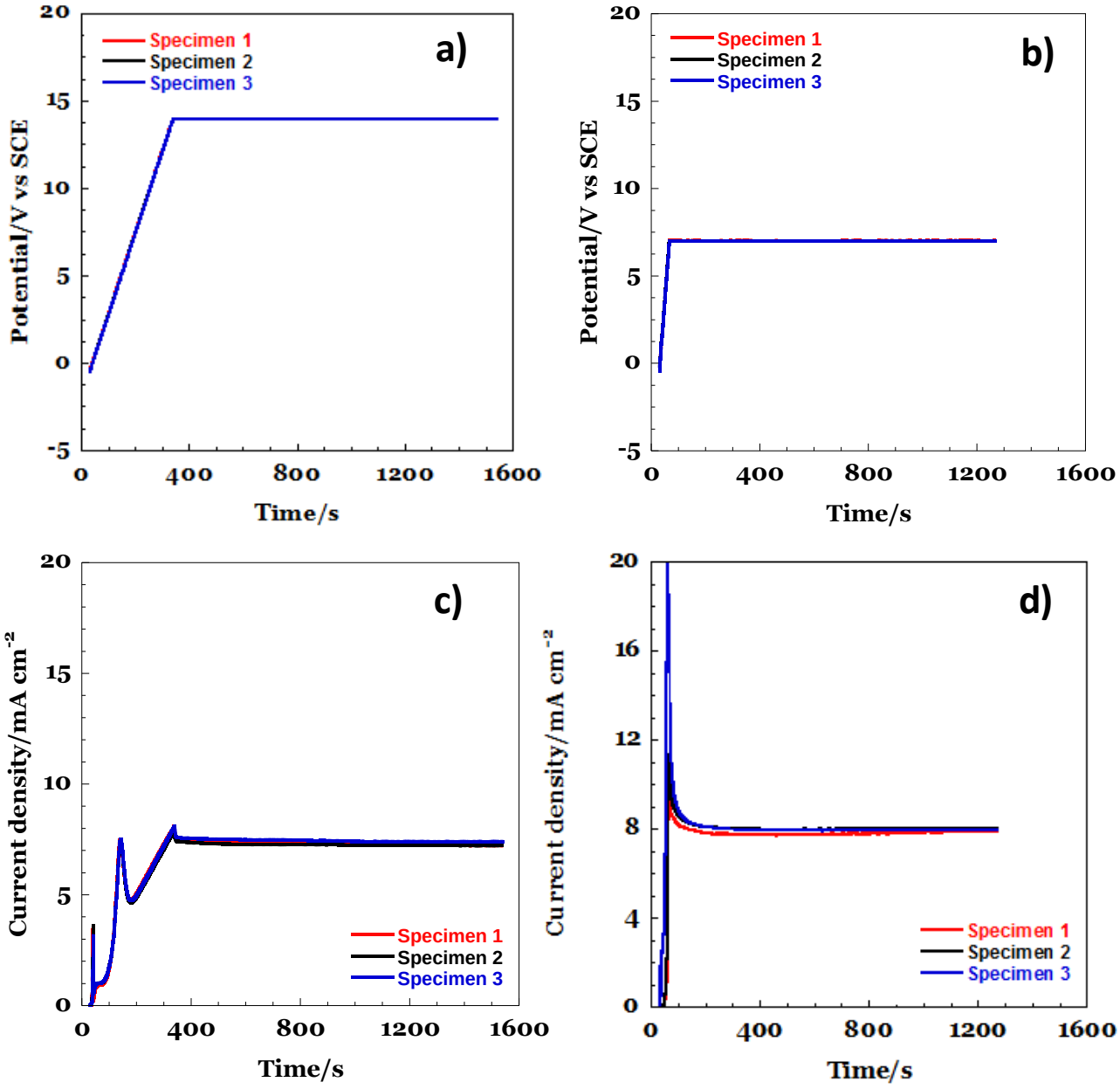

Figure 30 – Applied potential -time regimes (a, b) and resulting current responses (c,d) for traditional TSA (a, c) and modified TSA (b, d).

The first electrical regime (traditional TSA) is the typical cycle applied in industry for the tartaric-sulfuric anodizing process and involves an initial potential ramp from 0 to 14 V (SCE) during the first 5 minutes of anodizing, followed by 20 minutes of potentiostatic anodizing at 14 V (SCE). The time evolution of the applied potential is presented in Figure 30a. The alternative electrical regime (modified TSA), involved a much faster potential ramp (0.2 V/s) followed by a potentiostatic hold at 7 V (SCE) and was performed in the electrolyte with higher concentration of sulfuric acid maintained at room temperature. The initial fast potential ramp in this cycle is not required to improve the properties of the anodic oxide, but it has been applied here to avoid current overloading in the potentiostat, which has a limit of 100 mA and interrupts the experiment in case of overloading. With a conventional two electrode power supply that is capable of self-limiting current in case of overload without interrupting the test, the first ramp would not be required.

The current responses presented in Figures 30c, indicate that the steady current during the potentiostatic hold in the two conditions was very similar (in the region of 8 mA cm^{-2}). This is due to the fact that the lower anodizing potential is applied in the more concentrated solution. This result is expected, since these conditions have been selected based on previous works focusing on optimization of the anodizing cycles [169, 185, 186]. The aim here was to generate films with comparable thickness but different oxide morphologies. In particular, traditional TSA exhibits very fine pores in the outer regions, generated initially at low potential during the ramp, which progressively coarsen toward the metal interface. The majority of the film, thus, has a coarse morphology, generated during high potential step at 14 V. In contrast, oxides generated with the modified TSA have much finer pores throughout the thickness and do not display the outer regions of very fine porosity, since the initial ramp is fast and terminates before the pores fully nucleate. All the morphological aspects associated with the two processes are presented and discussed in detail elsewhere [169, 185, 186]. It is worth also noticing that the oxides obtained by traditional and modified TSA are expected to have a very similar chemical composition, since the only difference

between the two anodizing electrolytes is the concentration of sulfuric acid. Concerning the electrical response recorded during the initial ramp, for the traditional TSA process, two peaks, associated with the oxidation of second phases were clearly visible. During the fast ramp applied in the second cycle, peaks in the current response were not clearly visible, since the charge passed was not sufficient to induce complete oxidation of the second phases, but only to generate a thin oxide layer on the alloy surface. After the ramp was terminated, the current decreased rapidly, to attain a steady value after approximately 200 seconds. Such decrease is associated with the initial thickening of the oxide layer, followed by pore nucleation and propagation [189, 190].

Simultaneously, second phase oxidation occurs. In particular, it is well known that the traditional TSA oxide displays a porosity that is relatively closed in the external regions, since these are generated during the early stages of the potential ramp, thus at low potential, and relatively coarse throughout the majority of the thickness, since it is generated later during the stage of high potential hold. Conversely, the modified TSA cycle displays a much finer porosity throughout the thickness, since the film is generated by anodizing at 7 V.

7.1.2 EIS responses during and post-sealing treatments

The impedance spectra recorded on the two porous anodic oxides immediately and after 24 minutes of immersion in cold water with the addition of sodium sulphate are reported in Figure 31.

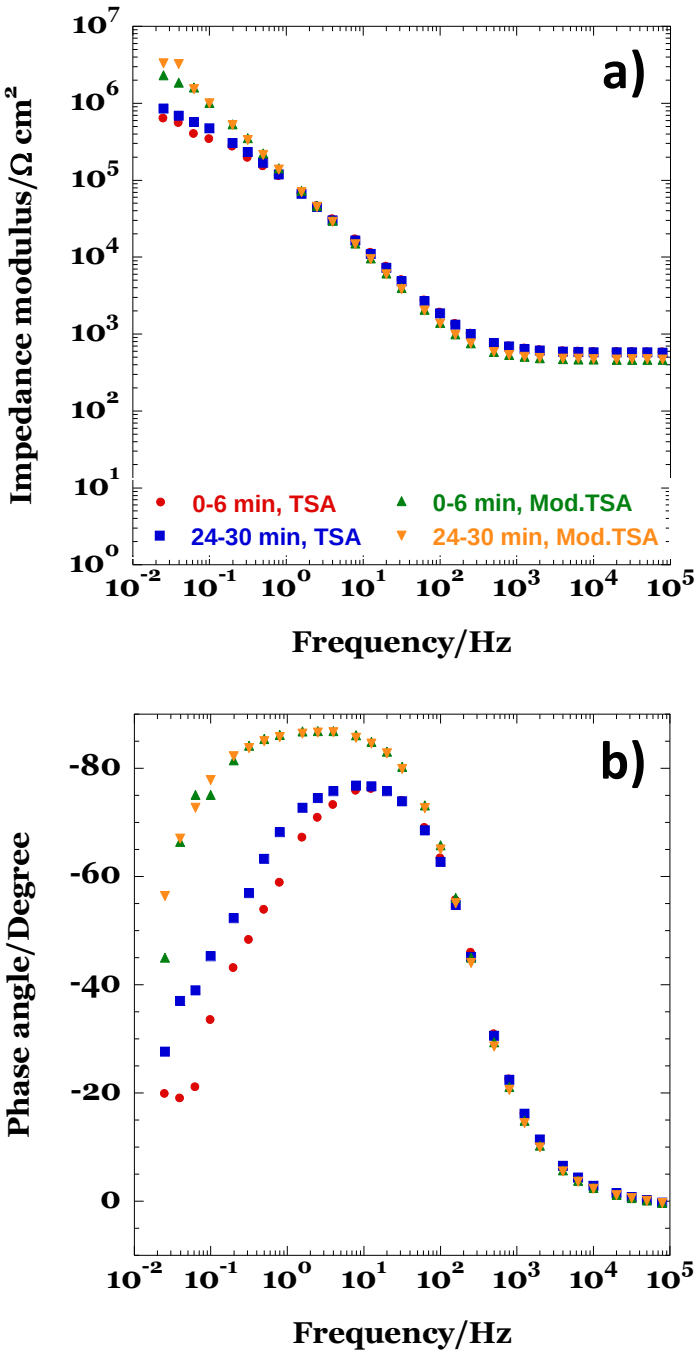

Figure 31 - EIS spectra (a,b) acquired from specimens supporting porous anodic oxides generated by traditional TSA and by modified TSA. Spectra presented were acquired immediately after and after 24 minutes of immersion in the cold water solution.

This is considered the control condition, where no sealing occurs in both cases. Clearly, the impedance spectra are dominated by the capacitive response associated with the presence of the barrier layer beneath the pores. Interestingly, in the control condition, the values of low frequency

impedance associated with the modified TSA cycle were slightly higher than that of the traditional TSA cycle. The EIS spectra acquired in the cold control conditions (not aggressive to the oxide or to the alloy) already reveal significant differences between the oxides generated by the two treatments. In particular, it is evident that the oxide generated at lower potential has a slightly higher capacitance (consistent with a thinner barrier layer) but higher low-frequency impedance modulus.

This observation suggests that the low-frequency impedance modulus is not uniquely determined by the thickness of the barrier layer on the multiphase alloy under study, since if this was the case a thinner barrier layer would necessarily also be associated to a lower impedance modulus.

The impedance response measured during sealing in hot water for both anodizing cycles is reported in Figure 32.

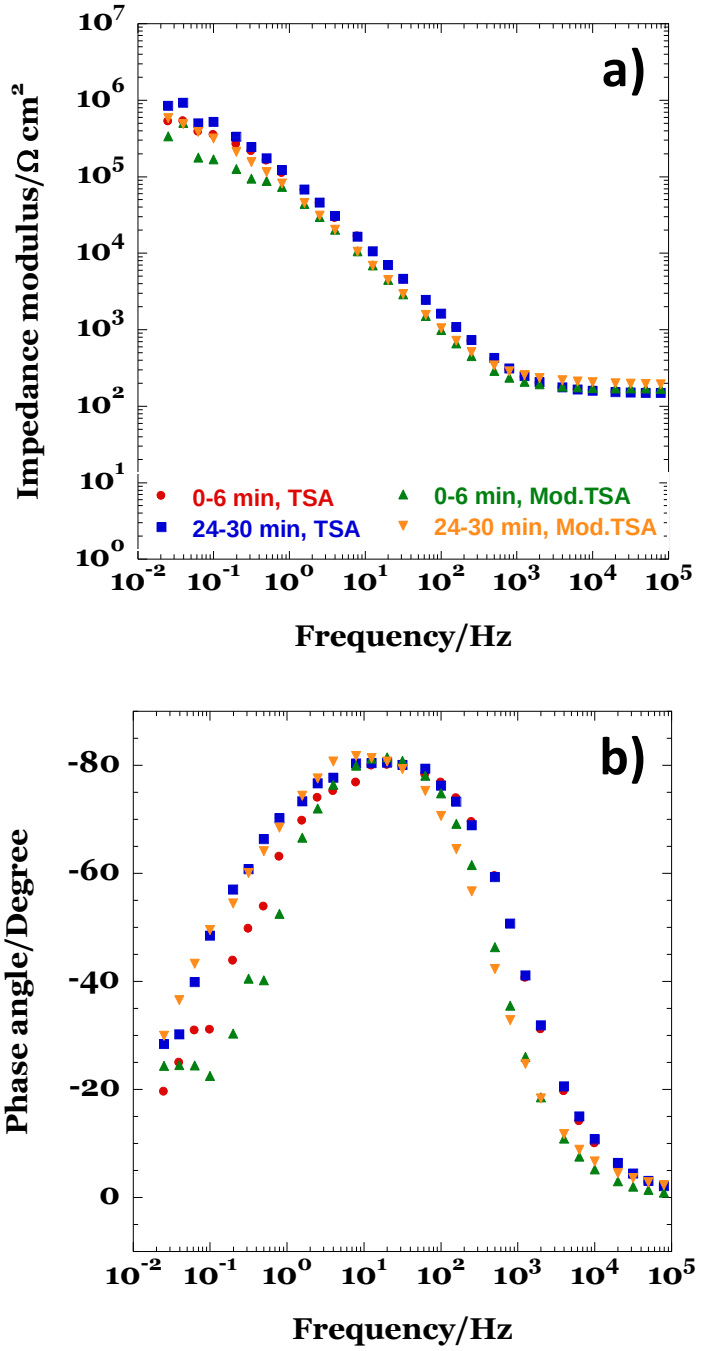

Figure 32 - EIS spectra acquired from specimens supporting porous anodic oxides generated by traditional TSA and by modified TSA. Spectra presented were acquired immediately after and after 24 minutes of immersion in the hot water solution.

For clarity, only the first spectrum (acquired immediately after immersion) and the last spectrum (acquired between 24 and 30 minutes of immersion approximatively) are reported here. No major differences are observed for both treatments compared to the cold water control condition, except a

slight increase in the low frequency values of the modulus of impedance with increasing sealing time. The behaviour during sealing in sodium chromate (Figure 33) was markedly different.

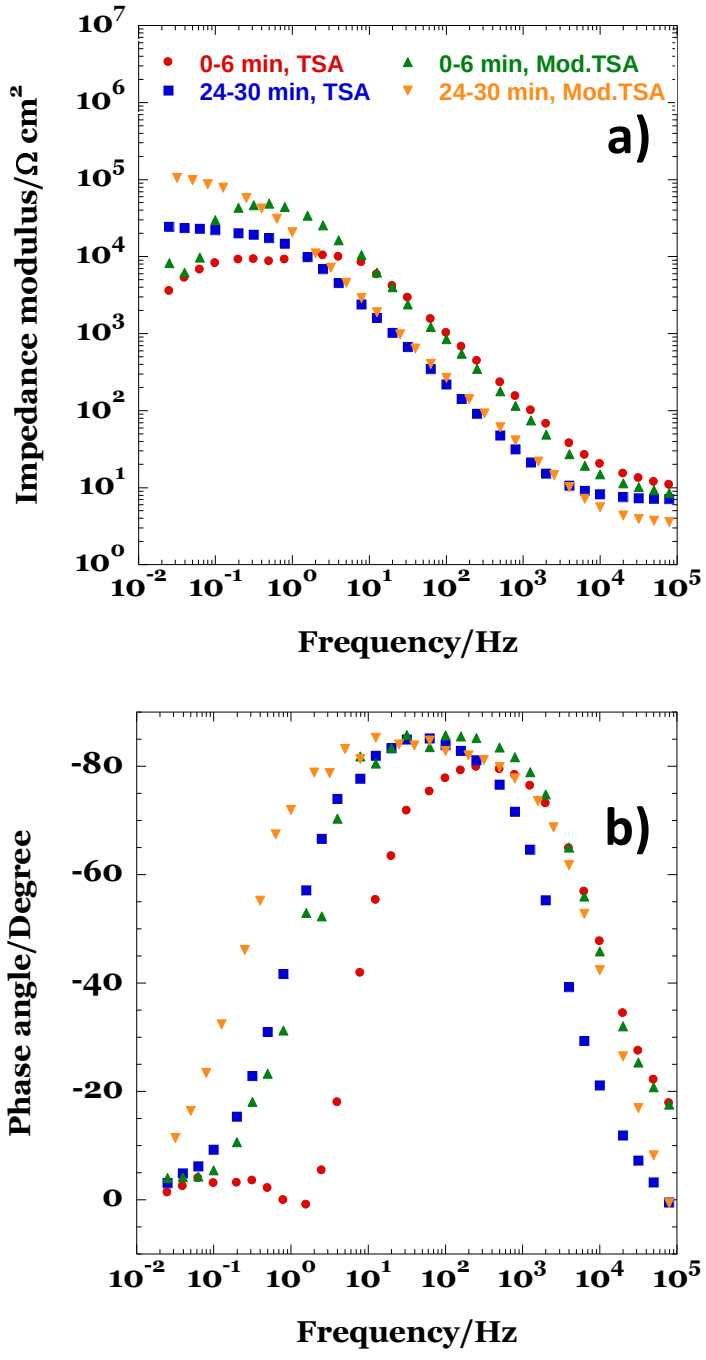

Figure 33 - EIS spectra acquired from specimens supporting porous anodic oxides generated by traditional TSA and by modified TSA. Spectra presented were acquired immediately after and after 24 minutes of immersion in the sodium chromate solution.

In particular, a significant increase in capacitance (evident as a left shift of the medium-frequency regions of the spectra) was observed during the sealing process, and an increase in the low-frequency values of the impedance modulus. However, the increase in capacitance was proportionally more significant for the films obtained in the traditional TSA compared to those obtained with the modified TSA process. Such increase in capacitance observed during chromate sealing is due to a substantial thinning of the barrier layer due to the relatively aggressive sealing solution [191, 192]. The impedance spectra obtained during cerium sealing are presented in Figure 34.

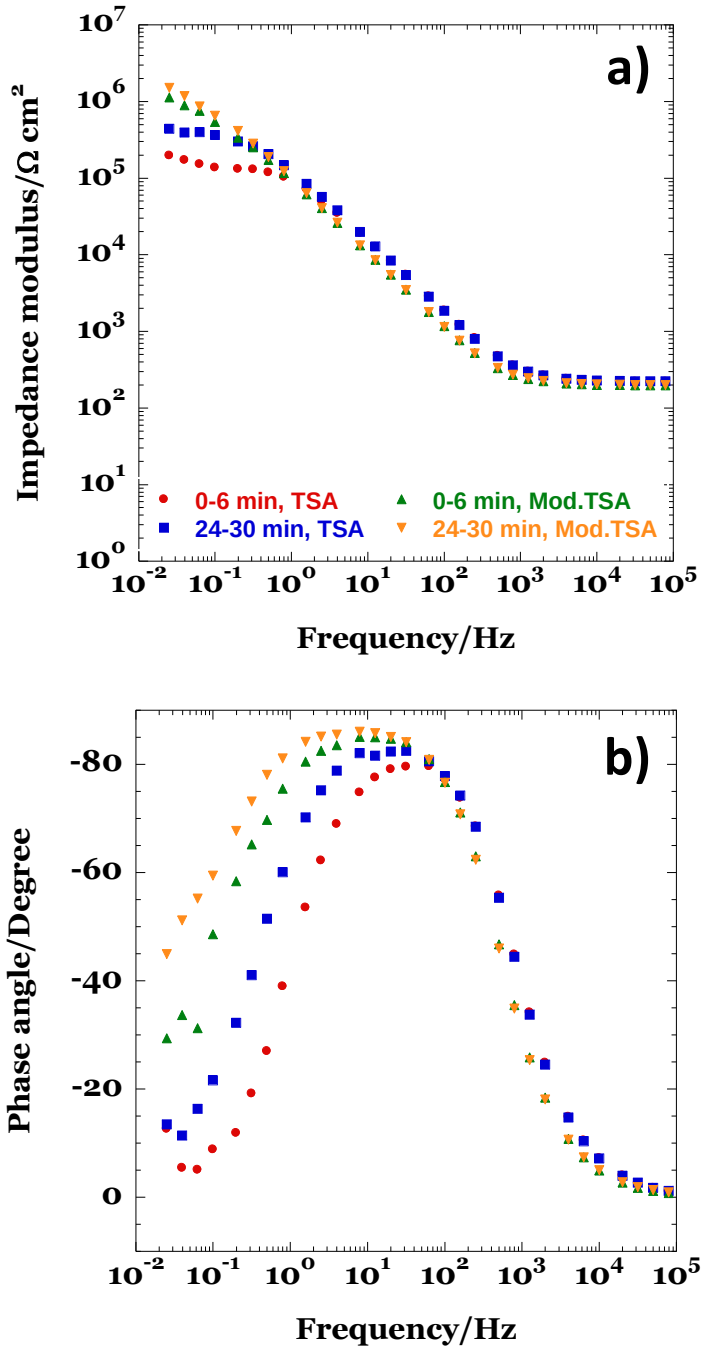

Figure 34 - EIS spectra acquired from specimens supporting porous anodic oxides generated by traditional TSA and by modified TSA. Spectra presented were acquired immediately after and after 24 minutes of immersion in the cerium-based solution.

For both anodic oxides, no variation in capacitance during sealing was observed, indicating little or no attack of the barrier layer. However, for the traditional TSA cycle, a slight increase in low frequency values of the impedance modulus was revealed. On the other hand, the modified

TSA cycle showed virtually no variation during the sealing process, but the initial value was significantly higher than for traditional TSA [191, 193]. Figure 35 presents the comparison of the impedance spectra measured in the cold solution of sodium sulphate after the various sealing treatments were applied.

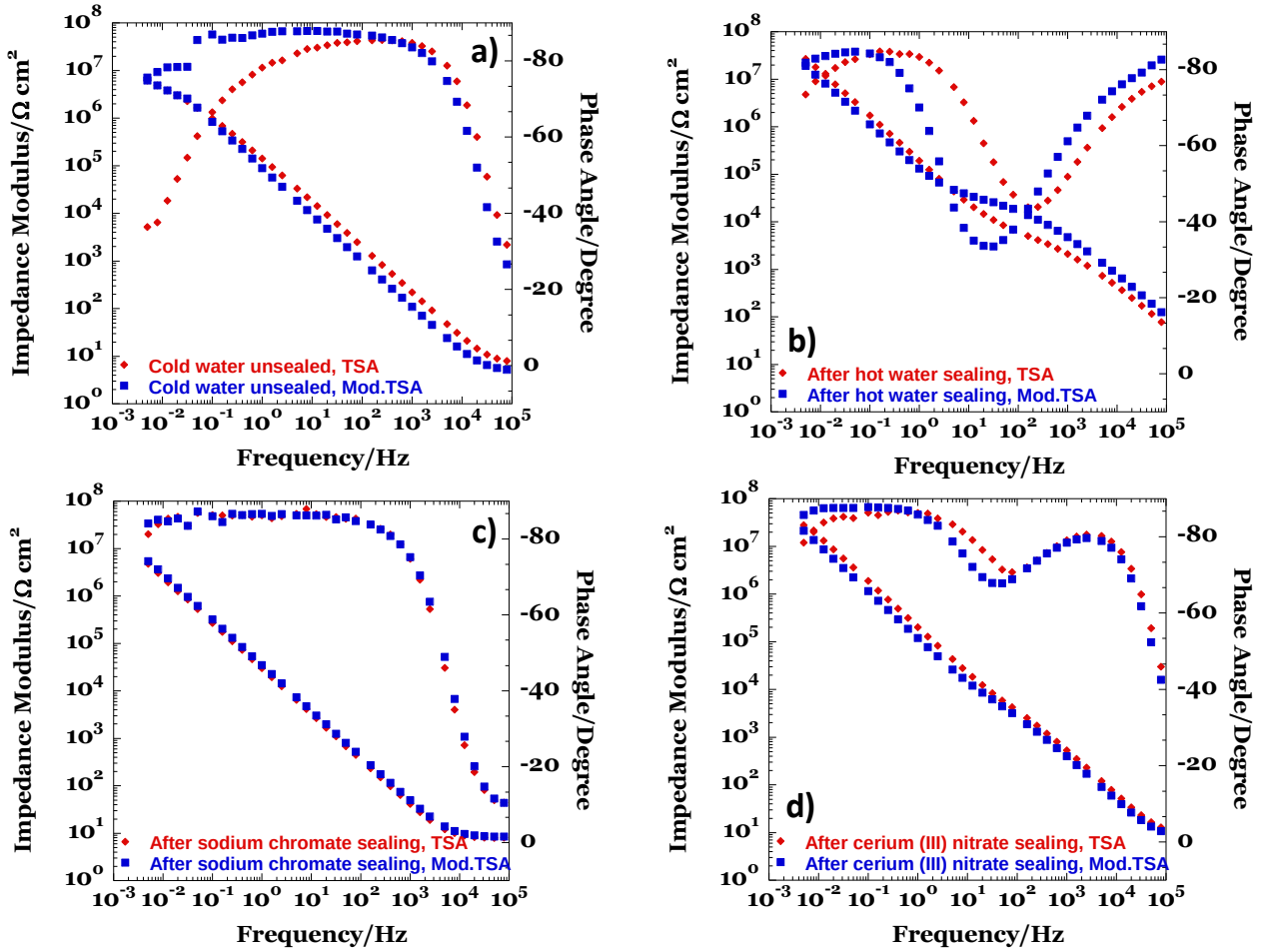

Figure 35 - EIS spectra acquired at room temperature in 1M Na_2SO_4, **a)** unsealed oxides, **b)** hot water sealed oxides, **c)** sodium chromate sealed oxides and **d)** cerium sealed oxides. Comparison between responses of the oxides generated by traditional TSA (red diamonds) and modified TSA (blue squares).

It is evident that the qualitative effect of each treatment was similar for both the anodizing cycles. Furthermore, the second time constant that appeared in the medium frequency range in hot water and cerium treatments, was more evident for the specimens anodized by the modified TSA

process. This second time constant is evident only after sealing, when the measurement is performed at low temperature, because it is associated to the precipitation of the hydrated sealing products within the pores. During sealing, at higher temperature, such hydrated products are in the form of gels and, due to the relatively low resistance, cannot be resolved by EIS measurement [192]. The behaviour during the various sealing treatments also indicates that the anodic oxides obtained with the modified TSA process respond better to sealing. In particular, higher values of low frequency impedance modulus are consistently observed during the last cycle of the in situ EIS measurements. This can be rationalized again by considering the reduced presence of defects in the oxides generated by the modified TSA process. Specifically, it is evident that no significant modification of the barrier layer properties (and, by extension, of the majority of the porous skeleton) is associated with the application of any of the non-chromium containing sealing processes. This is highlighted by the fact that the capacitance of the barrier layer, and thereby its thickness, does not change substantially during sealing in chromate-free solution. Thus, the effects of such procedures are limited to the external regions of the oxide, and are likely to involve only a limited dissolution of the porous skeleton. In contrast, when sealing is performed in sodium chromate, the dissolution of the pre-existing porous skeleton is very substantial, as it is evident for the rapid increase in capacitance, associated with barrier layer thinning, and corresponding decrease in resistance during the first minutes of sealing. Thus, the original porous skeleton is substantially attacked during chromium sealing, and the final properties of the sealed film are mainly determined by the properties of the re-precipitated layer. Upon cooling, the precipitation of the sealing products takes place, followed by crystallization. After sealing, the comparison between the two treatments is of particular interest; clearly, the time constant present at medium frequency range and associated with the precipitation of the sealing products was more pronounced for the modified TSA process compared to the traditional TSA. This can be rationalized by considering that finer pores are much easier to completely seal once the precipitation processes are triggered.

7.1.2.1 Equivalent circuit analysis of sealed oxides generated by Traditional TSA

Before analysing the information obtained from equivalent circuits, it is appropriate to report the graphs showing the complete monitoring of the sealing of the oxides anodized in TSA (Figure 36).

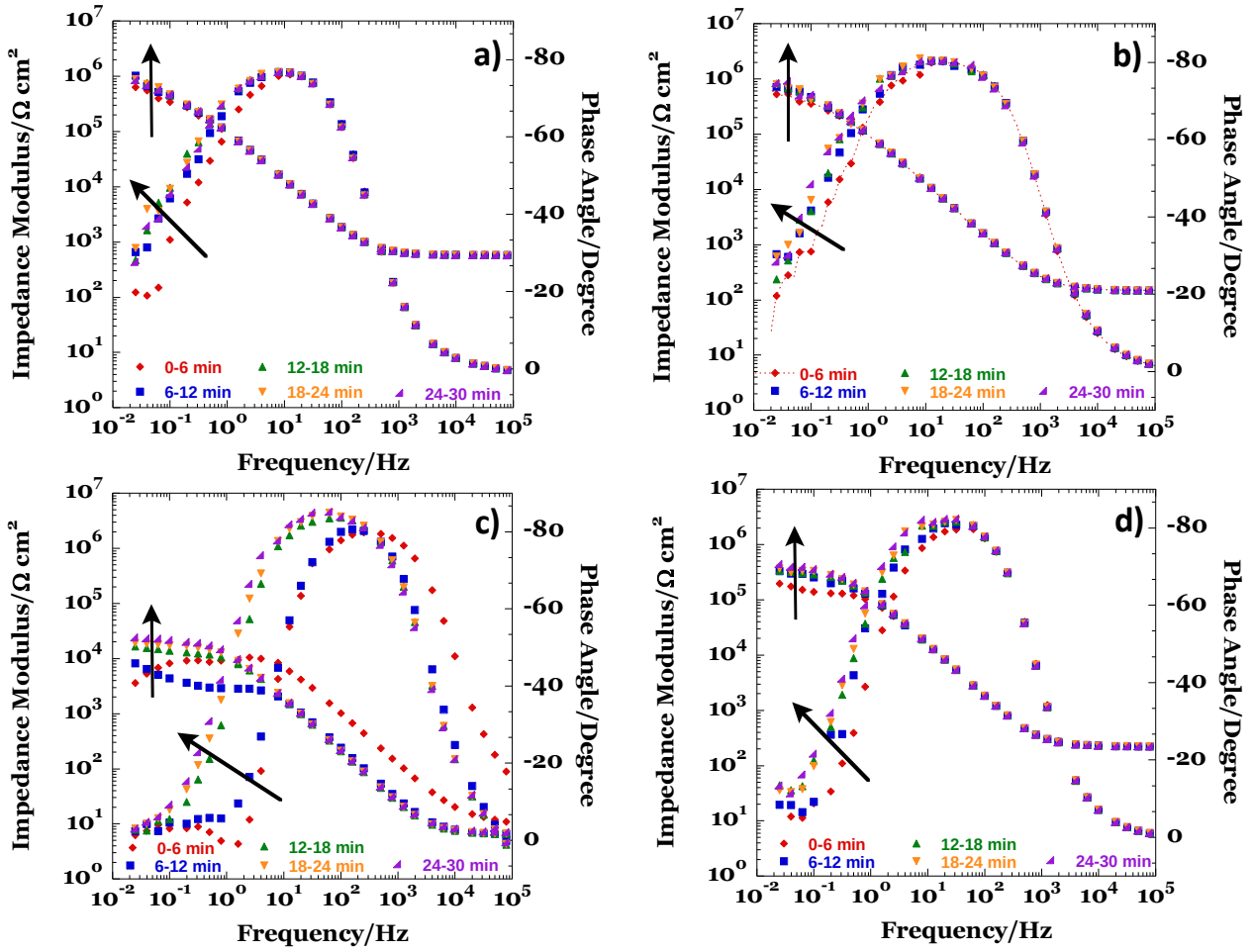

Figure 36 - Evolution of impedance modulus and phase angle measured a) in the control condition (cold water), b) during hot water sealing, c) during sodium chromate sealing and d) during cerium (III) nitrate sealing. Arrows in the spectra indicate increasing treatment time and lines between points are intended as a guide to the eyes.

This is necessary to better understand the information obtained from equivalent circuits. In order to obtain quantitative information from the impedance spectra of the sealed oxides generated

by traditional TSA, two equivalent circuits models were used to fit the data (Figure 37). The software used to fit the experimental EIS data was ZView.

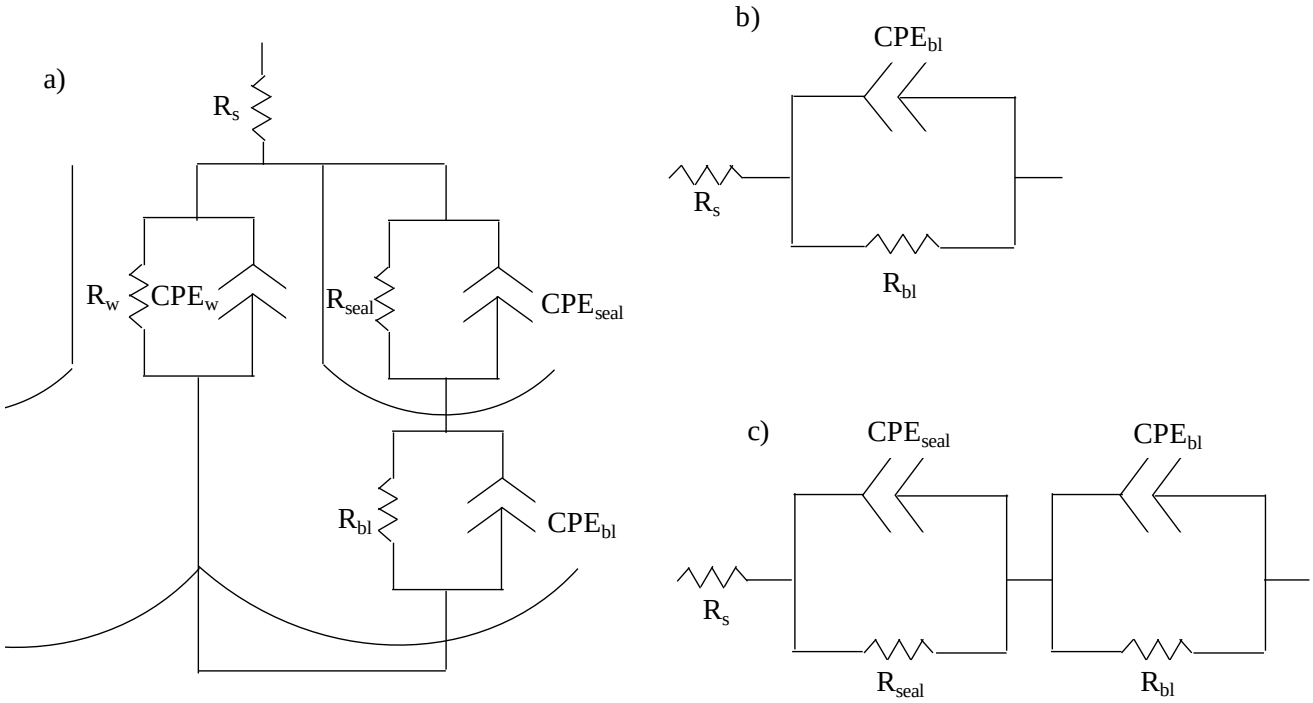

Figure 37 - Equivalent circuits representing sealed porous anodic oxide **(a)** general model, **(b)** model used to fit the data acquired during sealing and **(c)** model used to fit the data acquired after sealing.

Since Hoar and Wood [194], various equivalent circuits have been proposed to model the EIS response of porous anodic films, particularly the equivalent circuit proposed by Hitzig et al. [195], which is presented in Figure 37a. In this model, R_s represents the solution resistance, R_w and CPE_w represent resistance and capacitance associated to the pore walls, R_{bl} and CPE_{bl} represent the capacitance and resistance due to the presence of the barrier layer, and R_{seal} and CPE_{seal} represent the capacitance and resistance associated to the presence of sealing products within the pores.

Generally, since the thickness of the porous layer is of the order of microns, CPE_w is very low and R_w is very high, therefore the time constant associated with the pore walls is not normally apparent in EIS spectra acquired within the usual frequency ranges. For unsealed porous oxides, the

circuit of Figure 37b can be used, and it was employed here to analyse the data obtained during sealing [135], when the resistance of the sealing products is comparatively low. Constant phase elements were used for the fitting and, values of capacitance for the plots were obtained by using the approach described in Hirschorn, et al. [196] applicable to a distribution of time constants perpendicular to the electrode surface. During sealing, the re-precipitated hydroxide layer is likely to contain significant amount of water and is likely to be in the form of gel until it is maintained at high temperature. As a result, the conductivity is relatively high, and the layer cannot be resolved directly by EIS measurement. On the contrary, after cooling, the sealing product precipitate and might crystallize. As a result, ionic migration becomes significantly more difficult compared to the gel products. Thus, the sealing product layer appears as a second time constant in the spectra, and for this reason a circuit that include the resistance and the capacitance associated to the precipitated sealing products (Rseal and CPEseal) is used for the fitting, and the circuit of Figure 37c is used to analyse the data. In order to account for the non-planarity of the various layers, constant phase elements are used for the fitting in lieu of ideal capacitors. Figures 38 and 39 show typical calculated (lines) and experimental (symbols) spectra obtained during (Figure 38) and after (Figure 39) sealing. The results of the fitting procedure are reported in Tables 16 and 17.

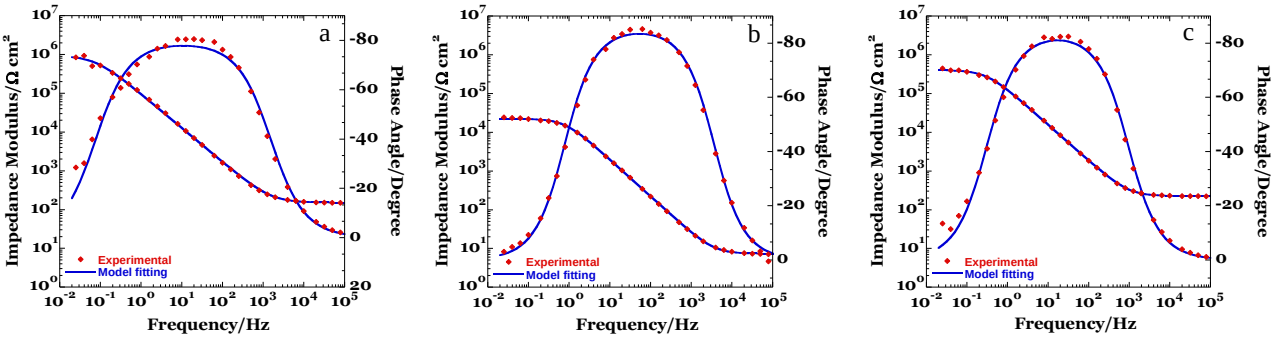

Figure 38 - Typical experimental (symbols) and calculated (line) impedance spectra acquired (**a**) during hot water sealing, (**b**) during sodium chromate sealing and (**c**) during cerium (III) nitrate sealing.

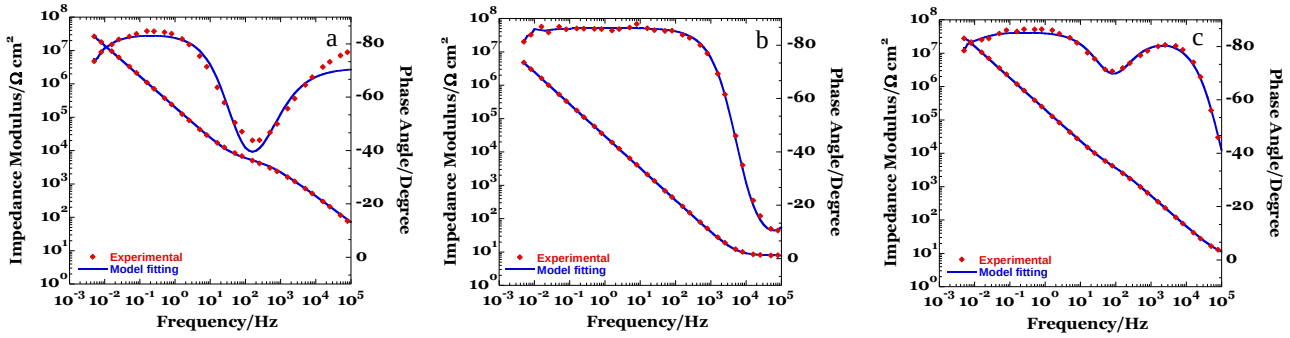

Figure 39 - Typical experimental (symbols) and calculated (line) impedance spectra acquired (**a**) after hot water sealing, (**b**) after sodium chromate sealing and (**c**) after cerium (III) nitrate sealing.

Table 16 - Results of the fitting procedure during sealing treatment.

During Sealing												
Time	**Cold water**			**Hot water**			**Sodium Chromate**			**Cerium (III) Nitrate**		
(min)	R_{bl} $\Omega \cdot cm^2$	CPE_{bl} $s^n \Omega^{-1} cm^{-2}$	n	R_{bl} $\Omega \cdot cm^2$	CPE_{bl} $s^n \Omega^{-1} cm^{-2}$	n	R_{bl} $\Omega \cdot cm^2$	CPE_{bl} $s^n \Omega^{-1} cm^{-2}$	n	R_{bl} $\Omega \cdot cm^2$	CPE_{bl} $s^n \Omega^{-1} cm^{-2}$	n
0-6	$5.01 \cdot 105$	$2.10 \cdot 10^{-6}$	0.87	$4.93 \cdot 10^5$	$2.02 \cdot 10^{-6}$	0.89	$6.30 \cdot 10^3$	$2.18 \cdot 10^{-6}$	0.94	$1.53 \cdot 10^5$	$1.37 \cdot 10^{-6}$	0.93
6-12	$8.23 \cdot 10^5$	$2.17 \cdot 10^{-6}$	0.86	$7.94 \cdot 10^5$	$2.07 \cdot 10^{-6}$	0.89	$3.46 \cdot 10^3$	$9.38 \cdot 10^{-6}$	0.94	$2.68 \cdot 10^5$	$1.39 \cdot 10^{-6}$	0.93
12-18	$9.78 \cdot 10^5$	$2.23 \cdot 10^{-6}$	0.86	$8.02 \cdot 10^5$	$2.05 \cdot 10^{-6}$	0.89	$1.40 \cdot 10^4$	$1.03 \cdot 10^{-5}$	0.95	$3.22 \cdot 10^5$	$1.41 \cdot 10^{-6}$	0.93
18-24	$1.00 \cdot 10^6$	$2.22 \cdot 10^{-6}$	0.86	$9.02 \cdot 10^5$	$2.07 \cdot 10^{-6}$	0.88	$1.79 \cdot 10^4$	$1.00 \cdot 10^{-5}$	0.95	$3.54 \cdot 10^5$	$1.37 \cdot 10^{-6}$	0.93
24-30	$9.39 \cdot 10^5$	$2.18 \cdot 10^{-6}$	0.86	$9.36 \cdot 10^5$	$2.05 \cdot 10^{-6}$	0.88	$2.24 \cdot 10^4$	$9.87 \cdot 10^{-6}$	0.95	$4.03 \cdot 10^5$	$1.35 \cdot 10^{-6}$	0.93

Table 17 - Results of the fitting procedure after sealing treatment.

After sealing						
	R_{bl} $\Omega \cdot cm^2$	CPE_{bl} $s^n \Omega^{-1} cm^{-2}$	n	R_{seal} $\Omega \cdot cm^2$	CPE_{seal} $s^n \Omega^{-1} cm^{-2}$	n
Cold water	$6.79 \cdot 10^6$	$2.30 \cdot 10^{-6}$	0.94	$7.07 \cdot 10^5$	$2.30 \cdot 10^{-6}$	0.94
Hot water	$1.50 \cdot 10^8$	$9.10 \cdot 10^{-7}$	0.93	$5.12 \cdot 10^3$	$4.44 \cdot 10^{-7}$	0.78
Sodium Chromate	$7.50 \cdot 10^7$	$5.78 \cdot 10^{-6}$	0.96	7.73	$3.08 \cdot 10^{-8}$	1.00
Cerium(III) Nitrate	$2.40 \cdot 10^8$	$8.57 \cdot 10^{-7}$	0.95	$1.96 \cdot 10^3$	$1.36 \cdot 10^{-6}$	0.91

The time evolution of the barrier layer resistance and of the barrier layer capacitance during sealing, together with the final values obtained after sealing, are presented in Figures 40 and 41, respectively.

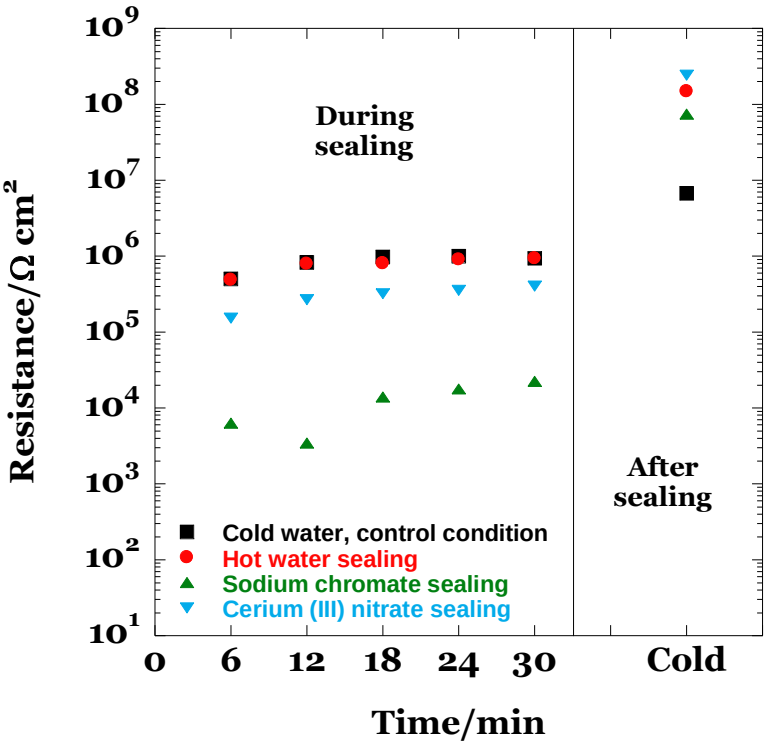

Figure 40 - Time Evolution of the barrier layer resistance measured during and after sealing processes.

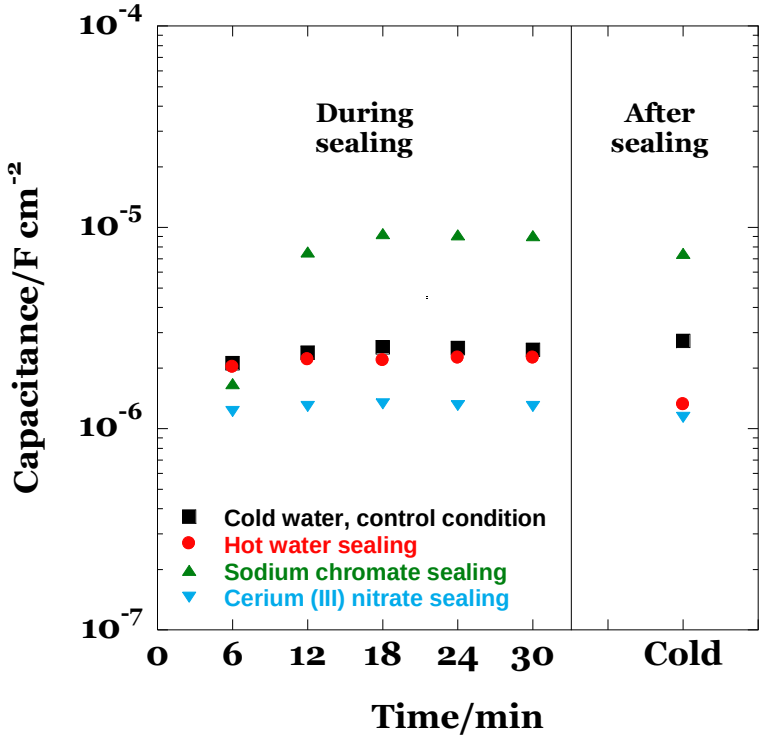

Figure 41 - Time evolution of the barrier layer capacitance measured during and after sealing processes.

It is interesting to notice that the both the values of capacitance and resistance measured immediately after immersion for the specimens in cold and hot water were very similar. This indicates that the increase in temperature, per se, does not have a direct effect on the values of capacitance and resistance estimated, since oxide generated under nominally identical conditions (having the same geometry), produce very similar response in terms of resistance and capacitance at both temperatures. For all the sealing treatments, the resistance associated to the barrier layer slightly increased with time during sealing. However, the resistance estimated for the chromate sealing treatment was approximately two orders of magnitude lower than that for all the other conditions.

After sealing, the values of resistances for all the three treatments increased substantially, to values of the order of 10^8ohm cm^2. The slight increase in the resistance associated with the barrier layer for the unsealed specimens might be attributed to the fact that the process of immersion in the

first test electrolyte, followed by rinsing and drying, might have induced some hydration of the oxide, with subsequent re-precipitation (self-sealing). Such re-precipitation, although not substantial, might have contributed to cover some defects statistically present in the oxide layer.

The time evolution of the estimated capacitance associated to the barrier layer is presented in Figure 41. The capacitance inversely correlates with the thickness of the barrier layer beneath the pores. For the control condition, the capacitance was unchanged for all the measurements, as expected since no significant reduction of the barrier layer thickness should occur at low temperatures. The behaviour was similar for both hot-water sealing and cerium sealing, although for cerium sealing slightly lower values of capacitance were estimated. After sealing, the capacitances of hot water and cerium-sealed films coincided. Substantially different behaviour was observed during chromium sealing. Initially the value of capacitance was similar to that measured for the other treatments but, after 6 minutes, the capacitance increased substantially and remained approximately constant until 30 minutes. After sealing, the capacitance slightly decreased, but it was still higher compared to that measured for the control specimen.

7.1.3 SEM

Scanning electron micrographs of specimens treated in TSA solution after anodizing and after sealing are presented in Figure 42.

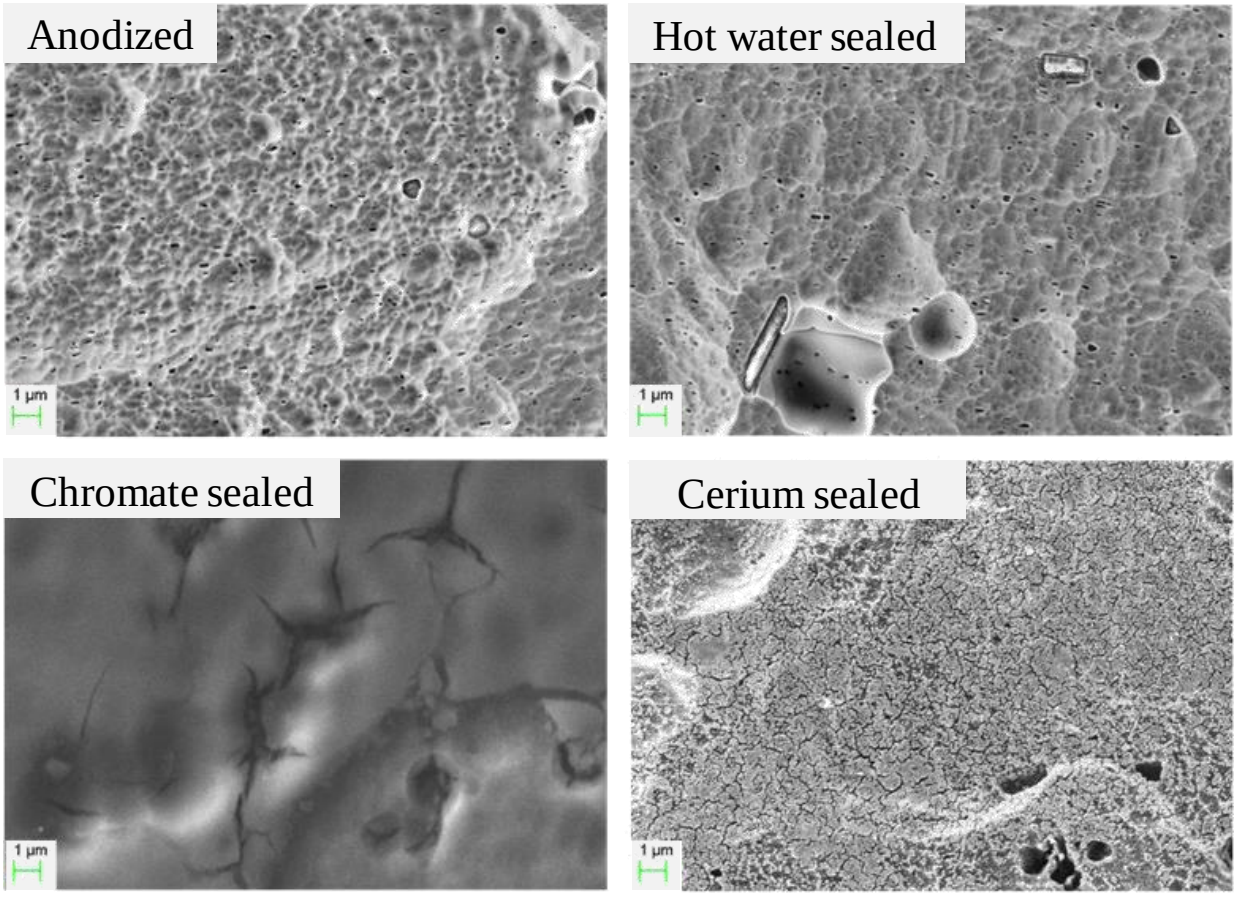

Figure 42 - Scanning electron micrographs of the surface of specimen treated in TSA solution (a) anodized, (b) hot water sealed, (c) sodium chromate sealed and (d) cerium (III) nitrate sealed.

After anodizing (Figure 42a), the surface of the anodic oxide reflected the scalloped morphology generated on the alloy by the initial alkaline etching treatment. Cavities and regions of altered film morphology are evident on the surface and associated to the different oxidation behaviour of the various metallurgical phases present on the alloy [186, 189, 197]. After sealing in hot water (Figure 42b), the surface morphology did not appear substantially different from the one

observed on the as anodized specimen. Conversely, after sealing in chromate-containing solution, the surface of the oxide film appeared substantially modified, with a homogeneous deposit of sealing products clearly evident above the anodic oxide layer. The cerium treatment (Figure 42d), induced the precipitation of finely dispersed cerium-rich clusters above the porous anodic oxide film. Such cerium-rich deposits on anodized aluminium and aluminium alloy surfaces have been observed previously and characterized in detail by Gordovskaya et al.[198]. The attack of the porous oxide skeleton associated with cerium sealing is minimal, but a significant amount of precipitation products are formed, as evident from SEM images.

The SEM images of specimens treated in Modified TSA solution are shown in Figure 43.

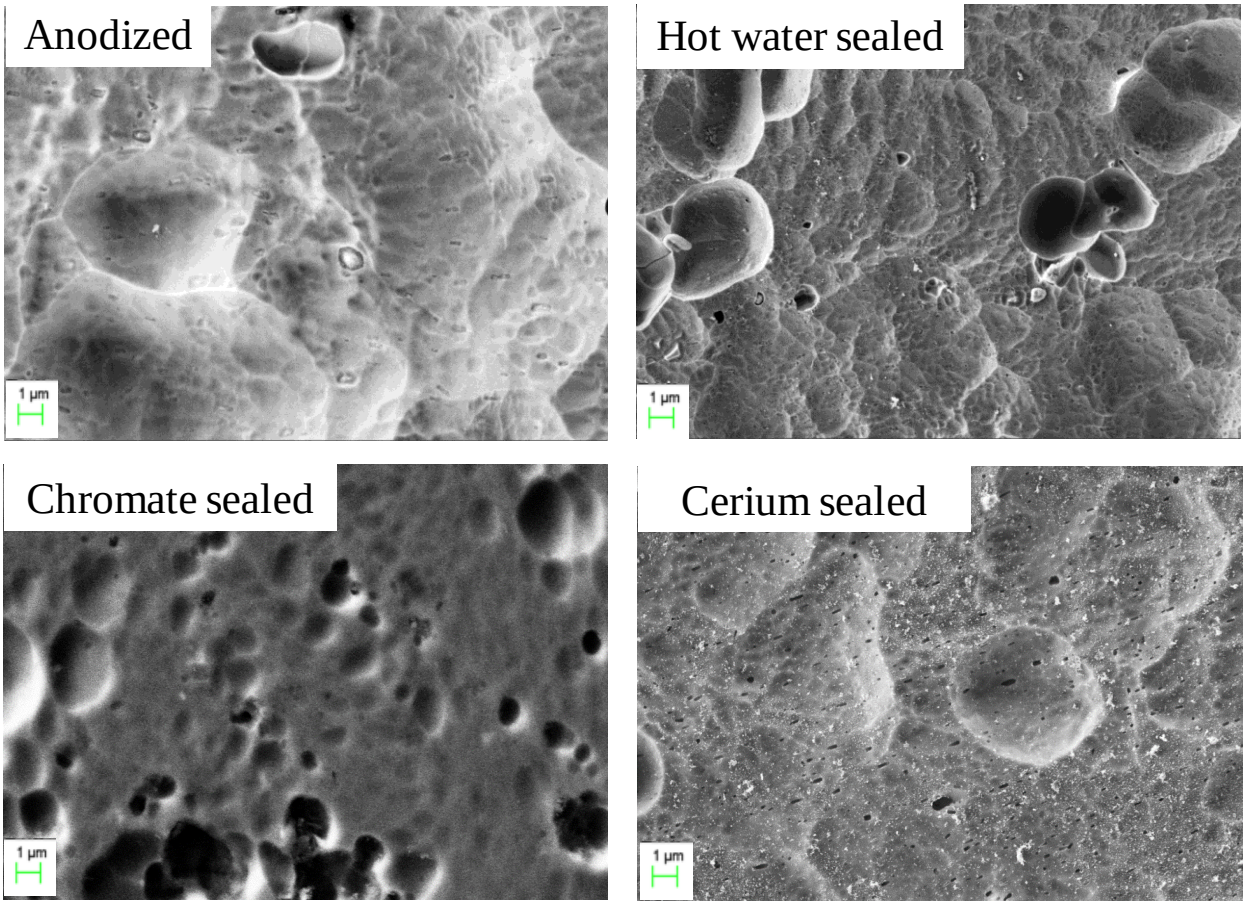

Figure 43 - Scanning electron micrographs of the surface of specimen treated in Mod.TSA solution (a) anodized, (b) hot water sealed, (c) sodium chromate sealed and (d) cerium (III) nitrate sealed.

Also in this case the surface of specimen anodized (Figure 43a) reflected the scalloped morphology generated by etching treatment. The surface of samples after sealing in hot water (Figure 43b) and chromate-based solution (Figure 43c) are similar to that observed for TSA oxides sealed. The cerium treatment (Figure 43d), induced the precipitation cerium-rich clusters but are less evident compared to TSA oxide.

7.1.4 EIS measurements during corrosion tests

After the selected anodizing and sealing treatments, the specimens were immersed in 3.5 wt.% NaCl and impedance measurements were taken at regular intervals for 14 days. In Figure 44, the results obtained from the control unsealed specimens are presented.

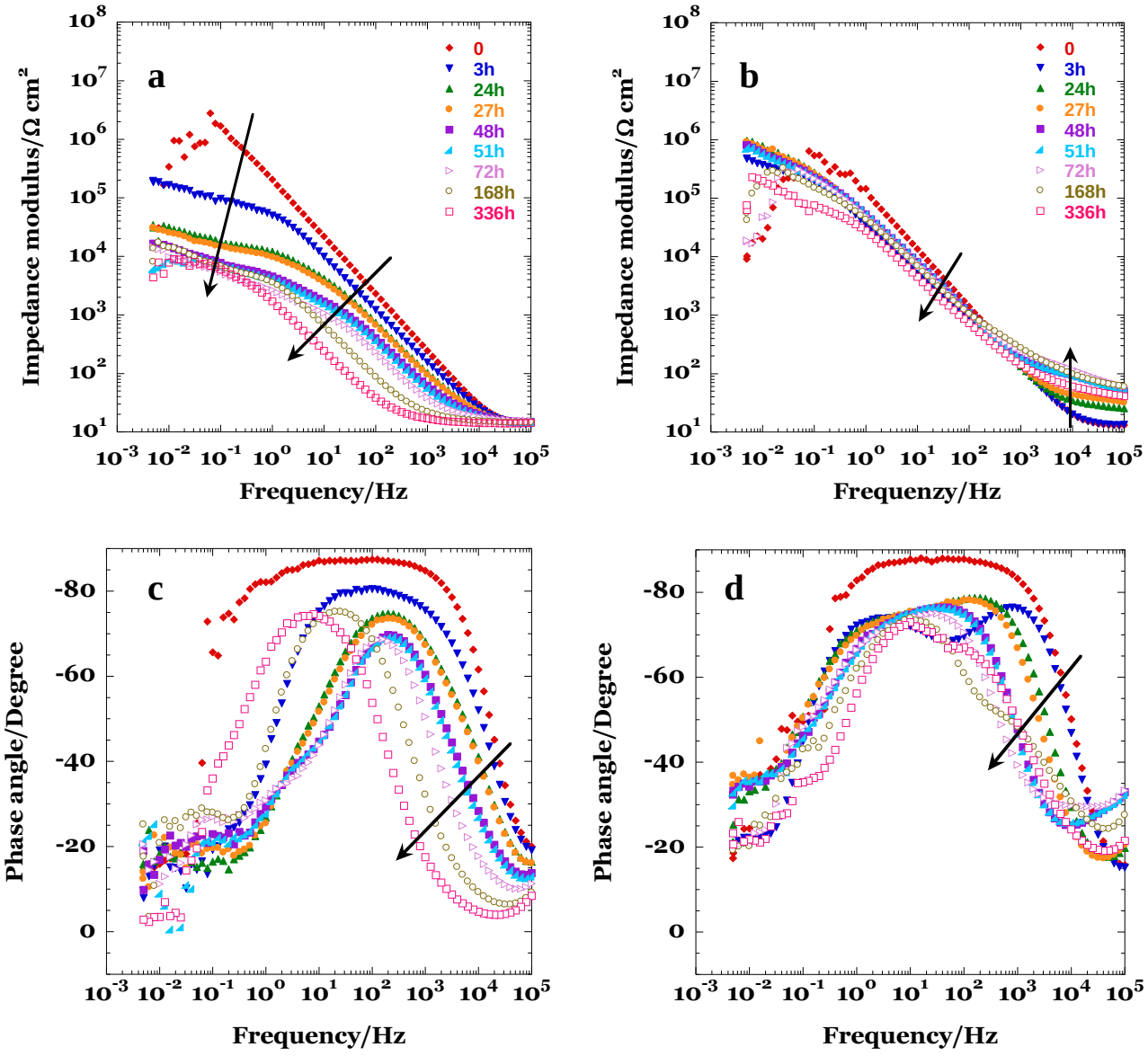

Figure 44 - Series of EIS spectra of unsealed anodic oxides obtained during 336 hours of exposure in 3.5% NaCl: **a, c)** TSA and **b, d)** modified TSA.

During the 336 hours of immersion, for both anodizing treatments, a progressive decrease in values of impedance was observed. However, such decrease was more marked for the specimen anodized with the traditional TSA cycle, which attained a low frequency value of impedance modulus of 10^4 ohm cm^2 after 336 hours. The low-frequency impedance modulus of the specimen anodized by the modified TSA cycle also decreased with time, but the final value was approximately one order of magnitude higher. Importantly, a substantial increase in capacitance, evident as a shift toward the left of the EIS spectra, was revealed for the traditional TSA process, whereas such increase was almost absent for the modified TSA process. Further, the modified TSA process displayed a new high-frequency time constant for long immersion times, which was not evident for the traditional TSA process. The behaviour measured after hot water sealing (Figure 45) was significantly different.

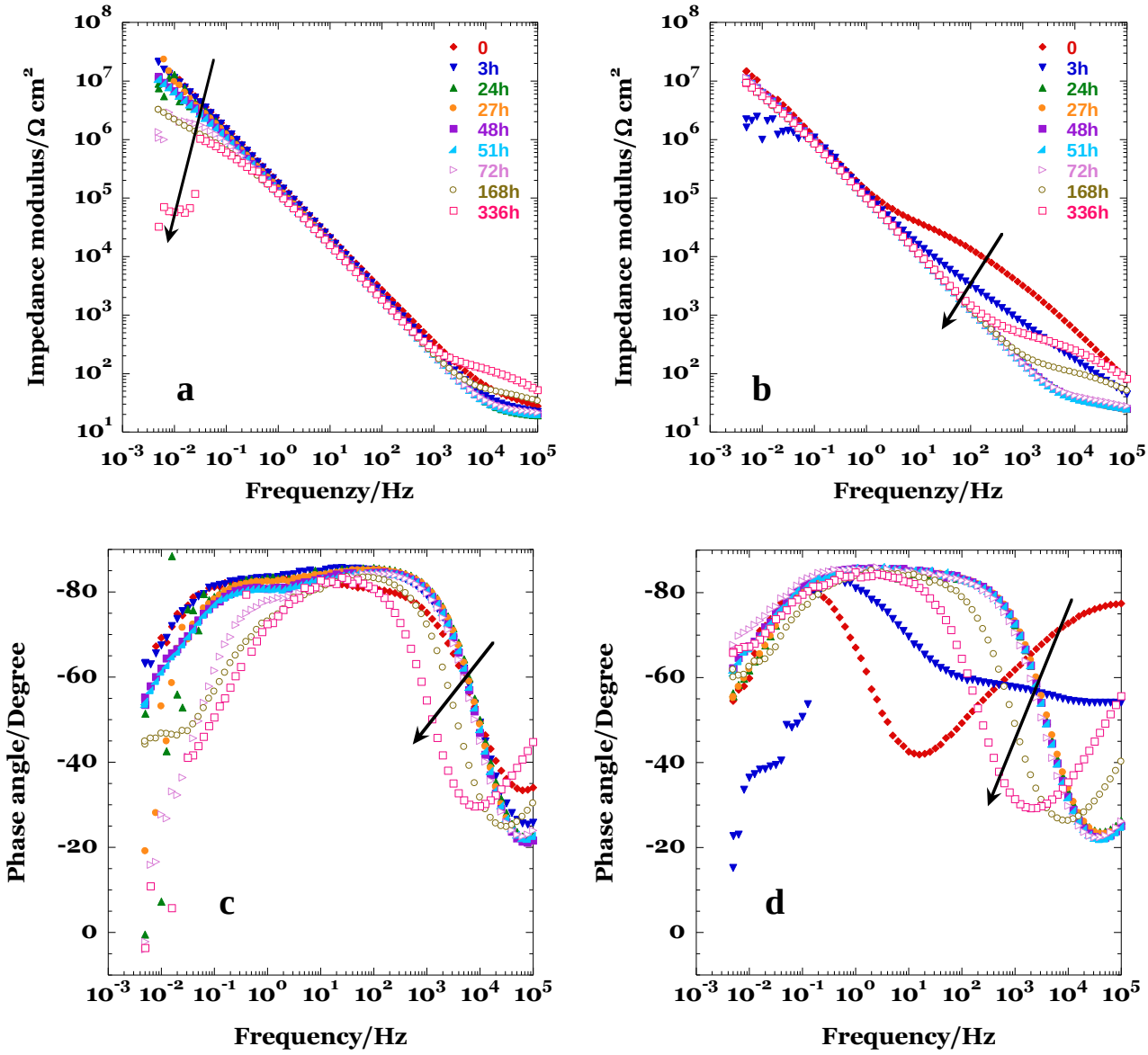

Figure 45 - Series of EIS spectra of hot water sealed anodic oxides obtained during 336 hours of exposure in 3.5% NaCl: **a, c)** TSA and **b, d)** modified TSA.

Both anodizing treatments maintained high values of impedance throughout the test duration. Some decrease in the low frequency values was observed for the specimens anodized in the traditional TSA. Both treatments displayed a reduction of the contribution of the medium-frequency time constant with increasing immersion times, but such reduction was more marked for the specimens anodized by the modified TSA cycle. During corrosion of the specimen anodized by the traditional TSA cycle and sealed in sodium chromate (Figure 46), a decrease in low-frequency

impedance values was observed after 7 days, and a significant increase in capacitance was evident between 168 and 336 hours.

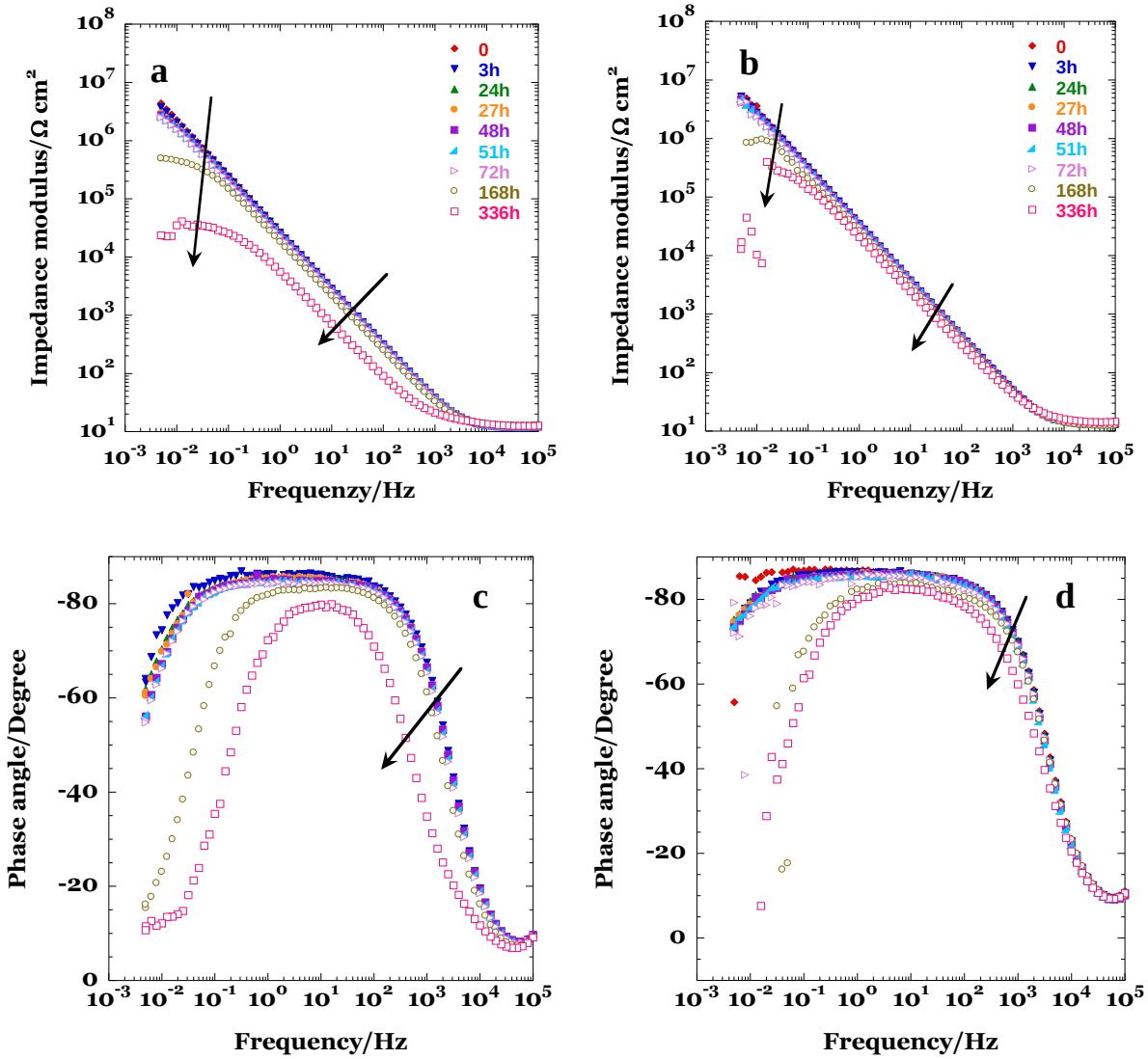

Figure 46 - Series of EIS spectra of chromate sealed anodic oxides obtained during 336 hours of exposure in 3.5% NaCl: **a, c)** TSA and **b, d)** modified TSA.

Such behaviour was much less evident on the specimens anodized with the modified TSA cycle. In particular, the decrease in impedance modulus was moderate and no increase in capacitance was observed during the 336 hours immersion time. The specimens anodized by

traditional TSA and subsequently cerium sealed (Figure 47) displayed a progressive decrease in impedance values over 336 hours, with a corresponding increase in capacitance.

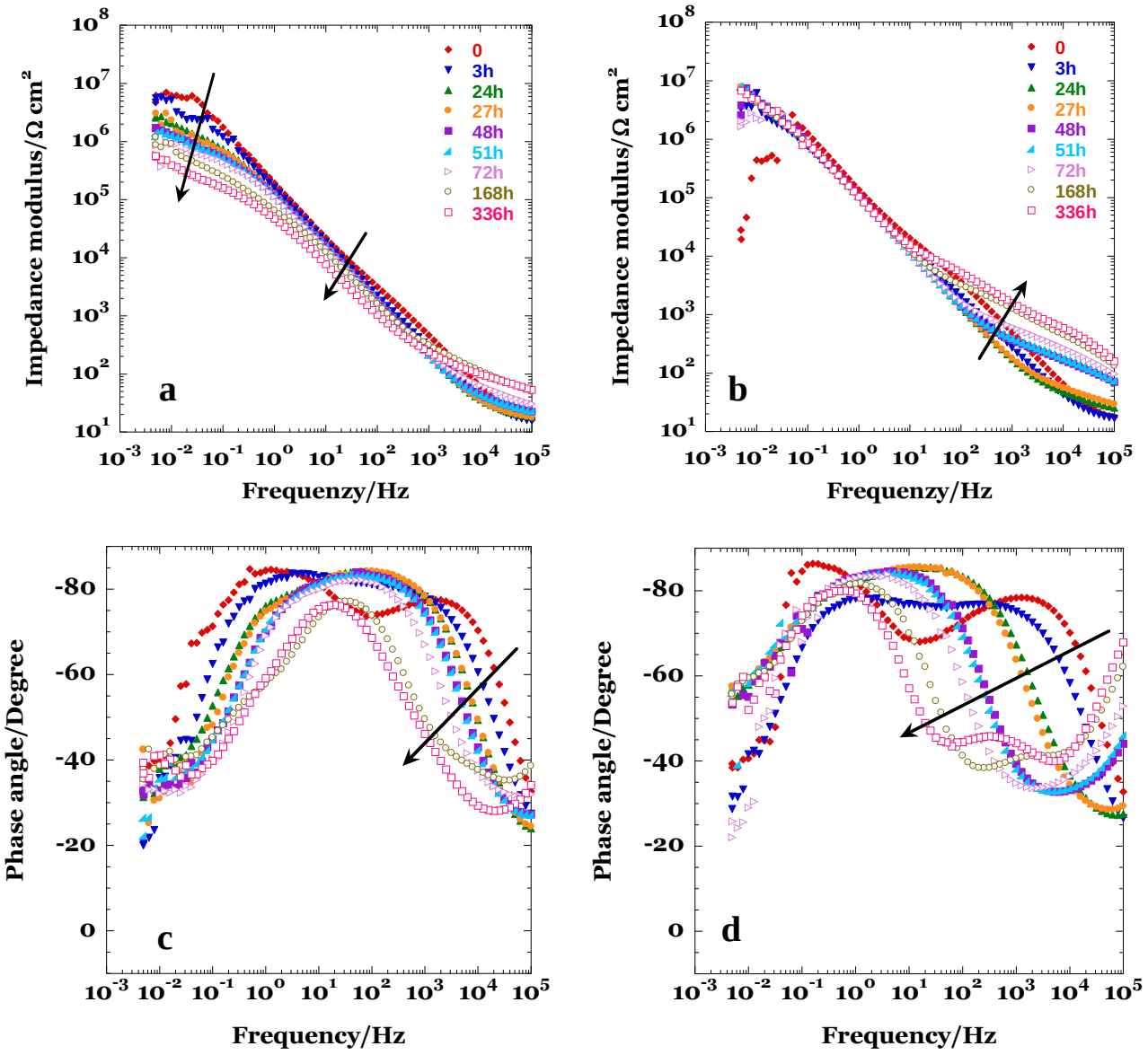

Figure 47 - Series of EIS spectra of cerium sealed anodic oxides obtained during 336 hours of exposure in 3.5% NaCl: **a, c)** TSA and **b, d)** modified TSA.

This was not observed for the specimens anodized by the modified TSA cycle, which did not show an increase in capacitance or a substantial drop in the low-frequency impedance values. Both cycles exhibited an additional high frequency time constant, which was more visible, and

increased more, with increasing immersion time. The modified TSA process, due to the finer porosity that is more impervious to the penetration of aggressive species (in the unsealed condition) and that respond better to sealing, consistently displayed an impedance that is much higher than the traditional TSA process, as evident from the EIS spectra acquired during corrosion in 3.5 wt.% NaCl. The behaviour revealed by EIS was mirrored by the observations from real time imaging of the corroding surfaces. On traditional TSA, the anticorrosion performance of cerium sealing was comparable with that of chromate sealing, with only minor signs of corrosion after 328 hours. On the modified TSA process, with reduced pore diameter, the corrosion performance of both hot water and cerium sealing was significantly increased compared to that of films generated in traditional TSA and subsequently sealed in the same solutions.

In contrast, the performance of chromate sealing was similar or marginally worse. These observations can be rationalized considering that chromate sealing is much more aggressive to the pre-existing anodic oxides and the anticorrosion performance arises from active inhibition provided by the residual chromate ions, rather than from an improvement in barrier effect. Thus, given the aggressiveness of chromium sealing and the active inhibition due to chromate ions, the geometry of the initial porous skeleton is not particularly important in determining the anticorrosion performance after sealing. In contrast, for the other two treatments (hot water and cerium based), the geometry of the pre-existing anodic oxide is much more important, since it is not disrupted as much as for chromate sealing. For hot water sealing, the improvement in corrosion resistance is mainly due to barrier effects associated with the precipitation of hydrated products and pore closure.

Thus, if the pore geometry is finer, it is easier to be filled homogeneously by hydration products. Similar arguments apply to the cerium sealing, where the hydration of the porous skeleton is less important, but a significant precipitation of cerium products occurs within and above the pores, as shown by the appearance of the second time constant (see Figure 35).

7.1.5 Corrosion imaging

In order to corroborate the EIS results, couples of anodized and sealed specimens were masked and immersed vertically in 3.5 wt.% NaCl solution, at the free corrosion potential. In Figures 48-51, the surface appearance of the specimens during corrosion is compared.

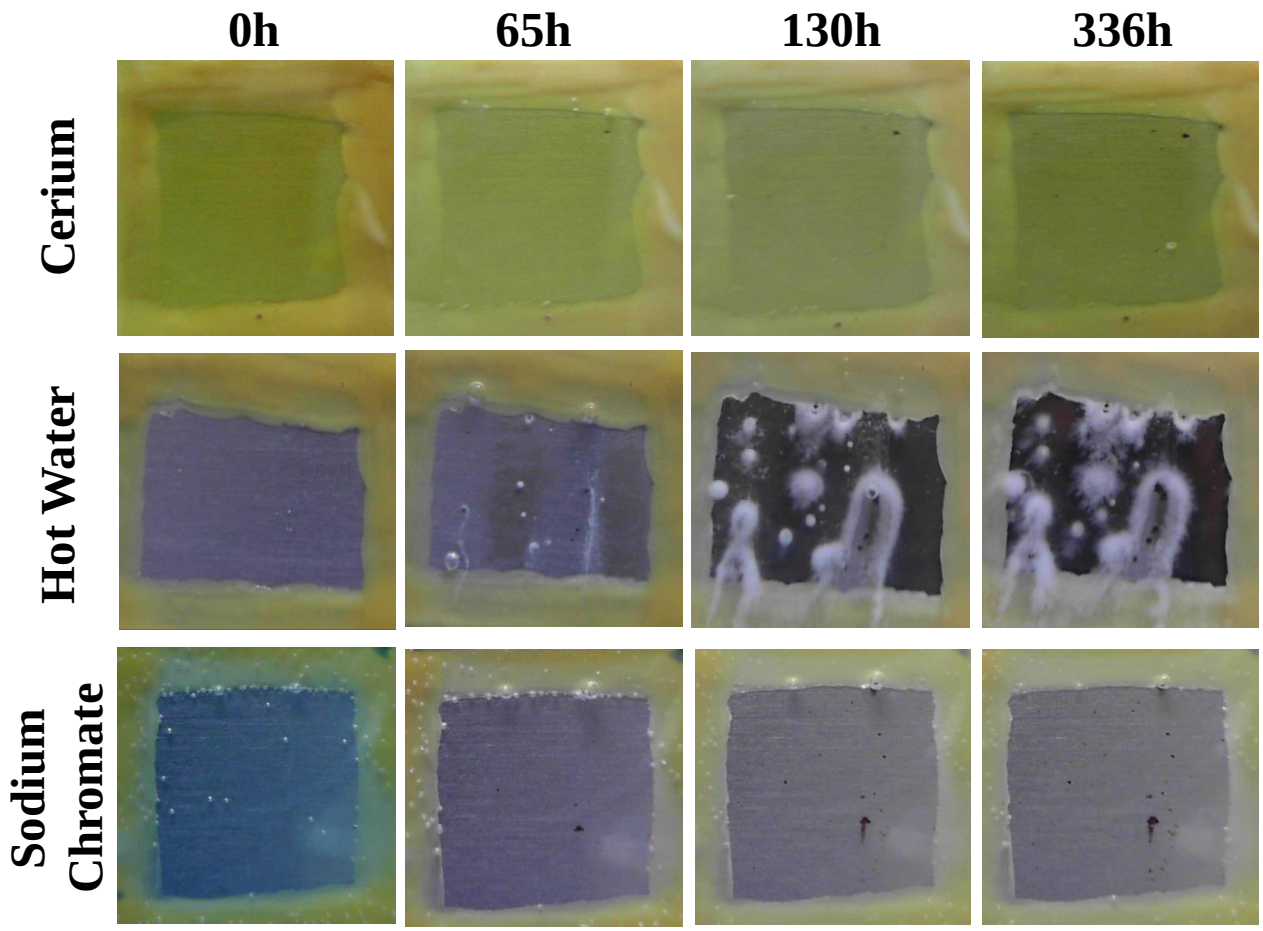

Figure 48 - Surface appearance during corrosion in 3.5 wt% NaCl of the specimens anodized by the traditional TSA process and sealed with the different treatments. Pairs of nominally identical specimens were corroded and this figure reports the specimen appearing less corroded.

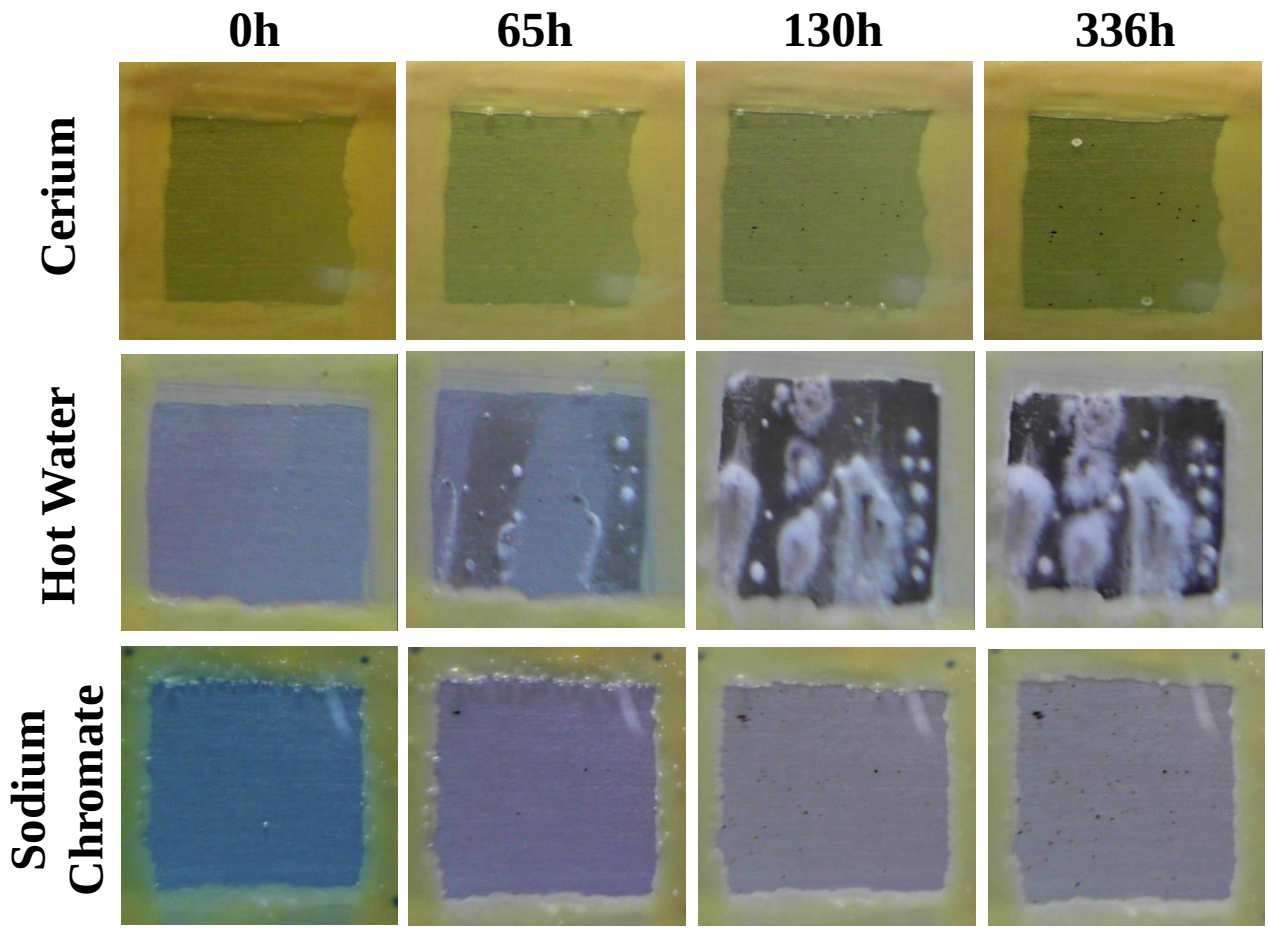

Figure 49 - Surface appearance during corrosion in 3.5 wt% NaCl of the specimens anodized by the traditional TSA process and sealed with the different treatments. Pairs of nominally identical specimens were corroded and this figure reports the specimen appearing more corroded.

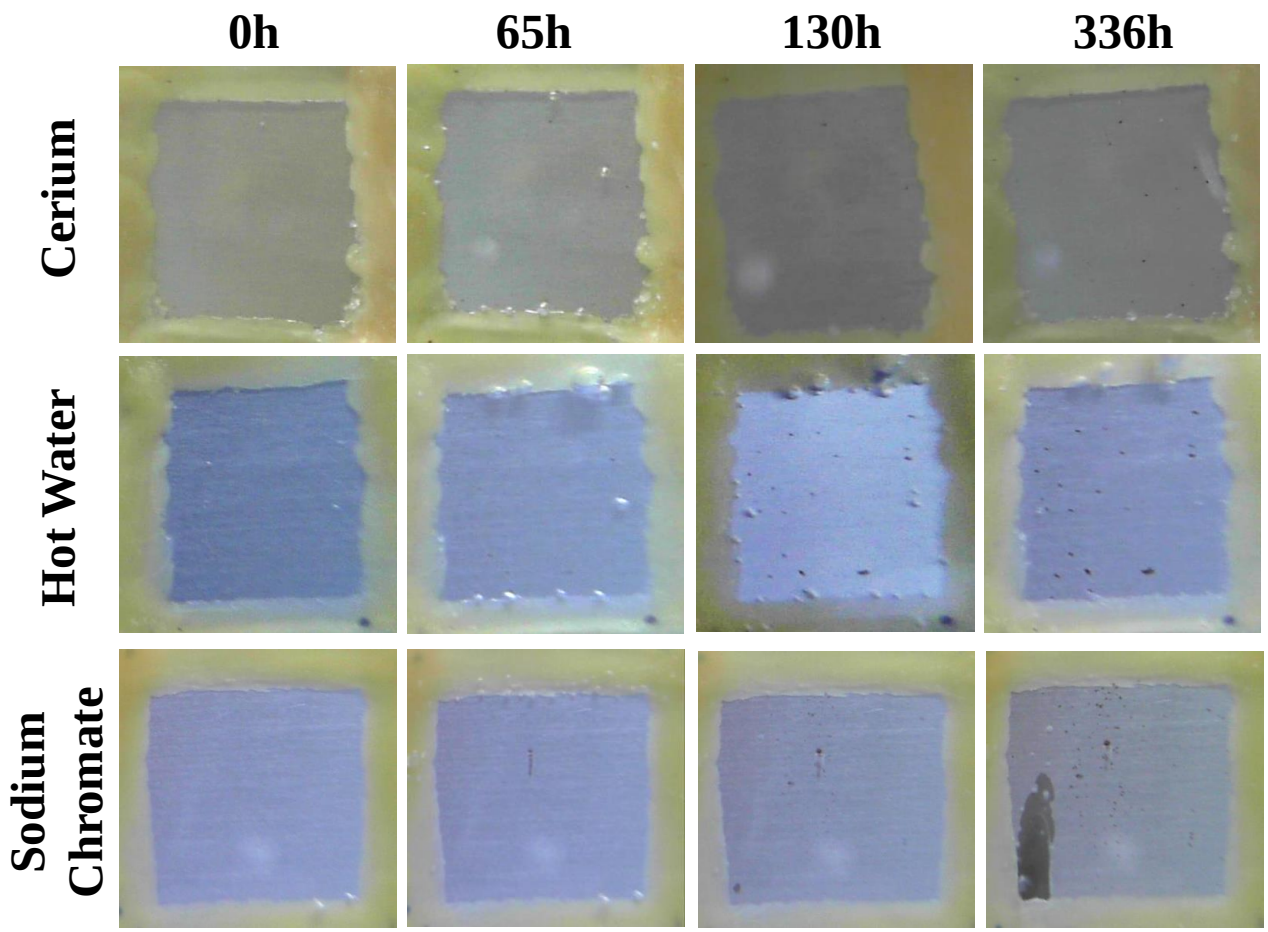

Figure 50 - Surface appearance during corrosion in 3.5 wt% NaCl of the specimens anodized by the modified TSA process and sealed with the different treatments. Pairs of nominally identical specimens were corroded and this figure reports the specimen appearing less corroded.

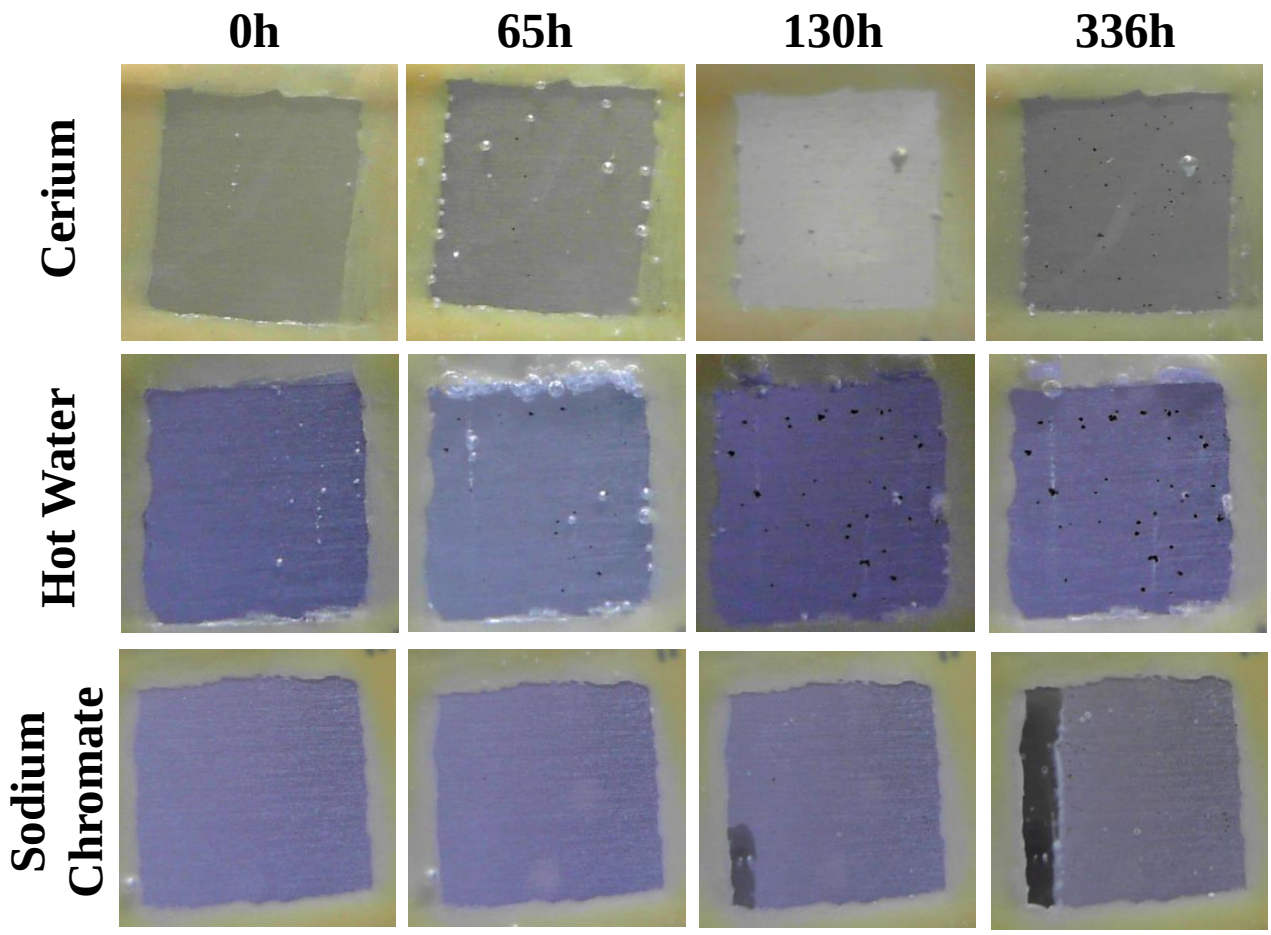

Figure 51 - Surface appearance during corrosion in 3.5 wt% NaCl of the specimens anodized by the modified TSA process and sealed with the different treatments. Pairs of nominally identical specimens were corroded and this figure reports the specimen appearing more corroded.

It is evident that the sealing treatment that provided the best anticorrosion performance was the cerium-based treatment, followed by the chromate treatment and the hot-water sealing. Further, the modified TSA cycle was substantially better than the traditional TSA cycle, with no sign of corrosion after cerium treatment and minimal corrosion after hot water and after chromate sealing.

Similar trends were observed for the worst of the two specimens, i.e. the cerium treatment was the more protective, and the modified TSA produced the best anticorrosion performance. Overall, cerium treatment on modified TSA provided better anticorrosion performance when compared to the sodium chromate sealing of traditional TSA. Overall, the experimental evidence presented here indicates that the combined use of the modified TSA anodizing cycle, together with

cerium based sealing, produces film with anticorrosion performance that is equivalent or exceeds that of chromate sealed traditional TSA. This is due to the effect of the fine pore morphology that enhances the barrier properties and facilitates the sealing, combined with the active inhibition provided by cerium ions.

7.2 Trivalent Chromium conversion coatings

7.2.1 Industrial cycle Alodine 1200s

The potentiodynamic polarizations are performed in order to determine the characteristics of the aluminium alloy when it is exposed in aggressive environments. Such measures have been carried out according to ASTM G3 and ASTM G5.

7.2.1.1 Potentiodynamic polarization results

The analysis of the various step of the Alodine cycle have performed, particularly the corrosion behaviour of the alloy after two degreasings, after chromate pickling and after pickling with Alodine 1200s conversion coating will be analysed. Electrochemical tests were carried out in an aggressive solution containing Cl^- ions (3.5 wt.% NaCl). Experiments were repeated at least three times in order to evaluate the reproducibility. The area exposed for these measurements was 3 cm^2. In Figure 52, the alloy behaviour is compared at each step of the cycle.

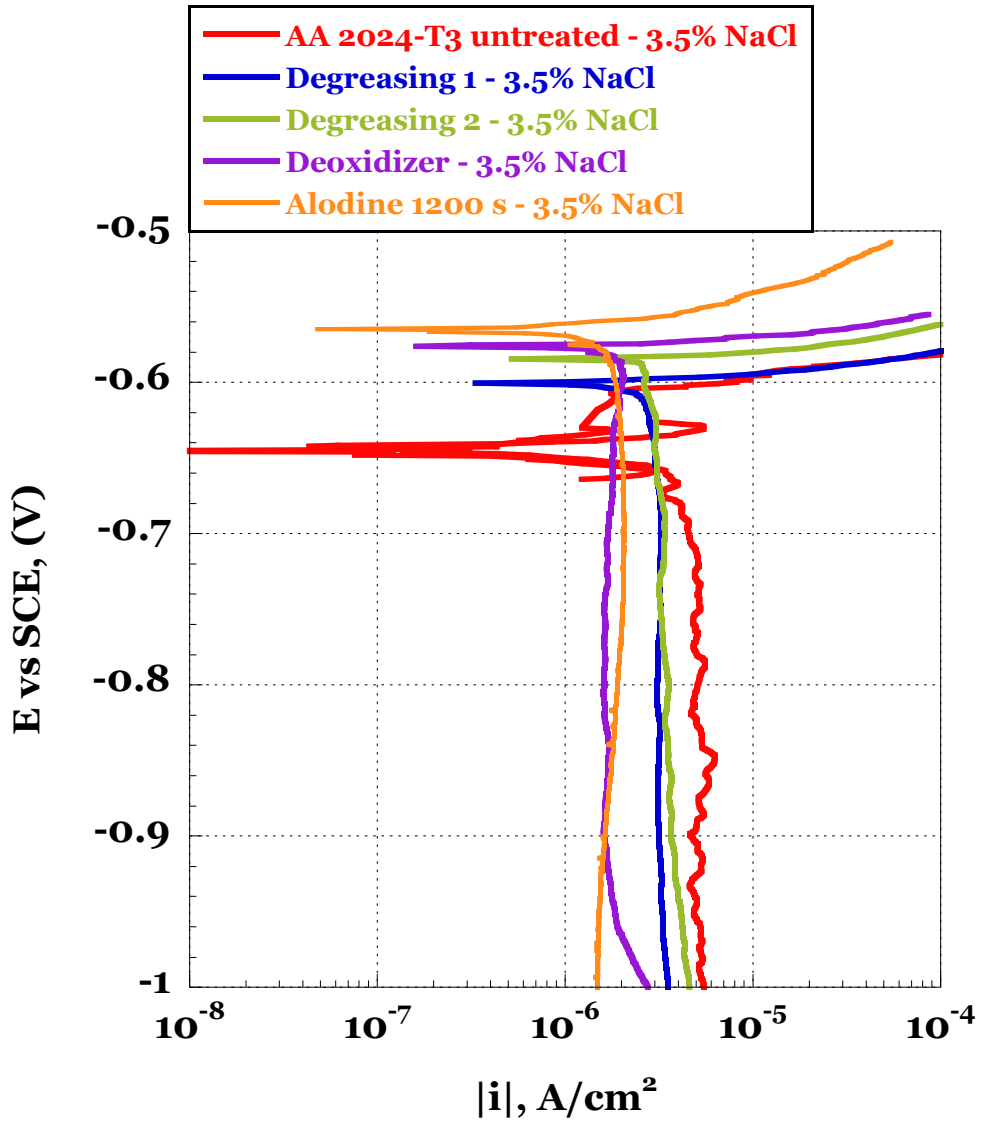

Figure 52 - Electrochemical behaviour of the Alodine cycle in 3.5 wt.% NaCl solution.

The anodic process and the cathodic processes are shown in the potentiodynamic polarization. Observing the behaviour of the cathodic curve, for untreated alloy, it is very fluctuating and this is indicative of a strong unevenness of the surface. Thickness of surface oxide not uniform are present, with active systems and presence of second phases, responsible for the corrosion phenomenon.

After the first and second degreasing, the cathodic curve assume lower current values than that of the untreated alloy. The kinetic of oxygen reduction diminishes and the surface is more homogeneous with the first degreasing.

Following acid pickling, the oxide and the second phase are eliminated and the presence of Cr^{+6} allows the formation of a first conversion layer protecting the aluminium alloy. This is found in the cathodic curve where it can be noted that currents assume lower values.

After Alodine 1200s conversion coatings, the cathodic curve greatly improves by obtaining lower currents of one order of magnitude than that untreated alloy.

Instead, considering the curves that represent the anode process, it is noted that E_{corr} value increases with the various steps of the process. It can be noted, in Table 18, that its value increases by 40 mV compared to the value that it assume with the alloy subject only the first degreasing.

Table 18 – Potentiodynamic polarization results of classical industrial cycle.

Steps	**E_{corr}, V vs SCE**	**i_{corr}, A/cm^2**	**E_{pit}, V vs SCE**
AA 2024-T3 untreated	-0.645	$3.98 \cdot 10^{-7}$	-0.645
Degreasing 1	-0.600	$9.74 \cdot 10^{-7}$	-0.600
Degreasing 2	-0.584	$1.22 \cdot 10^{-6}$	-0.584
Deoxidizer	-0.576	$6.15 \cdot 10^{-7}$	-0.576
Alodine 1200 s	-0.610	$2.38 \cdot 10^{-7}$	-0.564

7.2.1.2 EIS results

Electrochemical impedance spectroscopy were carried out perturbing to the least one the corrosion potential, therefore, are designed to not destroy the specimen. A monitoring was performed for 15 days in a solution containing 3.5 wt. % NaCl. The area of the specimen exposed was 7 cm^2.

The impedance modulus trend of the untreated alloy is shown in Figure 53, while the trend of the corresponding phase angle is reported in Figure 54.

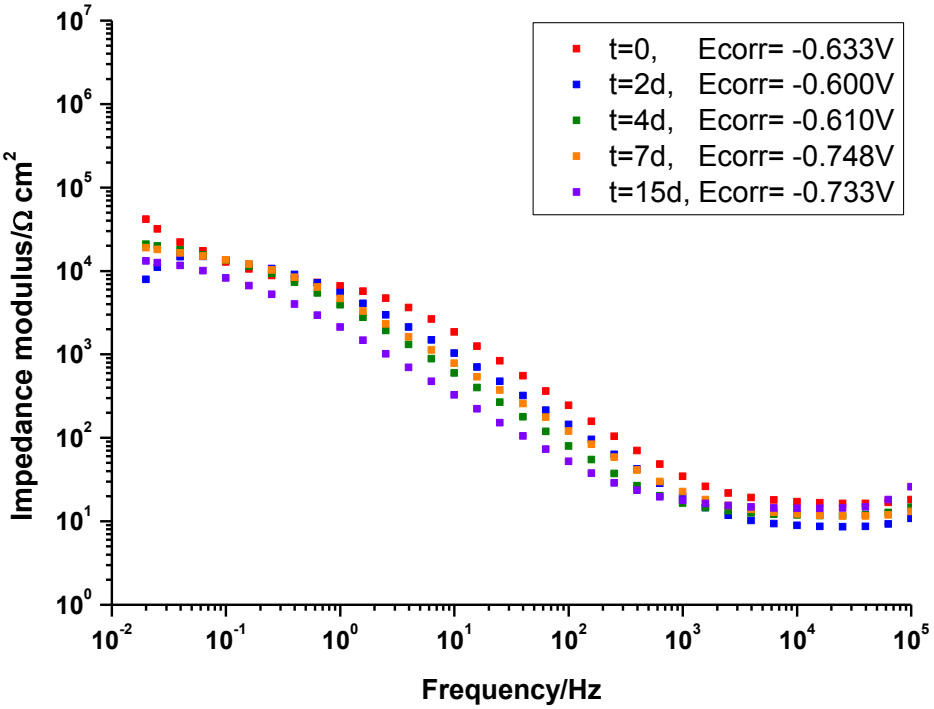

Figure 53 – Impedance modulus of untreated alloy 2024-T3 obtained during 15days of exposure in 3.5% NaCl.

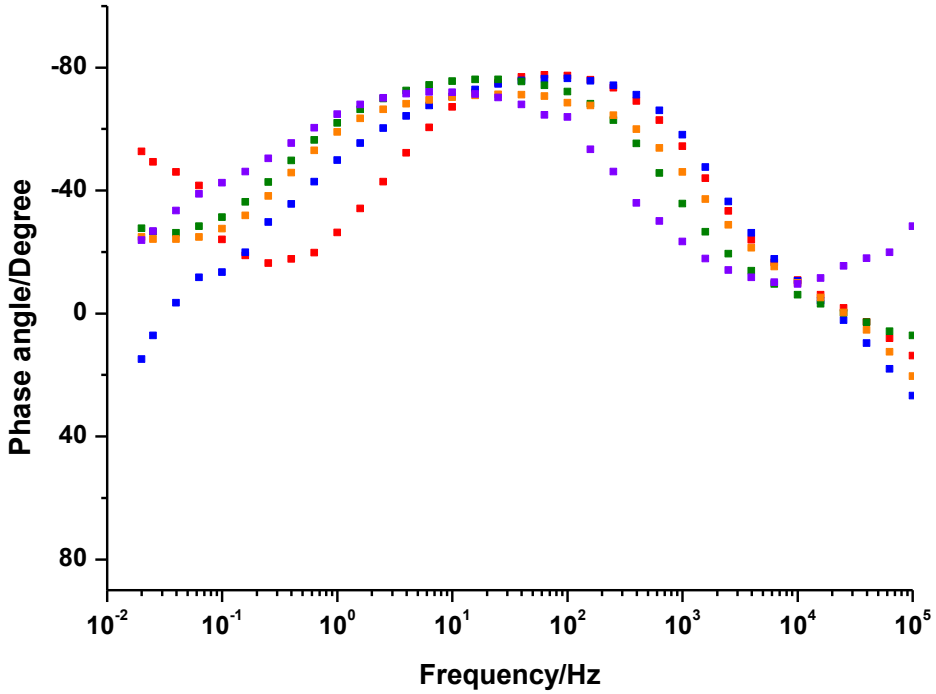

Figure 54 – Phase angle of untreated alloy 2024-T3 obtained during 15 days of exposure in 3.5% NaCl.

Considering the low-frequency values, a low impedance can be observed at the beginning of immersion in the solution test. This is an indication of a high corrosion rate and the presence of pits on the aluminium surface. After 4 days of exposure, the low-frequency impedance modulus increases and the phase angle is more sable. Overall, the impedance modulus increases up to 7 days, while after 15 days the modulus returns to lower values.

The impedance modulus trend of the alloy after the first degreasing is shown in Figure 55, while the trend of the corresponding phase angle is reported in Figure 56.

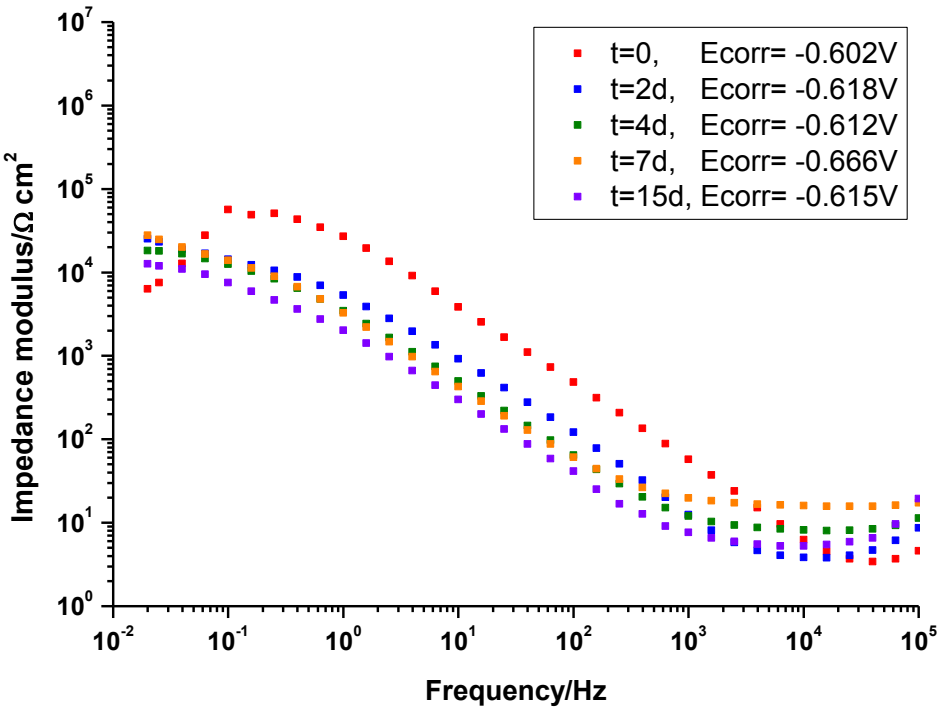

Figure 55 - Impedance modulus of alloy after first degreasing obtained during 15days of exposure in 3.5% NaCl.

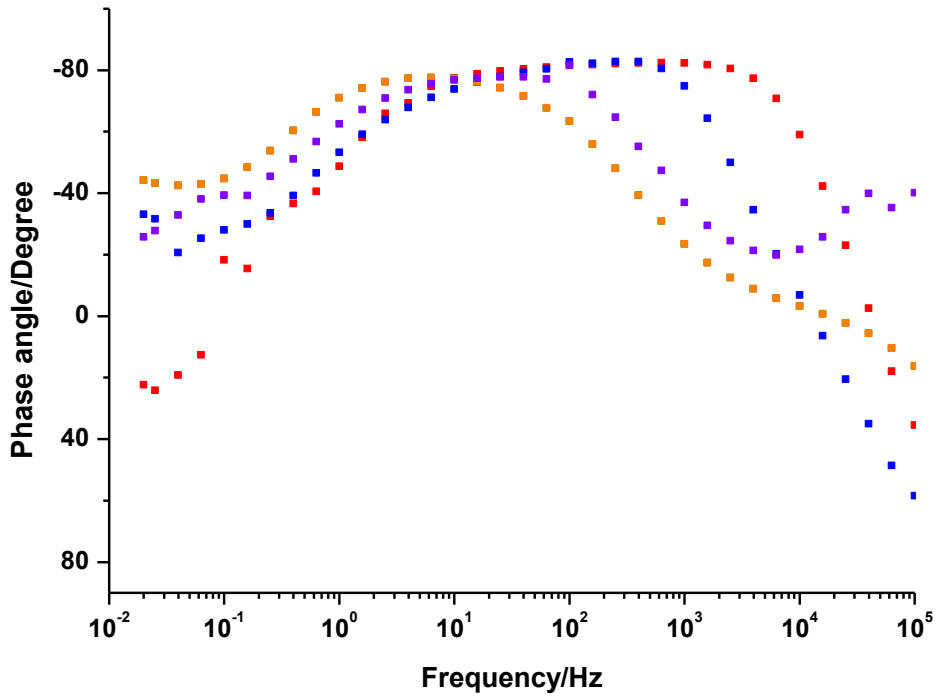

Figure 56 – Phase angle of alloy after first degreasing obtained during 15days of exposure in 3.5% NaCl.

Even in this case, considering the measured values at very low frequencies, it can be seen that Considering the low-frequency values, a low impedance can be observed at the beginning of immersion in the solution test, a low impedance value is detected. This is a pits trigger index on the surface. After 2 day of exposure, the low-frequency impedance modulus increases and the phase angle is stable. Overall, the impedance modulus increases up to 7 days, after 15 days the modulus reveals slightly lower values.

The impedance modulus behaviour of the alloy after second degreasing is reported in Figure 57, while the trend of the corresponding phase angle is shown in Figure 58.

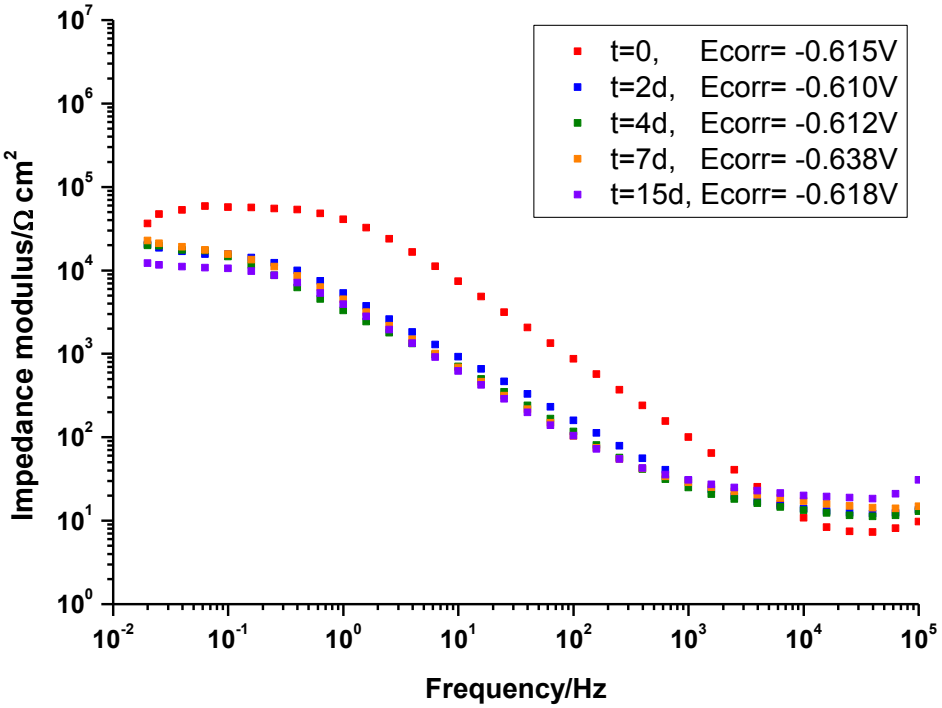

Figure 57 - Impedance modulus of alloy after second degreasing obtained during 15days of exposure in 3.5% NaCl.

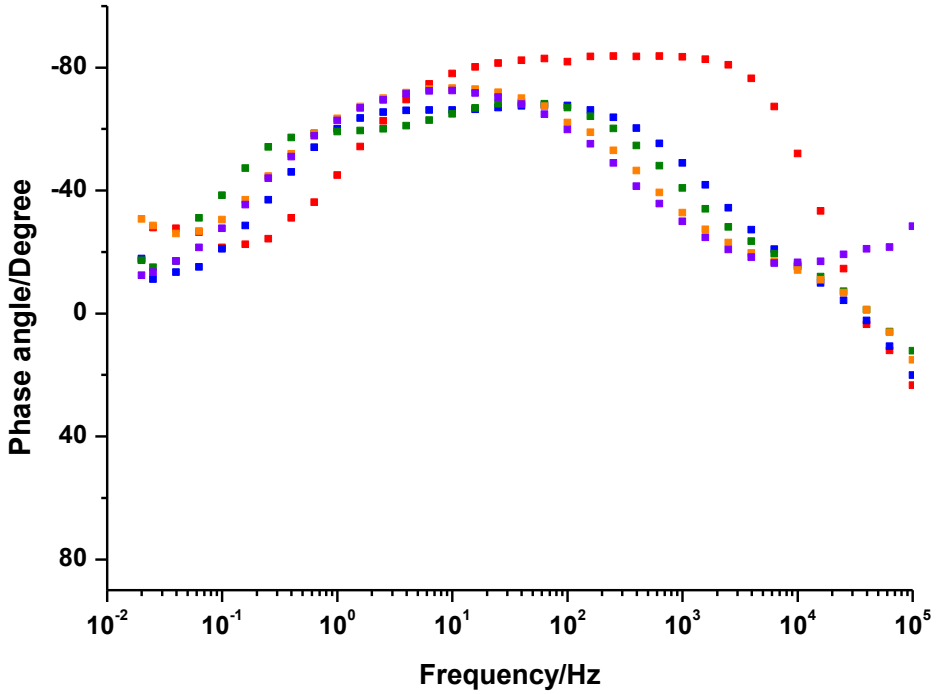

Figure 58 - Phase angle of alloy after second degreasing obtained during 15days of exposure in 3.5% NaCl.

Considering the low-frequency values, a low impedance can be observed at the beginning of immersion in the aggressive solution. This indicate the presence of the pits on the surface. After 2 days of exposure, the low-frequency impedance modulus increases and the phase angle is stable that remain unchanged up to 4 days of exposure. Subsequently a reduction of the impedance modulus is observed after 7 and 15 days after which the modulus assumes slightly lower values.

The impedance modulus trend of the alloy after pickling process is reported in Figure 59, while the trend of the corresponding phase angle is shown in Figure 60.

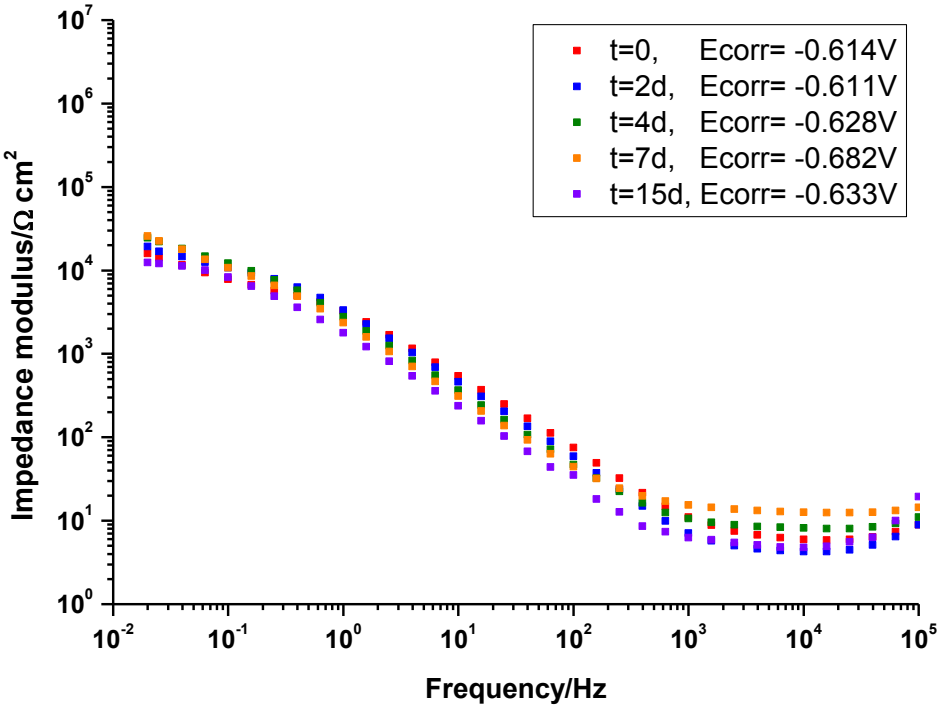

Figure 59 - Impedance modulus of alloy after Deoxidizer 6-16 acid pickling obtained during 15days of exposure in 3.5% NaCl.

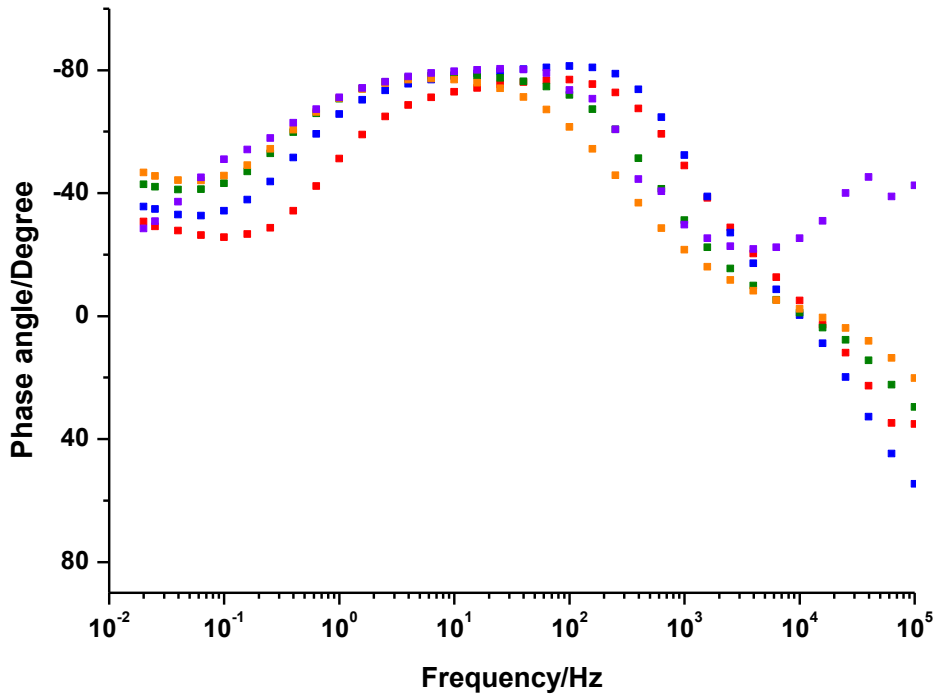

Figure 60 – Phase angle of alloy after Deoxidizer 6-16 acid pickling obtained during 15days of exposure in 3.5% NaCl.

The low-frequency impedance modulus behaviour is very similar in the different exposure days and the phase angle is more stable than that in the previous steps. This behaviour is attributable to the presence of hexavalent chromium which forms a first conversion layer protecting the alloy from corrosion.

The impedance modulus trend of the alloy after Alodine process is displayed in Figure 61, while the trend of the corresponding phase angle is reported in Figure 62.

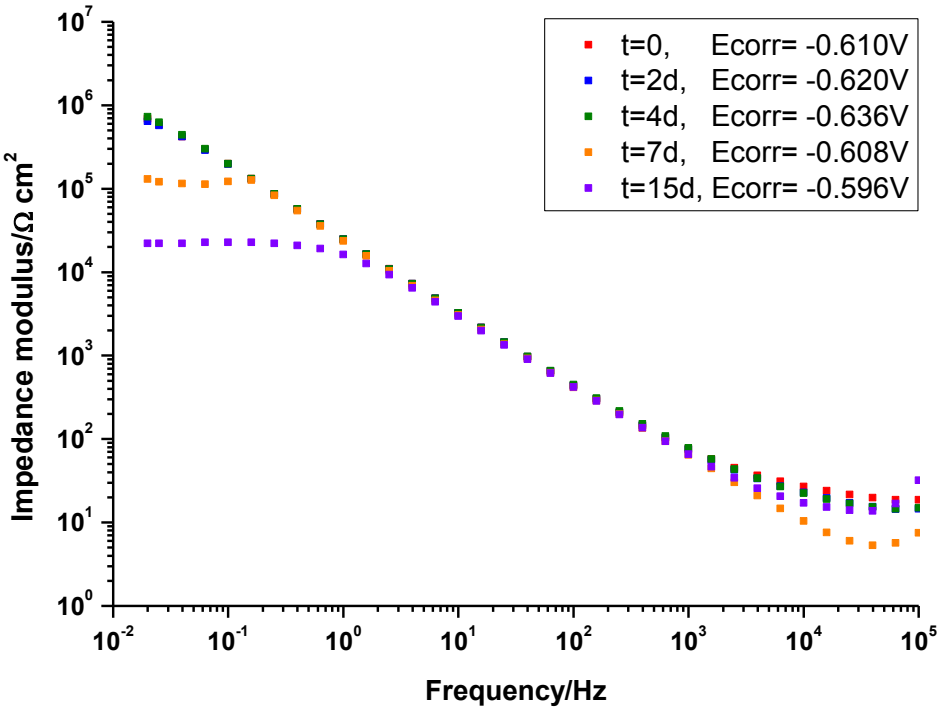

Figure 61 – Impedance modulus of alloy after Alodine 1200s obtained during 15days of exposure in 3.5% NaCl.

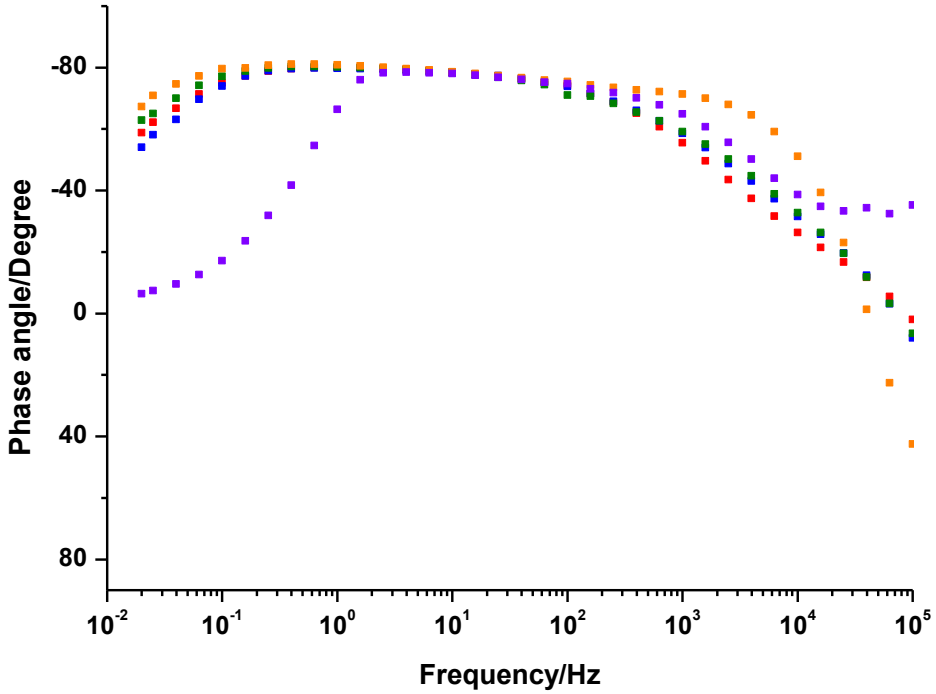

Figure 62 – Phase angle of alloy after Alodine 1200s obtained during 15days of exposure in 3.5% NaCl.

The low-frequency impedance modulus increases up to 4 days of exposure. An ideal behaviour of the specimen is noticed because the curve assume a slope of -1. After 7 days of exposure, the impedance modulus behaviour decreases slightly, reaching higher values than that measured in the other steps of the industrial cycle. The phase angle is stable at 80° for four frequency ranges, indicating that the material are assuming an ideal dielectric behaviour.

The electrochemical measurements carried out on AA202-T3 after the various treatment, reveal the each step of the industrial cycle improved the corrosion resistance of the alloy. This is visible not only with an increase of 40 mV of the corrosion potential but also by the increasing behaviour of the low-frequency impedance modulus and by a greater stability of the phase angle observed during EIS. The EIS spectra exhibited that the incubation times of the pits extended considerably after an exposure of 15 days in the considered solution. So all process steps are functional to have an improvement in corrosion resistance of the alloy AA202-T3.

7.2.1.3 Surface analysis

After performing the electrochemical tests on aluminium alloy, the evaluation of the degradation of the sample is carried out by observation its surface. The specimens are examined after 15 days exposure in aggressive environment.

The images were processes with ImageJ software, obtaining a percentage estimate of the pitting areas. ImageJ can view, edit, analyse, process, save and print images in gray (8 bit, 16 bit, 32 bit) and color (8 bit and 24 bit) scales. Processing is done with a few steps: (i) the whole or portion image is selected, (ii) the color of each pixel is converted to a grayscale and adjusting the brightness and the contrast, the minimum and maximum values of the scale can be change. In this way, the program, through the light-dark, can distinguish the areas where the pits are present; only then it can estimate the area affected by the pitting phenomenon by providing absolute values (according to the scale set) or expressed as a percentage of surface area.

AA2024-T3 untreated

The Figures 63 and 64 display an uniform distribution of small pits. In particular a percentage of area affected by pitting is estimated at about 53% (Figure 63).

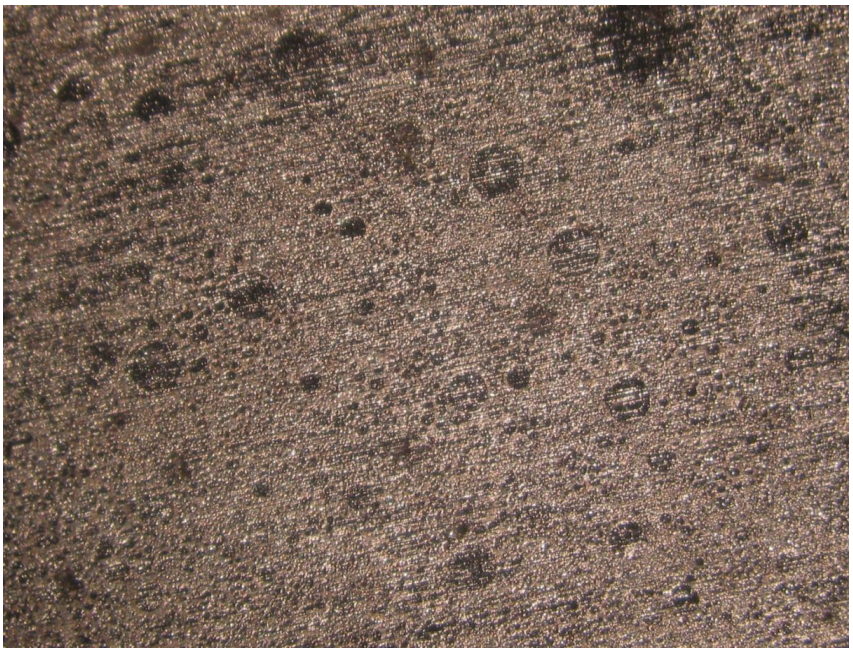

Figure 63 – Image of untreated AA2024-T3 surface after corrosion test, 35x.

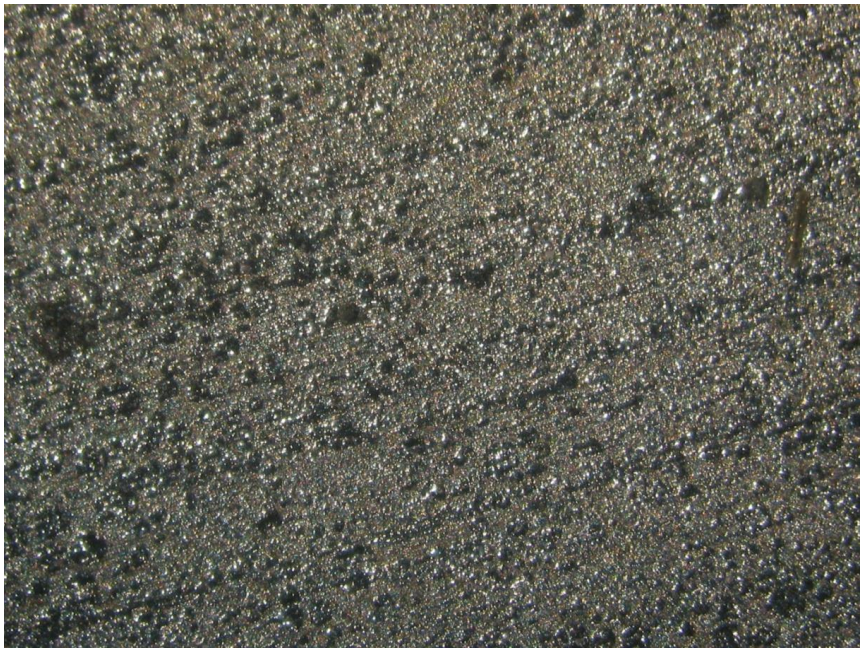

Figure 64 - – Image of untreated AA2024-T3 surface after corrosion test, 100x.

AA2024-T3 after first degreasing

Analysing the alloy, a not uniformly distribution of medium sized pits is observed on the surface, as shown in Figures 65 and 66; the percentage of area affected by pitting is 10% (Figure 65).

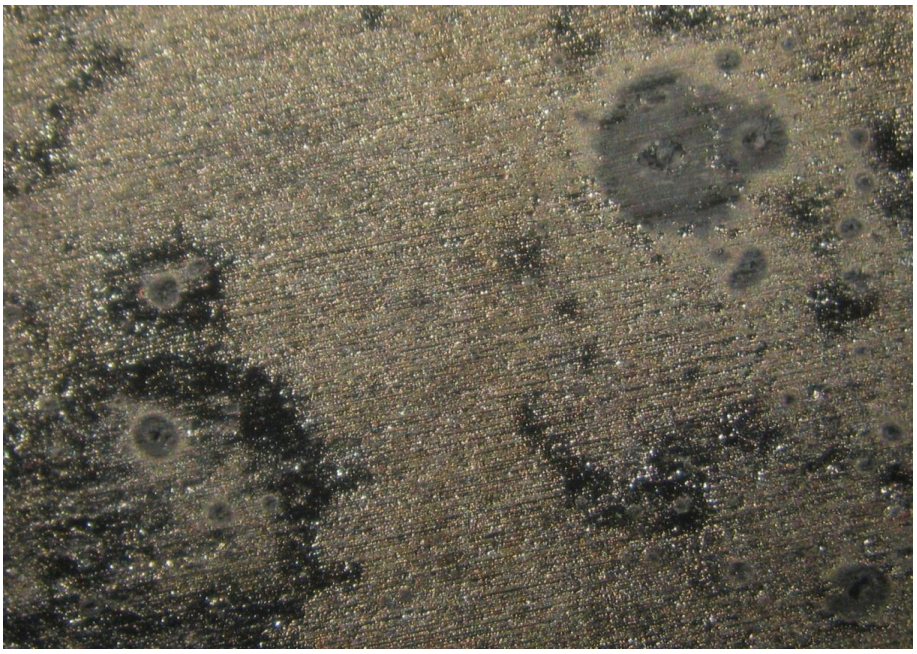

Figure 65 – Image of aluminium alloy 2024-T3 after first degreasing at the end of corrosion test, 35x.

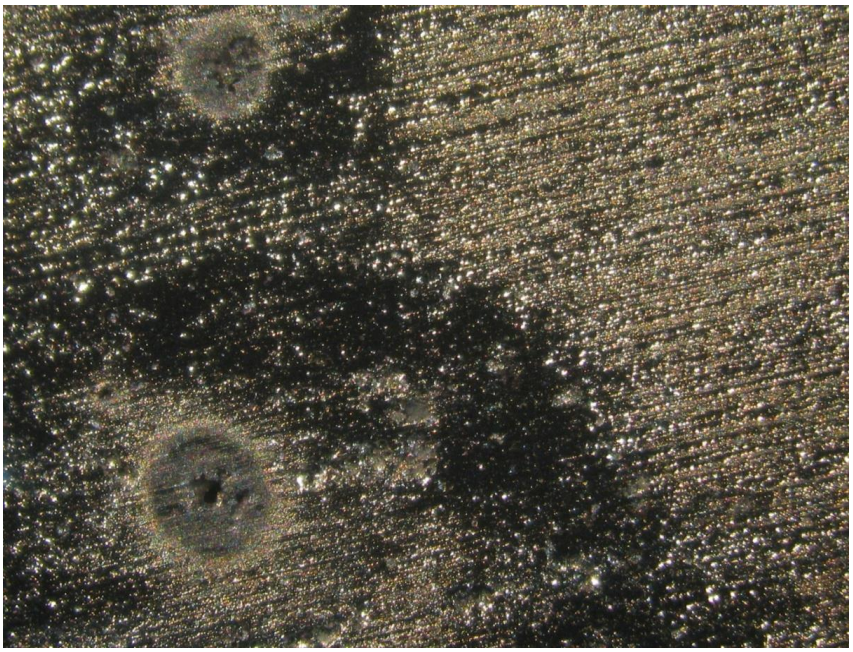

Figure 66 - Image of aluminium alloy 2024-T3 after first degreasing at the end of corrosion test, 100x.

AA2024-T3 after second degreasing

The alloys surface after the second degreasing exhibits a few pits as reported in Figures 67 and 68; in fact the percentage of area affected by pitting is 6%.

Figure 67 - Image of aluminium alloy 2024-T3 after second degreasing at the end of corrosion test, 35x.

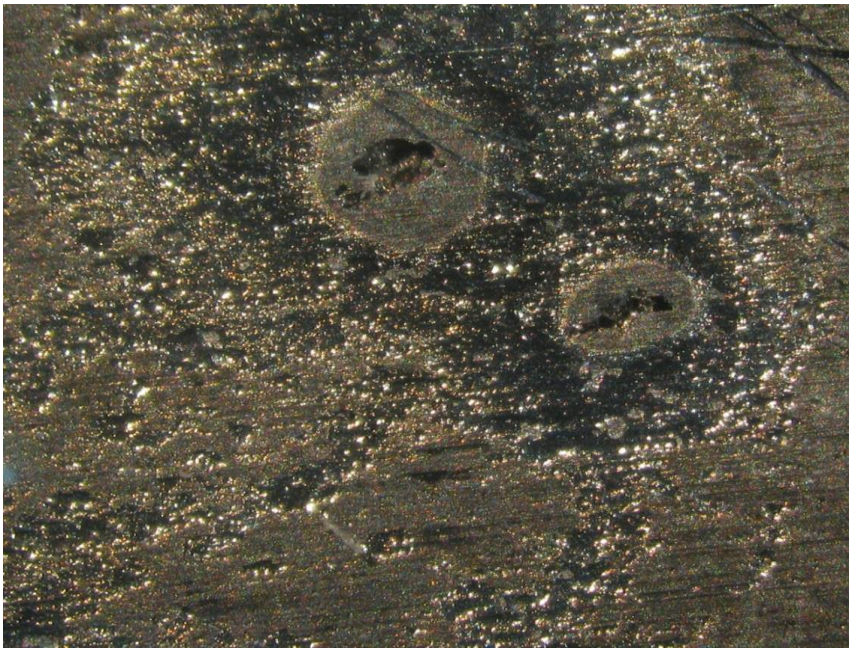

Figure 68 - Image of aluminium alloy 2024-T3 after second degreasing at the end of corrosion test, 100x.

AA2024-T3 after Deoxidizer 6-16 acid pickling

The alloy surface after the pickling exhibits a few pits. Figures 69 and 70 show the area most affected by pits but they should not be considered as a representative of the whole surface. In particular, as seen in Figure 69, a percentage of area affected by pitting is estimated at 10%.

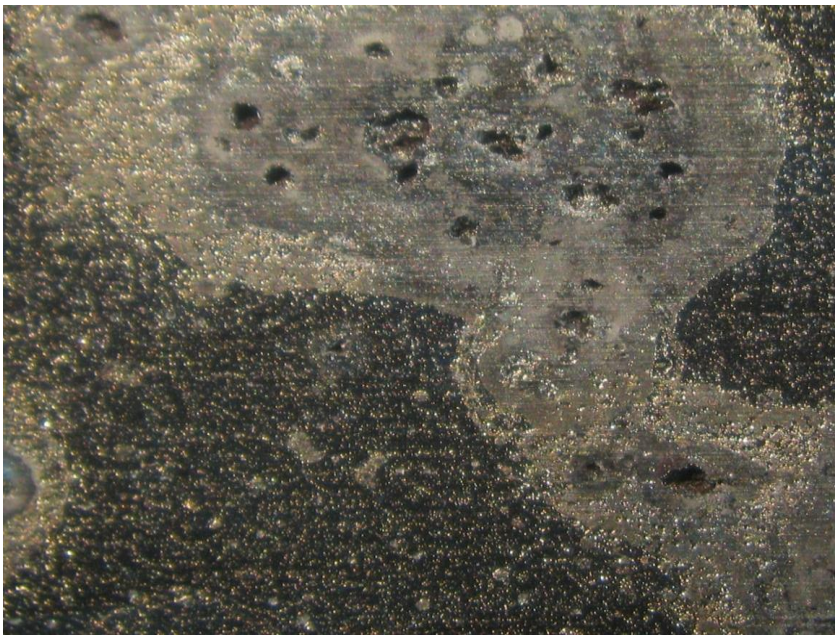

Figure 69 – Image of area detail of aluminium alloy most affected by pits after Deoxidizer 6-16 acid pickling, at the end of corrosion test, 35x.

Figure 70 – Image of area detail of aluminium alloy most affected by pits after Deoxidizer 6-16 acid pickling, at the end of corrosion test, 100x.

AA2024-T3 after treatment Alodine 1200s

The alloy surface after treatment in Alodine displays very few pits of extremely small dimensions, as shown in Figures 71 and 72; the percentage of area affected by pitting is estimated by 1% (Figure 71).

Figure 71 - Image of aluminium alloy 2024-T3 after Alodine 1200 s conversion coating at the end of corrosion test, 35x.

Figure 72 - Image of aluminium alloy 2024-T3 after Alodine 1200 s conversion coating at the end of corrosion test, 100x.

In each step of the industrial process, the number of pits decreases as well as their size, ranging from an uniform distribution of 53% to 1%. In can be concluded that all steps of the process are functional to have an improvement in corrosion resistance of the alloy AA2024-T3.

7.2.2 Chromium free picklings

In order to identify the pickling with competitive characteristics with that of chromium pickling, the electrochemical behaviour of each selected pickling was compared to deoxidizer containing hexavalent chromium.

7.2.2.1 SEM analysis with EDS probe

SEM analysis with EDS probe was carried out on the material provided by Leonardo Company, which does not undergone any tests to verify its initial state and surface composition.

Deoxidizer 6-16 pickling

Figures 73 and 7 show different magnifications of the specimen surface after Deoxidizer 6-16 pickling treatment.

The surface observed reveals the presence of precipitates. The elements of the typical alloy composition (Cu, Fe, Mn, Mg) are observed by performing an EDS, whose results are shown in Table 19. In addition, EDS analysis exhibit Cu and Fe islands and elements such as N, Cr, (whose compounds are present in the pickling solution).

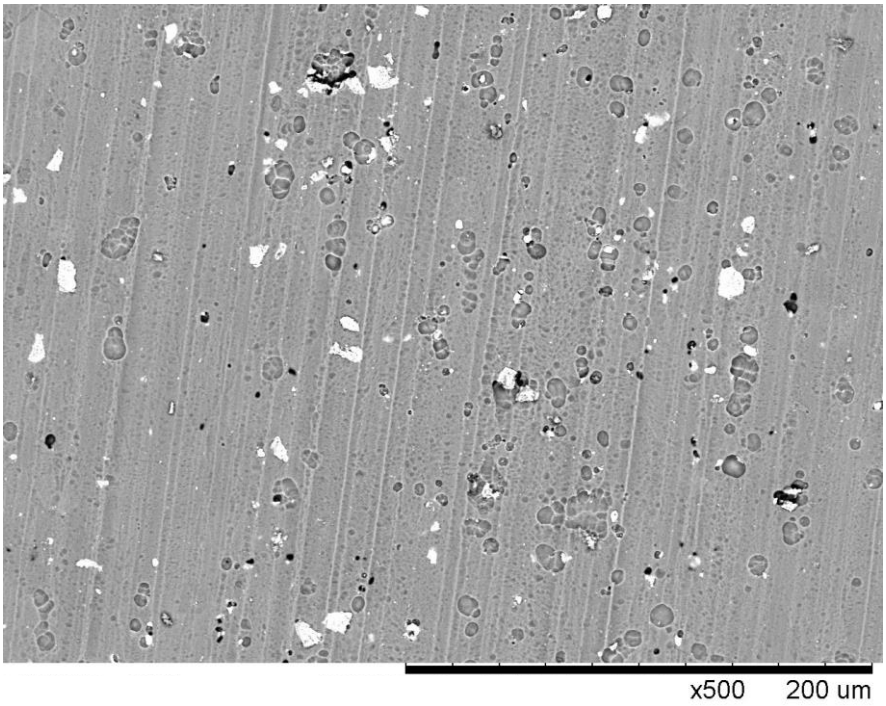

Figure 73 - Scanning electron micrographs of the surface of AA-2024-T3 after Deoxidizer 6-16 acid pickling, 500x.

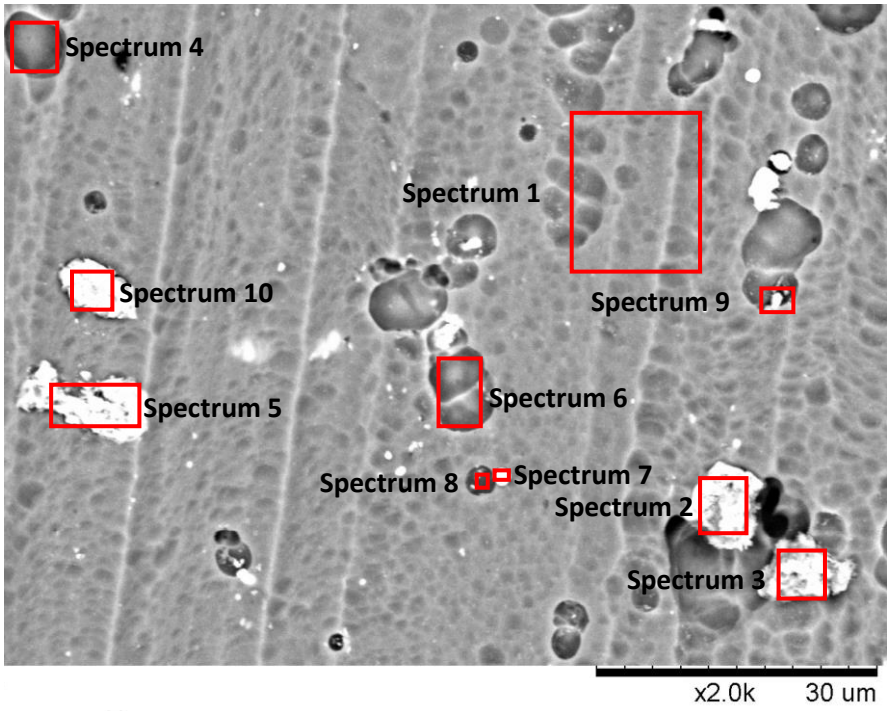

Figure 74 - Scanning electron micrographs of the surface of AA-2024-T3 after Deoxidizer 6-16 acid pickling, 2000x.

Table 19 – EDS analysis of AA2024-T3 after Deoxidizer 6-16 hexavalent pickling.

Name	**wt.% N**	**wt.% O**	**wt.% Mg**	**wt.% Al**	**wt.% Cr**	**wt.% Mn**	**wt.% Fe**	**wt.% Cu**
Spectrum 1		1.988	1.639	89.97		0.519		5.881
Spectrum 2	2.294	15.84	0.384	35.01	0.613	4.202	6.058	35.6
Spectrum 3	2.586	17.53	0.355	37.9	0.692	3.723	4.873	32.34
Spectrum 4	1.729	2.529	1.332	89.45		0.957		4
Spectrum 5	1.391	8.15	0.901	61.36	0.472	3.049	3.437	21.24
Spectrum 6	0.687	1.548	1.434	91.2	0.224	1.198		3.709
Spectrum 7		2.833	1.672	87.61	0.104			7.779
Spectrum 8		2.432	1.6	88.37	0.08	0.575		6.943
Spectrum 9	0.74	2.669	1.446	87.96		0.801		6.386
Spectrum 10	2.243	17.21	0.688	42	0.775	2.812	4.094	30.18

Smut Go NC Pickling

The different magnifications of specimen surface after Smut Go NC alkaline pickling treatment are shown in Figure 75 and Figure 76.

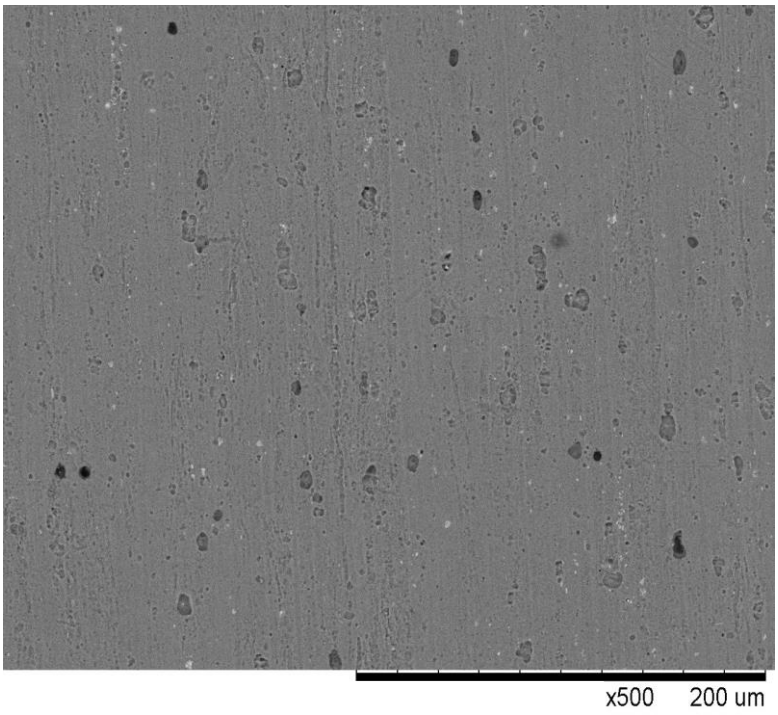

Figure 75 - Scanning electron micrographs of the surface of AA-2024-T3 after Smut Go NC alkaline pickling, 500x.

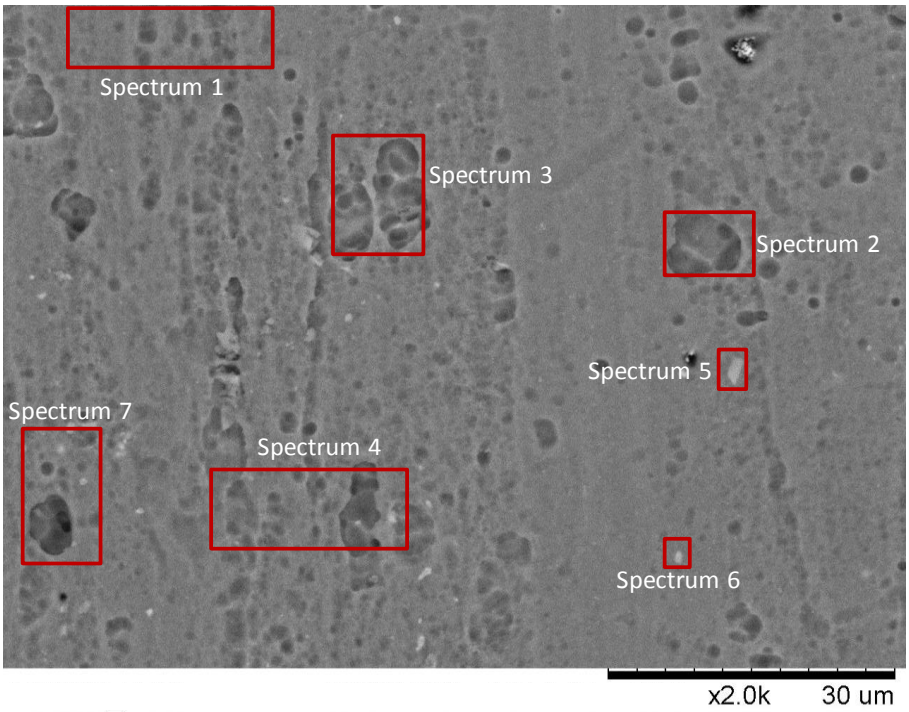

Figure 76 - Scanning electron micrographs of the surface of AA-2024-T3 after Smut Go NC alkaline pickling, 2000x.

The surface reveals the presence of precipitates. The elements of the typical alloy composition (Cu, Fe, Mn, Mg) are observed performing an EDS, whose results are shown in Table 20.

Table 20 - EDS analysis of AA2024-T3 after Smut Go NC alkaline pickling.

Name	**wt.% O**	**wt.% Mg**	**wt.% Al**	**wt.% Si**	**wt.% Mn**	**wt.% Cu**
Spectrum 1		1.361	93.295			5.344
Spectrum 2	2.207	1.363	89.947		1.252	5.231
Spectrum 3	1.903	1.383	90.284		0.72	5.709
Spectrum 4		1.345	93.267			5.387
Spectrum 5	5.296	1.34	86.147	1.481		5.736
Spectrum 6	4.658	1.241	87.121	1.584		5.396
Spectrum 7		1.519	92.656			5.824

Deoxalume 2310 pickling

The different magnifications of specimen surface after Deoxalume 2310 acid pickling treatment are shown in Figure 77 and Figure 78.

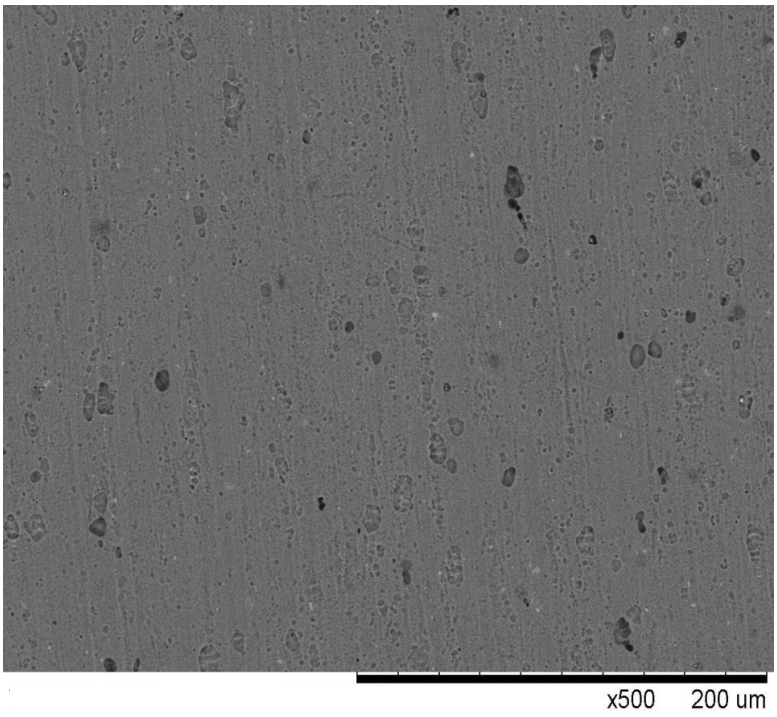

Figure 77 - Scanning electron micrographs of the surface of AA-2024-T3 after Deoxalume 2310 acid pickling, 500x.

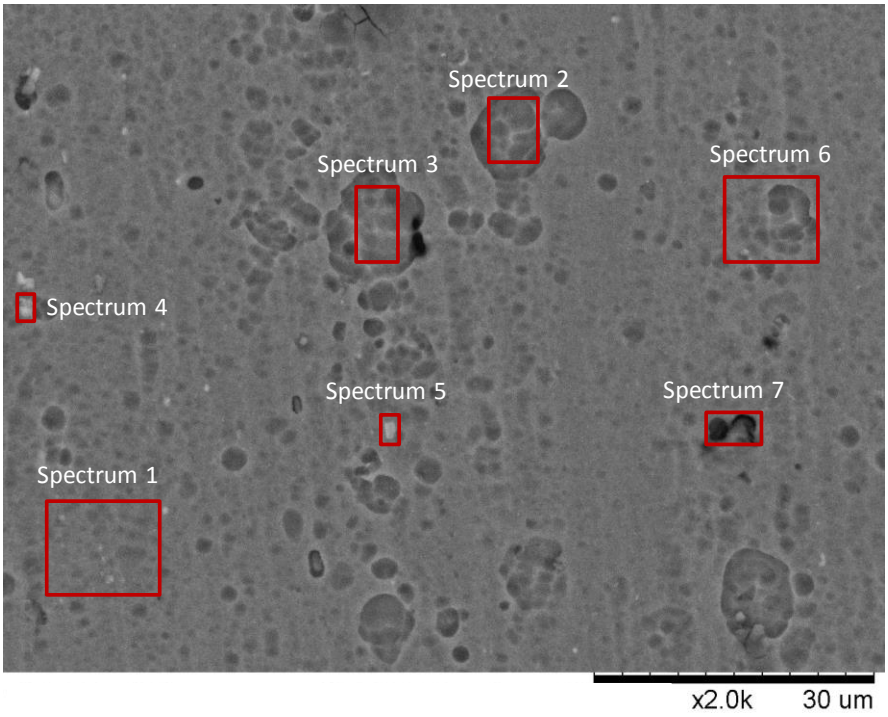

Figure 78 - Scanning electron micrographs of the surface of AA-2024-T3 after Deoxalume 2310 acid pickling, 2000x.

Table 21 - EDS analysis of AA2024-T3 after Deoxalume 2310 acid pickling.

Name	wt.% O	wt.% Mg	wt.% Al	wt.% Si	wt.% Mn	wt.% Cu
Spectrum 1	3.121	1.279	89.761			5.839
Spectrum 2	3.84	1.332	90.221			4.607
Spectrum 3	2.879	1.264	91.472			4.386
Spectrum 4	4.881	1.276	87.842	0.8		5.202
Spectrum 5	6.162	1.285	85.514	1.193		5.846
Spectrum 6	3.201	1.426	89.381		0.695	5.296
Spectrum 7	11.471	1.495	80.783			6.251

The surface is homogeneous without precipitates, both at low magnifications (Figure 77 – 500x) and at high magnifications (Figure 78 – 2000x). The EDS results, shown in Table 21, reveal

the element of the typical aluminium alloy composition (Cu, Fe, Mn, Mg) and a minimal presence of N contented in the pickling solution.

Oakite LNC pickling

The different magnifications of specimen surface after Oakite LNC acid pickling treatment are shown in Figure 79 and Figure 80.

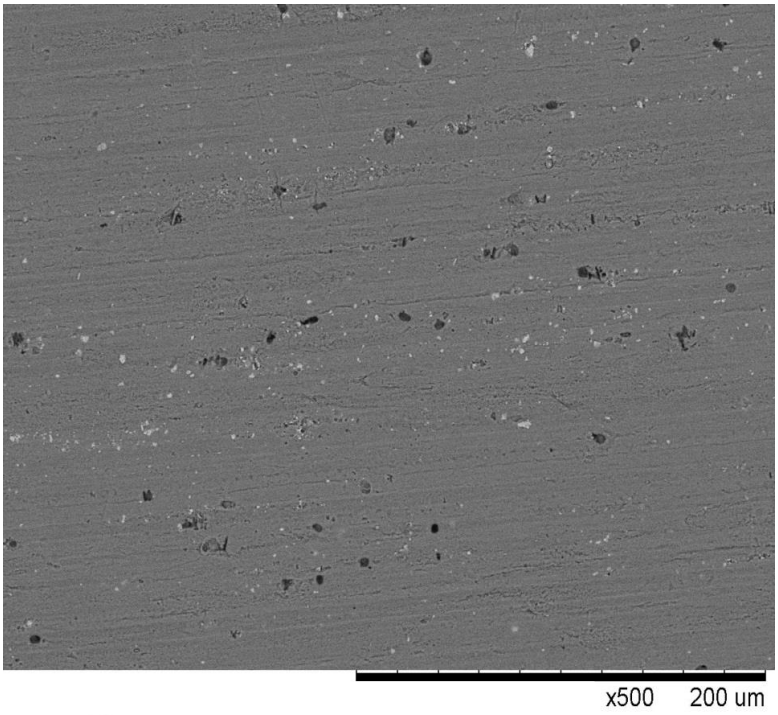

Figure 79 - Scanning electron micrographs of the surface of AA-2024-T3 after Oakite LNC acid pickling, 500x.

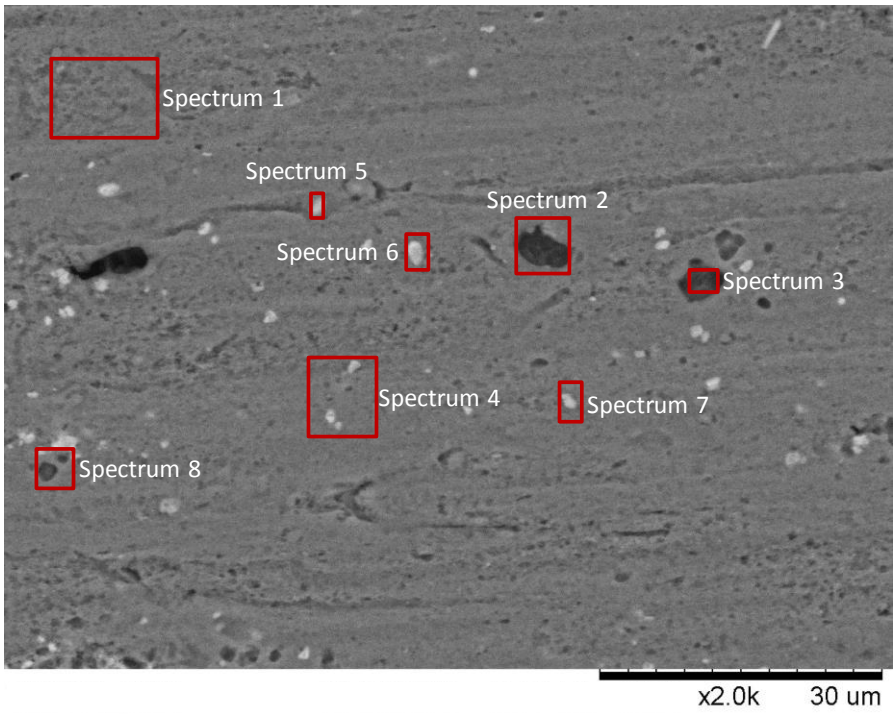

Figure 80 - Scanning electron micrographs of the surface of AA-2024-T3 after Oakite LNC acid pickling, 2000x.

Table 22 - EDS analysis of AA2024-T3 after Oakite LNC acid pickling.

Name	wt.% O	wt.% Mg	wt.% Al	wt.% Si	wt.% Mn	wt.% Fe	wt.% Cu
Spectrum 1	2.066	1.388	90.952				5.594
Spectrum 2	1.515	1.441	90.404				6.64
Spectrum 3	1.797	2.288	91.388				4.527
Spectrum 4	1.72	1.559	91.437				5.285
Spectrum 5	4.298	1.333	77.176	0.623			16.57
Spectrum 6	4.408	1.513	80.161	1.03	1.463	0.956	10.468
Spectrum 7	4.06	1.405	88.145	0.902			5.487
Spectrum 8	2.096	1.426	82.92		1.542	1.646	10.37

The presence of precipitates on the alloy surface is observed. The elements of the typical alloy composition (Cu, Fe, Mn, Mg) and Si and Cu islands, are observed by performing an EDS, whose results are shown in Table 22.

The samples surface, analysed by SEM with EDS probe, reveal a distribution of elements contained in the pickling solution and the presence of precipitates are present.

7.2.2.2 Potentiodynamic polarization results

Figure 81 shows the electrochemical behaviour of the specimens after pickling treatment reported in Table 2. Deoxidizer 6-16 pickling, containing hexavalent chromium and used for the classical Alodine cycle, is considered as benchmark.

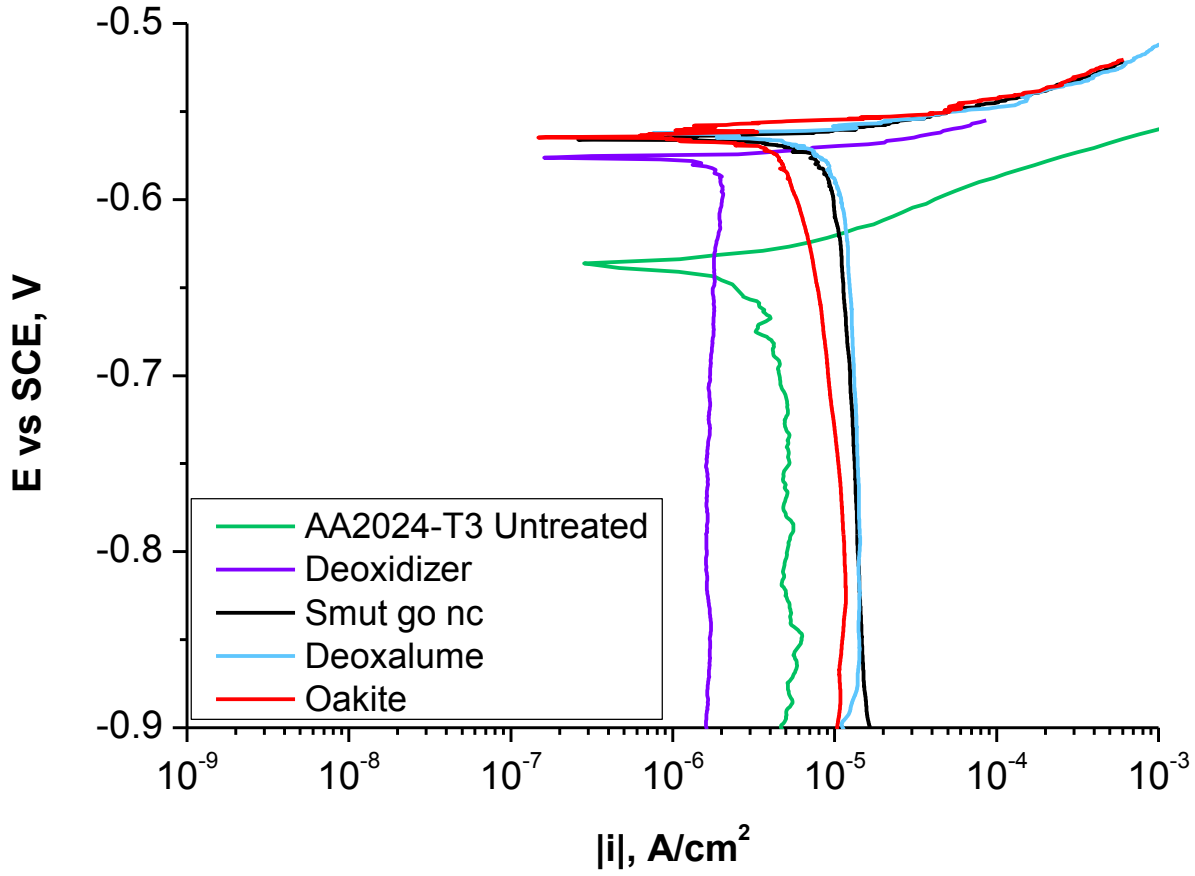

Figure 81 – Potentiodynamic polarization responses of the aluminium alloy after various pickling treatments.

In order to evaluate the electrochemical behaviour of different samples, the following parameters must be considered: the free corrosion potential (E_{corr}), the trend of cathodic and anodic currents. The curve of the sampled treated with Deoxidizer (purple curve) has a value of E_{corr} of -0.591V, cathode current is low, in order of 10^{-6} A/cm^2 and the trend of the anode is typical of localized or pitting corrosion. Following alkaline pickling, Aluminetch and Smut Go NC (black curve), the cathodic curve moves to slightly higher current values than that Deoxidizer 6-16 pickling, while E_{corr} potential and anodic curve assume lower values than those of the benchmark, highlighting the loss of nobility of the surface. Deoxalume 2310 acid pickling (blue curve) shows a lower E_{corr} than Deoxidizer 6-16 pickling and cathode currents values significantly higher than those of benchmark pickling. Following the Oakite LNC acid pickling (red curve) is reported. The curve of cathodic process moves to slight higher current values than the sampled pickled with deoxidizer and the potential E_{corr} and the anode curve are significantly lower than those with chrome benchmark.

7.2.2.3 EIS results

The corrosion behaviour of the pickled sample with Deoxidizer 6-16, in which hexavalent chromium is present, constitutes the benchmark of this comparison. In particular, Figure 82 shows the trend of the impedance modulus while Figure 83 shows the corresponding phase angle.

.

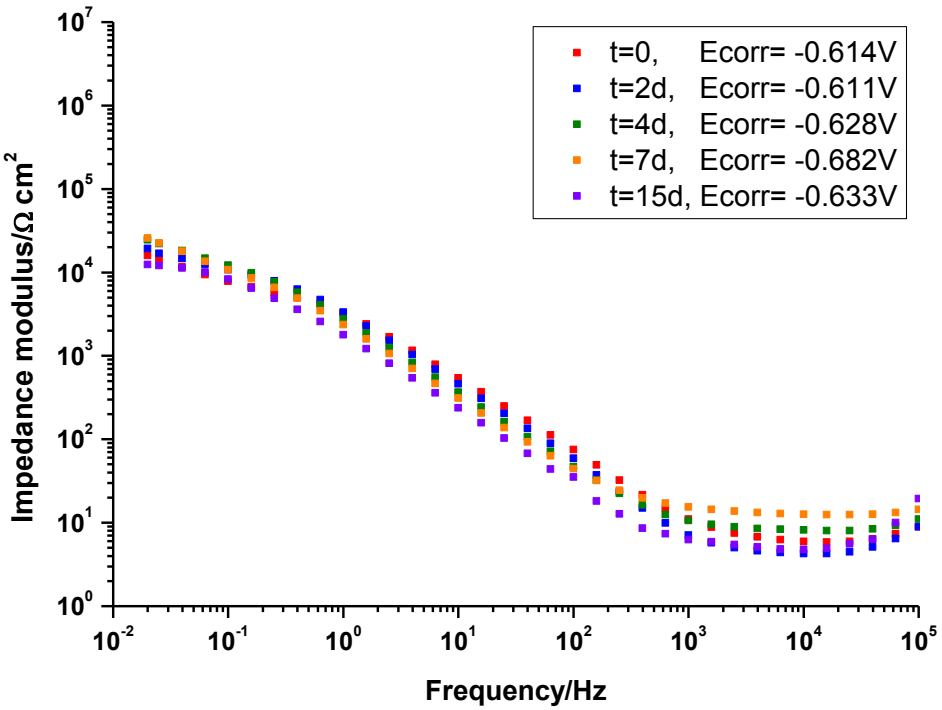

Figure 82 - Impedance modulus of alloy after Deoxidizer 6-16 acid pickling obtained during 15days of exposure in 3.5% NaCl.

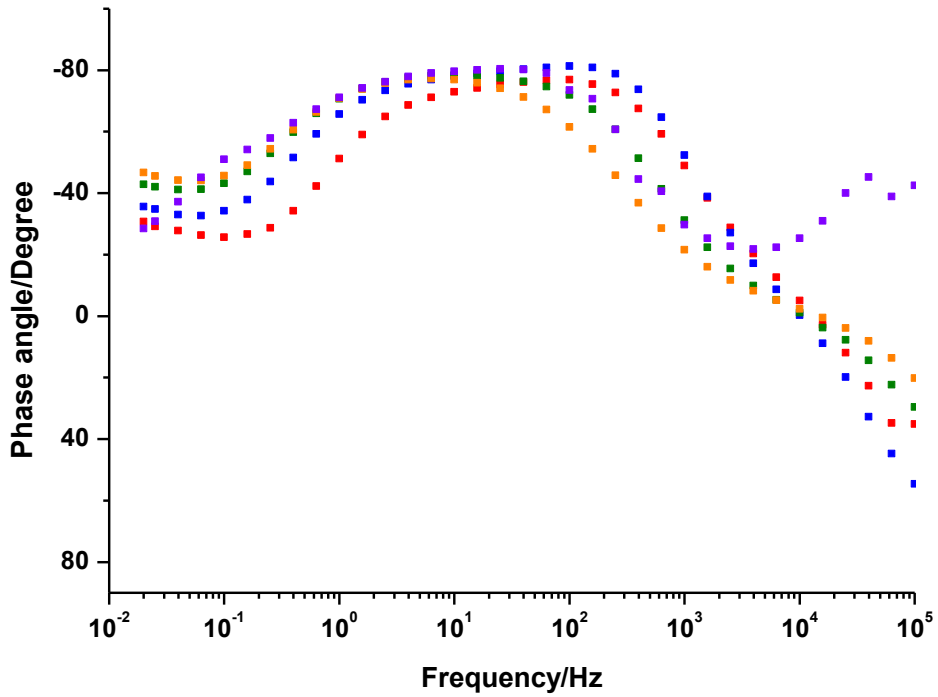

Figure 83 – Phase angle of alloy after Deoxidizer 6-16 acid pickling obtained during 15days of exposure in 3.5% NaCl.

The behaviour of low-frequency impedance modulus is very similar during different exposure day. This behaviour is attributable to the presence of hexavalent chromium which form a first layer of conversion coating in order to protect aluminium from corrosion. Capacitance decreases during test and the values of impedance modulus is 10^4Ohm cm^2.

Figure 84 reveals the trend of impedance modulus of AA2024-T3 after Smut Go NC alkaline pickling. The behaviour of corresponding phase angle is reported in Figure 85.

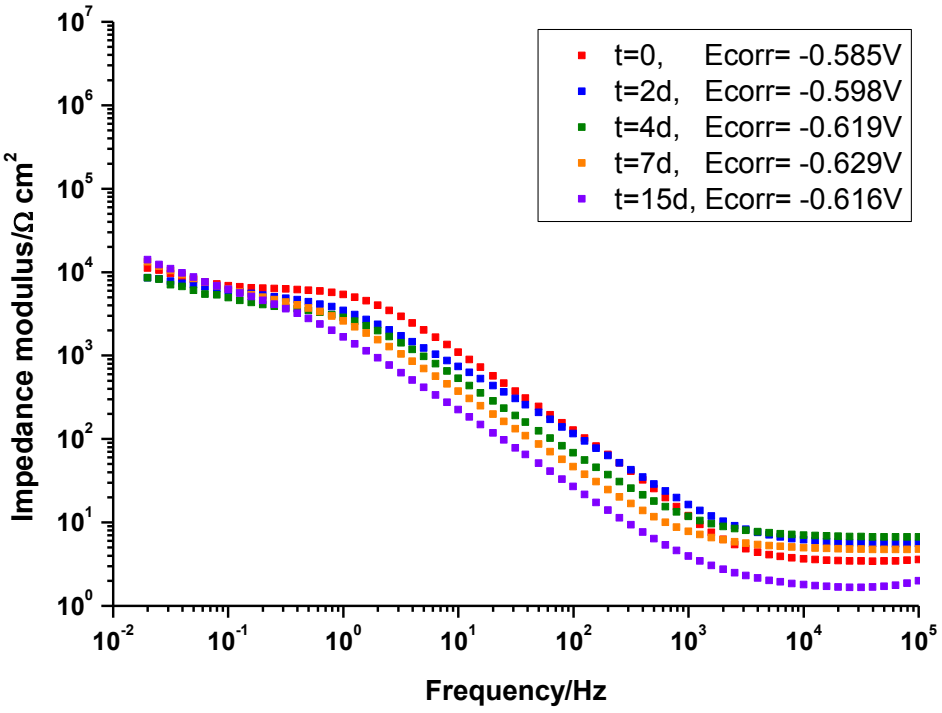

Figure 84 – Impedance modulus of alloy after Smut Go NC alkaline pickling obtained during 15days of exposure in 3.5% NaCl.

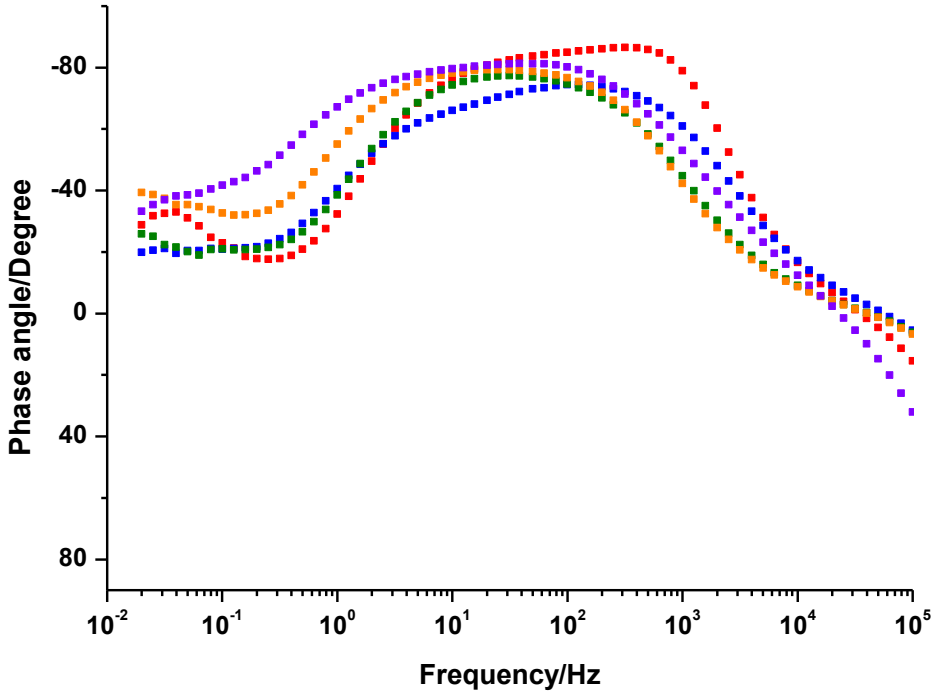

Figure 85 – Phase angle of alloy after Smut Go NC alkaline pickling obtained during 15days of exposure in 3.5% NaCl.

The capacitance is stable in medium frequency range. At low-frequency the impedance modulus is not stable. After two days of immersion in NaCl solution, the value of impedance modulus is 10^6Ohm cm^2 but the trend decreases with time.

The trend of impedance modulus of specimen AA2024 T3 after Deoxalume 2310 acid pickling is indicated in Figure 86, while the phase angle is reported in Figure 87.

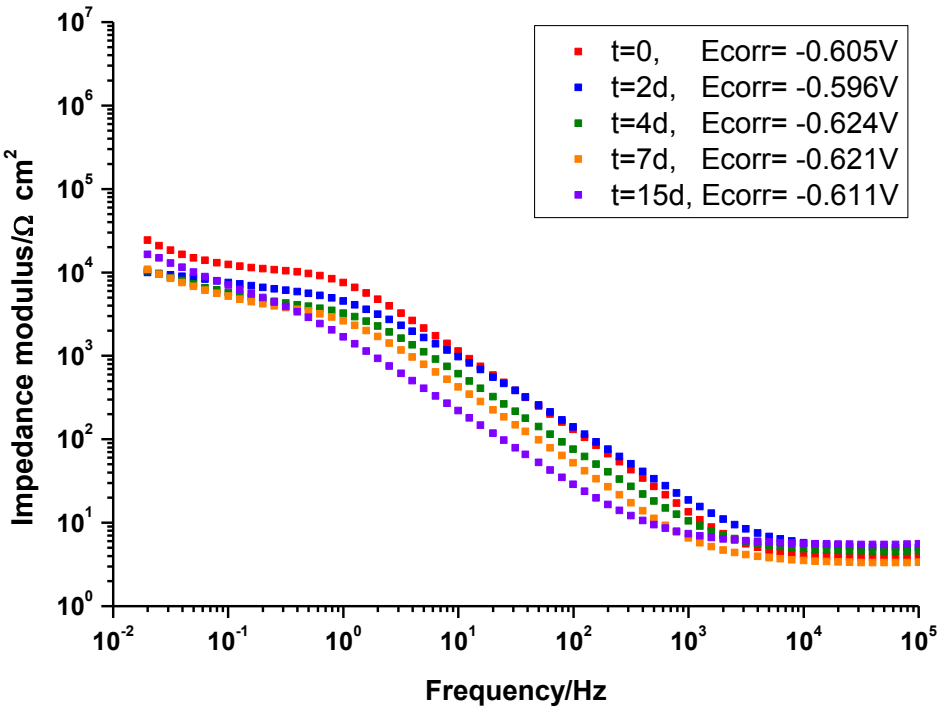

Figure 86 – Impedance modulus of alloy after Deoxalume 2310 acid pickling obtained during 15days of exposure in 3.5% NaCl.

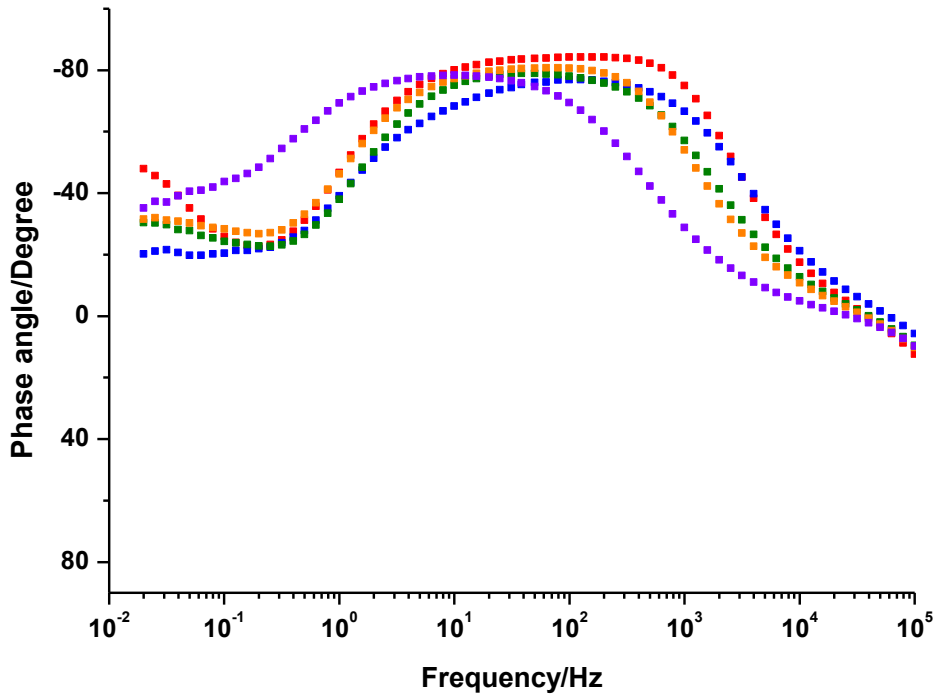

Figure 87 – Phase angle of alloy after Deoxalume 2310 acid pickling obtained during 15days of exposure in 3.5% NaCl.

The sample has a degreasing capacitance over time as demonstrated at medium frequencies. Contrary to the behaviour of the alkaline solution and similarly to benchmark sample, the low-frequency impedance modulus has stable value of 10^4Ohm cm^2.

In Figure 88 is reported the trend of sample pickled with Oakite LNC acid solution. The trend of corresponding phase angle is reported in Figure 89.

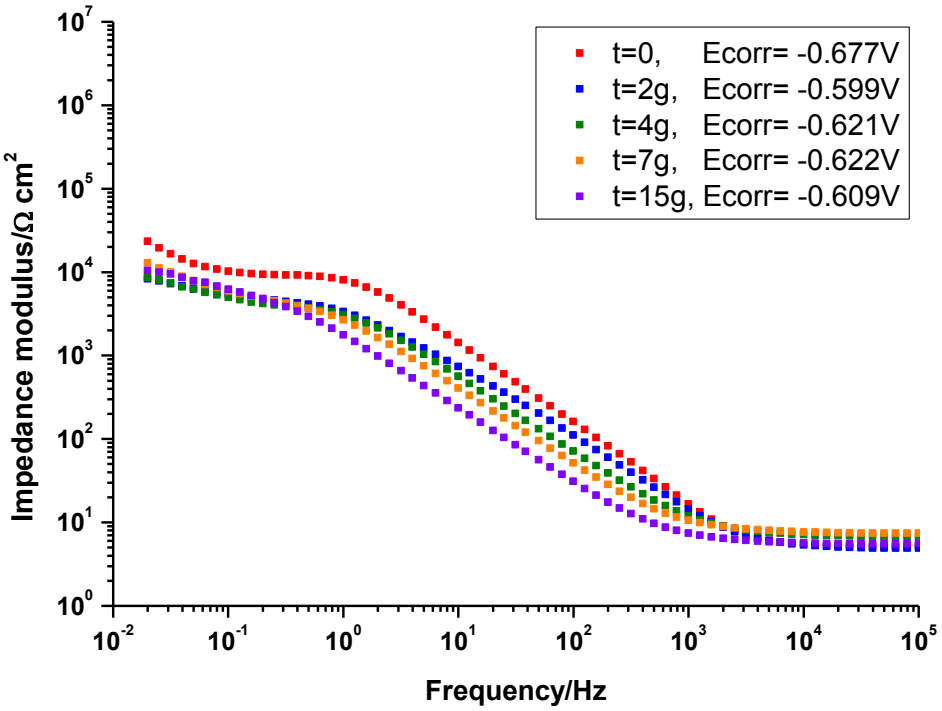

Figure 88 – Impedance modulus of alloy after Oakite LNC acid pickling obtained during 15days of exposure in 3.5% NaCl.

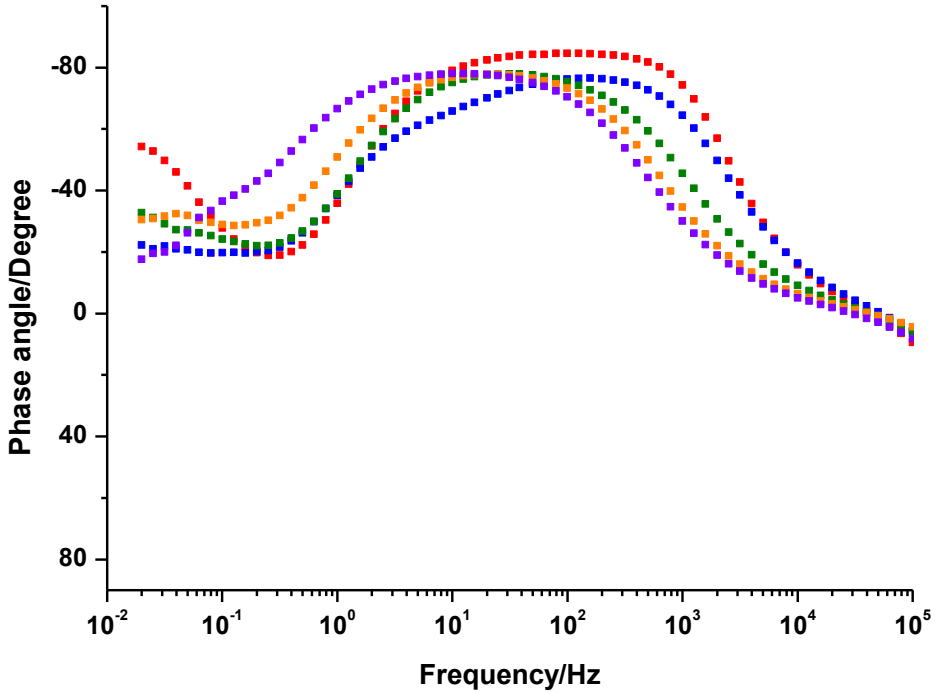

Figure 89 – Phase angle of alloy after Oakite LNC acid pickling obtained during 15days of exposure in 3.5% NaCl.

The capacitance, at medium frequencies, decreases during exposure time to the aggressive solution. The impedance modulus, after the first days of immersion, decreases slightly assuming values of the order of 10^4Ohm cm^2.

On the basis of the observed results ad in terms of ranking of the various pickling it is possible to conclude that:

DEOXIDIZER 6-16 > DEOXALUME 2310 = OAKITE LNC > SMUT GO NC

7.2.3 Cr-free picklings with Alodine conversion coating

7.2.3.1 SEM analysis with EDS probe

In order to better understand the role of hexavalent chromium within the steps of the industrial cycle, the specimens were analysed after Cr-free pickling and subsequent application of Alodine 1200s.

Here again SEM analysis with EDS probe was carried out on the material provided by Leonardo Company, which does not undergone any tests to verify its initial state and surface composition.

Deoxidizer 6-16 pickling with Alodine conversion coating

Figures 90 and 91 show different magnifications of the specimen surface after Deoxidizer 6-16 pickling treatment with Alodine 1200s conversion coating.

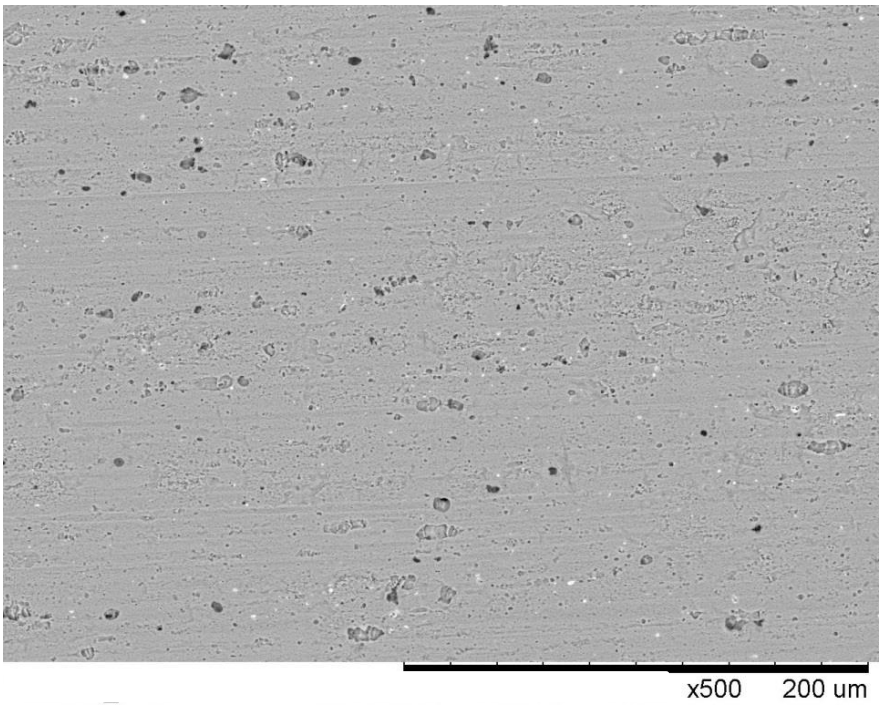

Figure 90 - Scanning electron micrographs of the surface of AA-2024-T3 after Deoxidizer 6-16 pickling treatment with Alodine 1200s conversion coating, 500x.

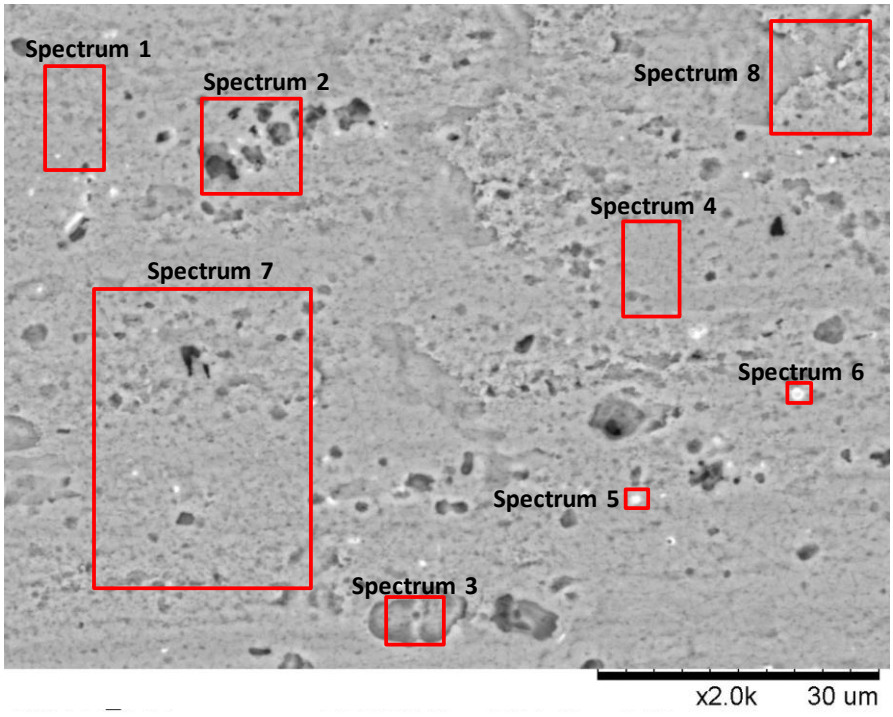

Figure 91 - Scanning electron micrographs of the surface of AA-2024-T3 after Deoxidizer 6-16 pickling treatment with Alodine 1200s conversion coating, 2000x.

Table 23 - EDS analysis of AA2024-T3 after Deoxidizer 6-16 pickling treatment with Alodine 1200s conversion coating.

Name	wt.% O	wt.% Mg	wt.% Al	wt.% Cr	wt.% Mn	wt.% Fe	wt.% Cu
Spectrum 1	17.392	1.019	72.081	4.366	0.458	0.350	4.335
Spectrum 2	18.447	1.118	69.289	5.719	0.708	0.341	4.377
Spectrum 3	12.673	1.000	72.822	8.804	0.945	0.699	3.055
Spectrum 4	17.372	1.094	72.501	4.156	0.497		4.381
Spectrum 5	17.099	1.003	66.682	4.049	0.987	1.486	8.694
Spectrum 6	13.998	0.875	60.913	2.933	0.376		20.906
Spectrum 7	17.488	1.142	72.122	4.302	0.461		4.485
Spectrum 8	18.969	1.073	70.160	4.956	0.459		4.382
Spectrum 9	21.431	0.891	64.855	7.402	0.386	0.482	4.553

The surface observed reveals the presence of precipitates. The elements of the typical alloy composition (Cu, Fe, Mn, Mg) are observed by performing an EDS, whose results are shown in Table 23. In addition, EDS analysis exhibit some Cu island and element such as Cr (which compound is present in the Alodine 1200s solution).

Smut Go NC pickling with Alodine conversion coating

Figures 92 and 93 show different magnifications of the specimen surface after Smut Go NC alkaline pickling treatment followed by Alodine 1200s conversion coating.

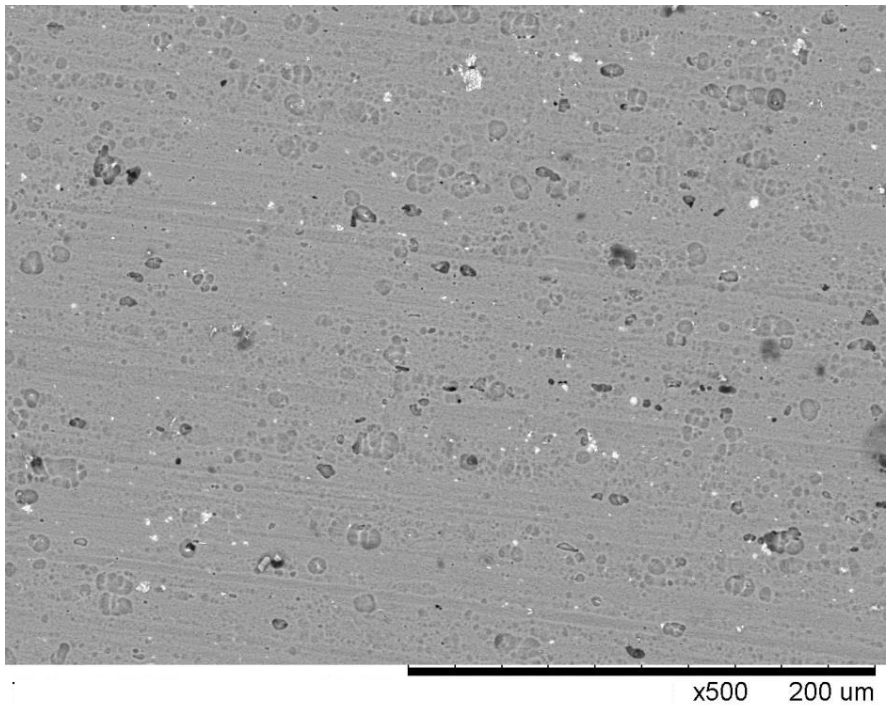

Figure 92 - Scanning electron micrographs of the surface of AA-2024-T3 after Smut Go NC pickling treatment with Alodine 1200s conversion coating, 500x.

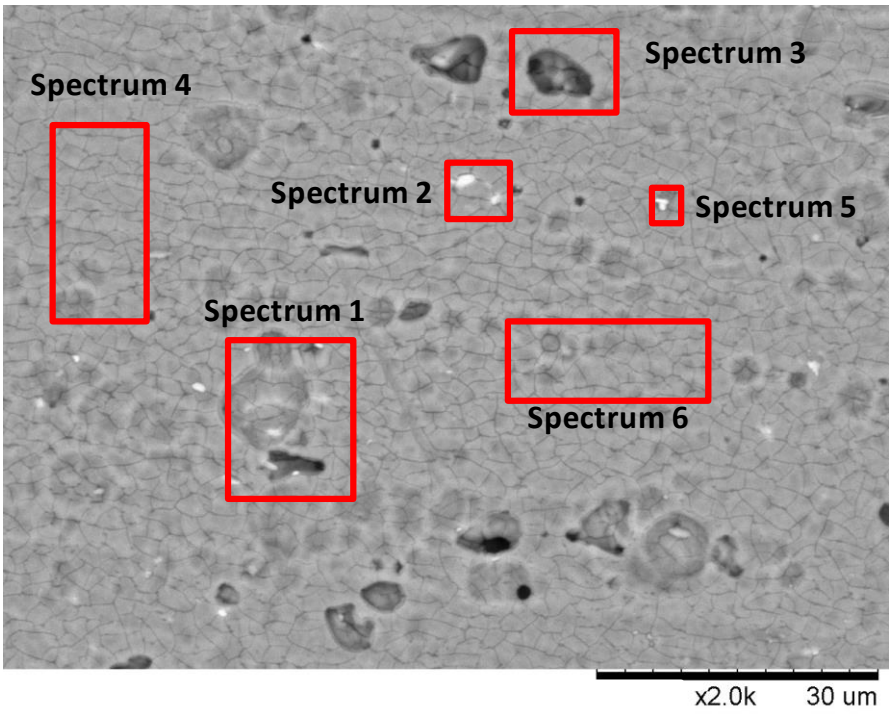

Figure 93 - Scanning electron micrographs of the surface of AA-2024-T3 after Smut Go NC pickling treatment with Alodine 1200s conversion coating, 2000x.

Table 24 - EDS analysis of AA2024-T3 after Smut Go NC pickling treatment with Alodine 1200s conversion coating.

Name	wt.% O	wt.% Mg	wt.% Al	wt.% Cr	wt.% Mn	wt.% Fe	wt.% Cu
Spectrum 1	23.692	1.002	61.81	7.795	0.718	0.929	4.054
Spectrum 2	21.915	0.958	63.238	6.709	1.098	1.065	5.017
Spectrum 3	23.979	1.022	61.938	8.31		0.945	3.805
Spectrum 4	23.696	0.922	63.573	7.038	0.482	0.849	3.44
Spectrum 5	19.468	1.121	69.672	4.706	0.639	0.413	3.981
Spectrum 6	23.535	0.988	63.78	6.869	0.507	0.758	3.563

The surface reveals, performing an EDS, the presence of elements of the typical alloy composition (Cu, Fe, Mn, Mg). EDS analysis, whose results are shown in Table 24, reveal an uniform distribution of Cu and the presence of Cr contained in the Alodine solution.

Deoxalume 2310 pickling with Alodine conversion coating

The different magnifications of specimen surface after Deoxalume 2310 acid pickling treatment with Alodine 1200s conversion coating are shown in Figures 94 and 95.

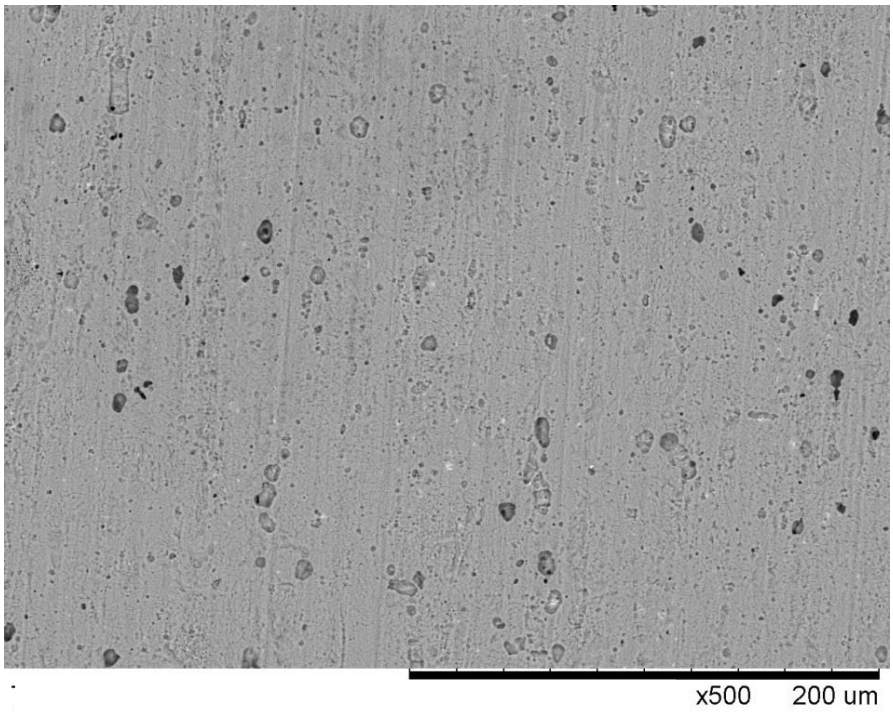

Figure 94 - Scanning electron micrographs of the surface of AA-2024-T3 after Deoxalume 2310 pickling treatment with Alodine 1200s conversion coating, 500x.

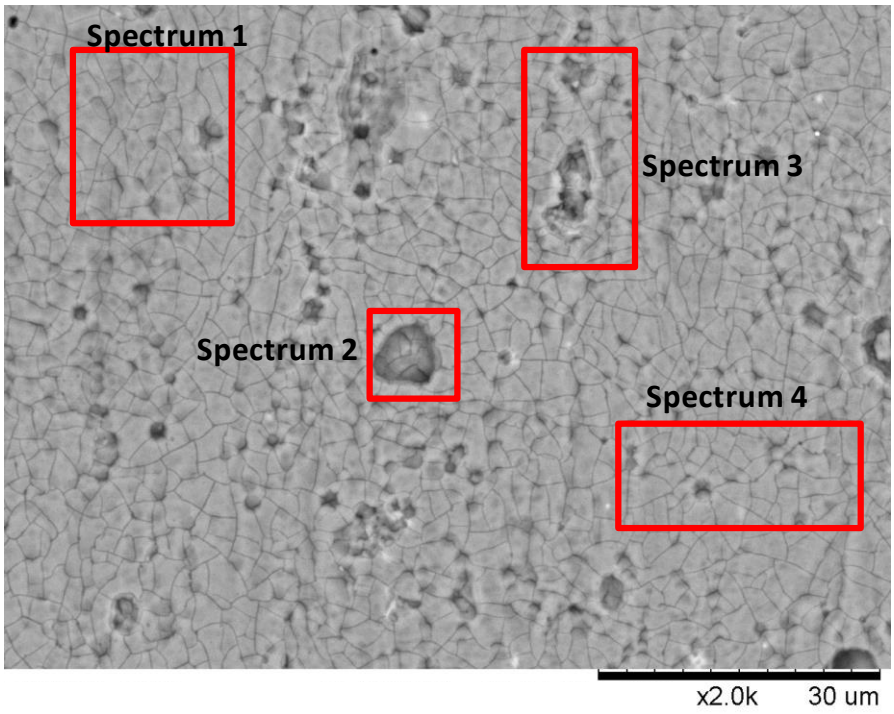

Figure 95 - Scanning electron micrographs of the surface of AA-2024-T3 after Deoxalume 2310 pickling treatment with Alodine 1200s conversion coating, 2000x.

Table 25 - EDS analysis of AA2024-T3 after Deoxalume 2310 pickling treatment with Alodine 1200s conversion coating.

Name	wt.% O	wt.% Mg	wt.% Al	wt.% Cr	wt.% Mn	wt.% Fe	wt.% Cu
Spectrum 1	24.611	1.018	61.981	7.87	0.508	0.864	3.148
Spectrum 2	23.928	0.997	61.257	9.031	0.468	1	3.319
Spectrum 3	24.306	0.974	60.919	8.342	0.558	1.149	3.752
Spectrum 4	24.16	0.944	62.38	7.975	0.565	0.841	3.135

The surface reveals an homogeneous surface. The EDS analysis, reported in Table 25, show the element of the typical aluminium alloy composition (Cu, Fe, Mn, Mg) and the presence of Cr, contained in the conversion coating solution.

Oakite LNC pickling with Alodine conversion coating

Figures 96 and 97 show different magnifications of the specimen surface after Oakite LNC acid pickling treatment with Alodine 1200s conversion coating.

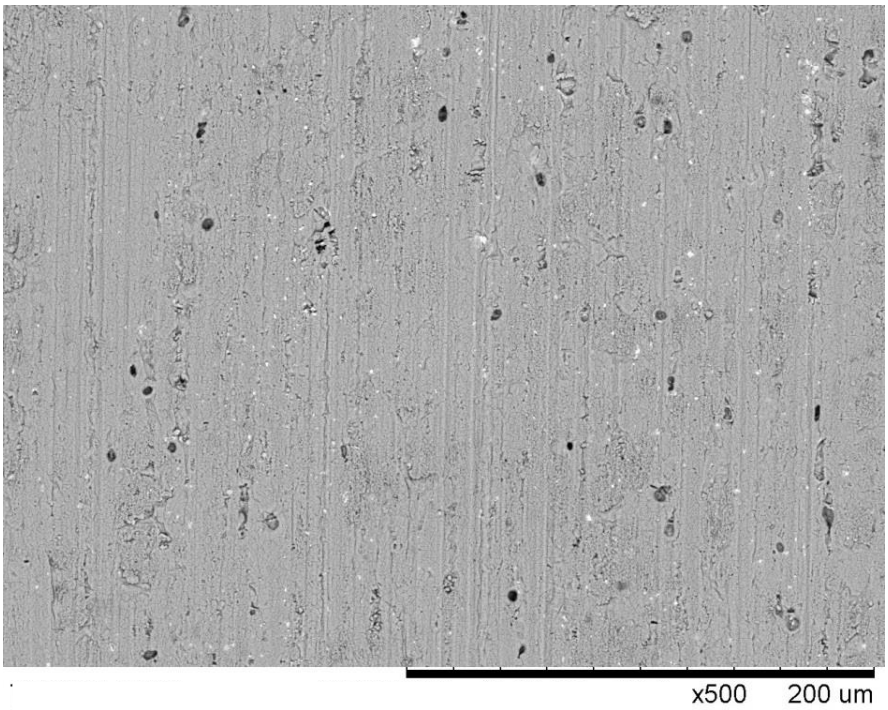

Figure 96 - Scanning electron micrographs of the surface of AA-2024-T3 after Oakite LNC pickling treatment with Alodine 1200s conversion coating, 500x.

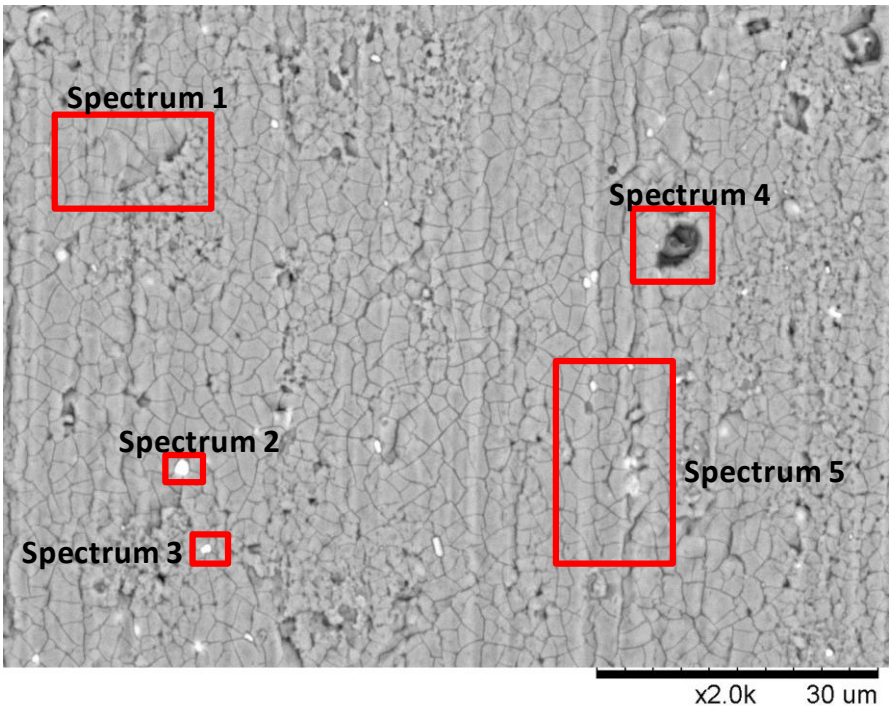

Figure 97 - Scanning electron micrographs of the surface of AA-2024-T3 after Oakite LNC pickling treatment with Alodine 1200s conversion coating, 2000x.

Table 26 - EDS analysis of AA2024-T3 after Oakite LNC pickling treatment with Alodine 1200s conversion coating.

Name	wt.% O	wt.% Mg	wt.% Al	wt.% Cr	wt.% Mn	wt.% Fe	wt.% Cu
Spectrum 1	23.669	1.031	63.582	7.104	0.441	0.729	3.444
Spectrum 2	13.471	0.728	59.899	3.072	1.758	5.02	16.051
Spectrum 3	23.041	0.888	54.809	4.586	0.43	9.484	6.76
Spectrum 4	24.148	1.008	61.075	8.229	0.4	0.942	4.198
Spectrum 5	23.908	1.044	62.739	7.353		0.946	4.01

The presence of precipitates on the alloy surface is observed. The elements of the typical alloy composition (Cu, Fe, Mn, Mg) are observed by performing an EDS, whose results are shown in Table 26. Furthermore the analysis reveal the presence of some Cu and Fe islands and element such as Cr (which compound is present in the Alodine 1200s solution).

The samples surface, analysed by SEM with EDS probe, reveal a distribution of hexavalent chromium contained in the Alodine 1200s solution and the presence of some precipitates, such as Cu and Fe, are present.

7.2.3.2 Potentiodynamic polarization results

Potentiodynamic polarization measurements were carried out on samples after various picklings and Alodine 1200s chemical conversion coating. Figure 98 shows the curves of all the analysed samples. The curve with Deoxidizer 6-16 and subsequent Alodine 1200s, in which hexavalent chromium is present in both steps, is the benchmark of this comparison.

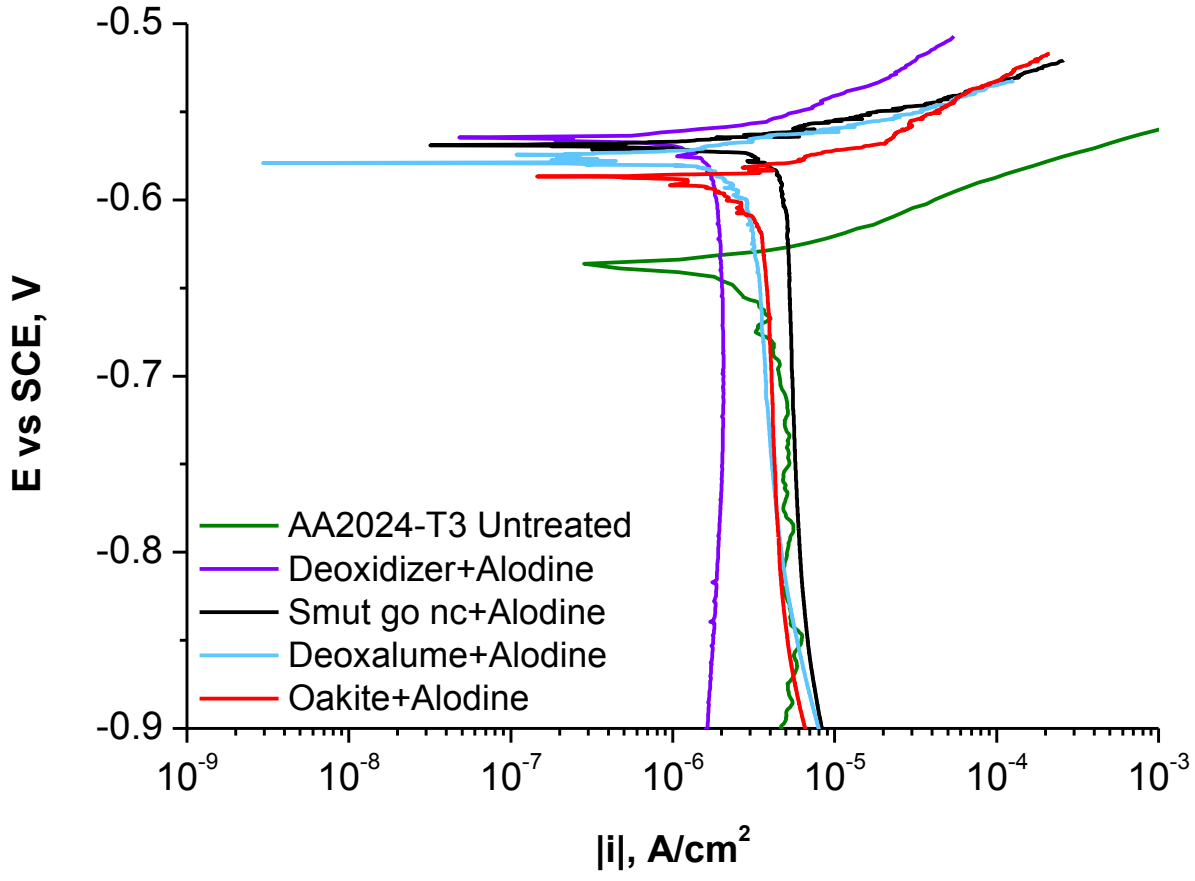

Figure 98 - Potentiodynamic polarization responses of the aluminium alloy after various pickling treatments followed by Alodine1200s conversion coating.

A clear improvement of polarization curve is noted compared to the curves obtained with the only picklings. In fact, there is a noticeable increase in the corrosion potential. Considering the cathode currents, no specimen approaches the performance obtained in the classical cycle Deoxidizer 6-16 with Alodine 1200s. Instead, observing the anode currents, it is noted that all the treated samples have very similar behaviour to that of the classical cycle.

7.2.3.3 EIS results

The corrosion behaviour of the specimen after classical treatment of Alodine 1200s is shown in Figure 99 while Figure 100 shows the corresponding phase angle.

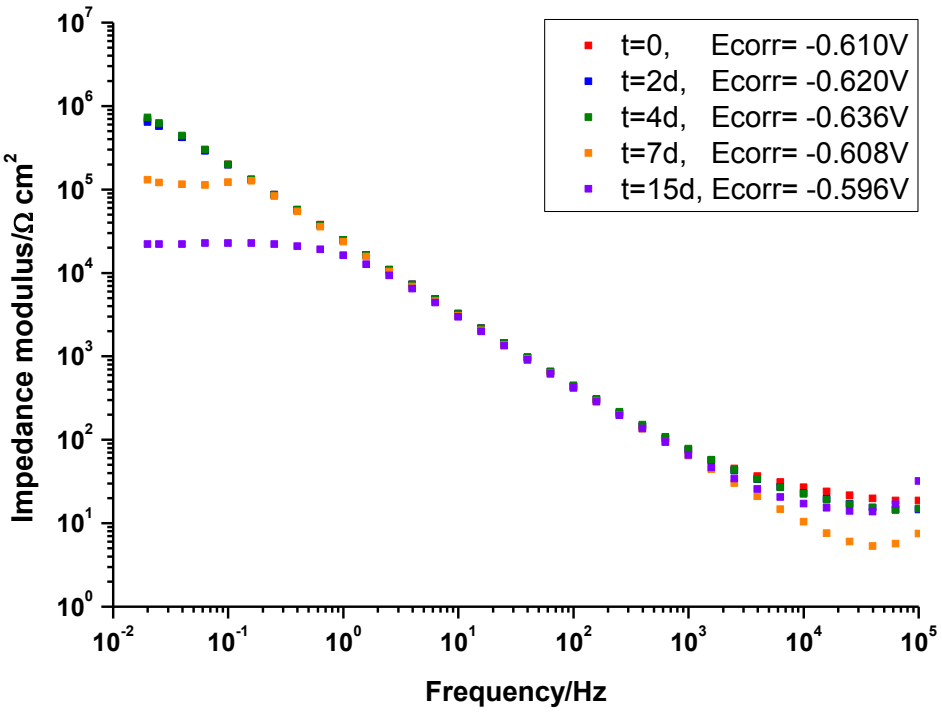

Figure 99 – Impedance modulus of alloy after classical treatment of Alodine 1200s obtained during 15days of exposure in 3.5% NaCl.

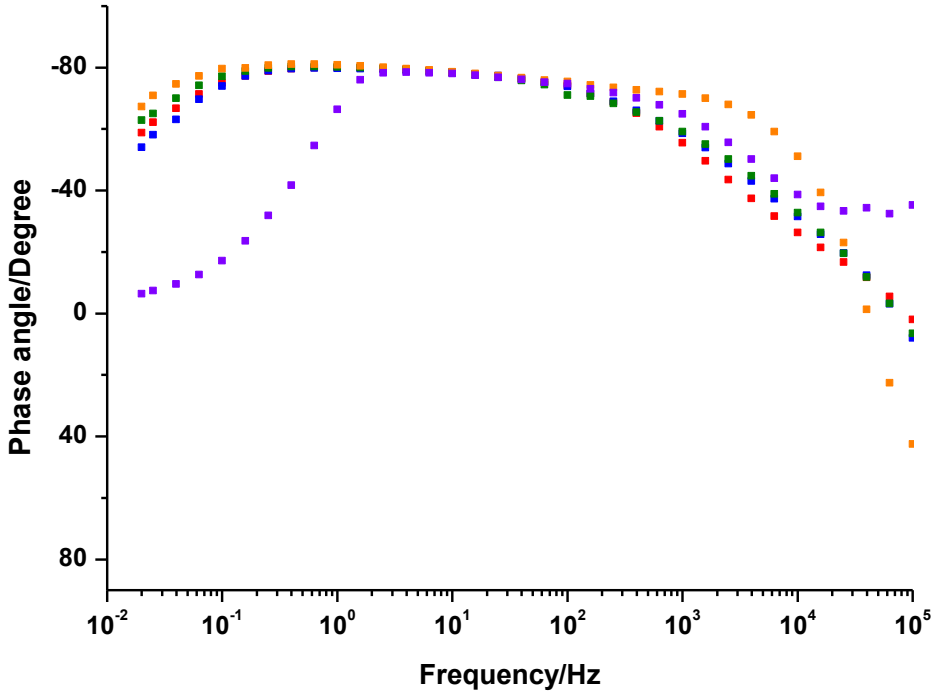

Figure 100 – Phase angle of alloy after classical treatment of Alodine 1200s obtained during 15days of exposure in 3.5% NaCl.

Considering the low frequencies, high impedance modulus values can be observed up to 4 days of exposure. An ideal behaviour of the specimen is noticed because the curve assume a slope of -1. After 7 days of exposure, the impedance modulus behaviour decreases and it assumes a lower value of two order of magnitude after exposure equal to 15 days.

The corrosion behaviour of the specimen after Smut Go NC alkaline pickling and following chemical conversion in Alodine 1200s is shown in Figure 101 while Figure 102 shows the corresponding phase angle.

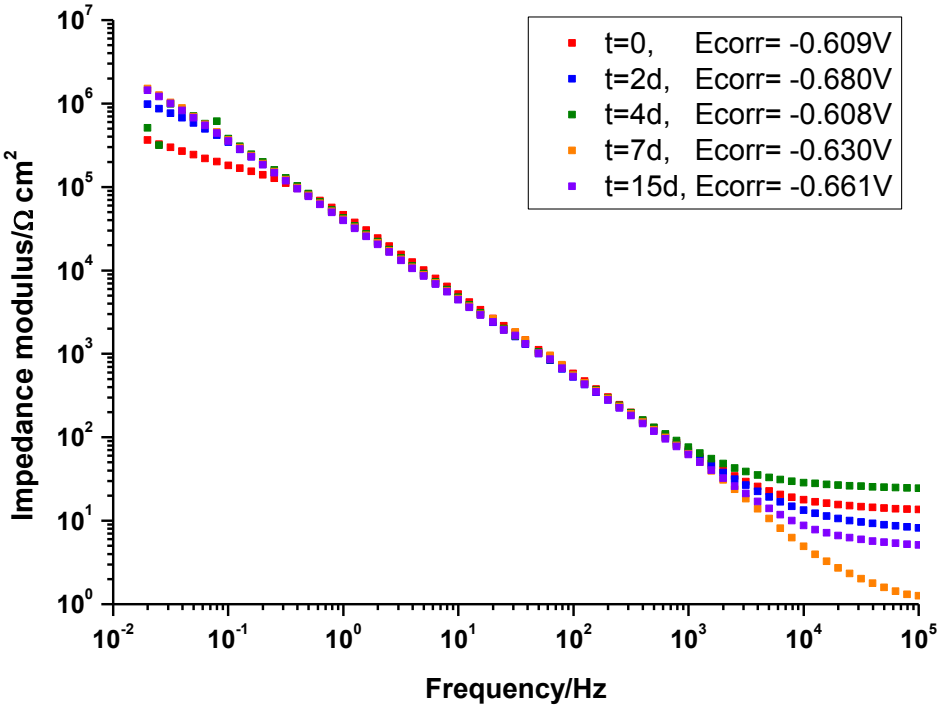

Figure 101 - Impedance modulus of alloy after Smut Go NC alkaline pickling followed by Alodine 1200s treatment obtained during 15days of exposure in 3.5% NaCl.

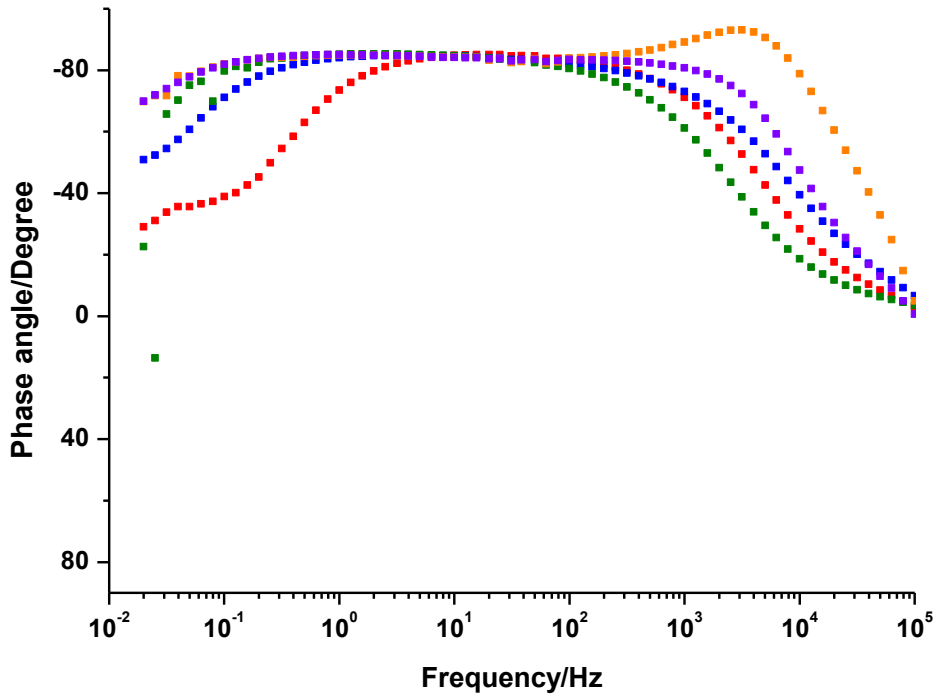

Figure 102 – Phase angle of alloy after Smut Go NC alkaline pickling followed by Alodine 1200s treatment obtained during 15days of exposure in 3.5% NaCl.

Considering the low-frequency values, a low impedance modulus can be observed at the beginning of immersion in the solution test; in fact the value of impedance modulus is lower than that it assumed in the following days. After 2 days of immersion, the low-frequency impedance modulus remains constant and the value is 10^6Ohm cm^2.

The trend of impedance modulus of specimen AA2024-T3 after Deoxalume 2310 acid pickling and following Alodine 1200s conversion coating is reported in Figure 103, while the phase angle is reported in Figure 104.

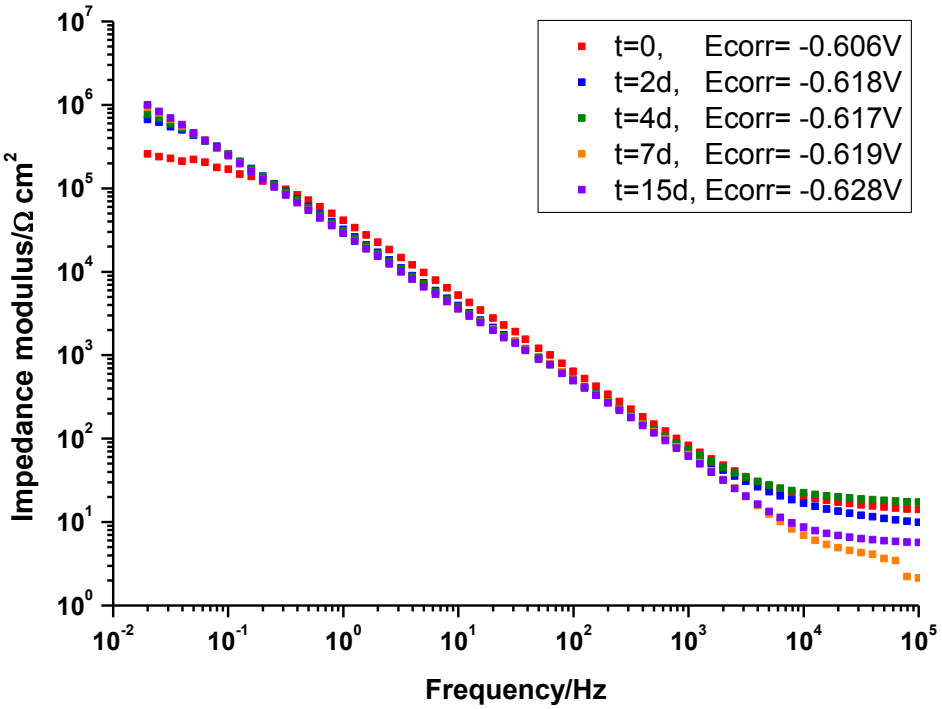

Figure 103 – Impedance modulus of alloy after Deoxalume 2310 acid pickling followed by Alodine 1200s treatment obtained during 15days of exposure in 3.5% NaCl.

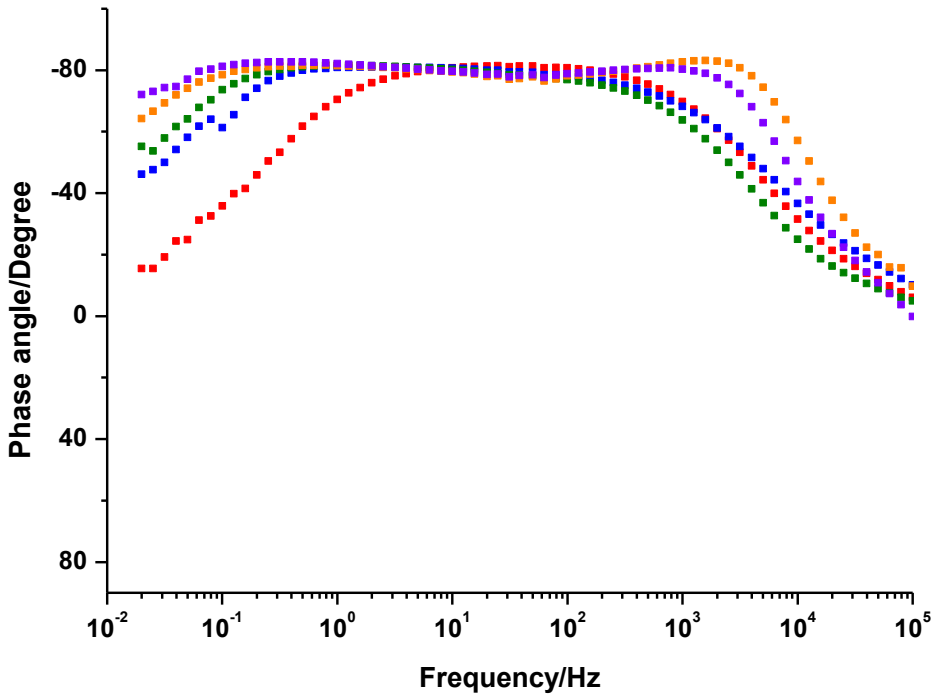

Figure 104 – Phase angle of alloy after Deoxalume 2310 acid pickling followed by Alodine 1200s treatment obtained during 15days of exposure in 3.5% NaCl.

The behaviour of low-frequency impedance modulus is similar to that found for alkaline pickling. Also in this case the impedance modulus remains constant after the second exposure day and the value magnitude is 10^6Ohm cm^2.

In Figure 105 is reported the trend of sample pickled with Oakite LNC acid solution with Alodine 1200s conversion treatment. The trend of corresponding phase angle is reported in Figure 106.

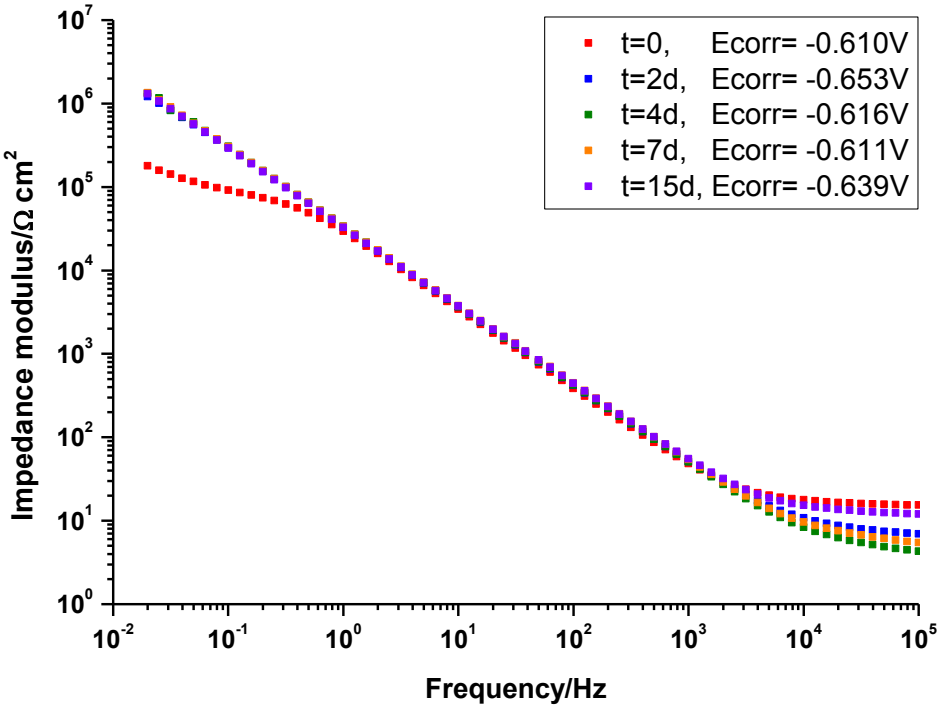

Figure 105 – Impedance modulus of alloy after Oakite LNC acid pickling followed by Alodine 1200s treatment obtained during 15days of exposure in 3.5% NaCl.

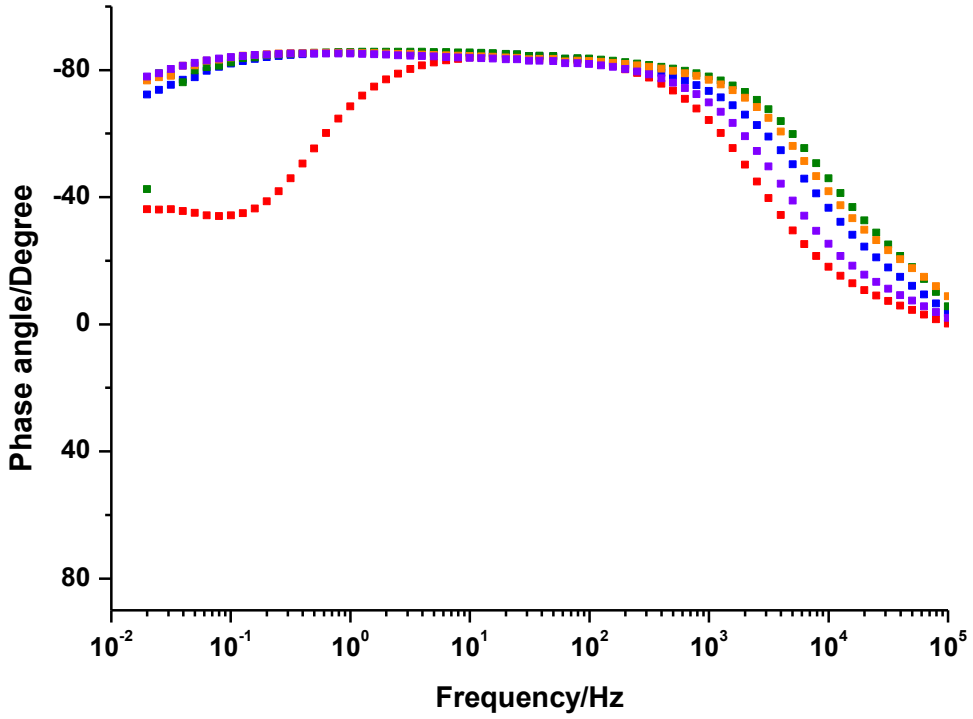

Figure 106 – Phase angle of alloy after Oakite LNC acid pickling followed by Alodine 1200s treatment obtained during 15days of exposure in 3.5% NaCl.

The behaviour of low-frequency impedance modulus is similar to the previous specimens while the capacitance is better than the previous ones. Even the phase angle is more stable than the previous samples.

Electrochemical impedance spectroscopy shows a marked improvement in corrosion resistance compared to the pickled samples and to the untreated alloy. The impedance modulus of all samples exhibit a stable trend during the 15 days of exposure in the aggressive solution, so it is better than the Deoxidizer 6-16. The order of magnitude of the impedance modulus is 10^6Ohm cm^2. On the basis of the observed results ad in terms of ranking of the various pickling and following conversion coating it is possible to conclude that:

DEOXIDIZER 6-16 with ALODINE >OAKITE LNC with ALODINE > DEOXALUME 2310 with ALODINE= SMUT GO NC with ALODINE.

7.2.4 Innovative cycle - Total Green

In order to create an innovative total green process, which involves the elimination of hexavalent chromium in the pickling process and the chemical conversion process, Cr-free picklings (previously discussed) followed by trivalent chromium conversion coating (SurTec 650) were analysed.

7.2.4.1 SEM analysis with EDS probe

SEM analysis with EDS probe was carried out on the material provided by Leonardo Company, which does not undergone any tests to verify its initial state and surface composition.

Smut Go NC pickling with SurTec conversion coating

Figures 107 and 108 show different magnifications of the specimen surface after Smut Go NC alkaline pickling treatment followed by SurTec 650 conversion coating.

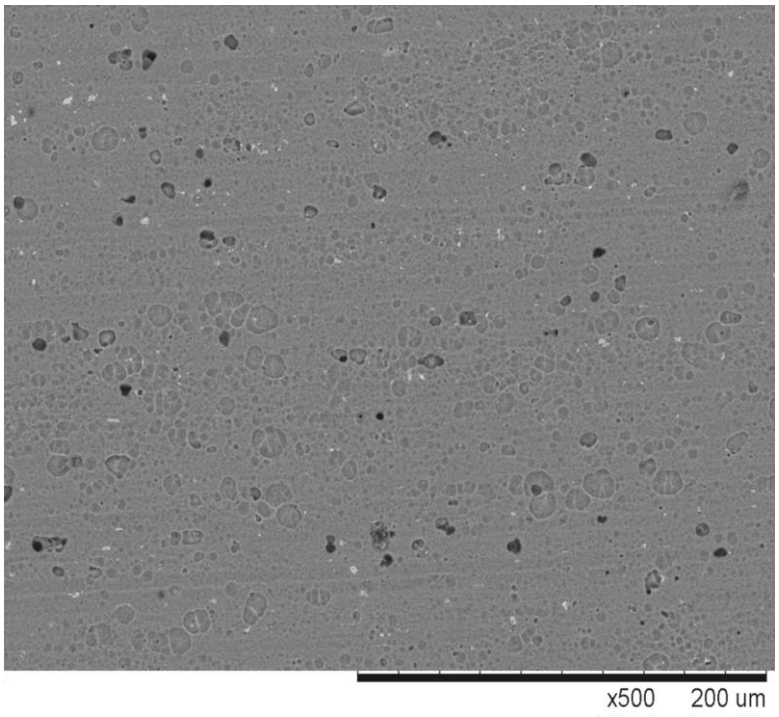

Figure 107 - Scanning electron micrographs of the surface of AA-2024-T3 after Smut Go NC alkaline pickling treatment followed by SurTec 650 conversion coating, 500x.

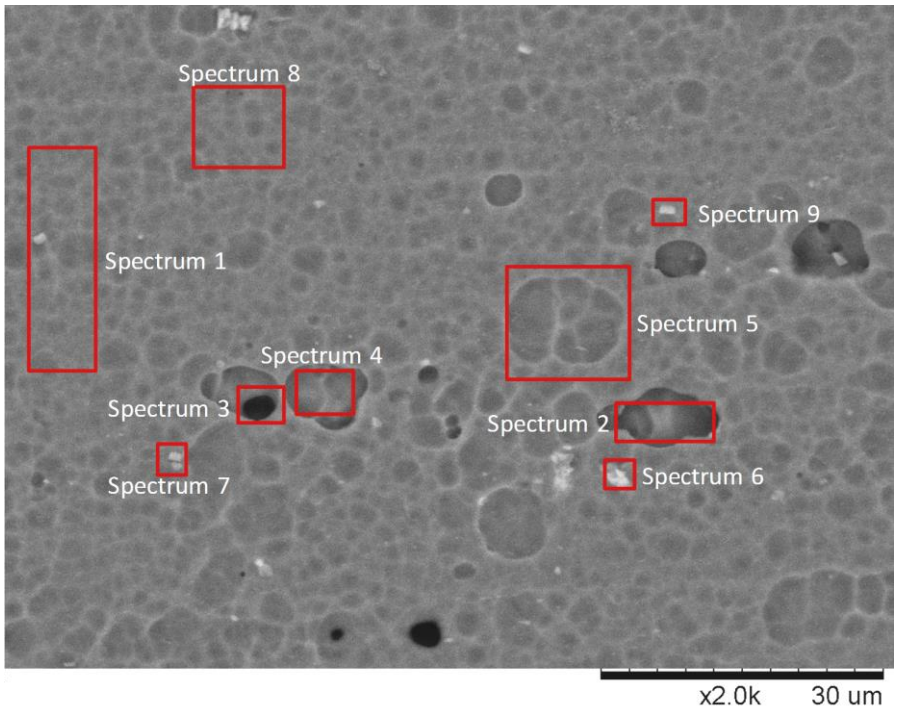

Figure 108 - Scanning electron micrographs of the surface of AA-2024-T3 after Smut Go NC alkaline pickling treatment followed by SurTec 650 conversion coating, 2000x.

Table 27 - EDS analysis of AA2024-T3 after Smut Go NC alkaline pickling treatment followed by SurTec 650 conversion coating.

Name	wt.% O	wt.% F	wt.% Mg	wt.% Al	wt.% Si	wt.% Mn	wt.% Cu	wt.% Zr
Spectrum 1	5.611	1.422	1.238	84.31		0.809	5.197	1.412
Spectrum 2	4.965		1.276	87.287			4.293	2.179
Spectrum 3	6.044		1.313	85.578			4.718	2.347
Spectrum 4	3.937	1.331	1.272	88.62			4.839	
Spectrum 5	5.936	1.238	1.394	84.788			5.019	1.625
Spectrum 6	5.691	1.482	1.392	83.399		0.861	5.34	1.834
Spectrum 7	8.454	1.706	1.132	80.487	1.229		5.369	1.622
Spectrum 8	5.837	1.185	1.315	85.206			4.753	1.704
Spectrum 9	6.354		1.04	76.434	1.001	1.293	12.294	1.584

The surface reveals an homogeneous surface. The EDS analysis, reported in Table 27, show the element of the typical aluminium alloy composition (Cu, Fe, Mn, Mg) and the presence of Si, F and Zr (contained in the conversion coating solution).

Deoxalume 2310 pickling with SurTec conversion coating

Figures 109 and 110 show different magnifications of the specimen surface after Deoxalume 2310 acid pickling treatment with SurTec 650 conversion coating.

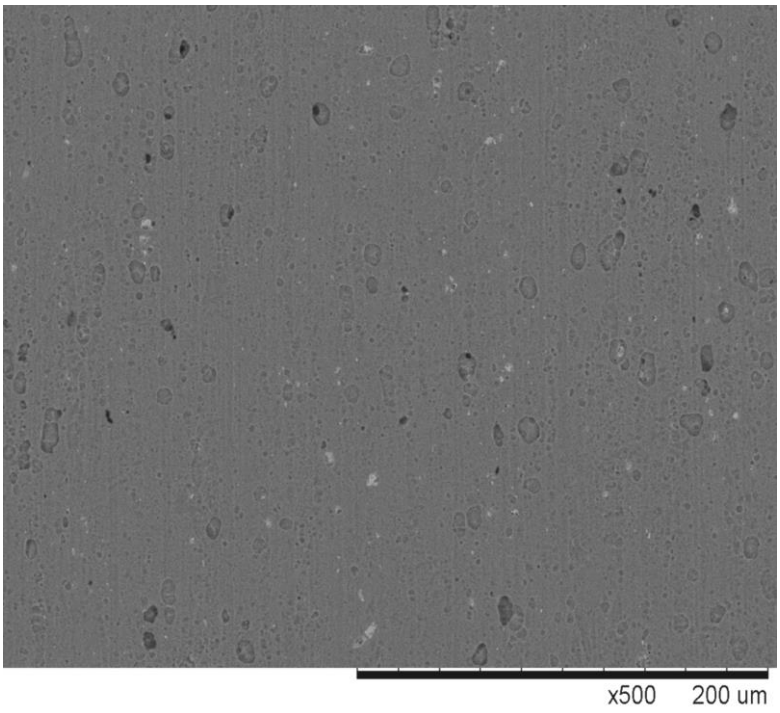

Figure 109 - Scanning electron micrographs of the surface of AA-2024-T3 after Deoxalume 2310 acid pickling treatment followed by SurTec 650 conversion coating, 500x.

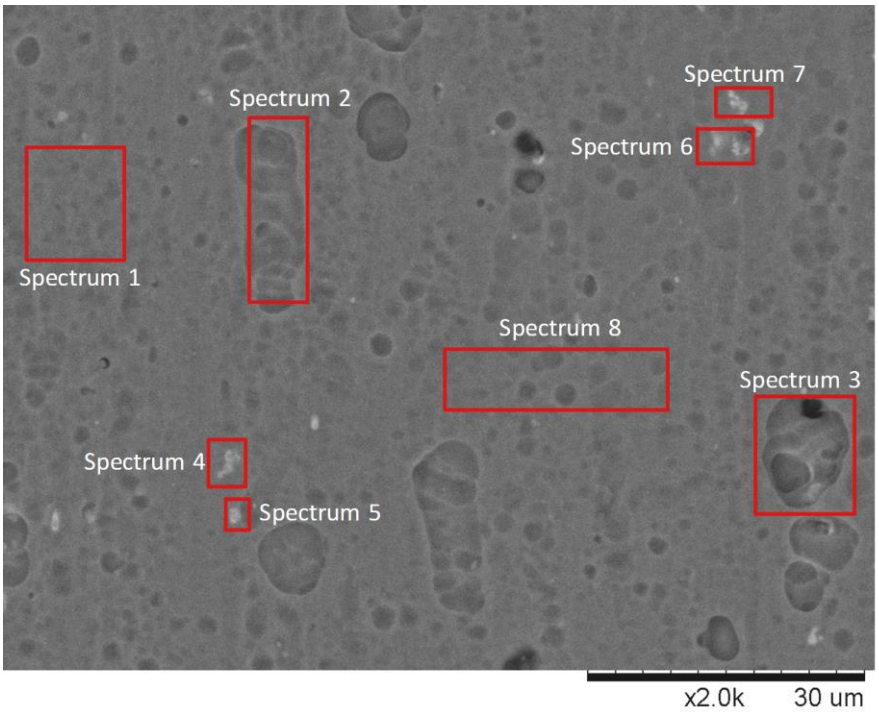

Figure 110 - Scanning electron micrographs of the surface of AA-2024-T3 after Deoxalume 2310 acid pickling treatment followed by SurTec 650 conversion coating, 2000x.

Table 28 - EDS analysis of AA2024-T3 after Deoxalume 2310 pickling treatment followed by SurTec 650 conversion coating.

Name	wt.% O	wt.% F	wt.% Mg	wt.% Al	wt.% Si	wt.% Mn	wt.% Fe	wt.% Cu	wt.% Zr
Spectrum 1	5.877	1.581	1.391	86.039				5.113	
Spectrum 2	6.578		1.22	85.258				4.936	2.007
Spectrum 3	6.046		1.411	87.537				5.006	
Spectrum 4	7.334	0.545	1.108	76.921	1.077	1.412	1.159	10.443	
Spectrum 5	10.342		1.038	65.718	0.992	1.037	2.653	15.6	2.619
Spectrum 6	7.328	1.492	1.482	81.184	1.255			7.258	
Spectrum 7	7.975	1.714	1.426	80.459	1.437			6.989	
Spectrum 8	5.431		1.365	85.816				5.649	1.739

The elements of the typical alloy composition (Cu, Fe, Mn, Mg) are observed by performing an EDS, whose results are shown in Table 28. Furthermore the analysis reveal the presence of some Cu and Fe islands and elements as F, Si and Zr (which compound is present in the SurTec 650 solution).

Oakite LNC pickling with SurTec conversion coating

Figures 111 and 112 show different magnifications of the specimen surface after Oakite LNC acid pickling treatment with SurTec 650 conversion coating.

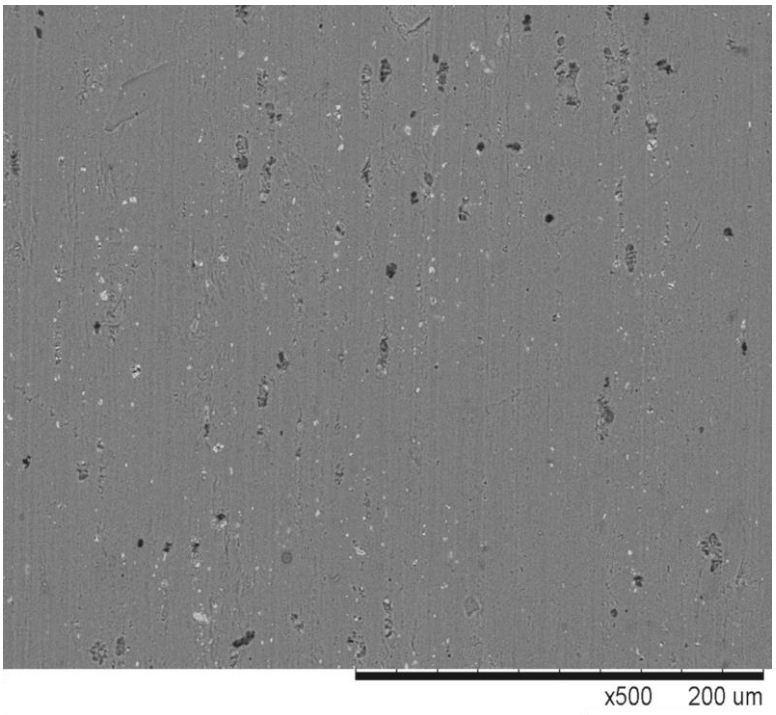

Figure 111 - Scanning electron micrographs of the surface of AA-2024-T3 after Oakite LNC acid pickling treatment followed by SurTec 650 conversion coating, 500x.

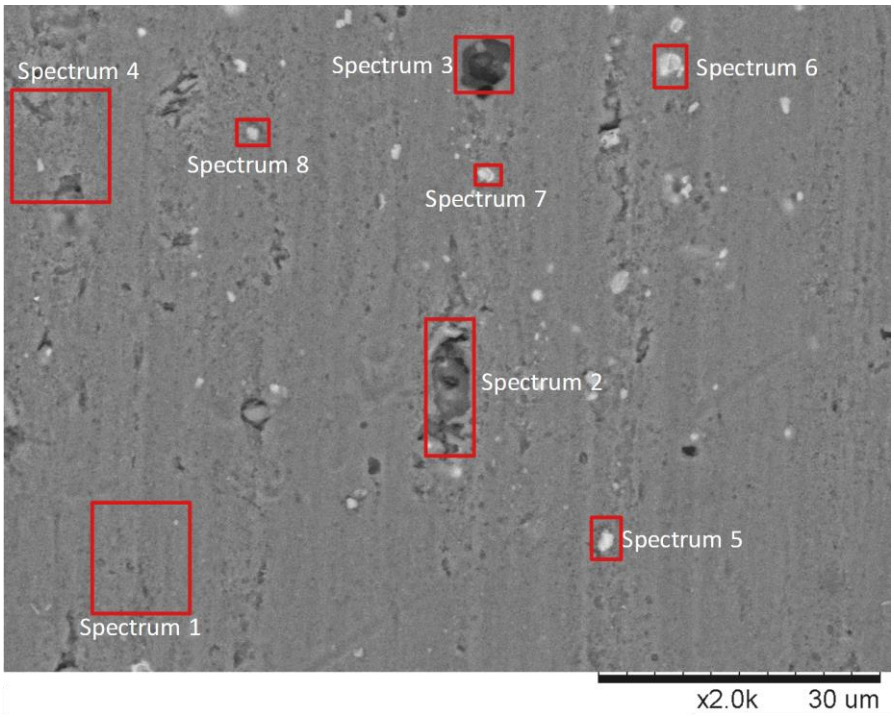

Figure 112 - Scanning electron micrographs of the surface of AA-2024-T3 after Oakite LNC acid pickling treatment followed by SurTec 650 conversion coating, 2000x.

Table 29 - EDS analysis of AA2024-T3 after Oakite LNC pickling treatment followed by SurTec 650 conversion coating.

Name	wt.% O	wt.% F	wt.% Mg	wt.% Al	wt.% Si	wt.% Mn	wt.% Fe	wt.% Cu	wt.% Zr
Spectrum 1	7.675	1.773	1.384	81.753				5.196	2.219
Spectrum 2	9.008	2.011	1.361	78.322		1.41		4.656	3.232
Spectrum 3	7.95	2.569	1.407	80.239				4.811	3.024
Spectrum 4	9.756	2.788	1.774	76.903				5.546	3.233
Spectrum 5	9.47	1.573	1.264	79.338	1.366			5.07	1.918
Spectrum 6	8.778		0.951	67.326	1.599	1.469	2.368	15.977	1.533
Spectrum 7	10.667	2.275	1.178	76.662	1.327			5.145	2.745
Spectrum 8	9.73	2.369	1.08	68.791	1.104	5.36		8.411	3.154

The presence of precipitates on the alloy surface is observed. The elements of the typical alloy composition (Cu, Fe, Mn, Mg) are observed by performing an EDS, whose results are shown in Table 29. Furthermore the analysis reveal the presence of some Cu and Fe islands and elements as F, Si and Zr (which compound is present in the SurTec 650 solution).

The samples surface, analysed by SEM with EDS probe, reveal a distribution of Zirconium contained in the SurTec 650 solution and the presence of some precipitates, such as Cu and F, are present.

7.2.4.2 Potentiodynamic polarization results

Potentiodynamic polarization measurements were carried out on samples after various picklings followed by SurTec 650 chemical conversion coating. Figure 113 shows the curves of all the analyzed samples.

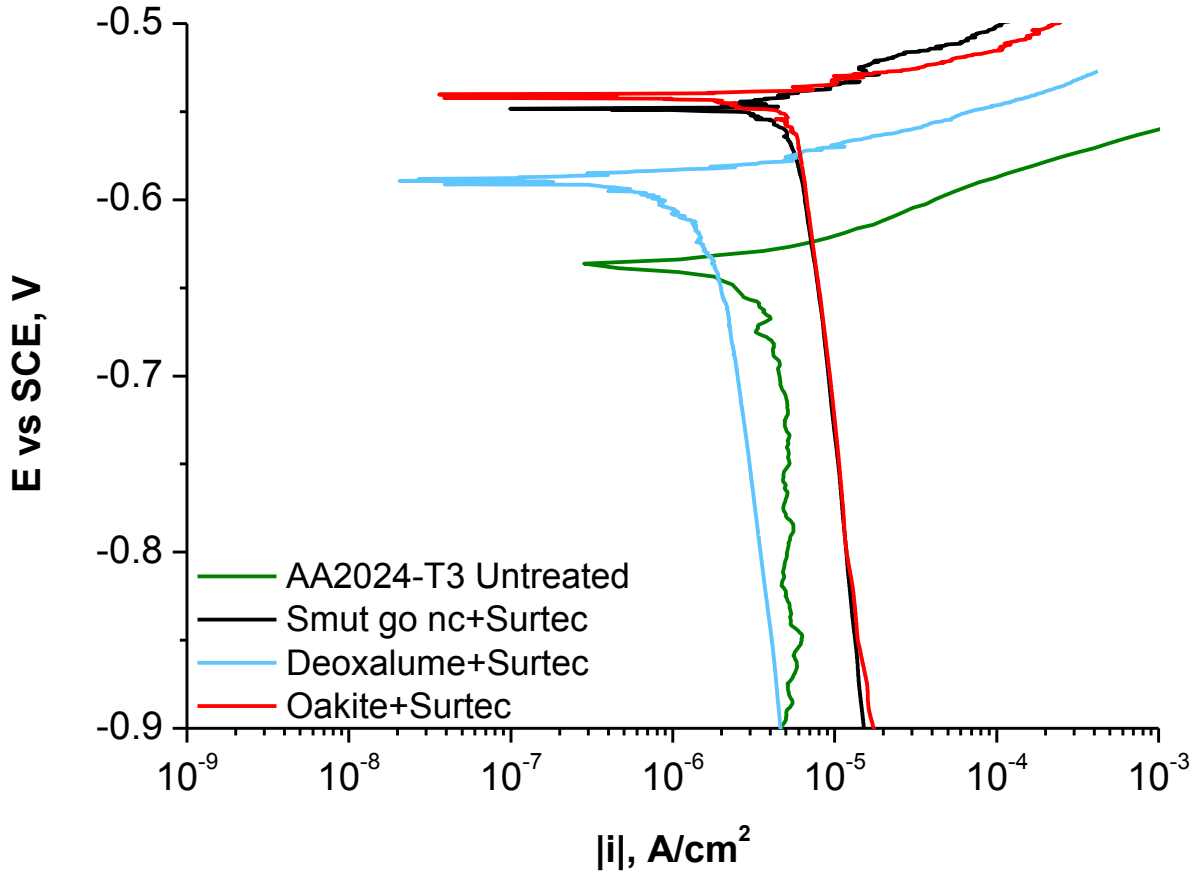

Figure 113 - Potentiodynamic measurements of the aluminium alloy after various pickling treatments followed by SurTec 650 conversion coating.

A clear improvement of Deoxalume 2310 anodic curve is noted compared to the curves obtained with picklings and Alodine 1200s. In fact, there is a noticeable increase in the corrosion potential and the cathode current is unchanged. The cathode currents of the other treatments are one order of magnitude lower than that samples with Alodine 1200s while the anode currents are unchanged.

7.2.4.3 EIS results

The corrosion behaviour of the specimen after Smut Go NC alkaline pickling and following chemical conversion in SurTec 650 is shown in Figure 114 while Figure 115 shows the corresponding phase angle.

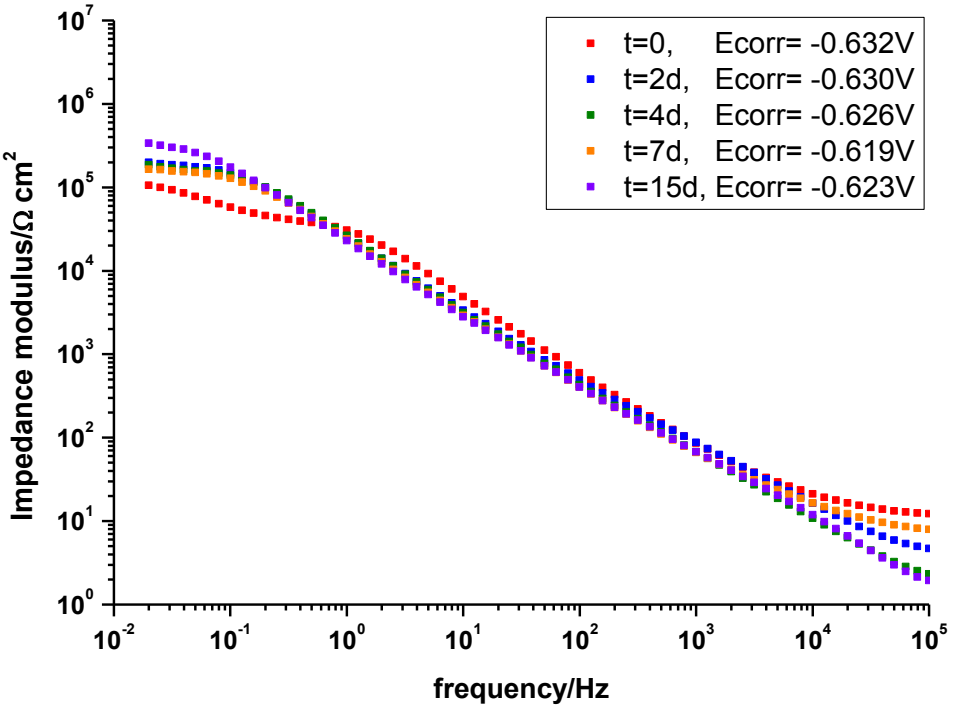

Figure 114 – Impedance modulus of alloy after Smut Go NC alkaline pickling followed by SurTec 650 treatment obtained during 15days of exposure in 3.5% NaCl.

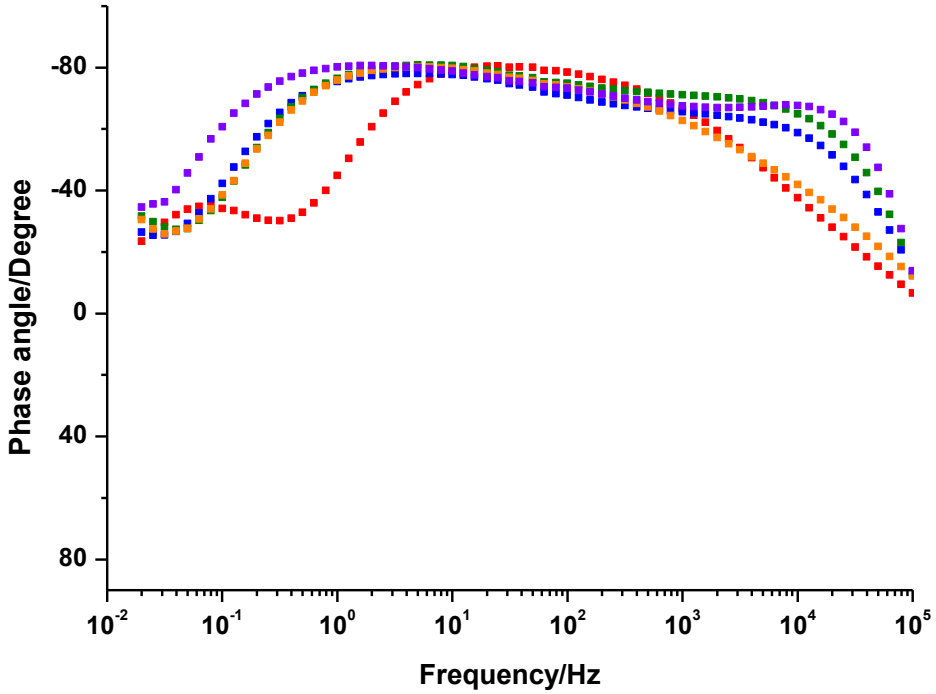

Figure 115 – Phase angle of alloy after Smut Go NC alkaline pickling followed by SurTec 650 treatment obtained during 15days of exposure in 3.5% NaCl.

Considering the low-frequency values, the impedance modulus slight increases during corrosion test and the value at 15th day of immersion is 10^5Ohm cm^2.

The trend of impedance modulus of specimen AA2024-T3 after Deoxalume 2310 acid pickling followed by SurTec 650 conversion coating is reported in Figure 116, while the phase angle is reported in Figure 117.

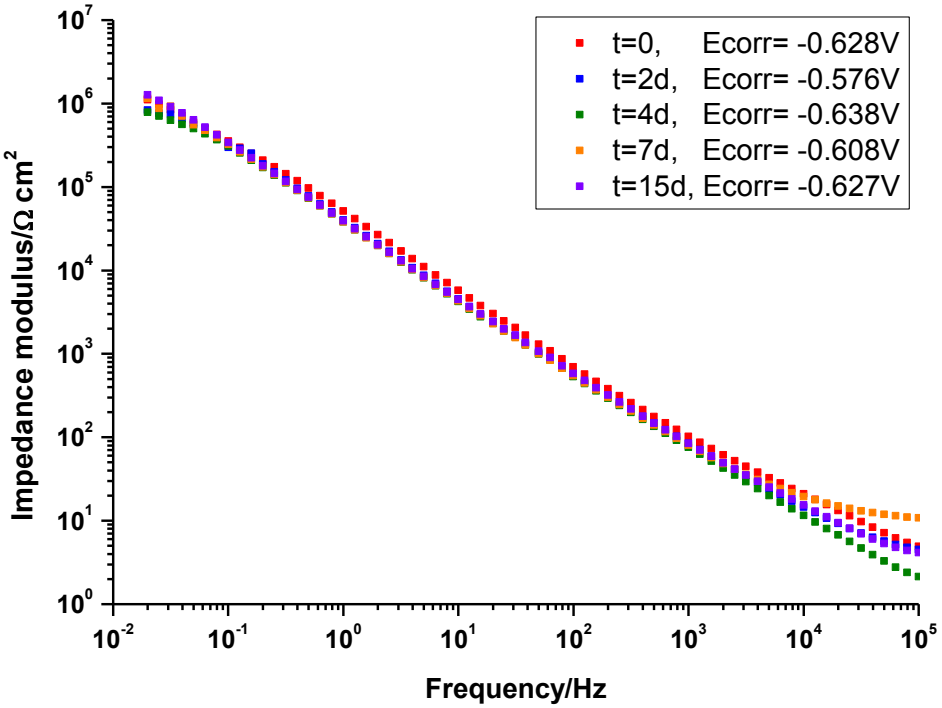

Figure 116 - Impedance modulus of alloy after Deoxalume 2310 acid pickling followed by SurTec 650 treatment obtained during 15days of exposure in 3.5% NaCl.

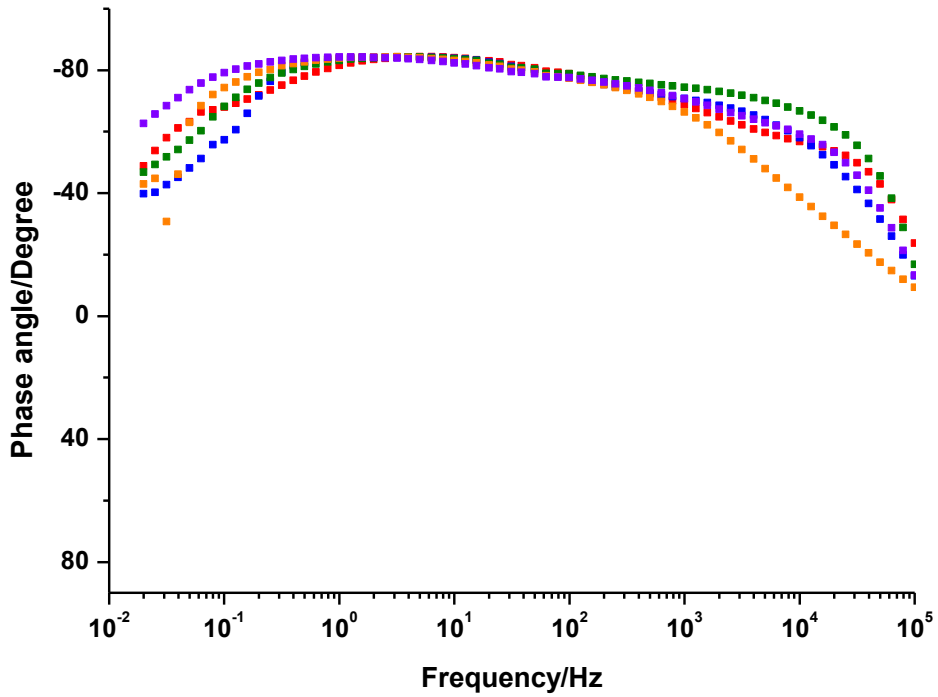

Figure 117 – Phase angle of alloy after Deoxalume 2310 acid pickling followed by SurTec 650 treatment obtained during 15days of exposure in 3.5% NaCl.

Considering the low-frequency values, a high impedance modulus can be observed at the beginning of immersion in the solution test and it remains constant during immersion time with a value of 10^6Ohm cm^2.

In Figure 118 is reported the trend of sample pickled with Oakite LNC acid solution followed by trivalent chromium conversion treatment. The trend of corresponding phase angle is reported in Figure 119.

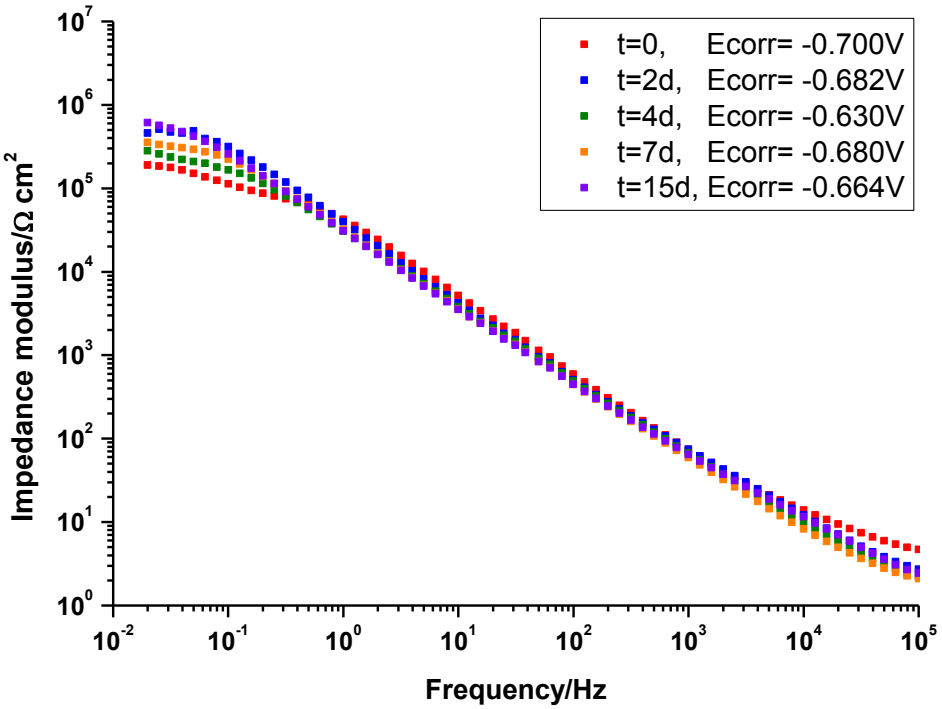

Figure 118 – Impedance modulus of alloy after Oakite LNC acid pickling followed by SurTec 650 treatment obtained during 15days of exposure in 3.5% NaCl.

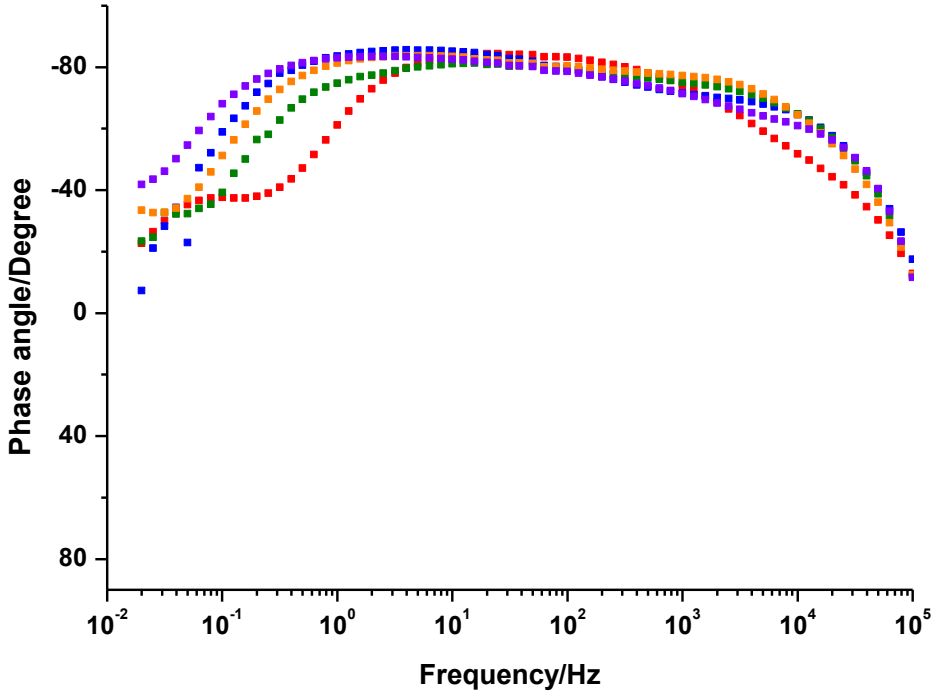

Figure 119 – Phase angle of alloy after Oakite LNC acid pickling followed by SurTec 650 treatment obtained during 15days of exposure in 3.5% NaCl.

The value of low-frequency impedance modulus slight increases during immersion time and the final vales is 10^6Ohm cm^2.

On the basis of the observed results ad in terms of ranking of the various pickling and following SurTec 650 conversion coating it is possible to conclude that:

Deoxalume 2310 with SurTec 650> Oakite LNC with SurTec 650> Smut Go NC with SurTec 650.

Furthermore the specimens treated in Deoxalume 2310 acid pickling followed by SurTec 650 chemical conversion show a corrosion resistance comparable, if not superior, to those that of classical cycle with hexavalent chromium.

7.2.5 Corrosion imaging

In order to corroborate the EIS results imagines of specimens were acquired. In Figure 120 the surface appearance of the specimens during corrosions is compared.

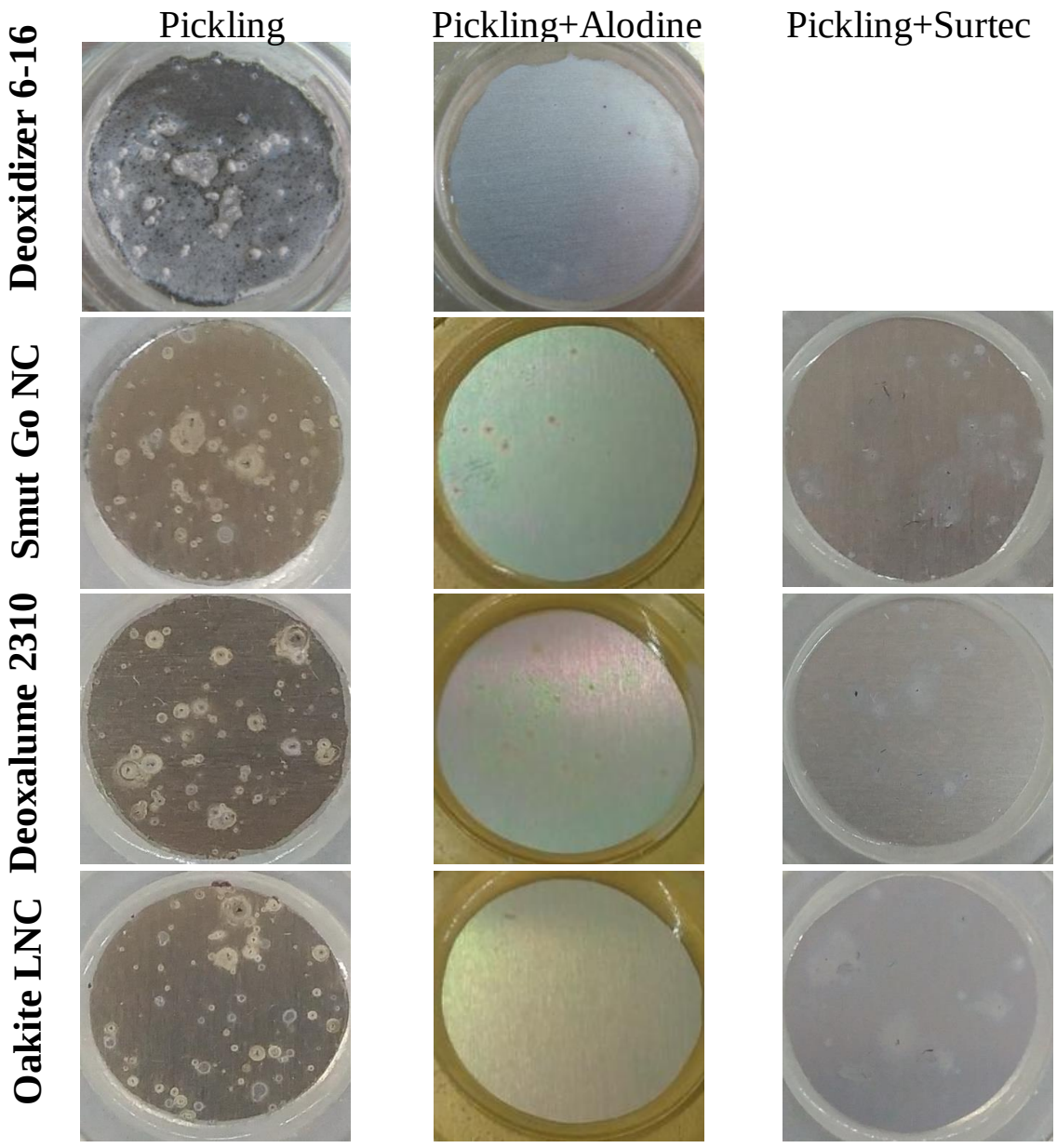

Figure 120 - Surface appearance after corrosion test in 3.5 wt.% NaCl of all specimens.

It is evident that the Cr-free treatment that provided the best anticorrosion performance was Deoxalume 2310 acid pickling with SurTec 650 conversion coating, followed by Oakite LNC acid pickling with SurTec 650 conversion coating and Smut Go NC alkaline pickling with SurTec 650. Further, the innovative cycle was substantially better than the traditional cycle, with minimal sign of corrosion for specimens treated with Deoxalume 2310 pickling followed by SurTec 650.

Overall, Deoxalume 2310 with SurTec 650 provided better anticorrosion performance when compared to the traditional industrial cycle. This imagines corroborate all electrochemical results showed previously.

Chapter 8 - Conclusions

In this study, electrochemical impedance spectroscopy was used to characterize in-situ the sealing behaviour of an aerospace aluminium alloy anodized with the industrially accepted tartaric-sulfuric anodizing process. Two treatments were compared: traditional TSA, producing a film with relatively coarse morphology, and modified TSA, producing a film with much finer porosity. The specimens anodized with the two treatments were sealed by three different processes: sodium chromate, hot water, and cerium based sealing.

Electrochemical impedance spectroscopy measurements performed during sodium chromate, cerium nitrate and hot water sealing, revealed that the overall behaviour is significantly different in the three solutions. In particular, during sodium chromate sealing, the porous oxide skeleton is heavily attacked by the solution, and a significant increase in capacitance is observed. This is associated with a substantial thinning of the barrier layer of the porous oxide, which is not observed during hot water and cerium nitrate sealing. On the contrary, cerium nitrate sealing does not attack the porous skeleton, but it induces the precipitation of cerium-containing compounds above the and within the pores of the anodic oxide. Furthermore, electrochemical impedance spectroscopy performed during sealing indicated that the finer morphology obtained by the modified TSA cycle responded better during sealing, as evident by higher values of low frequency impedance.

Post sealing measurements performed in non-aggressive electrolytes also indicated that the porosity was more closed for the specimens obtained by modified TSA, for all of the sealing treatments. In agreement, the anticorrosion performance of the modified TSA process was consistently better than that of the traditional TSA, regardless of the sealing method. Overall, cerium sealing has environmental advantages compared to the other processes since it requires a much lower temperature (37°C) compared to sodium chromate and hot water sealing (96°C), enable

energy saving, and does not use environmentally harmful compounds such as hexavalent chromium. Finally, the combination of modified TSA anodizing cycle with cerium sealing produced oxides with properties comparable, if not superior, to those that are achieved by chromate sealed traditional TSA.

Furthermore a number of different pre-treatments have been analysed to confirm the effectiveness of Trivalent Chromium Process in terms of corrosion protection. In general, in this work it has been found that the specimens treated in Deoxalume 2310 acid pickling followed by SurTec 650 chemical conversion show a corrosion resistance comparable, if not superior, to those that of classical cycle with hexavalent chromium.

References

[1] http://www.world-aluminium.org, (December 2008).

[2] M.E. Schlesinger, Aluminum recycling, CRC Press, 2013.

[3] I. Polmear, Light alloys: from traditional alloys to nanocrystals, Butterworth-Heinemann, 2005.

[4] A.E. Hughes, N. Birbilis, J.M. Mol, S.J. Garcia, X. Zhou, G.E. Thompson, High strength Al-alloys: microstructure, corrosion and principles of protection, in: Recent Trends in Processing and Degradation of Aluminium Alloys, InTech, 2011.

[5] R.J. Hussey, J. Wilson, Light Alloys: Directory and Databook, Springer Science & Business Media, 2013.

[6] P.A. Schweitzer, Metallic materials: physical, mechanical, and corrosion properties, CRC Press, 2003.

[7] Richard C. Rice, Jana L. Jackson, J. Bakuckas, S. Thompson, Material properties development and standardization (MMPDS), USA, National technical information service., (2003).

[8] C. Vargel, Corrosion of aluminium, Elsevier, 2004.

[9] J.R. Davis, Aluminum and aluminum alloys, ASM international, 1993.

[10] E. Tan, B. ÖGEL, Influence of heat treatment on the mechanical properties of AA6066 alloy, Turkish Journal of Engineering and Environmental Sciences, 31 (2007) 53-60.

[11] M. Jariyaboon, A. Davenport, R. Ambat, B. Connolly, S. Williams, D. Price, Corrosion of a dissimilar friction stir weld joining aluminium alloys AA2024 and AA7010, Corrosion engineering, science and technology, 41 (2006) 135-142.

[12] A.K. Dahle, Encyclopedia ofmaterials: science and technology: heat treatment of aluminium alloys, Elsevier, (2001).

[13] K. Nisancioglu, Electrochemical behavior of aluminum-base intermetallics containing iron, Journal of the Electrochemical Society, 137 (1990) 69-77.

[14] L.K. Reddy, Principles of engineering metallurgy, New Age International, 2007.

[15] Z. Szklarska-Smialowska, Insight into the pitting corrosion behavior of aluminum alloys, Corrosion science, 33 (1992) 1193-1202.

[16] P.R. Roberge, Corrosion Engineering, McGraw-Hill New York, NY, USA:, 2008.

[17] L.F. Mondolfo, Aluminum alloys: structure and properties, Elsevier, 2013.

[18] R. Buchheit, R. Boger, M. Carroll, R. Leard, C. Paglia, J. Searles, The electrochemistry of intermetallic particles and localized corrosion in Al alloys, Jom, 53 (2001) 29-33.

[19] M. Warmuzek, Aluminum-silicon casting alloys: an atlas of microfractographs, ASM international, 2004.

[20] D.O. Sprowls, HIGH STRENGTH ALUMINUM ALLOYS WITH IMPROVED RESISTANCE TO CORROSION AND STRESS-CORROSION CRACKING, Aluminium, 54 (1978) 214-217.

[21] L.L. Shreir, R.A. Jarman, G.T. Burstein, Corrosion: vol 1. Metal/environment reactions, 3rd Edition, (1994) 1:8.

[22] G.P. Halada, J.R. Kearns, M.E. Monserrat, M.J. Vasquez, C.R. Clayton, S. Jeanjaquet, M.W. Kending, Influence of surface chemistry on electrochemical behavior of intermetallic particles in AA2024-T3, Electrochemical Society Meeting, 193rd, (1998).

[23] R. G. Buchheit, R. P. Grant, P. F. Hiava, B. Mckenzie, G. Zender, Local Dissolution Phenomena Associated with S Phase (AI2CuMg) Particles in Aluminum Alloy 2024-13, J. Electrochem. Soc., 144 (1997) 2621-2628.

[24] N. Birbilis, R. Buchheit, Investigation and discussion of characteristics for intermetallic phases common to aluminum alloys as a function of solution pH, Journal of The Electrochemical Society, 155 (2008) C117-C126.

[25] N. Birbilis, R. Buchheit, Electrochemical characteristics of intermetallic phases in aluminum alloys an experimental survey and discussion, Journal of The Electrochemical Society, 152 (2005) B140-B151.

[26] W. Zhang, G.S. Frankel, Transitions between pitting and intergranular corrosion in AA2024, Electrochimica Acta, 48 (2003) 1193-1210.

[27] J.C. Scully, Fundamental of corrosion 3rd Ed., Pergamon Press, (1990).

[28] T.D. Burleigh, R. Rennick, F. Bovard, Corrosion potential for aluminum alloys measured by ASTM G 69, Corrosion, 49 (1993) 683-685.

[29] P.A. Schweitzer, Fundamentals of corrosion: mechanisms, causes, and preventative methods, CRC Press, 2009.

[30] R. Winston Revie, Uhlig's Corrosion Handbook 3rd Ed., John Wiley & Sons Inc., (2011).

[31] Z. Ahmad, Principles of corrosion engineering and corrosion control, Butterworth-Heinemann, 2006.

[32] D. Altenpohl, Aluminum viewed from within: an introduction into metallurgy of aluminum fabrication, Dusseldolf: Aluminium Verlag, (1982).

[33] J. Denny A., Principles and Prevention of corrosion 2nd Ed., Prentice Hall, (1996).

[34] M. Pourbaix, Atlas of electrochemical equilibria in aqueous solutions, National Association of Corrosion Engineers, (1974).

[35] J. Namahoot, Effects of deformations on corrosion of Al-Mn alloys, in, University of Birmingham, 2005.

[36] S. Sanchez-Majado, J.M. Torralba, A. Jiménez-Morales, Assessment of the corrosion behavior of a sintered al-cu-mg alloy in aeronautical environments as a function of the heat treatment, in: Materials science forum, Trans Tech Publ, 2007, pp. 497-500.

[37] E. T.E, Passivity of Metals: Growth of surface oxide films on metals and alloys by dissolution and precipitation processes, The Electrochemical Society, (1978) 410-412.

[38] R.T. Foley, T.H. Nguyen, The chemical nature of aluminium corrosion, Journal of Electrochemical Society: Electrochemical Science and Technology, 129 (1982) 464-467.

[39] G. Frankel, Pitting corrosion of metals a review of the critical factors, Journal of the Electrochemical Society, 145 (1998) 2186-2198.

[40] T.H. Muster, A.E. Hughes, G.E. Thompson, Cu distributions in aluminium alloys, Nova Science Publishers, (2009).

[41] M.A. Amin, S.S.A. El Rehim, E.E. El Sherbini, AC and DC studies of the pitting corrosion of Al in perchlorate solutions, Electrochimica acta, 51 (2006) 4754-4764.

[42] A. Berzins, R.T. Lowson, K.J. Mirams, Aluminium corrosion studies. III. Chloride adsorption isotherms on corroding aluminium, Australian Journal of Chemistry, 30 (1977) 1891-1903.

[43] K.S. Rao, K.P. Rao, Pitting corrosion of heat-treatable aluminium alloys and welds: a review, Trans. Indian Inst. Met, 57 (2004) 593-610.

[44] D. Weng, S. Huo, Characteristics of pit growth on aluminium in seawater, Corrosion science, 31 (1990) 509-514.

[45] E. McCafferty, Sequence of steps in the pitting of aluminum by chloride ions, Corrosion Science, 45 (2003) 1421-1438.

[46] W. Rudd, J. Scully, The function of the repassivation process in the inhibition of pitting corrosion on aluminium, Corrosion Science, 20 (1980) 611-631.

[47] M. Tabrizi, S. Lyon, G. Thompson, J. Ferguson, The long-term corrosion of aluminium in alkaline media, Corrosion science, 32 (1991) 733-742.

[48] P.A. Schweitzer, Corrosion and corrosion protection handbook, Marcel Dekker, (1983).

[49] J. Soltis, N. Laycock, D. Krouse, Temperature dependence of the pitting potential of high purity aluminium in chloride containing solutions, Corrosion Science, 53 (2011) 7-10.

[50] G. Scamans, J. Hunter, N.J.H. Holroyd, A surface engineering approach to the corrosion of aluminum, Aluminium Alloys Contemporay Research and Applications, Academic Press, (1989).

[51] T.D. Burleigh, Postulated mechanisms for stress corrosion cracking of aluminum alloys. A review of the literature 1980-1989, Corrosion, 47 (1991) 89-98.

[52] P.R. Roberge, Handbook of corrosion engineering, McGraw-Hill Professional, (2000).

[53] Z. Chen, F. Cui, R. Kelly, Calculations of the cathodic current delivery capacity and stability of crevice corrosion under atmospheric environments, Journal of The Electrochemical Society, 155 (2008) C360-C368.

[54] M. Hunter, G. Frank, D. Robinson, Proceedings of the Second International Congress on Metallic Corrosion, (1963).

[55] X. Zhao, G.S. Frankel, Quantitative study of exfoliation corrosion: Exfoliation of slices in humidity technique, Corrosion science, 49 (2007) 920-938.

[56] J.R. Davis, Corrosion of aluminum and aluminum alloys, Asm International, 1999.

[57] A. Mazhar, S. Arab, E. Noor, The role of chloride ions and pH in the corrosion and pitting of Al–Si alloys, Journal of applied electrochemistry, 31 (2001) 1131-1140.

[58] G. Scamans, N. Holroyd, C. Tuck, The role of magnesium segregation in the intergranular stress corrosion cracking of aluminium alloys, Corrosion Science, 27 (1987) 329-347.

[59] G. Scamans, N.J.H. Holroyd, Stress-corrosion of aluminium aerospace alloys, Journal of the Electrochemical Society, 133 (1986) C308-C308.

[60] B.F. Brown, Stress corrosion cracking control measures, in, AMERICAN UNIV WASHINGTON DC DEPT OF CHEMISTRY, 1977.

[61] T. Burleigh, The postulated mechanisms for stress corrosion cracking of aluminum alloys: A review of the literature 1980-1989, Corrosion, 47 (1991) 89-98.

[62] T.M. Yue, L.J. Yan, C.F. Dong, C.P. Chan, Stress corrosion cracking behaviour of laser treated aluminium alloy 7075 using a slow strain rate test, Materials Science and Technology, 21 (2005) 961-966.

[63] S. Garcia-Vergara, F. Colin, P. Skeldon, G.E. Thompson, P. Bailey, T.C.Q. Noakes, H. Habazaki, K. Shimizu, Effect of copper enrichment on the electrochemical potential of binary Al-Cu alloys, Journal of the Electrochemical Society. Vol. 151, no. 1, pp. B16-B21. 2004, (2004).

[64] R.G. Buchheit, Compilation of corrosion potentials reported for intermetallic phases in aluminum alloys, Journal of the Electrochemical Society, 142 (1995) 3994-3996.

[65] T. Dimogerontakis, L. Kompotiatis, I. Kaplanoglou, Oxygen evolution during the formation of barrier type anodic film on 2024-T3 aluminium alloy, Corrosion Science (USA). Vol. 40, no. 11, pp. 1939-1951. Nov. 1998, (1998).

[66] P. Campestrini, E.P.M. van Westing, H.W. van Rooijen, J.H.W. de Wit, Relation between microstructural aspects of AA2024 and its corrosion behaviour investigated using AFM scanning potential technique, Corrosion Science, 42 (2000) 1853-1861.

[67] J.D. Gorman, S.T. Johnson, P.N. Johnston, P.J.K. Paterson, A.E. Hughes, The characterisation of Ce-Mo-based conversion coatings on Al-alloys: Part II, Corrosion Science, 38 (1996) 1977-1990.

[68] P. Schmutz, G.S. Frankel, Corrosion study of AA2024-T3 by scanning Kelvin probe force microscopy and in situ atomic force microscopy scratching, Journal of the Electrochemical Society, 145 (1998) 2295-2306.

[69] C. Blanc, B. Lavelle, G. Mankowski, The role of precipitates enriched with copper on the susceptibility to pitting corrosion of the 2024 aluminium alloy, Corrosion Science, 39 (1997) 495-510.

[70] W. Zhang, B. Hurley, R. Buchheit, Characterization of chromate conversion coating formation and breakdown using electrode arrays, Journal of The Electrochemical Society, 149 (2002) B357-B365.

[71] K. Kowal, J. DeLuccia, J. Josefowicz, C. Laird, G. Farrington, In Situ Atomic Force Microscopy Observations of the Corrosion Behavior of Aluminum-Copper Alloys, Journal of The Electrochemical Society, 143 (1996) 2471-2481.

[72] A. Hughes, C. MacRae, N. Wilson, A. Torpy, T. Muster, A. Glenn, Sheet AA2024-T3: a new investigation of microstructure and composition, Surface and Interface Analysis, 42 (2010) 334-338.

[73] J. Scully, T. Knight, R. Buchheit, D. Peebles, Electrochemical characteristics of the Al2Cu, Al3Ta and Al3Zr intermetallic phases and their relevancy to the localized corrosion of Al alloys, Corrosion Science, 35 (1993) 185-195.

[74] H.-C. Shih, N.-J. Ho, J. Huang, Precipitation behaviors in Al-Cu-Mg and 2024 aluminum alloys, Metallurgical and materials transactions A, 27 (1996) 2479-2494.

[75] J. Galvele, S. de De Micheli, Mechanism of intergranular corrosion of Al-Cu alloys, Corrosion Science, 10 (1970) 795-807.

[76] R. Leard, R. Buchheit, Electrochemical characterization of copper-bearing intermetallic compounds and localized corrosion of Al-Cu-Mg-Mn alloy 2024, in: Materials Science Forum, Trans Tech Publ, 2002, pp. 1491-1496.

[77] R.G. Buchheit, Electrochemistry of ? (Al2Cu), S (Al2CuMg) and T1 (Al2CuLi) and localized corrosion and environment assisted cracking in high strength Al alloys, Materials Science Forum, 331 (2000).

[78] J. Scully, D. Peebles, A. Romig, D. Frear, C. Hills, Metallurgical factors influencing the corrosion of aluminum, Al-Cu, and Al-Si alloy thin films in dilute hydrofluoric solution, Metallurgical Transactions A, 23 (1992) 2641-2655.

[79] I. Muller, J. Galvele, Pitting potential of high purity binary aluminium alloys—I. Al□ Cu alloys. Pitting and intergranular corrosion, Corrosion Science, 17 (1977) 179191-189193.

[80] A. Boag, R. Taylor, T. Muster, N. Goodman, D. McCulloch, C. Ryan, B. Rout, D. Jamieson, A. Hughes, Stable pit formation on AA2024-T3 in a NaCl environment, Corrosion Science, 52 (2010) 90-103.

[81] V. Guillaumin, G. Mankowski, Localized corrosion of 2024 T351 aluminium alloy in chloride media, Corrosion Science, 41 (1999) 421-438.

[82] R. Buchheit, L. Montes, M. Martinez, J. Michael, P. Hlava, The electrochemical characteristics of bulk-synthesized Al2CuMg, Journal of the Electrochemical Society, 146 (1999) 4424-4428.

[83] R. Buchheit, M. Martinez, L. Montes, Evidence for Cu Ion Formation by Dissolution and Dealloying the Al2CuMg Intermetallic Compound in Rotating Ring-Disk Collection Experiments, Journal of The Electrochemical Society, 147 (2000) 119-124.

[84] H. Obispo, L. Murr, R. Arrowood, E. Trillo, Copper deposition during the corrosion of aluminum alloy 2024 in sodium chloride solutions, Journal of Materials Science, 35 (2000) 3479-3495.

[85] D. Zhu, W.J. van Ooij, Corrosion protection of AA 2024-T3 by bis-[3-(triethoxysilyl) propyl]tetrasulfide in neutral sodium chloride solution. Part 1: Corrosion of AA 2024-T3, Corrosion Science, 45 (2003) 2163-2175.

[86] C. Blanc, S. Gastaud, G. Mankowski, Mechanistic studies of the corrosion of 2024 aluminum alloy in nitrate solutions, Journal of the Electrochemical Society, 150 (2003) B396-B404.

[87] J.W. Bibber, A chrome-free conversion coating and sealant for aluminum and its alloys, in, Sanchem, Chicago, IL (US), 1999.

[88] J. Nordlien, J. Walmsley, H. Østerberg, K. Nisancioglu, Formation of a zirconium-titanium based conversion layer on AA 6060 aluminium, Surface and Coatings Technology, 153 (2002) 72-78.

[89] H. Katzman, G. Malouf, R. Bauer, G. Stupian, Corrosion-protective chromate coatings on aluminum, Applications of Surface Science, 2 (1979) 416-432.

[90] P.G.Sheasby, The surface treatment and finishing of aluminium and its alloys, ASM International, Materials Park, OH, 2001.

[91] O. Lunder, J. Walmsley, P. Mack, K. Nisancioglu, Formation and characterisation of a chromate conversion coating on AA6060 aluminium, Corrosion science, 47 (2005) 1604-1624.

[92] M. Kendig, S. Jeanjaquet, R. Addison, J. Waldrop, Role of hexavalent chromium in the inhibition of corrosion of aluminum alloys, Surface and Coatings Technology, 140 (2001) 58-66.

[93] M.M. HYLAND, Surface Chemistry of Adhesion to Aluminum, Handbook of Aluminum: Volume 2: Alloy Production and Materials Manufacturing, 2 (2003) 465.

[94] Q. Meng, G.S. Frankel, Characterization of chromate conversion coating on AA7075-T6 aluminum alloy, Surface and Interface Analysis, 36 (2004) 30-42.

[95] J. Waldrop, M. Kendig, Nucleation of Chromate Conversion Coating on Aluminum 2024-T3 Investigated by Atomic Force Microscopy, Journal of the Electrochemical Society, 145 (1998) L11-L13.

[96] G. Brown, K. Kobayashi, Nucleation and growth of a chromate conversion coating on aluminum alloy AA 2024-T3, Journal of the Electrochemical Society, 148 (2001) B457-B466.

[97] P.L. Hagans, C.M. Haas, Influence of metallurgy on the protective mechanism of chromium-based conversion coatings on aluminum–copper alloys, Surface and interface analysis, 21 (1994) 65-78.

[98] Y. Liu, P. Skeldon, G. Thompson, H. Habazaki, K. Shimizu, Chromate conversion coatings on aluminium: influences of alloying, Corrosion science, 46 (2004) 297-312.

[99] D.B. Mitton, A. Carangelo, A. Acquesta, T. Monetta, M. Curioni, F. Bellucci, Selected Cr(VI) replacement options for aluminum alloys: a literature survey, in: Corrosion Reviews, 2017.

[100] W. Nickerson, C. Matzdorf, Non-Chromate Aluminum Pretreatments, in, NAVAL AIR SYSTEMS COMMAND PATUXENT RIVER MD, 2012.

[101] V.S. Argawala, D.W. Beckert, A.S. Fabiszewski, F. Pearlstein, Paper presented at Corrosion'94, numer 621, 33 (1994).

[102] V.S. Argawala, F. Pearlstein, Trivalent chromium solutions for applying chemical conversion coatings to aluminum alloys or for sealing anodized aluminum, Plating and Surface Finishing, 91 (1994) 50-55.

[103] Official Journal of the European Union, L396/1 30.12.2006 Concerning the Registration, Evaluation, Authorisation and Restriction of Chemicals (REACH).

[104] Official Journal of the European Union, L37/19 13.2.2003 On the restriction of the use of certain hazardous substances in electrical and electronic equipment (RoHS).

[105] Official Journal of the European Union, L197/38 24.7.2012 on waste electrical and electronic equipment (WEEE).

[106] Official Journal of the European Union, L269/34 13.2.2003 On end-of life vehicles (ELV).

[107] Federal Registry 2006; Occupational Exposure to hexavalent chromium, Fed. Register: 71, Number 39: 10099–10385. .

[108] L. Li, G.P. Swain, A. Howell, D. Woodbury, G.M. Swain, The formation, structure, electrochemical properties and stability of trivalent chrome process (TCP) coatings on AA2024, Journal of The Electrochemical Society, 158 (2011) C274-C283.

[109] W. Nickerson, E. Lipnickas, Characterization of a Viable Non-Chromated Conversion Coating for Aluminum and Its Alloys by Electrochemical and Other Methods, in: TriService Corrosion Conf. Proc., paper no. AM025692 (Patuxent River, MD: Naval Air Systems Command, 2003), 2003.

[110] Y. Guo, A Study of Trivalent Chrome Process Coatings on Aluminum Alloy 2024-T3, in, The Ohio State University, 2011.

[111] L. Li, A.L. Desouza, G.M. Swain, In situ pH measurement during the formation of conversion coatings on an aluminum alloy (AA2024), Analyst, 138 (2013) 4398-4402.

[112] C. Matzdorf, M. Kane, J. Green, Corrosion resistant coatings for aluminum and aluminum alloys, in, Google Patents, 2002.

[113] Y. Guo, G. Frankel, Characterization of trivalent chromium process coating on AA2024-T3, Surface and Coatings Technology, 206 (2012) 3895-3902.

[114] J.-T. Qi, T. Hashimoto, J. Walton, X. Zhou, P. Skeldon, G. Thompson, Trivalent chromium conversion coating formation on aluminium, Surface and Coatings Technology, 280 (2015) 317-329.

[115] S. Dardona, M. Jaworowski, In situ spectroscopic ellipsometry studies of trivalent chromium coating on aluminum, Applied Physics Letters, 97 (2010) 181908.

[116] P. Puomi, H. Fagerholm, J. Rosenholm, K. Jyrkäs, Comparison of different commercial pretreatment methods for hot-dip galvanized and Galfan coated steel, Surface and Coatings Technology, 115 (1999) 70-78.

[117] V. Moutarlier, M. Gigandet, L. Ricq, J. Pagetti, Electrochemical characterisation of anodic oxidation films formed in presence of corrosion inhibitors, Applied Surface Science, 183 (2001) 1-9.

[118] V. Moutarlier, M. Gigandet, J. Pagetti, B. Normand, An electrochemical approach to the anodic oxidation of Al 2024 alloy in sulfuric acid containing inhibitors, Surface and coatings Technology, 161 (2002) 267-274.

[119] S. Verdier, N. Van der Laak, F. Dalard, J. Metson, S. Delalande, An electrochemical and SEM study of the mechanism of formation, morphology, and composition of titanium or zirconium fluoride-based coatings, Surface and Coatings Technology, 200 (2006) 2955-2964.

[120] L. Fedrizzi, F. Deflorian, P. Bonora, Corrosion behaviour of fluotitanate pretreated and painted aluminium sheets, Electrochimica acta, 42 (1997) 969-978.

[121] M. Smit, J. Sykes, J. Hunter, J. Sharman, G. Scamans, Titanium based conversion coatings on aluminium alloy 3003, Surface engineering, 15 (1999) 407-410.

[122] A. Aldykiewicz, A. Davenport, H. Isaacs, Studies of the Formation of Cerium-Rich Protective Films Using X-Ray Absorption Near-Edge Spectroscopy and Rotating Disk Electrode Methods, Journal of the Electrochemical Society, 143 (1996) 147-154.

[123] F. Seon, Rare earths for materials corrosion protection, Journal of the Less Common Metals, 148 (1989) 73-78.

[124] B. Hinton, Corrosion inhibition with rare earth metal salts, Journal of Alloys and Compounds, 180 (1992) 15-25.

[125] S. Ono, M. Saito, H. Asoh, Self-ordering of anodic porous alumina formed in organic acid electrolytes, Electrochimica Acta, 51 (2005) 827-833.

[126] J.S. Suh, J.S. Lee, Highly ordered two-dimensional carbon nanotube arrays, Applied physics letters, 75 (1999) 2047-2049.

[127] W. De Azevedo, D. De Carvalho, H. Khoury, E. De Vasconcelos, E. Da Silva, Spectroscopic characteristics of doped nanoporous aluminum oxide, Materials Science and Engineering: B, 112 (2004) 171-174.

[128] Y. Kim, B. Jung, H. Lee, H. Kim, K. Lee, H. Park, Capacitive humidity sensor design based on anodic aluminum oxide, Sensors and Actuators B: Chemical, 141 (2009) 441-446.

[129] S. Shingubara, Fabrication of nanomaterials using porous alumina templates, Journal of Nanoparticle Research, 5 (2003) 17-30.

[130] G. Wood, J. O'sullivan, B. Vaszko, The direct observation of barrier layers in porous anodic oxide films, Journal of The Electrochemical Society, 115 (1968) 618-620.

[131] E. Eichinger, J. Osborne, T. Van Cleave, Hexavalent chromium elimination: An aerospace industry progress report, Metal Finishing, 95 (1997) 36-41.

[132] A. Dattilo, C. Romano, S. Tamiro, Anodizing process, with low environmental impact, for a workpiece of aluminium or aluminium alloys, European Patent EP1233084, (2002).

[133] M. García-Rubio, P. Ocón, A. Climent-Font, R.W. Smith, M. Curioni, G.E. Thompson, P. Skeldon, A. Lavía, I. García, Influence of molybdate species on the tartaric acid/sulphuric acid anodic films grown on AA2024 T3 aerospace alloy, Corrosion Science, 51 (2009) 2034-2042.

[134] M. Curioni, P. Skeldon, E. Koroleva, G.E. Thompson, J. Ferguson, Role of tartaric acid on the anodizing and corrosion behavior of AA 2024 T3 aluminum alloy, Journal of the Electrochemical Society, 156 (2009) C147-C153.

[135] G. Boisier, N. Pebere, C. Druez, M. Villatte, S. Suel, FESEM and EIS study of sealed AA2024 T3 anodized in sulfuric acid electrolytes: Influence of tartaric acid, Journal of the Electrochemical Society, 155 (2008) C521-C529.

[136] L. Iglesias-Rubianes, S.J. Garcia-Vergara, P. Skeldon, G.E. Thompson, J. Ferguson, M. Beneke, Cyclic oxidation processes during anodizing of Al-Cu alloys, Electrochimica Acta, 52 (2007) 7148-7157.

[137] G.E.J. Poinern, N. Ali, D. Fawcett, Progress in nano-engineered anodic aluminum oxide membrane development, Materials, 4 (2011) 487-526.

[138] J.W. Diggle, T.C. Downie, C. Goulding, Anodic oxide films on aluminum, Chemical Reviews, 69 (1969) 365-405.

[139] C. Voon, M. Derman, U. Hashim, K. Ahmad, K. Foo, Effect of temperature of oxalic acid on the fabrication of porous anodic alumina from Al-Mn alloys, Journal of Nanomaterials, 2013 (2013) 40.

[140] G. Sulka, K. Parkoła, Temperature influence on well-ordered nanopore structures grown by anodization of aluminium in sulphuric acid, Electrochimica Acta, 52 (2007) 1880-1888.

[141] F. Li, L. Zhang, R.M. Metzger, On the growth of highly ordered pores in anodized aluminum oxide, Chemistry of materials, 10 (1998) 2470-2480.

[142] M.R. Lukatskaya, Y. Gogotsi, Three-dimensional nanostructures from porous anodic alumina, MRS Communications, 2 (2012) 51-54.

[143] G.D. Sulka, Highly ordered anodic porous alumina formation by self-organized anodizing, Nanostructured materials in electrochemistry, 1 (2008) 1-116.

[144] H. Masuda, K. Fukuda, Ordered metal nanohole arrays made by a two-step replication of honeycomb structures of anodic alumina, science, 268 (1995) 1466.

[145] S.-H. Su, C.-S. Li, F.-B. Zhang, M. Yokoyama, Characterization of anodic aluminium oxide pores fabricated on aluminium templates, Superlattices and Microstructures, 44 (2008) 514-519.

[146] F. Keller, M. Hunter, D. Robinson, Structural features of oxide coatings on aluminum, Journal of the Electrochemical Society, 100 (1953) 411-419.

[147] V. Parkhutik, V. Shershulsky, Theoretical modelling of porous oxide growth on aluminium, Journal of Physics D: Applied Physics, 25 (1992) 1258.

[148] L. Hao, B.R. Cheng, Sealing processes of anodic coatings—past, present, and future, Metal Finishing, 98 (2000) 8-18.

[149] V. López, M.J. Bartoloḿ, E. Escudero, E. Otero, J.A. González, Comparison by SEM, TEM, and EIS of hydrothermally sealed and cold sealed aluminum anodic oxides, Journal of the Electrochemical Society, 153 (2006).

[150] F. Mansfeld, C. Chen, C.B. Breslin, D. Dull, Sealing of anodized aluminum alloys with rare earth metal salt solutions, Journal of the Electrochemical Society, 145 (1998) 2792-2798.

[151] R.S. Alwitt, R.C. McClung, S. Jacobs, Anodized aluminium coating for thermal control, Part I: coating process and stresses. AIAA-922158-CP, AAIA Technical Papers (A92-31285 12-23), Washington DC, 39-45., (1992).

[152] S. Wernick, R. Pinner, P. Sheasby, The Surface Treatment and Finishing of Aluminium Alloys, Vol. 1/2, in, Finishing Publications Ltd., Teddington, 1996.

[153] A. Brace, P. Sheasby, The Technology of Anodizing AluminiumTechnicopy Ltd, Stonenhouse, Gloucestershire, England, (1979) 1.

[154] P. Sheasby, G. Bancroft, The Use of an Ammonium Acetate Buffer Solution for Sealing Anodized Aluminium, Transactions of the IMF, 48 (1970) 140-144.

[155] W. Friedemann, H. Germscheid, Sealing anodized aluminum, in, Google Patents, 1974.

[156] R.S. Dunham, Brit. Pat. 939, 996 (1931).

[157] J.D. Edwards, U.S. Pat. 1 , 946, 162 (1934).

[158] N. Tomashov, A. Tyukijna, Light futals, (1946) 22-35.

[159] L. Whitby, Anodic oxide coating. Influence of sealing treatments on protective value, Metal Industry, 72 (1948) 400-403.

[160] D.R. Arnott, B.R.W. Hinton, N.E. Ryan, Materials performance, 26 (1987) 42-47.

[161] D. Arnott, B. Hinton, N. Ryan, Cationic-film-forming inhibitors for the protection of the AA 7075 aluminum alloy against corrosion in aqueous chloride solution, Corrosion, 45 (1989) 12-18.

[162] F. Mansfeld, Y. Wang, S. Lin, Elimination of pitting of aluminum alloys by surface modification, Proc Electrochem Soc, 95 (1996) 308-322.

[163] F. Mansfeld, Y. Wang, Development of "stainless" aluminum alloys by surface modification, Materials Science and Engineering: A, 198 (1995) 51-61.

[164] L. Wilson, B. Hinton, A method of forming a corrosion resistant coating, Patent WO, 88 (1988) 06639.

[165] P. Campestrini, H. Terryn, A. Hovestad, J. De Wit, Formation of a cerium-based conversion coating on AA2024: relationship with the microstructure, Surface and Coatings Technology, 176 (2004) 365-381.

[166] A. Hughes, R. Taylor, B. Hinton, L. Wilson, XPS and SEM characterization of hydrated cerium oxide conversion coatings, Surface and interface analysis, 23 (1995) 540-550.

[167] A.E. Hughes, J.D. Gorman, P.R. Miller, B.A. Sexton, P.J.K. Paterson, R.J. Taylor, Development of cerium-based conversion coatings on 2024-T3 Al alloy after rare-earth desmutting, Surface and Interface Analysis, 36 (2004) 290-303.

[168] P. Yu, S.A. Hayes, T.J. O'Keefe, M.J. O'Keefe, J.O. Stoffer, The phase stability of cerium species in aqueous systems, Journal of the Electrochemical Society, 153 (2006) C74-C79.

[169] M. Curioni, A. Zuleta, E. Correa, X. Pan, A. Baron-Wiechec, P. Skeldon, J. Castaño, F. Echeverría, G. Thompson, Formation of protective anodic oxides on aluminium by low voltage anodising in sulphuric acid with cerium nitrate and tartaric acid additions, Transactions of the IMF, 90 (2012) 290-297.

[170] S.A. Hayes, P. Yu, T.J. O'Keefe, M.J. O'Keefe, J.O. Stoffer, The phase stability of cerium species in aqueous systems. I. E-pH diagram for the Ce-HClO4-H2O system, Journal of the Electrochemical Society, 149 (2002) C623-C630.

[171] P. Pedeferri, Corrosione e protezione dei materiali metallici, 2004.

[172] A. Lasia, Electrochemical impedance spectroscopy and its applications, in: Modern aspects of electrochemistry, Springer, 2002, pp. 143-248.

[173] X.-Z. Yuan, C. Song, H. Wang, J. Zhang, EIS equivalent circuits. In: Electrochemical Impedance Spectroscopy in PEM Fuel Cells, Springer, 2010.

[174] I. Raistrick, D. Franceschetti, Impedance Spectroscopy: Theory, Experiment, and Applications, edited by E. Barsoukov and JR Macdonald, in, Wiley-VCH, New York, 2005.

[175] J. Bisquert, Theory of the impedance of electron diffusion and recombination in a thin layer, The Journal of Physical Chemistry B, 106 (2002) 325-333.

[176] D.R. Franceschetti, J.R. Macdonald, R.P. Buck, Interpretation of Finite-Length-Warburg-Type Impedances in Supported and Unsupported Electrochemical Cells with Kinetically Reversible Electrodes, Journal of the Electrochemical Society, 138 (1991) 1368-1371.

[177] G. Walter, A review of impedance plot methods used for corrosion performance analysis of painted metals, Corrosion Science, 26 (1986) 681-703.

[178] J.R. Macdonald, J. Schoonman, A. Lehnen, Applicability and power of complex nonlinear least squares for the analysis of impedance and admittance data, Journal of Electroanalytical Chemistry and Interfacial Electrochemistry, 131 (1982) 77-95.

[179] Y.N. Mikhailovskii, V. Leonov, N. Tomashov, Measuring the resistance of insulating protective coatings on metals immersed in electrolytes, Zashchita Metal, 1 (1965) 577-582.

[180] M. Kendig, F. Mansfeld, S. Tsai, Determination of the long term corrosion behavior of coated steel with AC impedance measurements, Corrosion Science, 23 (1983) 317-329.

[181] G. Walter, Application of impedance measurements to study performance of painted metals in aggressive solutions, Journal of Electroanalytical Chemistry and Interfacial Electrochemistry, 118 (1981) 259-273.

[182] J. Castle, P. Zhdan, Characterization of surface topography by SEM and SFM: problems and solutions, Journal of Physics D: Applied Physics, 30 (1997) 722.

[183] D. Wlodzimierz, P. Jaroslaw, S. Witold, Three-dimensional characterization of microstructures in a SEM, Measurement Science and Technology, 17 (2006) 28.

[184] J. Goldstein, D.E. Newbury, P. Echlin, D.C. Joy, A.D. Romig Jr, C.E. Lyman, C. Fiori, E. Lifshin, Scanning electron microscopy and X-ray microanalysis: a text for biologists, materials scientists, and geologists, Springer Science & Business Media, 2012.

[185] M. Curioni, P. Skeldon, J. Ferguson, G.E. Thompson, Reducing the energy cost of protective anodizing, Journal of Applied Electrochemistry, 41 (2011) 773-785.

[186] M. Curioni, P. Skeldon, G.E. Thompson, J. Ferguson, Graded anodic film morphologies for sustainable exploitation of aluminium alloys in aerospace, in: Advanced Materials Research, 2008, pp. 48-55.

[187] M. Curioni, A.A. Zuleta, E. Correa, X. Pan, A. Baron-Wiechec, P. Skeldon, J.G. Castaño, F. Echeverría, G.E. Thompson, Formation of protective anodic oxides on aluminium by low voltage

anodising in sulphuric acid with cerium nitrate and tartaric acid additions, Transactions of the Institute of Metal Finishing, 90 (2012) 290-297.

[188] M. Curioni, F. Scenini, T. Monetta, F. Bellucci, Correlation between electrochemical impedance measurements and corrosion rate of magnesium investigated by real-time hydrogen measurement and optical imaging, Electrochimica Acta, 166 (2015) 372-384.

[189] M. Curioni, M. Saenz De Miera, P. Skeldon, G.E. Thompson, J. Ferguson, Macroscopic and local filming behavior of AA2024 T3 aluminum alloy during anodizing in sulfuric acid electrolyte, Journal of the Electrochemical Society, 155 (2008) C387-C395.

[190] M. Curioni, P. Skeldon, G.E. Thompson, Anodizing of aluminum under nonsteady conditions, Journal of the Electrochemical Society, 156 (2009) C407-C413.

[191] A. Carangelo, A. Acquesta, T. Monetta, F. Bellucci, M. Curioni, Corrosion behaviour of AA2024-T3 anodized in tartaric sulphuric acid and sealed in environmentally friendly solutions, Metallurgia Italiana, 109 (2017) 83-86.

[192] A. Carangelo, M. Curioni, A. Acquesta, T. Monetta, F. Bellucci, Application of EIS to in situ characterization of hydrothermal sealing of anodized aluminum alloys: Comparison between hexavalent chromium-based sealing, hot water sealing and cerium-based sealing, Journal of the Electrochemical Society, 163 (2016) C619-C626.

[193] A. Carangelo, M. Curioni, A. Acquesta, T. Monetta, F. Bellucci, Cerium-based sealing of anodic films on AA2024T3: Effect of pore morphology on anticorrosion performance, Journal of the Electrochemical Society, 163 (2016) C907-C916.

[194] H. Habazaki, X. Zhou, K. Shimizu, P. Skeldon, G.E. Thompson, G.C. Wood, Mobility of copper ions in anodic alumina films, Electrochimica Acta, 42 (1997) 2627-2635.

[195] J. Hitzig, W.J. Lorenz, J. Juttner, W. Paatsch, AC-impedance measurements on porous aluminium oxide films, Corrosion Science, 24 (1984) 945-952.

[196] B. Hirschorn, M.E. Orazem, B. Tribollet, V. Vivier, I. Frateur, M. Musiani, Constant-phase-element behavior caused by resistivity distributions in films, in: ECS Transactions, 2010, pp. 77-94.

[197] Y. Ma, X. Zhou, G.E. Thompson, M. Curioni, P. Skeldon, X. Zhang, Z. Sun, C. Luo, Z. Tang, F. Lu, Anodic film growth on Al-Li-Cu alloy AA2099-T8, Electrochimica Acta, 80 (2012) 148-159.

[198] I.V. Gordovskaya, T. Hashimoto, J. Walton, M. Curioni, G.E. Thompson, P. Skeldon, Development of cerium-rich layers on anodic films formed on pure aluminium and AA7075 T6 alloy, Journal of the Electrochemical Society, 161 (2014) C601-C606.